Fundamentals and Applications of Semiconductor Nanocrystals

A study on the synthesis, optical properties, and interactions of quantum dots

Cover art designed by ADA, inspired by Roy Lichtenstein's "Magnifying Glasses"

This research was funded by the European Union network "FULLSPECTRUM"
(SES6-CT-2003-502620)
Printed by Gildeprint Drukkerijen
ISBN: 978-90-393-4919-9

Fundamentals and Applications of Semiconductor Nanocrystals

A study on the synthesis, optical properties, and interactions of quantum dots

Fundamentele Eigenschappen en Toepassingen van Halfgeleider Nanokristallen

Een studie naar de synthese, optische eigenschappen en interacties van quantum dots

(met een samenvatting in het Nederlands)

Proefschrift

ter verkrijging van de graad van doctor aan de Universiteit Utrecht op gezag van de rector magnificus, prof.dr. J.C. Stoof, ingevolge het besluit van het college voor promoties in het openbaar te verdedigen op woensdag 15 oktober 2008 des middags te 2.30 uur

door

Roelof Koole

geboren op 18 juni 1980, te Arcen en Velden

Promotores: Prof.dr. A. Meijerink
Prof.dr. D. Vanmaekelbergh

Co-promotor: Dr. C. de Mello Donegá

Table of Contents

Chapter 1: 7
Introduction to the Fundamental Properties of Quantum Dots and their Applications

Chapter 2: 39
Synthesis and Self-assembly of PbSe Nanospheres, Nanostars and Nanocubes

Chapter 3: 59
Optical Investigation of Quantum Confinement in PbSe Nanocrystals at Different Points in the Brillouin Zone

Chapter 4: 75
Exciton Energy Transfer in Cross-Linked CdTe Quantum Dots

Chapter 5: 89
Differences in Cross-link Chemistry between Rigid and Flexible Dithiol-molecules Revealed by Optical Studies of CdTe Quantum Dots

Chapter 6: 109
Time-Dependent Photoluminescence Spectroscopy as a Tool to Measure the Ligand Exchange Kinetics on a Quantum Dot Surface

Chapter 7: 133
Quantum Dots with a Paramagnetic Coating as a Bimodal Molecular Imaging Probe

Chapter 8: 147
On the Incorporation Mechanism of Hydrophobic Quantum Dots in Silica Spheres by a Reverse Microemulsion Method

Chapter 9: 167
Paramagnetic Lipid-coated Silica Nanoparticles with a Fluorescent Quantum Dot Core: a New Contrast Agent Platform for Multimodality Imaging

Samenvatting in het Nederlands 185

Acknowledgements 189

List of Publications 191

Curriculum Vitae 195

Chapter 1

Introduction to the Fundamental Properties of Quantum Dots and their Applications

1.1 Introduction

There is currently a strong drive among researchers to explore the possibilities of making and characterizing materials of smaller and smaller sizes. This drive is caused by two factors. First of all, there is a great fundamental interest in the new electronic or optical properties that arise when a material becomes so small that it consists of only a few tens to thousands of atoms. At this length-scale of typically a few nanometers, quantum mechanical effects start to dominate the properties of the bulk material, as will be explained below. To synthesize such small nanomaterials with a high degree of control is one part of the challenge in nanotechnology; to develop highly sensitive techniques for investigating the morphological, electronic and optical properties of the (individual) nanocomponents is equally important.

Besides the scientific interest, the wide range of potential applications based on nanomaterials is an important driving force to push the size of materials to the smallest limits. The most illustrative example is that of the chip-technology, where the continuation of Moore's law is currently dictating industry to make transistors that are only a few tens of nanometers wide.[1] It is not only a challenge to construct such small patterns in silicon with a high precision, also avoiding (undesired) quantum mechanical coupling between the individual components of the transistors that start to occur at this length-scale is crucial. As another example, the large effective surface area that can be achieved using nanomaterials can be very beneficial in, for example, solar cells or catalytic materials. The tunable electronic or optical properties of nanomaterials (explained below) can be of great value for applications like LED's, displays, solar cells, detectors, biomarkers, and so on.

This thesis focuses on both the fundamental properties and applications of one specific class of nanomaterials, called colloidal nanocrystalline quantum dots (QDs)[2]: very small nanocrystals (2-10 nanometer) made of a semiconductor material (*e.g.* CdSe, PbSe, Si, InP). By changing the size of the nanocrystal, one can tune the emission wavelength of QDs over a broad range. After a general introduction to quantum dots, the first part of this introduction will explain the origin of these interesting size-dependent optical properties of quantum dots. The second part of the introduction focuses on two important applications of colloidal QDs: as contrast agent for bio-imaging applications, and as building blocks for novel types of solar cells.

1.2.1 Quantum Dot Structures

The most general definition of a quantum dot is a semiconductor crystal in which electrons and/or holes are confined in all three dimensions. This requires a structure with dimensions between approximately 2 and 10 nm, the typical spatial extension of electrons and holes in semiconductors. As a consequence of the confinement of electrons and holes in a small volume, the kinetic energy of the carriers rises above their bulk value. These so-called *quantum confinement effects*[3-5] are size-dependent and result in discrete (quantized) energy levels, as will be explained in detail in sections 1.2.3 and 1.2.4. The confinement of electrons and holes in quantum dots results from the fact that the (potential) energy of charge carriers within the dot is smaller than in the surrounding matrix. Such a

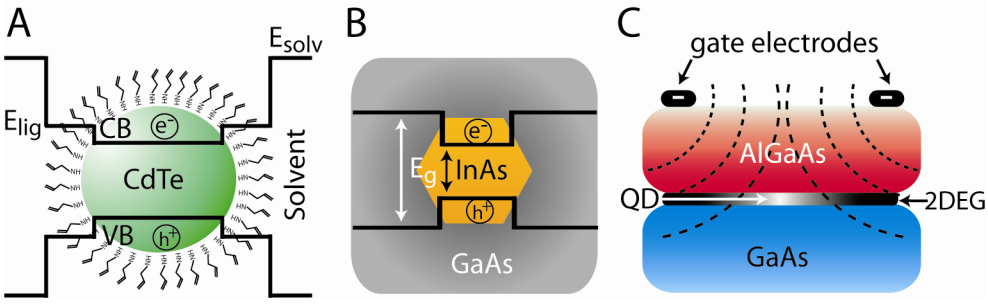

Figure 1.1 Schematic representation of three types of QD-structures. (A) Colloidal CdTe QD in dispersion. The potential well in the QD is formed by the much higher potential energy for electrons (holes) of the surrounding solvent. The organic ligands at the surface of the QD form an intermediate energy barrier. (B) Epitaxially grown InAs QD in a GaAs matrix that has a larger bandgap, resulting in a potential well for charge carriers within the InAs QD. (C) Laterally gated QD. A 2-dimensional electron gas (2DEG) is formed at the interface between (n-type) AlGaAs and GaAs and confined in two more dimensions by an electric field generated by gate electrodes on top of the device.

potential well for electrons and holes can be achieved by various architectures, of which three examples are given below.

The first type of quantum dots is represented by colloidal semiconductor nanocrystals (the subject of this thesis). Colloidal quantum dots are prepared by a wet chemical synthesis, and by varying the reaction conditions (temperature, growth time, reactants), the size and shape of the nanocrystals can be accurately controlled (see Chapter 2). The potential well for electrons (holes) within the quantum dot is caused by the much higher potential energy of the surrounding medium, which is typically a solvent. The passivating organic ligands that are attached to the surface of the quantum dot (to stabilize the QDs in dispersion) form an intermediate energy barrier between the semiconductor nanocrystal and the surrounding medium, schematically depicted in Figure 1.1A.

The second example is that of epitaxially grown quantum dots, where the potential well for electrons (holes) within a small semiconductor sphere is the result of a surrounding semiconductor material which has a conduction band (valence band) that is higher (lower) in energy (Figure 1.1B). A typical example of such a system is the combination of small InAs islands embedded in a matrix of GaAs. These structures can be grown with a high degree of control using molecular beam (Stranski-Krastanow) epitaxy.[6, 7] One of the advantages of this technique is that the position of vertically aligned InAs quantum dots in the GaAs matrix can be precisely controlled, which allows one to study the interactions between neighboring quantum dots. For example, strong electronic coupling and entanglement of states between two adjacent quantum dots has been observed by optical spectroscopy.[8]

The final example concerns a more complicated quantum-dot design and is formed in a semiconductor crystal by the field effect of a gate electrode. In such a gated semiconductor quantum dot, one starts with a 2-dimensional electron gas (2DEG) that is formed at the interface between a GaAs and (n-doped) AlGaAs layer. The 2DEG is confined in two more dimensions by applying a negative potential to metal gate electrodes that are deposited on top of the device (see

Figure 1.1C). The negative potential causes a depletion of electrons in the 2DEG in the close vicinity of the gate electrodes, which confines the electron to a well-defined spot in between the electrodes. This potential well in between the gate electrodes forms the laterally gated quantum dot. A source and drain electrode can also be integrated in the device, which allows one to add (or remove) one or more electrons to the quantum dot, or to study the tunneling of individual electrons through a single quantum dot.[9] By applying an (oscillating) magnetic field to the device, Zeeman splitting and coherent control of a single electron spin can also be studied.[10, 11]

1.2.2 Description of bulk semiconductors using perturbation theory

To understand the unique properties of (colloidal) semiconductor quantum dots that result from quantum confinement, it is instructive to first look at the quantum mechanical description of a bulk semiconductor. In contrast to a free electron traveling through vacuum, electrons in a semiconductor experience a periodic potential caused by the crystal lattice. The Hamiltonian to describe such a system (in one dimension) is as follows:

$$H = H^0 + V(x) = -\frac{\hbar^2}{2m}\frac{\partial^2}{\partial x^2} + V(x) \qquad (1.1)$$

where *V(x)* describes the periodic potential set by the crystal lattice. The potential is periodic over the lattice constant *a*, so that *V(x)=V(x+a)*. This means that the Schrödinger equation after translation of the wavefunction *ψ(x)* by a distance *a* (*ψ(x+a)*), can be written as:

$$-\frac{\hbar^2}{2m}\frac{\partial^2}{\partial x^2}\psi(x+a) + V(x)\psi(x+a) = E\psi(x+a) \qquad (1.2)$$

After translation over distance *a*, the wavefunctions should still have the same eigenvalue *E*. This implies that the wavefunctions *ψ(x)* and *ψ(x+a)* should only differ by a phase-factor. A wavefunction that obeys this criterium and that is an eigenfunction of the Schrödinger equation 1.2 can be written as follows:[12]

$$\psi_{bloch,k}(x) = e^{ikx} \cdot u_k(x) \qquad (1.3)$$

where *k* is defined as the wavevector ($k=2\pi/\lambda$) and $u_k(x)$ is a function that is periodic with the lattice constant ($u_k(x)=u_k(x+a)$). The resulting wavefunction is called a Bloch function and is a plane wave (e^{ikx}) that is modulated by a periodic function ($u_k(x)$). Physically, the plane wave represents the phase (*i.e.* the sign of the amplitude) of the wavefunction, whereas $u_k(x)$ describes the response of the valence electrons to the periodic potential of the crystal lattice. This will be illustrated further in section 1.2.4. Translation of the Bloch function over a distance *a* gives:

$$\psi_{bloch,k}(x+a) = e^{ika} \cdot \psi_{bloch,k}(x) \tag{1.4}$$

which shows that the wavefunction indeed only differs by a (phase) constant after translation over *a*.

A free electron in vacuum (described by only the plane wave $\psi(x)=e^{ikx}$) has a continuum of energy levels with the dispersion relation (see also Figure 1.2A):

$$E(k) = \frac{\hbar^2 k^2}{2m_0} \tag{1.5}$$

The periodic potential in a crystal lattice causes an important change in the dispersion relation for electrons. Electrons that propagate through the lattice with a wavelength that is very different from the lattice spacing *a* are only slightly disturbed and therefore the energy is similar to that of free electrons. However, when the wavelength of electrons is similar to twice the lattice spacing, or in other words when $k=\pi/a$, the electrons are reflected by the periodic potential. The Bragg reflection results in standing waves, described by a linear combination of the plane waves with $k=\pi/a$ and $k=-\pi/a$. The two resulting standing waves ψ^{+}_{bloch} and ψ^{-}_{bloch} are very similar except for a displacement by $a/2$. This causes a significant difference in energy between the two standing waves, because the first one concentrates the electron probability at the ions (lowering the potential energy), whereas the second standing wave concentrates the probability exactly in between the ions (increasing the potential energy). The energy difference between the two standing waves causes an energy gap in the dispersion relation of electrons in a periodic potential at $k=n\pi/a$ (where *n* is an integer), which is called the bandgap (see Figure 1.2A).

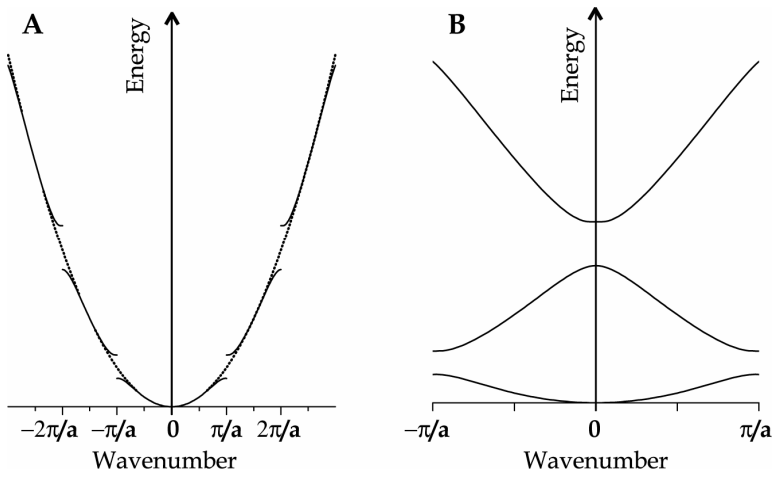

Figure 1.2 (A) Dispersion relation of free electrons in vacuum (dotted line), and of electrons in the periodic potential of an infinite crystal with lattice constant *a* (solid line). (B) Reduced zone representation of the dispersion relation for electrons in a periodic potential in (A). Reprinted with permission from ref [13].

Another property of the Bloch function is the periodicity in k: wavefunctions with k-values that differ by $n2\pi/a$ are equivalent, as can be derived from equation 1.4. This may be interpreted as follows: the value of the phase (*i.e.* e^{ikx}) at the ions ($x=qa$, where q is an integer) is exactly the same for k and $k+2\pi/a$, thus describing the same physical situation. Consequently, the energy dispersion relation may be restricted to k-values between $-\pi/a<k<\pi/a$. Values of larger k can be folded inside this region by subtracting $2\pi/a$ from the k-value. The resulting interval (in 1 dimension) is called the first Brillouin zone, and the energy dispersion relation can be plotted within this reduced zone (Figure 1.2B). By reducing the dispersion relation to the interval $-\pi/a<k<\pi/a$, energy bands appear, and one k-value has multiple corresponding energies (which may be regarded as overtones). The bandgaps between the different bands occur at $k=\pi/a$ and $k=0$.

What happens if we consider a semiconductor of more than one dimension? Bragg reflection will occur for k-values that have the periodicity of the lattice. For a simple (primitive) cubic lattice, this means that in the <110> direction reflection will occur when $k=\sqrt{2}\pi/a$, and in the <111> direction when $k=\sqrt{3}\pi/a$. This implies that bandgaps will arise not only at $k=\pi/a$, but also at $k=\sqrt{2}\pi/a$ (where $k_x=k_y=\pi/a$ and $k_z=0$) and at $k=\sqrt{3}\pi/a$ (with $k_x=k_y=k_z=\pi/a$). The first Brillouin zone (BZ) of a simple cubic lattice in 3 dimensions is a plain cube in reciprocal space, and has different bandgaps at different point in this Brillouin zone. For the hexagonal close-packed lattice (HCP, *e.g.* the wurtzite crystal structure of CdSe), the first Brillouin zone is more complicated, as depicted in Figure 1.3A. The (Greek) letters are the conventional symbols to denote the different points in the BZ of the HCP lattice. For example, the Γ-point is located at $k_{x,y,z}=0$, and in the specific case of CdSe, the fundamental bandgap is located at this point. It can be seen that there is only one Γ-point in the first BZ of a HCP lattice. In case of a cubic face-centered cubic (FCC) crystal structure (*e.g.* the rock salt lattice of PbSe, or the zinc blende lattice of CdTe), the first Brillouin Zone has the shape of a truncated octahedron (Figure 1.3B). In the case of PbSe (and PbS and PbTe), the fundamental bandgap is located at the L-point in the BZ. In contrast to for example CdSe, the value for k at the fundamental bandgap is not zero, but maximal ($k_{x,y,z}=\pi/a$, and $|k|=\sqrt{3}\pi/a$). It is apparent from Figure 1.3B that there are 8 L-point at the edges of the first BZ, but since every L-point is shared by a neighboring BZ, the fundamental bandgap of

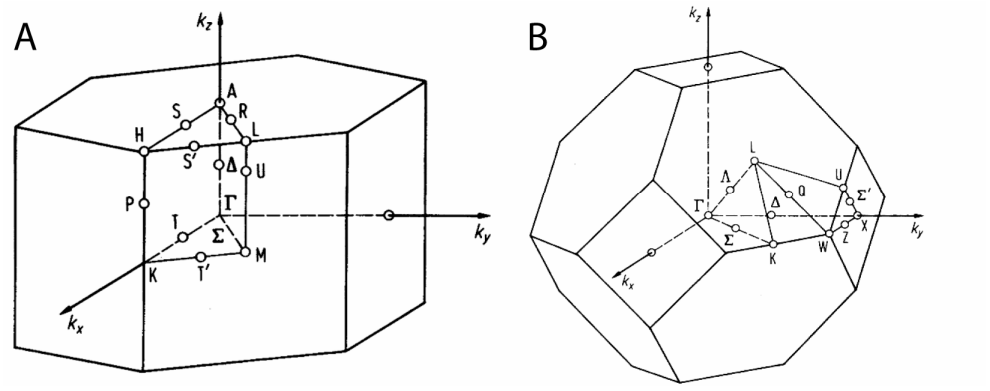

Figure 1.3 First Brillouin Zone of an HCP (A) and FCC (B) crystal structure.

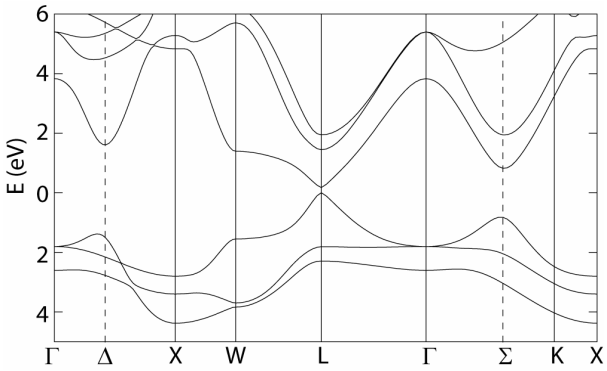

Figure 1.4 Band structure of bulk PbSe. The zero of energy is at the top of the valence band at the L-point, where the fundamental bandgap is located.[14]

PbSe is (8/2=) 4-fold degenerate (8-fold including spin). The L-point is in the <111> direction in reciprocal space, and the four L-states can be seen as states with the same absolute value of *k*, but with a momentum in four different directions (<111>, <11-1>, 1-11>, and <-111>).

It is difficult to draw the complete dispersion relation as displayed in Figure 1.2 for a three dimensional system. The usual way of plotting the energy dependence of electrons in a 3-D semiconductor is plotted in Figure 1.4, which shows the band structure of PbSe. The symbols on the x-axis correspond to the symbols in Figure 1.3B, and the diagram shows the evolution of energy when going from one point in the BZ to the other. It should be noted that such a band diagram does *not* show all *k*-values and therefore is only a representation of the dispersion relation for some of the most relevant points in the BZ, in only a few directions in reciprocal space. For example, it is clear from the band structure of PbSe in Figure 1.4 that the bandgap with the lowest energy is located at the L-point.

1.2.3 Quantum Confinement: the Top-Down approach

The description of the band structure of semiconductors in the previous section was based on an infinite crystal. But what happens when the semiconductor crystal becomes very small? There are two ways to look at this problem: the first method (called the top-down approach from now on) is to correct the bulk electronic properties of a semiconductor for the finite crystal size, by taking into account the effects of confining electrons and holes into a small volume. The second method is to view a quantum dot as a very large molecule or cluster that consists of a few hundred or thousand atoms (ions), and by building up the electronic and optical properties of such a nanocrystal from the atomic orbitals. This last method can be seen as the bottom-up approach, and will be explained in the next section.

In the top down approach, the Bloch wavefunctions describing the bulk properties of the semiconductor (including Brillouin zone, and band structure) are maintained, but multiplied by an envelope function to correct for the confinement of electrons (and holes) in the small QD-container:

$$\Psi_{total}(x) = \psi_{bloch}(x) \cdot \varphi_{env}(x) \tag{1.6}$$

The total wavefunction (Ψ_{total}) is thus the product of the Bloch function describing the bulk-properties of the semiconductor, and the envelope function (φ_{env}) that describes the confinement effects of the charge carriers in the quantum dot. The envelope function is the solution of the Schrödinger equation for a particle-in-a-sphere problem. For a 3-D box with dimensions *L*, the wavefunction would simply be the product of sinusoidal functions in *x*, *y*, and *z*-directions. However, for a particle in a sphere (which is a better representation of a quantum dot), the eigenfunctions can be best described as the product of spherical harmonics ($Y(\theta,\varphi)$) and a radial Bessel function ($R(r)$)[12]:

$$\varphi_{env}(\theta,\phi,r) = Y_l^m(\theta,\phi) \cdot R(r) \tag{1.7}$$

The envelope function has a close resemblance with the wavefunctions describing the electron of a hydrogen atom; in that case however, the potential experienced by the electron is determined by the positively charged proton ($V(r) \sim 1/r$). In the case of a quantum dot there is no positively charged core, instead the electrons experience a spherical potential well (of diameter *D*) as defined in section 1.2.1: $V(r) = -V_0$ (finite) for $r < D/2$ and $V(r) = 0$ elsewhere. Inserting equation 1.7 in the Schrödinger equation gives the solutions for the discrete energy-levels of a confined electron in a sphere[12]:

$$E_{n,l}^{conf}(D) = \frac{2\hbar^2 \chi_{nl}^2}{m^* D^2} \tag{1.8}$$

where m^* is the effective mass of electrons (or holes), and χ_{nl} are the roots of the Bessel function, which are absolute values depending on (and increasing with) the principal quantum numbers *n* (1, 2, 3,…) and azimuthal quantum number *l* (0, 1, 2, 3…) (written as S, P, D…etc.). The lowest energy level ($n=1$, $l=0$) has the symmetry of a 1S-orbital in a hydrogen atom. A direct consequence of the difference in the potential function ($V(r)$) between the hydrogen-atom and a quantum dot is that the latter system has no restriction of quantum number *l* with respect to quantum number *n*, as is the case in the hydrogen atom ($l \leq n-1$). Therefore the second energy level in a quantum dot has quantum numbers $n=1$ and $l=1$ with a 1P-shaped orbital. The third level is described by a 1D-orbital ($n=1$, $l=2$), and the fourth level in a quantum dot is a 2S level ($n=2$, $l=0$). Due to the atomic-like envelope wavefunctions of the lowest lying energy levels, quantum dots are often referred to as “artificial atoms”.

The bandgap of a quantum dot is now the sum of the fundamental bandgap arising from the bulk properties (E_g^0) and the confinement energy (E^{conf}) as defined in equation 1.8 of both electrons and holes:

$$E_g^{tot}(D) = E_g^0 + E_{n,l}^{conf}(D) = E_g^0 + \frac{2\hbar^2 \chi_{nl}^2}{m_e^* D^2} + \frac{2\hbar^2 \chi_{nl}^2}{m_h^* D^2} \tag{1.9}$$

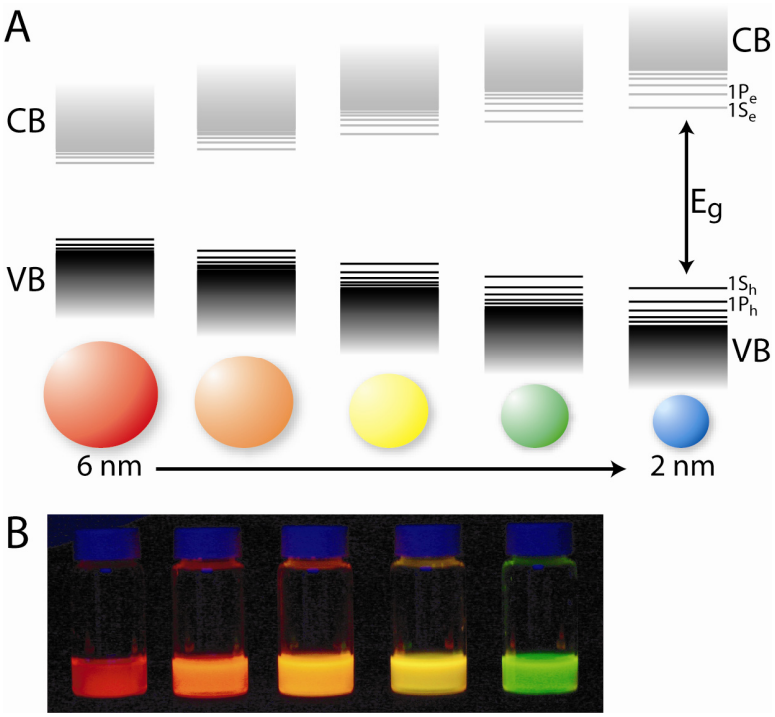

Figure 1.5 (A) Schematic representation of the quantum confinement effects: the bandgap of the semiconductor material increases with decreasing size, and discrete energy levels arise at the band-edges. Note that the energy difference between the band-edge levels also increases with decreasing size. (B) Photograph of the fluorescence of 5 dispersions of CdTe QDs with different sizes, under excitation with a UV-lamp in the dark.

Smaller terms describing the Coulomb interactions between electrons and holes (that become significant in a quantum dot) are neglected here. Equation 1.9 contains the two most important effects of quantum confinement. The first effect is that the bandgap of a semiconductor nanocrystal becomes larger with decreasing size, scaling as D^{-2}. The second effect is that discrete energy levels (with different quantum numbers) arise at the band-edges of both the conduction band and valence band. These two size-dependent effects are schematically depicted in Figure 1.5A. In practice, this means that the optical bandgap of quantum dots can be tuned by simply changing their size. For quantum dots emitting in the visible (*e.g.* CdTe or CdSe QDs) this is nicely visualized by their size-dependent fluorescence color (Figure 1.5B).

The quantum confinement effects are also apparent from the optical absorption spectra of QDs. Figure 1.6 shows the absorption spectra of PbSe quantum dots (with a fundamental bandgap in the near-infrared) of different sizes, and it can be observed that the first transition shifts to higher energy when the size of the quantum dot decreases. The energy-spacing between the discrete levels of the envelope functions with different quantum numbers (equation 1.8) is in the order of hundreds of meV. This implies that the optical transitions between these different levels can be clearly distinguished in the optical absorption spectrum (Figure 1.6).

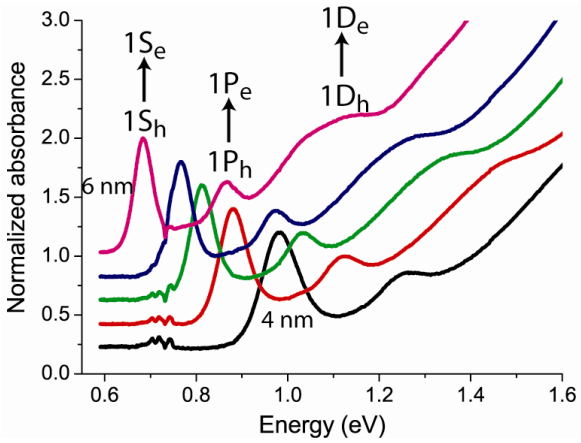

Figure 1.6 Absorption spectra of PbSe QDs ranging in size between 4 and 6 nm. The spectra shift to higher energy with decreasing size. Assignment of the different transitions within one spectrum is indicated for the spectrum shown in magenta (6 nm).

The first optical transition can be assigned to the $1S_h$ to $1S_e$-level (*h* denotes the hole and *e* the electron), the second transition to the $1P_h$ to $1P_e$ level, and so on. The optical selection rules in a quantum dot will be explained in more detail in section 1.2.5. It must be noted that there is still some controversy on the nature of the second transition in PbSe QDs.[15-18] However, there are strong arguments that indicate that the second transition is the allowed $1P_h$ to $1P_e$ transition.[19, 20] A detailed study on the assignment of the different transitions in the absorption spectra of PbSe QDs is presented in Chapter 3 of this thesis.

1.2.4 Quantum Confinement: the Bottom-Up approach

Another method to explain the unique properties of a quantum dot is based on a bottom-up approach. In this approach, the quantum dot is seen as a big molecule or cluster. In analogy with quantum chemical methods for obtaining molecular orbitals (*i.e.* the Linear Combination of Atomic Orbitals (LCAO) and Hückel methods), the overall wavefunctions in a QD can be constructed from the individual atomic orbitals.[2] The simplest case is that of a molecule consisting of only two atoms, where two atomic orbitals combine to make a bonding and an anti-bonding molecular orbital (MO). When only the low-energy (bonding) MO is filled with electrons, it is called the Highest Occupied Molecular Orbital (HOMO). In that case, the high-energy (anti-bonding) level is empty and referred to as the Lowest Unoccupied Molecular Orbitals (LUMO) (Figure 1.7). When the molecule becomes larger (*e.g.* a small CdSe cluster), more energy levels arise, and the energy spacing between the HOMO and LUMO becomes smaller. A quantum dot can be regarded as a very large molecule or cluster consisting of a few hundred or thousand atomic valence orbitals, forming as many MOs. Still, there exist discrete energy levels at the edges of the “bands”, and the spacing between the HOMO and LUMO levels (i.e. the bandgap) becomes smaller when the quantum dot increases in size (Figure 1.7). This explains both quantum confinement effects discussed in

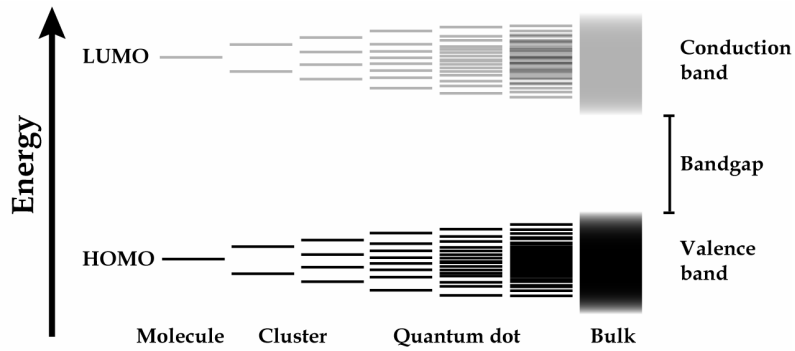

Figure 1.7 Evolution of the energy level-distribution when going from a two-atom molecule (left) to a bulk semiconductor, with a small cluster and a quantum dot as intermediate cases. The more atoms (atomic orbitals) a system has, the more energy levels arise with a decreasing energy difference between the levels, and between the HOMO and LUMO level (*i.e.* a decreasing bandgap). The figure illustrates that a quantum dot can be viewed as a very large molecule, but also as a small semiconductor crystal. Reprinted with permission from ref [13].

the previous section from a molecular point-of-view. Finally, when the semiconductor becomes even larger, the energy-spacing between the MO levels becomes so small that the different energy levels cannot be distinguished experimentally; one speaks of a continuous band of levels in a bulk semiconductor. The energy spacing between the valence and conduction band (HOMO and LUMO) is then called the fundamental bandgap. Below, we will use the LCAO-approach in one dimension to describe the properties of a quantum dot, using CdSe and PbSe as two examples.

In CdSe, the two valence 5s electrons of Cd are donated to the hybridized 4s and 4p valence orbitals of Se. The valence band of CdSe (HOMO) can be regarded as the linear combination of the (filled) $4sp^3$ valence orbitals of Se, whereas the conduction band (LUMO) is comprised of linear combinations of the (empty) 5s atomic orbitals of Cd.[2] What happens if we make a linear combination of valence Se orbitals? In the treatment below we will only consider the problem in one dimension, or in other words a linear CdSe molecule consisting of 8 Cd and 8 Se units. Furthermore, the $4sp^3$ orbitals are viewed as (σ-bonding/anti-bonding) p_x orbitals. Note that the example below is thus a simplified illustration of the complete 3-dimensional description of a real nanocrystal.

Figure 1.8 shows the possible linear combinations of the $4p_x$ orbitals of Se. A sinusoidal function that describes the phase (*i.e.* the sign of the amplitude) of each orbital (unit cell) is also plotted. The energetically most favorable combination takes place when the phase of each p-orbital changes sign at each selenium site (each unit cell), to form σ-bonding p_x-orbitals only. This MO has the lowest energy of all "valence band" levels. The number of σ-bonding p-orbitals decreases when the number of phase-changes decreases, with an increasing number of σ-antibonding p-orbitals. The linear combination of the Se 4p orbitals with the highest energy consists of p-orbitals that have the same phase with respect to each other (all anti-bonding).[2]

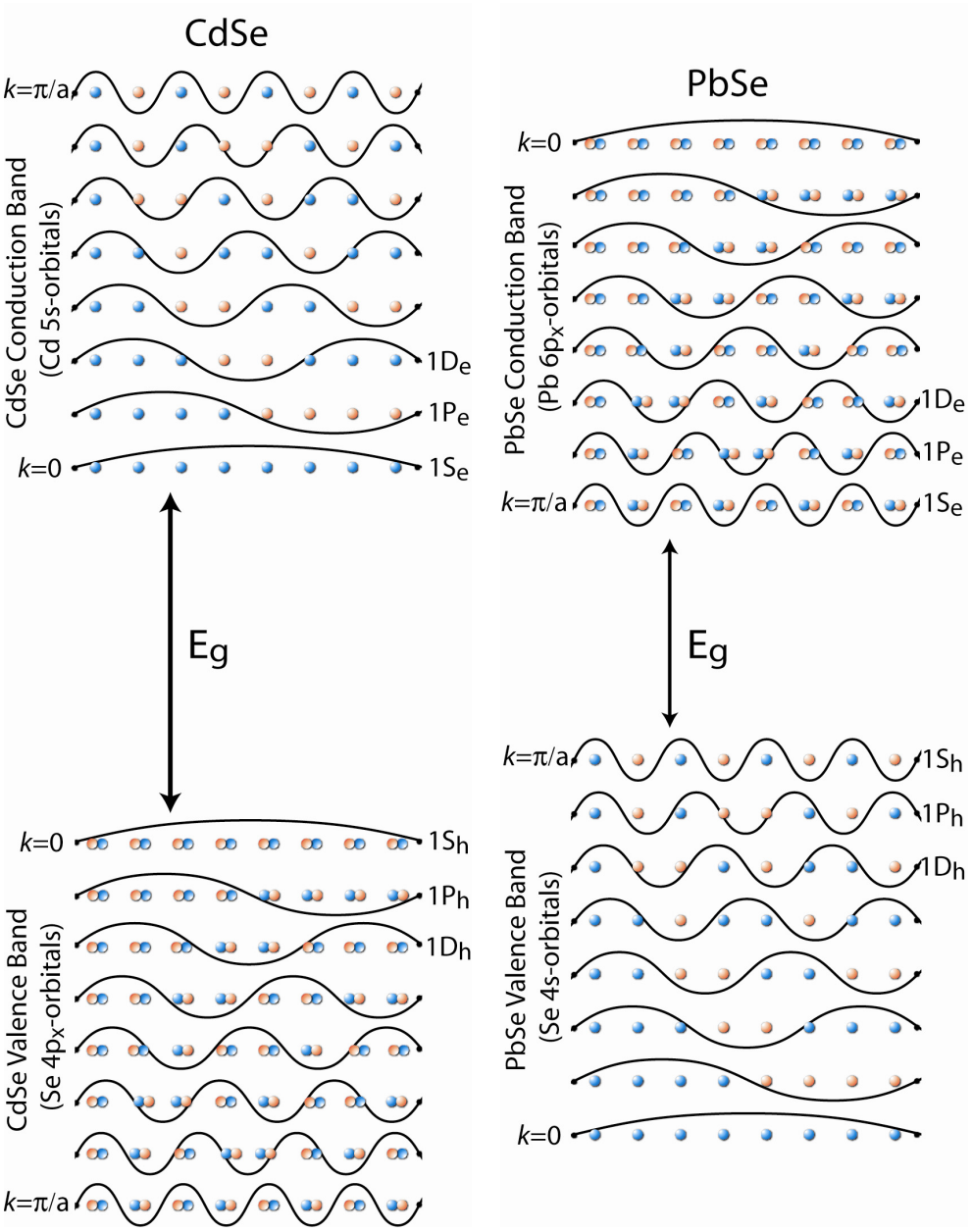

Figure 1.8 LCAO-representation of the MO levels in a CdSe (left) and PbSe (right) QD in one dimension. The sinusoidal functions describe the phase of the atomic orbitals, and can be seen as the plane wave-part of the Bloch function.

At this point, it is instructive to compare the LCAO-approach with the Bloch-functions described above. The sinusoidal function describing the phase of the p-orbitals may be seen as the plane wave (e^{ikx}) of the Bloch function. It was

mentioned in section 1.2.2 that the fundamental bandgap of CdSe is located at the Γ-point in the Brillouin zone. This means that the *k*-value at the top of the valence band is zero. This is consistent with all the p-orbitals being in phase for the highest lying valence band level (HOMO), described by the sinusoidal function with the longest wavelength (i.e. smallest *k*). On the other hand, the lowest valence band level has the maximum *k*-value of π/a, which corresponds with all the p-orbitals changing phase at each selenium site (described by the sinusoidal function with the smallest wavelength). The periodic function ($u_k(x)$) in the Bloch-equation can be seen as the function describing the atomic orbitals; it is periodic over the lattice constant *a* because at each (selenium) site there is an identical atomic (p) orbital. Only the phase changes, which is described by the plane wave.

A similar treatment can be used to describe the conduction band levels of a CdSe quantum dot. They consist of linear combinations of the (empty) 5s-orbitals of Cd. The level with the lowest energy is the linear combination of (bonding) s-orbitals that are all in phase (compare with $k=0$ for CdSe at the bottom of the conduction band). The number of anti-bonding s-orbitals (and thus the energy) increases with increasing number of phase-flips (increasing *k*-value), and the conduction band level with the highest energy consists of a molecular orbital with only anti-bonding s-orbitals ($k=\pi/a$).

For a PbSe quantum dot, the situation is a bit more complicated. The conduction band is made up of a linear combination of (empty) 6p orbitals of Pb. The valence band however, consists of a complex combination of filled hybridized Se $4sp^3$ orbitals, mixed with the filled 6s orbitals of Pb.[16] As a result, the highest lying atomic orbitals that make up the top of the valence band have an s-symmetry.[16, 21] Nevertheless, it should be noted other groups have reported that the top of the valence band of PbSe consists of selenium 4p-orbitals.[15, 22] For the qualitative discussion here however we will assume that the top of the valence band is made up of the selenium 4s orbitals. As mentioned before, the fundamental bandgap of PbSe is located at the L-point of the Brillouin zone, where $k=\pi/a$. This means that the phase of the atomic orbital should change sign at each lattice point for the highest (lowest) MO level of the valence (conduction) band. As is shown in Figure 1.8B, the resulting MO of anti-bonding s-orbitals at the top of the valence band has indeed the highest energy of all possible linear combinations. Similarly, the value of $k=\pi/a$ at the bottom of the conduction band results in a MO of σ-bonding p-orbitals, which has the lowest energy.

The discrete energy levels of the CdSe and PbSe quantum dots are represented by the different molecular orbitals in Figure 1.8. Naturally, the number of levels is much higher when all three dimensions are taken into account. The atomic-like symmetry of the band-edge levels (1S, 1P, …) is not apparent from the sinusoidal functions (plane waves) in Figure 1.8 describing the phase of the atomic orbitals. However, it is clear that the probability of finding an electron at the edge of the quantum dot (in real space) can not be the same as in the centre of the quantum dot. In this qualitative description, an envelope function (explained in the previous section) can be inserted to obtain the atomic-like symmetries for the band-edge MOs. When performing tight-binding or pseudo-potential calculations (based on the LCAO-approach), these atomic-like symmetries automatically arise from the boundary conditions that define the quantum dot.[15, 16]

1.2.5 Optical Transitions in a Quantum Dot

To understand the optical transitions in a quantum dot (and the corresponding selection rules), we first look at what exactly happens during an optical transition in the simpler case of a two level system. In such an optical transition, an electron is excited from a ground state orbital $|1\rangle$ of the molecule to an excited state orbital $|2\rangle$. The underlying process of the excitation is the mixing of the ground state and excited state orbitals into a combined (mixed) state ($\psi = c_1|1\rangle + c_2|2\rangle$).[23] This mixing of the two orbitals is induced by the oscillating electric field of an incoming electromagnetic (EM) wave (photon), and can *only* take place if the mixed state has a dipole moment. The two wavefunctions are mixed because of a distortion (polarization) caused by the oscillating electric field of a photon, which can only happen if a dipole moment is induced in the mixed state, and if the frequency of the EM field corresponds to the frequency difference between the two states. Figure 1.9 shows what happens when different orbitals (with different phases) are combined. It is clear that two orbitals with the same parity combine into a symmetric mixed wavefunction, without a dipole moment. Mixing of these orbitals can not be induced by an oscillating electric field. On the other hand, when two orbitals with a different parity are mixed, the net result is an orbital with a dipole moment. In summary, optical transitions can only occur between orbitals with a different parity (*e.g.* S to P, P to S, or P to D, etc.). This corresponds to the famous

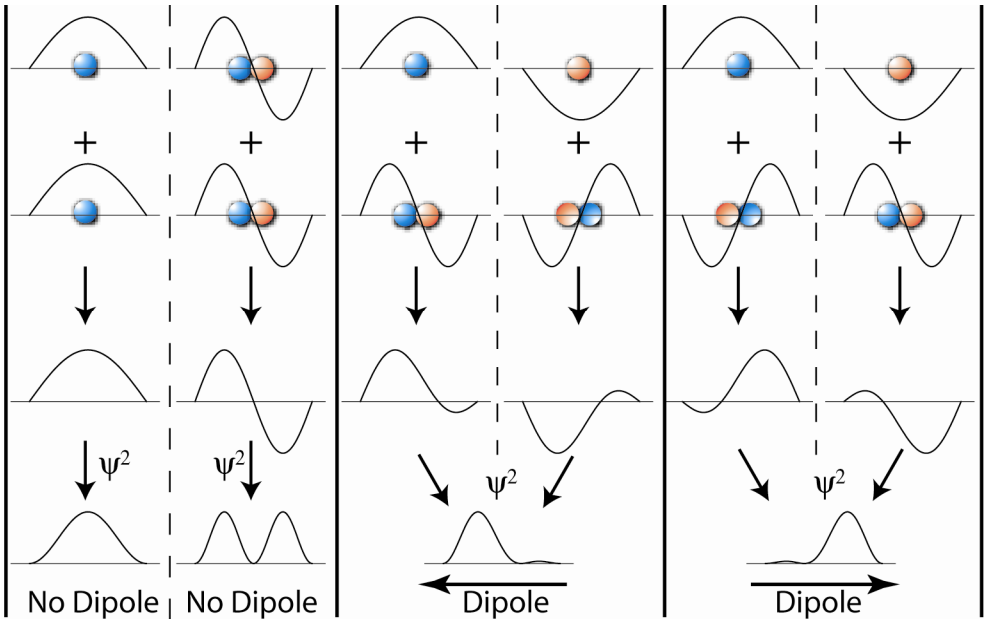

Figure 1.9 Schematic representation of the linear combination of S and P orbitals. When two S or two P orbitals are mixed (left), a symmetric wavefunction results without a dipole moment. Mixing of an S and P orbital (middle and right) results in an asymmetric wavefunction with a dipole moment, the direction of which depends on the phase of the original wavefunctions.

optical selection rule in atoms or molecules: $\Delta\ell=\pm1$. In the treatment below, we focus on this parity selection rule. Other selection rules involving spin and angular momentum are not considered here.

Let us now consider the (coherent) excitation of an electron from the 1S to 1P state in a hydrogen atom. During excitation, the combined state of the 1S and 1P orbitals (with a net dipole moment, see Figure 1.9) starts to oscillate with the frequency of the EM field, and by doing so, the states become more and more mixed. Note that this only happens when the frequency of the incoming wave is resonant with the eigen-frequency of the oscillating dipole (in other words, when the energy of the photon matches the energy difference between the ground and excited state). Initially, the mixed state has mainly 1S-character ($\psi = c_1|1\rangle + c_2|2\rangle$ with $c_1>>c_2$). After a certain number of oscillations (typically ~10^8 for a molecule, depending on the intensity of the EM field)[23] the S and P orbitals are in the maximally mixed state ($c_1=c_2$), which is illustrated in Figure 1.9 (middle and right panels). After this, the mixed state becomes more and more P-like, and after again ~10^8 oscillations the state has purely P-character ($c_1=0$ and $c_2=1$); the excitation is complete. However, the oscillations can continue, to go back to the maximally mixed state and finally the pure S-state again (which can be regarded as stimulated emission, see below). The complete cycle from 1S to 1P and back to the 1S-state is called the Rabi-cycle, and is a fully coherent process. The coherent excitation from the ground state (1S) to the excited state (1P) takes half of the Rabi-cycle, which typically involves ~10^8 oscillations of the EM field (~ μs). In practice, excitation (using an incoherent light source) in atoms or molecules is incoherent, which means that already after a few oscillations (<<ps), the mixed state collapses (decoheres) to either the ground state or excited state.

What about an optical transition in a quantum dot? We will use the bottom-up (LCAO) approach to find how the optical transitions and corresponding selection rules in a quantum dot look like. In contrast to the case of a hydrogen atom, electrons in a quantum dot (*e.g.* CdSe) occupy molecular orbitals. Therefore, we have to look at optical transitions between two molecular orbitals in a quantum dot. The first interband transition is between the highest valence-level ($1S_h$) and lowest conduction-level ($1S_e$), as plotted in Figure 1.10A. It involves the transition from the linear combination of Se 4p-orbitals to the linear combination of Cd 5s orbitals. Within each unit cell, mixing of these states yields a dipole moment (indicated by the small arrows in Figure 1.10). Because the atomic orbitals are all in phase ($k=0$), all the dipoles of the individual unit cells point in the same direction. Note that the length scale of the collection of individual dipoles (~5 nm) is much smaller than the wavelength of the excitation light (~500 nm). Therefore, the individual dipoles all experience the same oscillating field of the incoming EM wave. As a result, the individual dipoles may be added up to a total net dipole moment of the two mixed molecular orbitals. Because the mixed state of the MOs involved in the $1S_h$-$1S_e$ transition thus has a finite dipole moment, the optical transition is allowed.

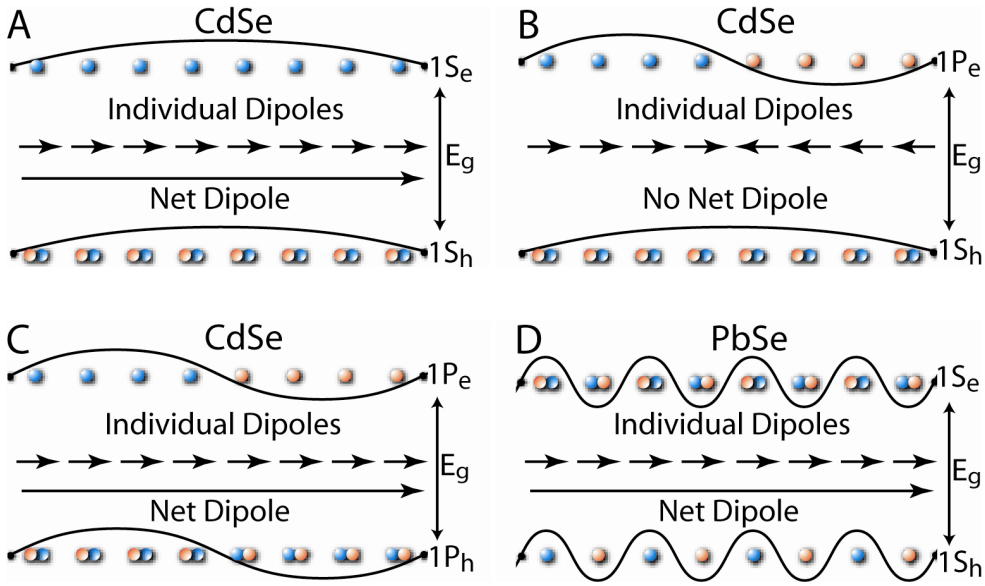

Figure 1.10 Schematic representations of the individual dipoles and net dipole moments that arise when VB atomic orbitals are mixed with CB orbitals, for three different interband transitions in a CdSe QD (A-C), and for the $1S_h$-$1S_e$ interband transition in a PbSe QD. The direction of the individual dipole can be deduced from Figure 1.9. When the individual dipoles add up to a net dipole, the optical transition is allowed. If they cancel out (B), the transition is (parity) forbidden.

The situation is different for the $1S_h$ to $1P_e$ transition (or $1P_h$ to $1S_e$ transition). Again, the mixing of the 4p selenium orbitals with the Cd 5s orbitals gives rise to a dipole in each of the unit cells (Figure 1.10B). However, the direction of the individual dipoles changes half-way of the quantum dot (in real space) because of the phase-shift in the 5s-orbitals in the conduction band. The individual dipoles now cancel out resulting in a net dipole moment of exactly zero (no dipole). Therefore, the optical transition from the $1S_h$ MO to the $1P_e$ MO is not allowed. As a third example, we look at the optical transition from the $1P_h$ level to the $1P_e$ level (Figure 1.10C). In this case, the individual dipoles do add up again to a net dipole moment, and therefore the optical transition is allowed.

The same approach can be applied to for example the $1S_h$ to $1S_e$ transition in a PbSe QD (Figure 1.10D). Even though the phase of each atomic orbital changes ($k=\pi/a$), the dipoles of all individual unit cells point in the same direction (as can be deduced from Figure 1.9). Therefore, the $1S_h$ to $1S_e$ transition in PbSe is allowed. Just as in the case of CdSe, the $1S_h$ to $1P_e$ transition in PbSe is forbidden (not shown). From these examples, we see that the selection rule for an optical interband transition in a quantum dot is $\Delta\ell=0$ for the envelope-wavefunctions. The parity-selection rule in *e.g.* a CdSe QD is still obeyed because the interband transition involves the transition from (a linear combination of) 4p orbitals to (a linear combination of) 5s orbitals (hence $\Delta\ell=1$).

For an *intraband* transition, a similar treatment can be used to obtain the optical selection rules. An intraband transition involves the transition from for example the Cd 5s to 5s atomic orbitals within the conduction band (*i.e.* $\Delta\ell=0$ for the atomic

orbitals, see Figure 1.8). In this case no dipoles arise within the individual unit cells; the mixing of individual atomic s-orbitals does not lead to a dipole (see Figure 1.9). Therefore, the dipole has to arise from a change in parity of the envelope functions ($\Delta\ell$=±1), which means that for example the $1S_e$ to $1P_e$ intraband transition is allowed, whereas the $1S_e$ to $1D_e$ transition is forbidden. In case of the $1S_e$ to $1P_e$ transition for example, the net dipole arises because half of the 5s-orbitals (that are in phase) add up, whereas the other half of the 5s-orbitals cancel out because they have a different phase (although not specifically indicated, this can be seen in Figure 1.8). This causes an asymmetric electron density in the quantum dot when the $1S_e$ and $1P_e$ levels are mixed, and hence a net dipole arises (and therefore the transition is allowed).

After absorption of a photon, an electron occupies the $1S_e$ level, and a hole the $1S_h$ level. There is a significant Coulomb interaction between the electron and hole, and the two remain coupled due to the small size of the quantum dot. This bound electron-hole pair is also called an exciton. The exciton can relax back to the ground state by radiative or non-radiative recombination. The latter process can occur for example by trapping of one of the charge carriers at a surface state, after which it thermally relaxes to the ground state. Another non-radiative recombination pathway is through energy transfer, as will be explained in the next section.

Radiative recombination (by emission of a photon) is the reverse process of absorption. Therefore, the selections rules for absorption (discussed above) also apply for emission. Just as in the case of absorption, emission of a photon results from the mixing of the excited state orbital with the ground state orbital. This mixing also has to be induced by an external oscillating field. Without this external "trigger", an electron can theoretically reside in the excited state for an infinite time. An incoming EM wave that is resonant with the transition can induce the mixing (just as in case of absorption) resulting in radiative recombination. This is called stimulated emission, which is used in lasers.

Usually, the fluorescence of dyes, phosphors, and quantum dots takes place without the stimulus of external oscillating field. In that case we speak of spontaneous emission, where mixing of the excited and ground state is induced by so-called vacuum modes (or vacuum fluctuations). The rate of spontaneous emission is not only dependent on the magnitude of the transition dipole moment $\mu_{i,f}$ of the transition between initial and final states (proportional to the oscillator strength), but also on the density of optical modes to couple with. The density of optical modes in vacuum is frequency-dependent and increases with frequency. The radiative decay rate Γ_{rad} for spontaneous emission in an ideal two-level atom system can be deduced from Fermi's Golden Rule[24] and contains both the "atomic" part (transition dipole moment) and "field" part (density of optical modes):

$$\Gamma_{rad}(\omega) = \frac{\omega^3 n \left|\mu_{i,f}\right|^2}{3\pi\varepsilon_0 \hbar c^3} \tag{1.10}$$

where ω is the frequency of light, n is the refractive index, ε_0 is the permittivity of free space, and c is the speed of light. The rate of spontaneous emission can be modified by changing the density of optical modes, which can be achieved in photonic crystals.[25]

1.2.6 Exciton Energy Transfer

When two quantum dots are in close proximity, an exciton in one QD (donor) can be transferred to the neighboring quantum dot (acceptor) through a dipole-dipole interaction. This process is called resonant exciton energy transfer (ET), and is an alternative pathway for an exciton in the donor quantum dot to recombine. Exciton ET should not be confused with radiative energy transfer, where a QD re-absorbs light that was emitted by another quantum dot. Classically, resonant energy transfer can be seen as an oscillator (*e.g.* a spring) that induces a neighboring oscillator (with the same resonance frequency) to oscillate as well. In the case of exciton energy transfer, the oscillating dipole in a donor QD induces the oscillation of a dipole in the acceptor QD. Through this dipole-dipole interaction, the energy of the exciton in the donor QD can be transferred to the acceptor QD. The net result is a physical displacement of the exciton from the donor quantum dot to its neighbor (see Figure 1.11), which is not mediated by an external EM field. Exciton energy transfer between neighboring QDs can be studied using (time-resolved) fluorescence spectroscopy, by analyzing the emission decay curves of the donor and acceptor QDs (presented in Chapters 4 and 5 of this thesis).

Several conditions have to be satisfied for exciton ET to occur. In the first place, the distance between the two QDs has to be sufficiently small to give a strong interaction. Secondly, the (absorption) transition of the acceptor QD must be resonant with the (emission) transition of the donor QD (there must be spectral overlap). This implies that the bandgap of the acceptor QD has to be equal to (Figure 1.11), or smaller than the bandgap of the donor QD (ET to higher-lying transitions in the acceptor QD is also possible). Finally, the orientation of the oscillating dipoles in both quantum dots also influences the transfer rate. Based on the conditions described above, the total energy transfer rate (Γ_{rad}) can be written as:

$$\Gamma_{ET} = \frac{2\pi}{\hbar}\frac{\mu_D^2\mu_A^2\kappa^2}{r^6 n^4}\Theta \qquad (1.11)$$

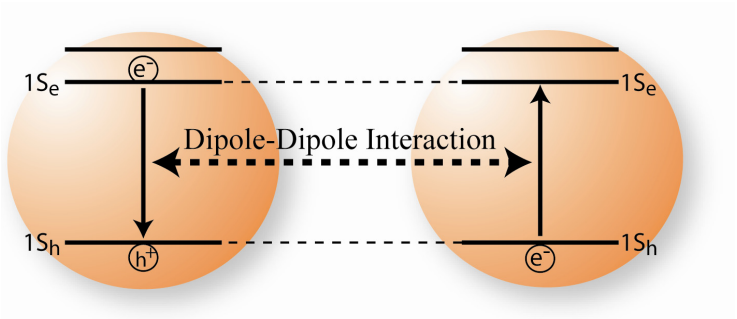

Figure 1.11 Schematic representation of resonant exciton energy transfer from the donor QD (left) to the acceptor QD. The exciton in the donor QD recombines, inducing an exciton in the acceptor QD through a dipole-dipole interaction.

as was first derived by Förster[26], where μ_D and μ_A denote the transition dipole moments of the transitions involved on the donor and acceptor quantum dot, respectively, r is the distance between the (point) dipoles, and n is the refractive index of the surrounding medium. The r^{-6} distance dependence is only valid when r is larger than l, where l is the length of the dipole and defined as $l=\mu/q$ (and q the elemental charge). The orientational average of the dipoles κ in quantum dots is 2/3, assuming that the dipoles are randomly oriented. The spectral overlap is represented by Θ, which is defined as:

$$\Theta = \int E_D(\lambda) \cdot A_A(\lambda) d\lambda \qquad (1.12)$$

where $E_D(\lambda)$ is the (normalized) emission spectrum of the donor QD, and $A_A(\lambda)$ represents the (normalized) absorption spectrum of the acceptor QD.

1.3 Colloidal Quantum Dots and their applications

The unique optical properties of colloidal nanocrystalline quantum dots can be used for many different applications. The bright, size-dependent luminescence of QDs can be used in for example light emitting devices (LEDs)[27], lasers[28, 29], or displays.[30, 31] Similarly, the high absorption cross-section of quantum dots at tunable wavelengths make them promising candidates for ultra sensitive photodetectors[32], or photovoltaic applications. As will be discussed in more detail in section 1.3.2, quantum dots can be used to improve the efficiency of existing solar cell-concepts, or as the basis of new types of solar cells. The only application of QDs that is currently commercial is their usage as fluorescent bio-labels, as explained in the section below.

1.3.1 QDs for bio-imaging applications

A wide variety of complementary imaging techniques is used in the clinic nowadays to obtain quick and reliable diagnostics of patients. Within biomedical research, imaging of disease processes is an important technique to obtain insight in the underlying mechanisms of diseases, or to follow the results of newly developed therapies. The quality (contrast, resolution, scan-time) of imaging techniques like MRI (magnetic resonance imaging), CT (computed tomography), or PET (positron emission tomography) has revolutionized since their early invention. Combinatory techniques like PET-CT or MRI-CT scans are currently being developed, making use of their complementary properties. For example, it offers the possibility to simultaneously obtain (anatomic) information of hard tissues (CT) and soft tissue (MRI). A general way to enhance contrast for the different imaging modalities is to use contrast agents. Contrast agents can be administered to the body and give a very high and local signal for the imaging technique used. By attaching targeting ligands to the contrast agent that specifically bind to the spot-of-interest, one can enhance the contrast at the particular spot, for instance a tumor. This helps clinical doctors and researchers to localize (and follow) a disease or anomaly with high accuracy. Because, as mentioned, the different imaging techniques are complementary, it is a current challenge to develop multimodal contrast agents that can be detected by multiple imaging techniques simultaneously.

One of the most rapidly developing and exciting applications of nanotechnology in biomedical research is the use of nanosized materials as contrast agents for (*in vivo*) imaging. For example, iron oxide nanoparticles (NPs) can be used as contrast agents for MRI, and gold or bismuth particles are suitable CT-contrast agents. Quantum dots exhibit a number of exceptional optical properties compared to fluorescent dyes, which greatly enhances their potential as contrast agent in fluorescence based bio-imaging. The most significant properties include: (1) a high photoluminescence quantum yield (QY), (2) broad absorption range with narrow, symmetric photoluminescence spectra, and (3) a high resistance against photobleaching and chemical degradation. In addition, the surface chemistry of QDs allows the inclusion of entities for improved pharmacokinetics and bio-applicability, and the conjugation of specific targeting molecules. Since the early studies describing the first biological application of QDs as fluorescent biological

labels appeared in the late nineties the field has undergone a revolution.[33, 34] These studies demonstrated the use of QDs for labelling cultured cells, and since the publication demonstrating the use of phospholipid micelle-coated QDs for *in vivo* imaging[35], numerous studies exploit their unique fluorescent properties for the same purpose. Gao *et al.* used QDs for *in vivo* cancer targeting and imaging[36], while Stroh *et al*. used multiphoton microscopy techniques to spectrally distinguish quantum dots of different sizes concurrently within one tumor milieu *in vivo*.[37] Another example of how surface modification can contribute to extending the applicability of QDs was demonstrated by So *et al.* They created self-illuminating QDs by conjugation of a mutant of the bioluminescent protein Renilla reniformis luciferase to the surface of QDs.[38] When this protein binds its substrate coelenterazine, it emits blue light which can excite the bound quantum dot, resulting in QD-emission.

All the aforementioned examples demonstrate the broad range of exciting possibilities QDs exhibit as optical biolabels. Interestingly, new developments in nanochemistry allow for the creation of QD-based nanoparticulate materials that can also be detected with other imaging techniques, so-called multimodal QD-labels. Recently, the combination of QDs with a radiolabel has shown to be valuable for the *in vivo* investigation of the pharmacokinetics and biodistribution of QDs with PET imaging.[39] Furthermore, QDs can be designed such that they also display (super)paramagnetic properties for their detection with magnetic resonance imaging (MRI). Below, we will first explain the technique of MRI in more detail, followed by a few examples of how the fluorescent properties of quantum dots can be combined with magnetic properties for detection by MRI to obtain a bimodal contrast agent.

Short introduction to MRI

MRI is a diagnostic tool which is characterized by its ability to generate three dimensional images of opaque and soft tissue with relatively high spatial resolution and tissue contrast, and therefore is one of the most versatile imaging techniques available in the clinic. Apart from anatomical information, metabolic and functional parameters can also be obtained with MRI. Contrast agents are currently applied in 30 to 40 percent of clinical MRI scans. Nanoparticulate MRI contrast agents, utilized primarily for molecular imaging purposes, have been developed since the mid 1990s.

Most MRI contrast agents generate contrast by locally shortening the ^{1}H relaxation times of surrounding water.[40] Relaxation is the process describing a return to thermal equilibrium of protons in a magnetic field, which were initially excited by the application of a radio-frequency magnetic field pulse in the MRI scanner. The relaxation is usually divided into two principal relaxation processes: spin-lattice or longitudinal relaxation (characteristic time T_1 [s] or relaxation rate R_1 [s^{-1}] = $1/T_1$) and spin-spin or transverse relaxation (T_2, R_2). The MR scanner can be made sensitive to differences and changes in the relaxation times by appropriately tuning of the MRI sequences. T_1-weighted MRI sequences produce images in which areas with low T_1 are bright (positive contrast), while T_2-weighted MR sequences result in images with dark areas of low T_2 (negative contrast).

The ability of a contrast agent to accelerate relaxation is defined by the change in relaxation rate per unit concentration of the contrast agent. The proportionality constants are denoted as r_1 and r_2 (units [$mM^{-1}s^{-1}$]), where $r_2 \geq r_1$. The total

(observed) relaxation rate of a medium ($R_{1,obs}$) in the presence of a T_1-contrast agent is defined as:

$$R_{1,obs} = R_{1,dia} + R_{1,CA} = R_{1,dia} + r_{1,CA} \cdot [CA] \quad (1.13)$$

where $R_{1,dia}$ is the intrinsic relaxation rate of the medium without contrast agent, and [CA] the concentration of contrast agent. Similarly, the observed relaxation time $T_{1,obs}$ of a medium in the presence of a contrast agent can be written as:

$$\frac{1}{T_{1,obs}} = \frac{1}{T_{1,dia}} + r_{1,CA} \cdot [CA] \quad (1.14)$$

The same equations hold in case of T_2-weighted imaging. Since T_1 and T_2 relaxation are not completely independent processes, a contrast agent is never exclusively a positive or negative contrast agent. In practice the ratio between the r_2 and r_1 value determines whether a contrast agent is more suitable for T_1-weighted positive contrast imaging or for T_2-weighted negative contrast. As a rule of thumb, agents with an r_2/r_1 between 1 and 2 are most suitable T_1 contrast agents, while contrast agents with larger r_2/r_1 ratio become progressively more suitable for T_2-weighted imaging.

T_1 contrast agents are commonly paramagnetic metal ions (*e.g.* Gd^{3+}) coordinated to a protective chelate to form a non-toxic complex.[41] The principal action of the agent is electron-proton dipolar coupling which falls off rapidly with distance. This means that water molecules should be directly coordinated to the paramagnetic ion for effective relaxation and preferably should undergo fast exchange with other water molecules (so that more water molecules are affected by the paramagnetic ion per unit time). Slowing down the rotational motion of the complex, *e.g.* by attaching the contrast agent to a nanoparticle, results in improved relaxation and hence better contrast.

The most effective way to decrease T_2 is to use agents that are generally classified as superparamagnetic contrast agents.[42] These are typically iron oxide nanoparticles composed of magnetite (Fe_3O_4) or maghemite (γ-Fe_2O_3).[43] Local field inhomogeneities surrounding the magnetic particles lead to rapid dephasing of transverse magnetization and therefore a short T_2 relaxation time. Above the so-called blocking temperature (T_b), these nanoparticles are superparamagnetic because the magneto crystalline anisotropy is overcome by temperature fluctuations causing the magnetic moment to randomly change directions within the particle. Inversely, these particles are ferromagnetic below T_b.

Paramagnetic Quantum Dots

Due to the complementary characteristics of optical techniques and MRI, combinatory probes, which exhibit both fluorescent and (super)paramagnetic properties, offer significant advantages. In the past years, several strategies have been developed to make QDs that also have (super)paramagnetic properties, which will be briefly discussed below. Schematic representations of the four approaches are shown in Figure 1.12

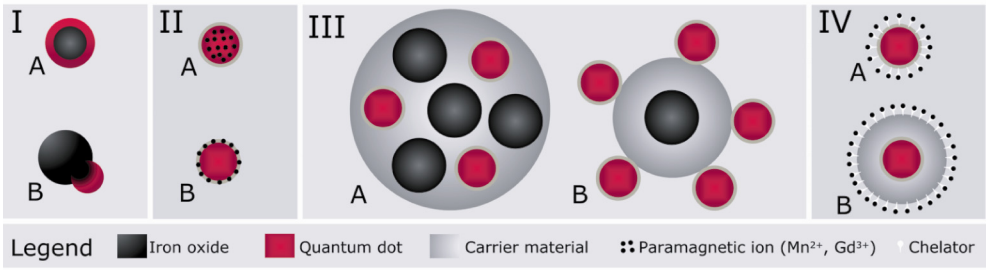

Figure 1.12 Schematic representation of four types of magnetic QDs. Type I resembles a core/shell or heterostructure comprised of a QD and magnetic (*e.g.* iron oxide) material. Type II represents a QD doped by paramagnetic ions, located at either the core or shell of the QD. Type III consists of a composite particle that carries both magnetic NPs and QDs. Type IV is based on a QD core surrounded by a paramagnetic coating of Gd-chelates.

The first type of particles is created by the growth of heterostructures in which a quantum dot is either overgrown with a layer of a magnetic material (Type Ia) or linked to a magnetic nanoparticle (Type Ib). Despite the generally large lattice mismatch between magnetic and semiconductor nanocrystals, it has recently been shown that it is possible to combine the two materials within one nanocrystal, although the mechanism of attachment has not been fully resolved yet.[44] As examples, FePt/CdSe[45] and Cobalt/CdSe core/shell nanocrystals[46] have been synthesized, as well as FePt-CdS[47] and Fe_2O_3-CdSe heterodimers.[48] The resulting particles are all superparamagnetic (T_2 contrast agents), but generally show a low overall QY (~10%). The low QY is probably caused by an interaction with the magnetic particle (causing emission quenching) and may therefore be an intrinsic problem of this architecture.

The second approach involves doping of paramagnetic ions into quantum dots, which provides a direct method to incorporate fluorescence and magnetic properties into a single nanoparticle. The dopants can be incorporated either in the core (Type IIa) or shell (Type IIb) of the quantum dot (Figure 1.12). The luminescence may originate from the paramagnetic ion itself or involve recombination to bandgap states related to the paramagnetic dopant. There is a long tradition in doping paramagnetic ions into semiconductors[49], but their potential as multimodal probes (magnetic and luminescent) in imaging has only been realized recently. In a paper by Santra *et al.* the use of CdS:Mn/ZnS QDs for bimodal imaging was demonstrated (Type IIa). The QDs showed a bright yellow Mn^{2+} emission and exhibited a clear magnetic response.[50] Bimodal imaging with $CdSe/Zn_{1-x}Mn_xS$ nanoparticles (Type IIb) was reported by the group of Louie.[51] The fluorescence from this bimodal particle originated from the CdSe core and had a QY over 20%, and it was shown that the particles are suitable for T_1-weighted MR imaging.

Another approach to add magnetic functionalities to quantum dots is by using a carrier material to create a composite particle in which both magnetic and semiconductor nanocrystals are integrated (Type III in Figure 1.12). The different types of NPs can be either *incorporated in* the carrier material (Type IIIa), *attached to* the outside of the carrier material, or a combination of both (Type IIIb). Both silica and polymer matrices can be used as a carrier material, resulting in a

construct that is generally larger than particles of Type I or Type II. For example, composite silica particles with both Fe_2O_3 NPs and CdSe QDs incorporated was recently reported (Type IIIa)[52], as well as iron oxide NPs incorporated in silica spheres with CdTe QDs attached to the outside (Type IIIb).[53] Similar designs using polymer microcapsules[54], nanospheres, [55] or polyelectrolyte-based layer-by-layer assemblies[56] as a matrix to embed both fluorescent QDs and magnetic NPs have been demonstrated.

The fourth and final category of particles is defined as quantum dots coated by organic complexes (chelates) containing paramagnetic ions, schematically drawn as Type IV in Figure 1. To decrease toxicity and enhance stability, the Gd^{3+} ions are complexated in organic chelates which coordinate to the paramagnetic ions through an ionic interaction. One of the most widely used MRI T_1 contrast agents for experimental and clinical use is Gd-DTPA (diethylenetriaminepentaacidic acid), but there is a wide variety of other compounds being studied to optimize the molar relaxivity as well as to explore the range of useful biomedical applications.[57] Chapter 7 of this thesis describes the micellar coating of hydrophobic QDs by a combination of paramagnetic and pegylated lipids (Type IVa). The paramagnetic lipids consist of two hydrophobic stearylamide groups (BSA) attached to a Gd-DTPA complex. Another approach is to use biotinylated Gd-DTPA complexes which can be directly coupled to streptavidin-coated QDs.[58] In order to increase the payload of paramagnetic complexes, the size of the particles can be increased by first coating the QDs by a layer of silica (Type IVb, see Chapter 8 of this thesis). The silica-coated QDs can be coated by a similar lipidic micelle as described above, by first making the silica spheres hydrophobic (Chapter 9 of this thesis). Another approach is to functionalize the silica surface with for example amine or thiol groups, to which paramagnetic complexes can be attached covalently.[59, 60]

1.3.2 Application of colloidal QDs for Solar Cells

The general idea of using quantum dots in solar cells, is that the bandgap of the material can be tuned to the solar spectrum. In a conventional silicon solar cell for example, photons with an energy lower than the bandgap are not absorbed, whereas the excess energy of high-energy photons is lost through thermal relaxation processes after absorption. Using layers of QDs of different sizes, one can in principle integrate all desired bandgaps (adapted to the solar spectrum) within a solar cell containing a single chemical composition. However, to extract the maximum power from such a multi-bandgap solar cell, all layers have to be connected individually to energy-specific electron and hole collectors. Ideally, every single quantum dot should be contacted individually, because the separation and transport of charge carriers within a layer of QDs is inefficient. Technically, such a solar cell is very difficult to realize. Still, researchers are looking at different possibilities to use QDs in various types of solar cells. As will become clear from the examples below, QDs also possess other properties besides the tunable bandgap that make them attractive candidates for solar cell applications.

The first example involves an ITO/CdTe/CdSe/aluminum structure. Here, the excellent processability of QDs in dispersion is used to create an all-inorganic nanocrystal solar cell. The device is easily produced by spin-coating a layer of rod-shaped CdTe NPs on top of conducting ITO (indium tin oxide) glass, followed by

the deposition of a layer of rod-shaped CdSe NP and finally a thin alumina conducting layer.[61] The conductivity of the device in the dark is very low, which is attributed to the extremely low carrier concentration. The cell may not be regarded as a conventional p-n junction (with high carrier concentrations due to dopants) with a depletion layer and built-in field that induces charge separation. Rather, it is the type II band off-set of a CdTe and CdSe heterojunction that is responsible for the dissociation of excitons, comparable to the operation of all-organic Donor-Acceptor solar cells.[62] After dissociation, holes diffuse over the lower hole-energy levels in CdTe nanorods towards the ITO-electrode, and electrons will find their way over the lower electron-energy levels in CdSe nanorods towards the aluminum electrode. Carrier mobility in nanocrystal films is generally very low, and this causes a poor conductivity and performance of the device. However, when the film was annealed and sintered (at 400 °C), the conductivity drastically increased and an overall efficiency of nearly 3% was achieved. The quantum confinement effects and tuneability of the bandgap in QDs is not the main operation principle of this type of nanocrystal-based solar cell. Rather, this concept makes use of the excellent ability of processing QDs in dispersion and the high effective surface area that can be achieved when films of nanocrystals are deposited. These advantages are also employed in a similar type of QD-solar cells, based on a blend of QDs and semiconductor organic polymers.[63]

A second example of the use of QDs for solar cells is based on spectral conversion. The response of conventional (silicon) solar cells is not uniform over the entire solar spectrum. For example, the external quantum efficiency of multicrystalline silicon solar cells rapidly drops below a wavelength of 550 nm.[64] It is therefore favorable to convert the blue-green part of the solar spectrum into red-shifted light where the response of the cell is optimal. QDs are promising candidates for spectral shifting of the solar spectrum, because the absorption band is broad, while the emission can be tuned to the desired optimal response wavelength of the solar cell. The QDs can be incorporated into a thin plastic film that is applied on top of a silicon solar cell. Depending on the concentration of QDs, part of the (non-absorbed) light will directly be absorbed by the solar cell, but the rest of the light is absorbed by QDs and re-emitted at lower energies. Due to internal reflections, up to 75% of the re-emitted light can still reach the silicon solar cell.[65] Assuming a QY of 80% and by optimizing the conditions (concentration, emission wavelength, layer thickness), it was calculated that an increase in short-circuit current by 6%, 10%, and 29% can be achieved for direct, global, and diffuse spectra respectively.[65] The higher increase for diffuse light is due to the larger blue/green content of diffuse light compared to direct and global spectra. In this application, the broad absorption band, efficient emission (at tunable wavelength), and high resistance against photo bleaching of QDs (compared to organic dyes) are employed to increase the overall efficiency of a conventional solar cell.

Quantum dots incorporated in polymer films can also be used in so-called fluorescent concentrators.[66-69] This concept was already developed in the mid-seventies[70, 71], and is based on a plastic plate containing fluorescent dyes that concentrates light to the edges of the slab, where solar cells can be attached. The concentration results from light that is emitted by the dye (after absorption) in all directions, and due to internal reflections, most of the light is directed to the sides of the plate (Figure 1.13A). Losses in such a fluorescent concentrator are caused by (1) light that is not absorbed by the plate (2) light emitted within the so-called

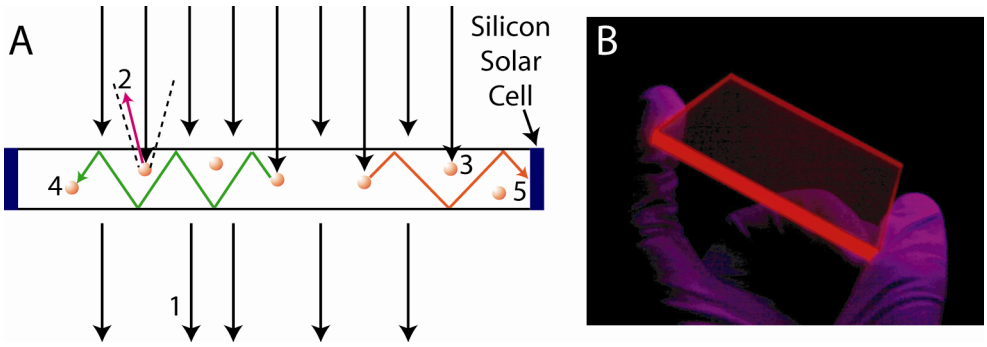

Figure 1.13 (A) Illustration of the working principle of a fluorescent concentrator. Incoming light is absorbed by fluorophores, and re-emitted in all directions. Due to internal reflections, most of the emitted light will reach the solar cells that are attached to the sides of the polymer plate. Loss mechanisms are: (1) light that is not absorbed; (2) light that is re-emitted within the escape cone; (3) light that is absorbed but not re-emitted due to a QY lower than unity; (4) emitted light that is re-absorbed by a second fluorophore (followed by *e.g.* (2) or (3)). (B) Photograph of a polymer plate containing CdSe quantum dots (illuminated by a UV-lamp) illustrating the concentrator effect.

escape cone that leaves the plate (3) a quantum efficiency of the dye lower than unity and (4) re-absorption of light due to spectral overlap between the absorption and emission spectra of the dye. Re-absorption strongly reduces the total light-output, because it introduces a new chance for non-radiative recombination (due to the QY<100%), and emission within the escape-cone. The main advantage of this fluorescent concentrators is that only a small area of *e.g.* a silicon solar cell is needed, resulting in a much cheaper device, assuming that the dye-containing plate is inexpensive to produce. Quantum dots are an attractive alternative for fluorescent dyes in these concentrators, because of their broader absorption band and larger resistance against photobleaching. In addition, the spectral overlap may be reduced by using for example type II QDs with a large Stokes-shift[72], which can drastically improve the efficiency of the concentrator due to the reduction in re-absorption.[68] As a proof-of-principle, we have incorporated CdSe/CdS/CdZnS/ZnS core/multi-shell QDs into a polymer plate, and the QD-fluorescence upon UV-excitation is clearly visible at the edges of the plate (Figure 1.13B). The chemical stability against incorporation into the polymer, QY, and Stokes-shift are still factors that can be improved to optimize fluorescent concentrators based on QDs.

A third option is to use quantum dots as a replacement for dyes in the dye-sensitized solar cells, as first developed by Grätzel and coworkers.[73, 74] This dye cell is comprised of a multi-crystalline TiO_2 electrode that is photosensitized by fluorescent dyes. Upon illumination, the excited electrons are injected from the dye into the conduction band of TiO_2, and the holes are transferred through an electrolyte to the counter electrode. Quantum dots can also act as photosensitizers in such a device by replacing the dye, with again the advantage of a broader absorption band and higher resistance against photobleaching. In addition, the conduction band level of the QDs can be adjusted to the conduction band level of TiO_2 (for efficient charge injection) by changing the size or composition of the QD. Finally, the high absorption cross-section of quantum dots is also favorable, because one only needs a few monolayers of QDs to almost completely absorb the

incident light. QD-sensitized solar cells based on this concept have been demonstrated for *e.g.* CdS[75], PbS, [76], CdSe[77], or InP[78] quantum dots, but the overall efficiency of these devices is still much lower than dye-sensitized cells.

The last example of how QDs may contribute to more efficient solar cells is still at an early stage of development. As first proposed by Nozik[79], and experimentally demonstrated for the first time by Klimov and co-workers[80], one high energy photon can generate multiple excitons in a single QD. This down-conversion process is called multi-exciton generation (MEG) or carrier multiplication (CM), and has the potency to increase the efficiency of solar cells; the excess energy of hot electrons and holes is not lost by thermal relaxation but used to generate additional excitons. The extraction of the multiple excitons (for photocurrent generation) is challenging due to the rapid decay (ps) of multi-excitons by Auger recombination.[81] The mechanism behind MEG is still under debate. Impact ionization (reverse effect of Auger recombination) is the most generally accepted mechanism[82, 83], but other, more exotic mechanisms have been proposed as well.[84-86] MEG was first demonstrated in PbSe QDs where a photon with an energy higher that three times the bandgap was shown to generate 2 excitons[80], and it was later reported that up to 7 excitons can be generated with photons that have eight times the bandgap energy.[87] These results have opened up a new area in quantum dot research, and not long after the first results in PbSe and PbS QDs, MEG was also demonstrated in CdSe[88], InAs[89], and silicon[90] nanocrystals. Some doubts on the existence of MEG in CdSe (and CdTe)[91] and InAs[92, 93] QDs have been raised afterwards, but the occurrence of carrier multiplication in PbSe QDs was recently confirmed unambiguously, albeit with a much lower efficiency than initially reported.[94] The true future impact of MEG (in QDs) on photovoltaics is therefore uncertain.

1.4 Outline of this thesis

In this thesis, both the fundamental and applicational aspects of colloidal quantum dots are presented. The order of chapters is such that the reader first obtains insight in some of the basic properties of semiconductor QDs, using PbSe QDs as key-actors. Next, CdTe QDs come into play to investigate the interactions and surface chemistry of quantum dots, key features for the translation towards applications. The last part of the thesis focuses on the usage of QDs as contrast agents, with CdSe QDs starring as bright bio-labels.

In the first part of the thesis, detailed investigations of the synthesis, self-assembly, and optical properties of PbSe QDs are presented. Chapter 2 demonstrates that small acetate impurities in the PbSe synthesis result in star-shaped nanocrystals. In addition, it is demonstrated that PbSe QDs of various shapes (spheres, stars, and cubes) form intriguing self-assembled monolayers on a TEM-grid. The role of a permanent dipole moment in PbSe QDs in the growth and self-organization of these nanocrystals is discussed. In Chapter 3, it is shown that up to 11 distinct features can be resolved in the absorption spectrum of a dispersion of PbSe QDs. Spectra of PbSe QDs ranging in size between 3.4 nm and 11 nm show that the low-energy features can be assigned to transitions at the L-point in the Brillouin zone, whereas high-energy transitions originate from the Σ-point in the Brillouin zone, at which quantum confinement also occurs.

The second part of the thesis describes the interactions between CdTe QDs in dispersion, and the exchange of native ligands by (cross-linker) thiol molecules. Using optical spectroscopy, efficient exciton energy transfer between cross-linked QDs is demonstrated, and analyzed with two different models (Chapters 4 and 5). Chapter 5 also shows that the efficiency of chemical cross-linkage of QDs depends on the rigidity of the dithiol linker-molecules. The cross-link experiments show that the original amine ligands of CdTe QDs are efficiently exchanged by thiols. Chapter 6 describes how time-dependent fluorescence spectroscopy can be used as a tool to investigate the kinetics of this ligand exchange, and to obtain quantitative information on the binding of commonly used ligands to the QD-surface.

The synthesis of multifunctional quantum-dot biolabels and their application in bio-imaging is described in the third part of this thesis. First, the synthesis of quantum dots with a paramagnetic and pegylated lipid-coating and their usage as bimodal contrast agents (fluorescence and MR imaging) is described in Chapter 7. The next step is to increase the versatility of this approach, by using a carrier material to host the different imaging functionalities. For this purpose, quantum dots are incorporated in silica nanospheres before applying the lipid coating. The incorporation mechanism of QDs in silica spheres using a reverse micelle method is elucidated in Chapter 8, explaining the high control with which QDs can be incorporated exactly in the middle of individual silica spheres. Chapter 9 describes how the silica-coated QDs can be made bio-applicable by applying a lipid coating. These lipid coated silica particles open up a new platform for multimodality contrast agents, because various functionalities can be integrated either in the silica core (QDs, Au, or Fe_2O_3 nanoparticles) or lipid coating (paramagnetic, pegylated, radioactive, or fluorescent lipids) of the architecture. A trimodal particle based on this concept is presented, comprised of a silica-coated Au nanoparticle (for CT imaging), surrounded by paramagnetic and fluorescent lipids (for MR and fluorescent imaging respectively).

1.5 References

1. G.E. Moore, *Electronics*, **1965**. *38* (8).
2. A.P. Alivisatos, *J. Phys. Chem.*, **1996**. *100* (31): p. 13226-13239.
3. A.I. Ekimov and A.A. Onushchenko, *JETP Lett.*, **1981**. *34* (6): p. 345-349.
4. R. Rossetti and L. Brus, *J. Phys. Chem.*, **1982**. *86* (23): p. 4470-4472.
5. L.E. Brus, *J. Lumin.*, **1984**. *31-2* (DEC): p. 381-384.
6. L. Goldstein, F. Glas, J.Y. Marzin, M.N. Charasse, and G.L. Roux, *Appl. Phys. Lett.*, **1985**. *47* (10): p. 1099-1101.
7. Q.H. Xie, A. Madhukar, P. Chen, and N.P. Kobayashi, *Phys. Rev. Lett.*, **1995**. *75* (13): p. 2542-2545.
8. M. Bayer, P. Hawrylak, K. Hinzer, S. Fafard, M. Korkusinski, Z.R. Wasilewski, O. Stern, and A. Forchel, *Science*, **2001**. *291* (5503): p. 451-453.
9. J.M. Elzerman, R. Hanson, L.H. Willems van Beveren, B. Witkamp, L.M.K. Vandersypen, and L.P. Kouwenhoven, *Nature*, **2004**. *430* (6998): p. 431-435.
10. R. Hanson, B. Witkamp, L.M.K. Vandersypen, L.H.W. van Beveren, J.M. Elzerman, and L.P. Kouwenhoven, *Phys. Rev. Lett.*, **2003**. *91* (19).
11. F.H.L. Koppens, C. Buizert, K.J. Tielrooij, I.T. Vink, K.C. Nowack, T. Meunier, L.P. Kouwenhoven, and L.M.K. Vandersypen, *Nature*, **2006**. *442* (7104): p. 766-771.
12. S.V. Gaponenko, *Optical Properties of Semiconductor Nanocrystals*. 1998, Cambridge: Cambridge University Press. 245.
13. A.J. Houtepen, *Charge injection and transport in quantum confined and disordered systems*. 2007, (Ph.D. Thesis, Utrecht University, Utrecht).
14. R. Koole, G. Allan, C. Delerue, A. Meijerink, D. Vanmaekelbergh, and A.J. Houtepen, *Small*, **2008**. *4* (1): p. 127-133.
15. G. Allan and C. Delerue, *Phys. Rev. B*, **2004**. *70* (24): p. 245321.
16. J.M. An, A. Franceschetti, S.V. Dudiy, and A. Zunger, *Nano Lett.*, **2006**. *6* (12): p. 2728-2735.
17. J.J. Peterson, L.B. Huang, C. Delerue, G. Allan, and T.D. Krauss, *Nano Lett.*, **2007**. *7* (12): p. 3827-3831.
18. B.L. Wehrenberg, C.J. Wang, and P. Guyot-Sionnest, *J. Phys. Chem. B*, **2002**. *106* (41): p. 10634-10640.
19. P. Liljeroth, P.A.Z. van Emmichoven, S.G. Hickey, H. Weller, B. Grandidier, G. Allan, and D. Vanmaekelbergh, *Phys. Rev. Lett.*, **2005**. *95* (8): p. 086801.
20. M.T. Trinh, A.J. Houtepen, J.M. Schins, J. Piris, and L.D.A. Siebbeles, *Nano Lett.*, **2008**.
21. I. Kang and F.W. Wise, *J Opt Soc Am B*, **1997**. *14* (7): p. 1632-1646.
22. M. Lach-hab, D.A. Papaconstantopoulos, and M.J. Mehl, *J Phys Chem Solids*, **2002**. *63* (5): p. 833-841.
23. J.C. Wright, *Chemistry 623 Notes-Experimental Spectroscopy*. 1990, Department of Chemistry, University of Wisconsin. p. 47-69.
24. A.F. van Driel, *Light Sources in Semiconductor Photonic Materials*. 2006, (Ph.D. Thesis, Utrecht University, Utrecht). p. 14-16.
25. P. Lodahl, A.F. van Driel, I.S. Nikolaev, A. Irman, K. Overgaag, D.L. Vanmaekelbergh, and W.L. Vos, *Nature*, **2004**. *430* (7000): p. 654-657.
26. T. Förster, *Naturwissenshaften*, **1946**. *33* (166): p. 166-175.
27. S. Coe, W.K. Woo, M. Bawendi, and V. Bulovic, *Nature*, **2002**. *420* (6917): p. 800-803.
28. V.I. Klimov, S.A. Ivanov, J. Nanda, M. Achermann, I. Bezel, J.A. McGuire, and A. Piryatinski, *Nature*, **2007**. *447* (7143): p. 441-446.
29. V.I. Klimov, A.A. Mikhailovsky, S. Xu, A. Malko, J.A. Hollingsworth, C.A. Leatherdale, H.J. Eisler, and M.G. Bawendi, *Science*, **2000**. *290* (5490): p. 314-317.
30. S. Coe-Sullivan, *Laser Focus World*, **2007**. *43* (3): p. 65-+.
31. K. Bulls, *Nanocrystal Displays*, in *Technology Reviews*. 2006 (May/June).
32. G. Konstantatos, I. Howard, A. Fischer, S. Hoogland, J. Clifford, E. Klem, L. Levina, and E.H. Sargent, *Nature*, **2006**. *442* (7099): p. 180-183.

33. W.C.W. Chan and S. Nie, *Science*, **1998**. *281* (5385): p. 2016-2018.
34. M. Bruchez, Jr., M. Moronne, P. Gin, S. Weiss, and A.P. Alivisatos, *Science*, **1998**. *281* (5385): p. 2013-2016.
35. B. Dubertret, P. Skourides, D.J. Norris, V. Noireaux, A.H. Brivanlou, and A. Libchaber, *Science*, **2002**. *298* (5599): p. 1759-1762.
36. X.H. Gao, Y.Y. Cui, R.M. Levenson, L.W.K. Chung, and S.M. Nie, *Nat. Biotechnol.*, **2004**. *22* (8): p. 969-976.
37. M. Stroh, J.P. Zimmer, D.G. Duda, T.S. Levchenko, K.S. Cohen, E.B. Brown, D.T. Scadden, V.P. Torchilin, M.G. Bawendi, D. Fukumura*, et al.*, *Nat. Med.*, **2005**. *11* (6): p. 678-682.
38. M.-K. So, C. Xu, A.M. Loening, S.S. Gambhir, and J. Rao, *Nat. Biotechnol.*, **2006**. *24* (3): p. 339-343.
39. M.L. Schipper, Z. Cheng, S.-W. Lee, L.A. Bentolila, G. Iyer, J. Rao, X. Chen, A.M. Wu, S. Weiss, and S.S. Gambhir, *J. Nucl. Med.*, **2007**. *48* (9): p. 1511-1518.
40. G.J. Strijkers, W.J.M. Mulder, G.A.F. van Tilborg, and K. Nicolay, *Anticancer Agents Med. Chem.*, **2007**. *7* (3): p. 291-305.
41. P. Caravan, J.J. Ellison, T.J. McMurry, and R.B. Lauffer, *Chem. Rev.*, **1999**. *99* (9): p. 2293-2352.
42. J.W.M. Bulte and D.L. Kraitchman, *NMR Biomed.*, **2004**. *17* (7): p. 484-499.
43. A.K. Gupta, R.R. Naregalkar, V.D. Vaidya, and M. Gupta, *Nanomedicine*, **2007**. *2* (1): p. 23-39.
44. K.W. Kwon and M. Shim, *J. Am. Chem. Soc.*, **2005**. *127* (29): p. 10269-10275.
45. J.H. Gao, B. Zhang, Y. Gao, Y. Pan, X.X. Zhang, and B. Xu, *J. Am. Chem. Soc.*, **2007**. *129* (39): p. 11928-11935.
46. H. Kim, M. Achermann, L.P. Balet, J.A. Hollingsworth, and V.I. Klimov, *J. Am. Chem. Soc.*, **2005**. *127* (2): p. 544-546.
47. H. Gu, R. Zheng, X. Zhang, and B. Xu, *J. Am. Chem. Soc.*, **2004**. *126* (18): p. 5664-5665.
48. S.T. Selvan, P.K. Patra, C.Y. Ang, and J.Y. Ying, *Angew. Chem. Int. Ed.*, **2007**. *46* (14): p. 2448-2452.
49. H.A. Klasens, *J. Electrochem. Soc.*, **1953**. *100* (2): p. 72-80.
50. S. Santra, H.S. Yang, P.H. Holloway, J.T. Stanley, and R.A. Mericle, *J. Am. Chem. Soc.*, **2005**. *127* (6): p. 1656-1657.
51. S. Wang, B.R. Jarrett, S.M. Kauzlarich, and A.Y. Louie, *J. Am. Chem. Soc.*, **2007**. *129* (13): p. 3848-3856.
52. D.K. Yi, S.T. Selvan, S.S. Lee, G.C. Papaefthymiou, D. Kundaliya, and J.Y. Ying, *J. Am. Chem. Soc.*, **2005**. *127* (14): p. 4990-4991.
53. V. Salgueirino-Maceira, M.A. Correa-Duarte, M. Spasova, L.M. Liz-Marzan, and M. Farle, *Adv. Funct. Mater.*, **2006**. *16* (4): p. 509-514.
54. N. Gaponik, I.L. Radtchenko, G.B. Sukhorukov, and A.L. Rogach, *Langmuir*, **2004**. *20* (4): p. 1449-1452.
55. H.Y. Xie, C. Zuo, Y. Liu, Z.L. Zhang, D.W. Pang, X.L. Li, J.P. Gong, C. Dickinson, and W.Z. Zhou, *Small*, **2005**. *1* (5): p. 506-509.
56. X. Hong, J. Li, M.J. Wang, J.J. Xu, W. Guo, J.H. Li, Y.B. Bai, and T.J. Li, *Chem. Mater.*, **2004**. *16* (21): p. 4022-4027.
57. L. Frullano and T.J. Meade, *J. Biol. Inorg. Chem.*, **2007**. *12* (7): p. 939-949.
58. L. Prinzen, R.J.J.H.M. Miserus, A. Dirksen, T.M. Hackeng, N. Deckers, N.J. Bitsch, R.T.A. Megens, K. Douma, J.W. Heemskerk, M.E. Kooi*, et al.*, *Nano Lett.*, **2007**. *7* (1): p. 93-100.
59. H.S. Yang, S. Santra, G.A. Walter, and P.H. Holloway, *Adv. Mater.*, **2006**. *18* (21): p. 2890.
60. D. Gerion, J. Herberg, R. Bok, E. Gjersing, E. Ramon, R. Maxwell, J. Kurhanewicz, T.F. Budinger, J.W. Gray, M.A. Shuman*, et al.*, *J. Phys. Chem. C*, **2007**. *111* (34): p. 12542-12551.

61. I. Gur, N.A. Fromer, M.L. Geier, and A.P. Alivisatos, *Science*, **2005**. *310* (5747): p. 462-465.
62. G. Yu, J. Gao, J.C. Hummelen, F. Wudl, and A.J. Heeger, *Science*, **1995**. *270* (5243): p. 1789-1791.
63. W.U. Huynh, J.J. Dittmer, and A.P. Alivisatos, *Science*, **2002**. *295* (5564): p. 2425-2427.
64. W.G.J.H.M. van Sark, A. Meijerink, R.E.I. Schropp, J.A.M. van Roosmalen, and E.H. Lysen, *Solar Energy Materials and Solar Cells*, **2005**. *87* (1-4): p. 395-409.
65. W.G.J.H.M. van Sark, *Appl. Phys. Lett.*, **2005**. *87* (15): p. 151117.
66. S.J. Gallagher, B. Norton, and P.C. Eames, *Solar Energy*, **2007**. *81* (6): p. 813-821.
67. A.J. Chatten, K.W.J. Barnham, B.F. Buxton, N.J. Ekins-Daukes, and M.A. Malik, *Semiconductors*, **2004**. *38* (8): p. 909-917.
68. K. Barnham, J.L. Marques, J. Hassard, and P. O'Brien, *Appl. Phys. Lett.*, **2000**. *76* (9): p. 1197-1199.
69. V. Sholin, J.D. Olson, and S.A. Carter, *J. Appl. Phys.*, **2007**. *101* (12): p. 123114.
70. A. Goetzberger and W. Greubel, *Appl. Phys.*, **1977**. *14*: p. 123-139.
71. W.H. Weber and J. Lambe, *Appl. Opt.*, **1976**. *15*: p. 2299-2300.
72. S. Kim, B. Fisher, H.J. Eisler, and M. Bawendi, *J. Am. Chem. Soc.*, **2003**. *125* (38): p. 11466-11467.
73. M. Gratzel, *J. Photochem. Photobiol. C*, **2003**. *4* (2): p. 145-153.
74. B. O'Regan and M. Grätzel, *Nature*, **1991**. *353* (6346): p. 737-40.
75. B. Vincent, *Colloid Surface*, **1990**. *50*: p. 241-249.
76. R. Vogel, P. Hoyer, and H. Weller, *J. Phys. Chem.*, **1994**. *98* (12): p. 3183-8.
77. I. Robel, V. Subramanian, M. Kuno, and P.V. Kamat, *J. Am. Chem. Soc.*, **2006**. *128* (7): p. 2385-2393.
78. A. Zaban, O.I. Micic, B.A. Gregg, and A.J. Nozik, *Langmuir*, **1998**. *14* (12): p. 3153-3156.
79. A.J. Nozik, *Physica E*, **2002**. *14* (1-2): p. 115-120.
80. R.D. Schaller and V.I. Klimov, *Phys. Rev. Lett.*, **2004**. *92* (18): p. 186601.
81. V.I. Klimov, *Annu. Rev. Phys. Chem.*, **2007**. *58*: p. 635-673.
82. A. Franceschetti, J.M. An, and A. Zunger, *Nano Lett.*, **2006**. *6* (10): p. 2191-2195.
83. G. Allan and C. Delerue, *Phys. Rev. B*, **2006**. *73* (20): p. 205423.
84. R.J. Ellingson, M.C. Beard, J.C. Johnson, P.R. Yu, O.I. Micic, A.J. Nozik, A. Shabaev, and A.L. Efros, *Nano Lett.*, **2005**. *5* (5): p. 865-871.
85. A. Shabaev, A.L. Efros, and A.J. Nozik, *Nano Lett.*, **2006**. *6* (12): p. 2856-2863.
86. R.D. Schaller, V.M. Agranovich, and V.I. Klimov, *Nat Phys*, **2005**. *1* (3): p. 189-194.
87. R.D. Schaller, M. Sykora, J.M. Pietryga, and V.I. Klimov, *Nano Lett.*, **2006**. *6* (3): p. 424-429.
88. R.D. Schaller, M.A. Petruska, and V.I. Klimov, *Appl. Phys. Lett.*, **2005**. *87* (25): p. 253102.
89. J.J.H. Pijpers, E. Hendry, M.T.W. Milder, R. Fanciulli, J. Savolainen, J.L. Herek, D. Vanmaekelbergh, S. Ruhman, D. Mocatta, D. Oron*, et al.*, *J. Phys. Chem. C*, **2007**. *111* (11): p. 4146-4152.
90. M.C. Beard, K.P. Knutsen, P.R. Yu, J.M. Luther, Q. Song, W.K. Metzger, R.J. Ellingson, and A.J. Nozik, *Nano Lett.*, **2007**. *7* (8): p. 2506-2512.
91. G. Nair and M.G. Bawendi, *Phys. Rev. B*, **2007**. *76* (8): p. 081304.
92. J.J.H. Pijpers, E. Hendry, M.T.W. Milder, R. Fanciulli, J. Savolainen, J.L. Herek, D. Vanmaekelbergh, S. Ruhman, D. Mocatta, D. Oron*, et al.*, *J. Phys. Chem. C*, **2008**. *112* (12): p. 4783-4784.
93. M. Ben-Lulu, D. Mocatta, M. Bonn, U. Banin, and S. Ruhman, *Nano Lett.*, **2008**. *8* (4): p. 1207-1211.
94. M.T. Trinh, A.J. Houtepen, J.M. Schins, T. Hanrath, J. Piris, W. Knulst, A.P.L.M. Goossens, and L.D.A. Siebbeles, *Nano Lett.*, **2008**. *8* (6): p. 1713-1718.

Chapter 2

Synthesis and Self-assembly of PbSe Nanospheres, Nanostars and Nanocubes

This chapter presents detailed investigations into the synthesis of PbSe nanocrystals with a controlled shape and their self-assembly into superstructures with long-range order. First, the synthesis of monodisperse spherical, cubic, and star-shaped PbSe nanocrystals is presented. It is shown that the size and shape of the NCs is determined by the concentration of acetate. The presence of acetate leads to efficient oriented attachment of smaller PbSe nanoparticles along the <100> crystal axis. We show that it is possible to obtain self-assembled monolayers of star-shaped nanocrystals with crystalline domains of several μm^2. Using wide-angle electron diffraction measurements we show that there is a high degree of atomic alignment in the self-assembled structures of spherical, cubic and star-shaped nanocrystals. The oriented attachment observed in the synthesis of star-shaped nanocrystals and the crystallographic alignment of spherical PbSe nanocrystals in self-assembled monolayers suggest the existence of a significant dipole moment in these PbSe NCs. Additional evidence for this dipole moment is obtained by Cryo-TEM analysis. Spherical, cubic and star-shaped PbSe nanocrystals all form chains in dispersion, as a result of a balance between dipolar interactions and thermal motion.

2.1 Introduction

Lead chalcogenide quantum dots hold great promise for a wide number of opto-electrical applications due to their tunable absorption and emission properties in the near-infrared.[1-3] For example, the use of PbSe QDs in novel types of solar cells, where the bandgap of the QDs can be tuned to a broad range of the solar spectrum, is frequently anticipated.[4] Especially the phenomenon of multi-exciton generation (MEG, explained in more detail in the next chapter) in PbSe QDs upon absorption of a high-energy photon makes these nanocrystals very promising for solar cell applications.[5] For such a solar cell, or any other electronic device based on PbSe QDs, it is crucial to have a high control over the synthesis procedure to obtain well-defined, monodisperse particles. Murray reported the first hot injection synthesis of monodisperse PbSe quantum dots.[2] In subsequent work a myriad of geometries of PbSe NCs was reported, like cubic nanocrystals, rings, rods, and wires.[6-9] Surprisingly, the dominant growth mechanism of these geometries appeared to be the oriented attachment of small PbSe NCs. To explain this mechanism Cho *et al*. suggested that PbSe nanocrystals have a sizable electric dipole moment that results from the distribution of Pb and Se terminated facets.[6] Direct evidence of a dipole moment in PbSe NCs has however not been published.

It is most likely that electronic devices based on (PbSe) QDs will not consist of a dispersion of nanocrystals but rather of a solid-state component based on QDs. One can make use of the unique self-assembly properties of nanocrystals to make such components. Highly ordered monolayers, multilayers, and even binary superlattices have already been reported, including their application in a solid-state device.[10-12] However, the mechanism behind this self-assembly of nanocrystals is not yet fully understood, and it is a current challenge to reveal the interactions and forces that induce the high ordering in these superlattices. For example, the dipole moment mentioned above was suggested to be important in the self-assembly of nanocrystals into ordered films.[10]

In this chapter, we present a systematic study of the role of acetate in the growth mechanism and the resulting geometry of the NCs. We show that the presence of even trace amounts of acetate in the reaction mixture leads to star-like geometries formed by oriented attachment. In the second part of this chapter we study the self-assembly of PbSe nanocrystals of different shapes. We present the first example of 2-D ordering of monodisperse star-shaped NCs. We also present self-assembled structures of spherical and cubic NCs and investigate the atomic alignment of the nanocrystal building blocks by wide-angle electron diffraction. In addition, we have performed Cryo-TEM measurements on dispersions of PbSe nanocrystals to look for direct evidence of a dipole moment.

2.2 Experimental Section

The syntheses were performed inside a nitrogen-purged glove box. All chemicals were stored inside this glovebox. The syntheses were carried out according to the recipe of Wehrenberg *et al*.[3] and consisted of the following steps:

1. A stock solution of 3.25 g lead acetate trihydrate (Aldrich, 99.999%), 10 ml diphenyl ether (DPE, Aldrich), 7.5 ml oleic acid (Aldrich, 90%) and 40 ml trioctyl phosphine (TOP, Fluka, 90%) was prepared. The lead oleate precursor was prepared in one of the three following ways:
   a. Preliminary – the stock solution was heated to 120ºC for 30 min inside the glovebox
   b. Thorough drying – the stock solution was heated to >70ºC under vacuum (<10^{-3} mbar) for >1 hour
   c. Literature procedure[6, 7] – the stock solution was heated to >150ºC under a nitrogen stream for 30 min
2. The solution was allowed to cool to room temperature. Subsequently 11.5 ml of this solution was mixed with 1.7 ml of 1.0 M selenium in TOP and rapidly injected into 10 ml of DPE that was preheated to the desired injection temperature. In a typical synthesis the injection temperature was 180ºC, the temperature dropped upon injection to 125ºC and quickly reached the growth temperature of 135ºC. The total growth time was usually 10 minutes.
3. The crude product was cleaned by the addition of a small volume of butanol, centrifugation, and dissolution of the precipitate in toluene. This cleaning procedure was repeated once.

The effect of acetate and water on the reaction product was studied by adding appropriate amounts of acetic acid or water to the precursor mixture after step 1. To investigate the effect of hexadecyl amine (HDA), the appropriate amount (1.33 g) of HDA was added to the 10 ml of DPE before the injection.

The films that are shown in section 2.3 were prepared by dipping a TEM grid for a few seconds in a dispersion of the NCs in toluene. The films that are shown in section 2.4 were prepared via a method described by Redl *et al*.[13] A TEM grid consisting of a carbon coated polymer film was placed on the bottom of a glass vial. The vial was tilted by 60º-70º inside a nitrogen-purged glovebox and 100 µL of concentrated NC dispersion was added, which exactly covered the complete substrate. In contrast to refs. [11, 13] we have not applied any pressure or temperature control. As the solvent evaporates the concentration of NCs increases. Because the vial is tilted, there is a gradient in the concentration along the surface of the substrate, yielding extended monolayers at the position where the concentration of the evaporating dispersion was optimal. The nanocrystals were studied by transmission electron microscopy (Philips Tecnai 12, Fei Tecnai 10 and Fei Tecnai 20 FEG) and scanning electron microscopy (Fei XL30 SFEG).

Cryo-TEM samples were prepared by pipetting a few microliters of a PbSe QD dispersion in decalin on a TEM-grid with holey carbon film (R2/2 Quantifoil Micro Tools, Jena, Germany). Subsequently, the excess of solvent was removed by blotting the grid for 2 seconds with a vitrobot, leaving behind an ultrathin film. Thereafter the film was rapidly vitrified by plunging the grid in liquid nitrogen.

2.3 The hidden role of acetate in the PbSe nanocrystal synthesis

The preparation of the Pb-oleate precursor, used for the hot injection synthesis of PbSe NCs, involves the following chemical reaction:

$$PbAc_2{\cdot}3H_2O + 2C_{17}H_{33}COOH \rightarrow Pb(C_{17}H_{33}COO)_2 + 3H_2O + 2HAc \quad (2.1)$$

Hence, if the precursor is not completely dried a significant amount of water and acetate will be present in the reaction mixture. To our surprise, our first attempts to synthesize quasi-spherical PbSe NCs resulted in what appeared to be “stars of David”. In this synthesis, the Pb-oleate was prepared by heating the precursors to 120ºC for 30 minutes, which we now know results in incomplete drying. To obtain spherical NCs we found that it is crucial to dry the Pb-oleate precursor mixture completely by heating to >70ºC under vacuum (<10^{-3} mbar) for more than one hour, see Figure 2.1A. It is thus clear that either water or acetic acid has a drastic effect on the shape of the NCs. Therefore we performed a systematic investigation on the effect of water and acetate on the shape and size of PbSe NCs. This was done by completely drying the precursor mixture and subsequently adding controlled amounts of water and acetic acid.

The addition of water (in a 3:1 H_2O:Pb molar ratio) to the carefully dried injection mixture did not result in a deviation from the spherical shape. This is shown in Figure 2.2A. The NCs synthesized in the presence of water appeared to be less monodisperse than those synthesized in carefully dried mixtures, but there is no systematic deviation from the quasi-spherical shape. We found this to be true even for high concentrations of water (up to Pb:H_2O = 1:15).

In contrast, the addition of acetic acid to the injection mixture resulted in a dramatic change in crystal shape and size, see Figure 2.1B-E. From these images it is evident that acetic acid leads to a star-like crystal shape; the amount of acetic acid has a strong effect on the size (10-120 nm) of these crystals. The “diameter” of the NCs, defined as the point to opposite point distance of the stars of David, is shown as a function of the Pb:Ac ratio in Table 2.1.

The hexagons in the TEM images of the largest crystals (Figure 2.1E) are actually 2D projections of octahedrons, as can be clearly seen in a SEM image of the same NCs (insert in Figure 2.1E). The transition from spherical particles to octahedral particles involves an intermediate shape. The growth in the six <100> directions is faster than the growth in other directions resulting in extensions in this direction.

This leads to star-shaped particles that usually show up as stars of David in the TEM images. Such a star corresponds to a <111> projection of a six-pointed star, which occurs when three points of the star are faced to the polymer film of the TEM grid. This is shown in Figure 2.3A. Other projections that are often encountered are also presented in Figure 2.3: a diamond shape (Figure 2.3B), corresponding to the <110> projection, when two points of the star face the substrate, and a notched square, when only one of the points faces the substrate (<100> projection, Figure 2.3C).

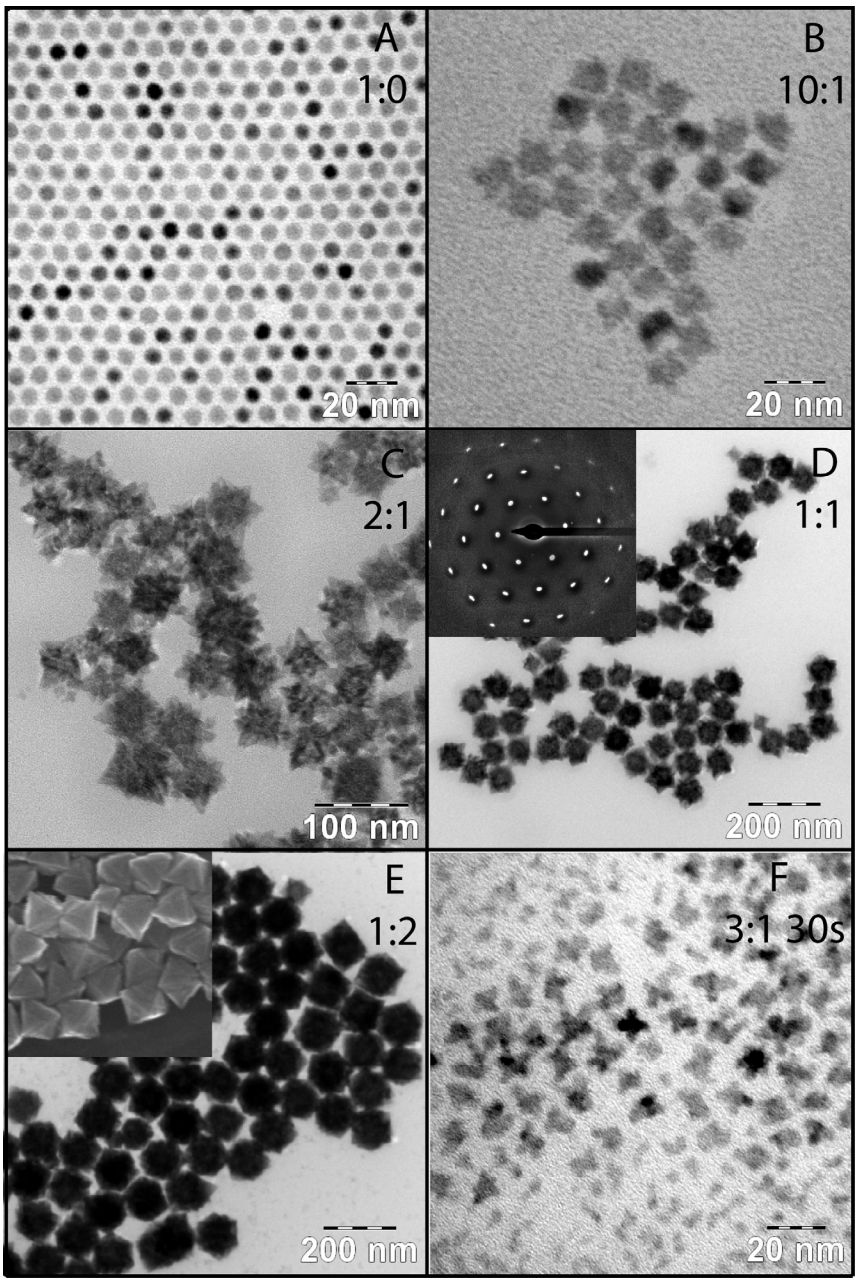

Figure 2.1. TEM images of PbSe nanocrystals grown at different concentrations of acetate. (A-E) PbSe NCs grown under identical reaction conditions with a Pb:Ac ratio as indicated in the images. Inserts show a diffraction pattern of a single octahedron (D) and a SEM image (E). (F) PbSe NCs after 30s of growth in the presence of acetate, in the initial stage of oriented attachment towards octahedrons.

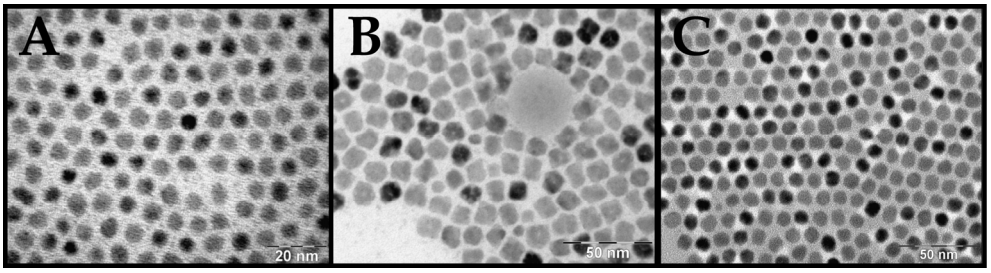

Figure 2.2. (A) PbSe NCs, synthesized in the presence of water (Pb:H_2O = 1:3). T_{inj} = 182ºC, T_{growth} = 135ºC, time = 10 min. There is no systematic deviation from the quasi-spherical shape. (B) Octahedral PbSe nanocrystals, synthesized with Pb-oleate precursor that was dried according to the drying procedure used by Lu *et al*.[7] and Cho *et al*.[6] The occurrence of octahedrons implies the incomplete drying of the precursor mixture. (C) PbSe NCs, synthesized in the presence of hexadecyl amine (HDA) (Pb:HDA = 1:3). T_{inj} = 231ºC, T_{growth} = 170ºC, time = 5 min, corresponding to the recipe of Cho *et al*.[6] The presence of HDA does not lead to the formation of octahedrons.

For very large nanocrystals the extensions in the <100> direction become so large that all the {100} facets have disappeared and perfect octahedrons result. This is illustrated in Figure 2.4, which shows nanocrystals that were synthesized in the presence of acetate (Pb:Ac = 1:1) at 230ºC and at different reaction times. After one minute the star-like shape is clearly visible (Figure 2.4A), while after 30 minutes only hexagons and squares can be seen on the TEM image (Figure 2.4B). Although it is tempting to assign the squares in this image to a cubic NC shape, it results from the <100> projection of nearly perfect octahedrons. This is shown in the lower three images of Figure 2.4, where the same NC is shown for different angles between the substrate and the electron beam. At -30º (Figure 2.4C) the 2D projection of the NC is a square, corresponding to the <100> projection; at 0º (Figure 2.4D) it is a hexagon, corresponding to the <111> projection, while at +30º (Figure 2.4E) it is a diamond, corresponding to the <110> projection. This clearly illustrates that one has to take care in assigning 3D shapes to TEM images, and that tilting the substrate (i.e. tomography) is a powerful tool to deduce the real shape.

Lu *et al*. proposed that octahedral PbSe nanocrystals are formed by the aggregation of smaller PbSe clusters.[7] Our observations confirm this mechanism. Figure 2.1F shows a TEM image of PbSe nanocrystals that were removed from the reaction mixture (in the presence of acetate) 30 seconds after the injection. A

Table 2.1. Relation between the Pb:Ac molar ratio in the synthesis and the diameter of the nanocrystals. The reaction conditions were identical for all samples: T_{inj} = 180ºC, T_{growth} = 135ºC, time = 10 min.

Pb:Ac	NC “diameter” (nm)
1:0	7.9
10:1	12.8
2:1	56.0
1:1	79.3
1:2	116.2

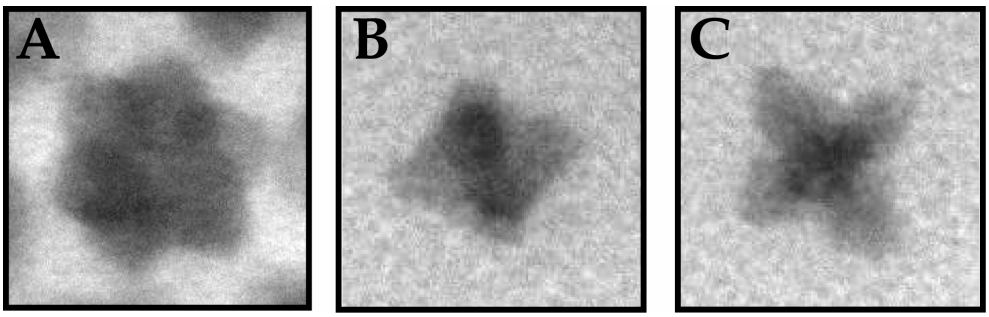

Figure 2.3. Different projections of 12.8 nm star-shaped nanocrystals. (A) <111> projection, or "star of David", (B) <110> projection ("diamond") and (C) <100> projection ("notched square").

mixture of small NCs of ~4 nm in diameter and aggregates of 2-6 of those NCs is visible in the initial stage of growth towards octahedrons. The largest of these aggregates already clearly possess the six-pointed star geometry. The final stars or octahedrons are single crystalline, as is illustrated by the discrete spots in the diffraction pattern of a single octahedron (insert in Figure 2.1D). An interesting observation is presented in Figure 2.5, which shows nanocrystals grown in the presence of acetate (Pb:Ac = 2:1) for only 1 minute. These NCs appear to be polycrystalline as the electron density over the crystals is not uniform. However, the corresponding electron diffraction pattern (insert in Figure 2.5) shows several discrete spots corresponding to the five star-shaped crystals in the image. This means that even before the NCs are annealed their "building blocks" are aligned. In addition, the crystal alignment of the five different NCs is very similar since all the spots in the diffraction pattern are closely grouped. Some of the smaller crystals that form the octahedrons are still visible in this early stage of the growth process. These observations strongly suggest that these smaller crystals self-assemble, with their crystallographic axes aligned, into the star-shaped PbSe nanocrystals. This is essentially the same mechanism of oriented attachment that was proposed by Cho *et al*.[6] for the formation of PbSe nanowires and nanorings. The formation of octahedrons implies that the oriented attachment of smaller PbSe crystals is fastest in the <100> direction, ultimately resulting in the elimination of all {100} facets.

This is in accordance with observations of Cho *et al*.[6] In the formation of many different crystal shapes, they most commonly observed oriented attachment along the <100> axis. As a possible explanation Cho *et al*. propose that the nanocrystals possess a dipole moment. The authors assume that quasi-spherical PbSe nancorystals are highly faceted and contain six {100} facets and eight {111} facets. The {100} facets are non polar, as they contain both Pb and Se atoms. The polar {111} facets contain only Pb or Se. To ensure charge neutrality the authors assume that the NCs contain four Se terminated {111} facets and four Pb terminated {111} facets. Figure 2.6 shows a schematic of nanocrystals possessing only {111} facets (i.e. octahedrons) with two different distributions of Pb and Se terminated facets giving rise to a dipole moment along the <100> axis (left octahedron in Figure 2.6) and zero dipole moment (right octahedron in Figure 2.6). If the distribution of Se and Pb terminated facets is assumed to be random the

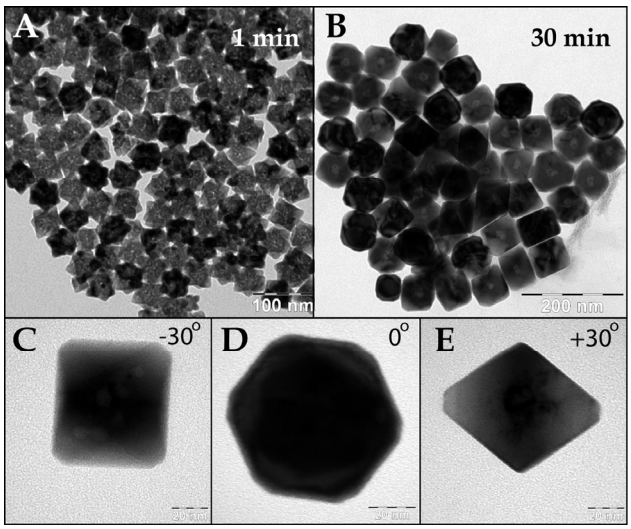

Figure 2.4. PbSe nanocrystals synthesized at 230ºC (injection and growth) in the presence of acetate (Pb:Ac = 1:1). The crystals evolve from stars (after 1 min, A) to octahedrons (after 30 minutes, B). Although some particles appear to be cubes they are actually <100> projections of octahedrons. The lower images illustrate the different projections of a single octahedron. The left image (-30º, C) is a <100> projection, the middle image (0º, D) is a <111> projection and the right image (+30º, E) is a <110> projection. Image (D) has a 30% higher magnification than (C) and (E).

relative probabilities of particles having zero dipole moment or a dipole along the <hkl> direction are 0:<100>:<110>:<111> = 4:15:12:4. Furthermore, the largest dipole moment is along the <100> axis. For a more elaborate treatment, see ref. [6]. According to this model the most efficient oriented attachment is expected in the <100> direction. The attachment depends on the formation of pairs of nanocrystals, driven by a dipolar interaction. It is important to realize that the equilibrium constant for the formation of such a pair, depends on the exponent of the difference in free energy. Thus, small energy differences, e.g. for the different orientations mentioned above, can have large effects.

The above explanation holds for quasi-spherical nanocrystals. The formation of octahedrons further enhances the effect: the dipole moment increases with the area of the polar {111} surface. Although the above model does not include effects of surface capping groups that may contain charges, and also does not include surface reconstructions that may alter the surface charge densities, it can qualitatively explain the observed crystal shapes.

The addition of acetic acid to the reaction mixture leads to a (partial) replacement of oleate at the Pb sites on the NC surface. Because acetate is so much smaller than oleate, this strongly reduces steric hindrance between different crystals which in turn drastically increases the rate of oriented attachment. This could explain why an increasing concentration of acetate leads to larger NCs. In addition, the acetate may have different binding strengths on different facets. This could enhance the rate of attachment for the facets to which it is bound the weakest. The final size and shape of the crystals does not depend strongly on the

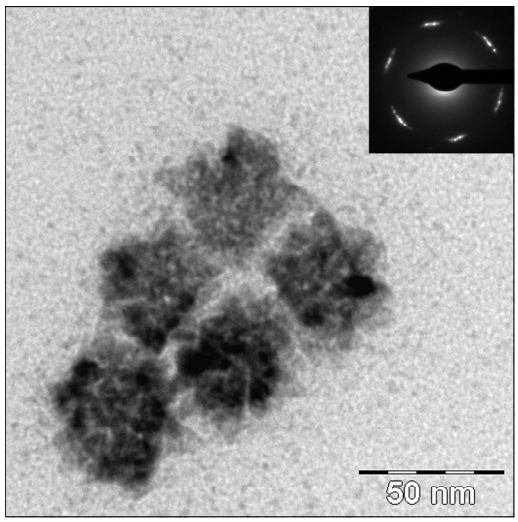

Figure 2.5. PbSe nanocrystals grown in the presence of acetate for 1 minute. T_{inj} = 183ºC, Tgrowth = 140ºC. The insert is the corresponding electron diffraction pattern. The NCs appear to be polycrystalline as the electron density over the crystals in not uniform. However the electron diffraction pattern shows several discrete spots corresponding to the five crystals in the image. This means that even before the NCs are annealed their building blocks are aligned, supporting the mechanism of oriented attachment.

growth temperature between 110 and 230°C. The acetate concentration is by far the most important parameter for this.

Lu *et al*. make no mention of the reason why their synthesis results in star-shaped nanocrystals. They prepare their Pb-oleate precursors by heating to 150°C for 30 minutes under an argon stream.[7] We have used this exact drying procedure and found that it results in a mixture of quasi-spherical and octahedral NCs (see Figure 2.2B). In contrast, Wehrenberg *et al*. and the Murray group report that they dry their precursors at >85°C *under vacuum* for at least one hour[3, 10, 12] when they prepare quasi-spherical PbSe NCs. Interestingly the Murray group reports the formation of octahedral-shaped PbSe NCs, when they do not dry under vacuum. This synthesis was performed in the presence of primary amines and they speculate that the octahedral shape is caused by blocking of the {111} facets by these amines.[6] We have repeated this experiment, but with a reaction mixture that

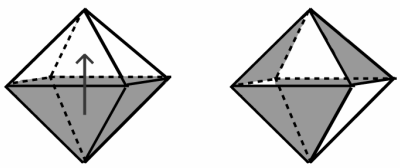

Figure 2.6. Schematic drawing of two octahedrons, possessing only {111} facets. The gray facets are selenium terminated, while the white facets are lead terminated. The distribution of these polar facets can results in a dipole moment (see text). The left octahedron has a dipole moment along a <100> axis (arrow), the right octahedron has no dipole moment.

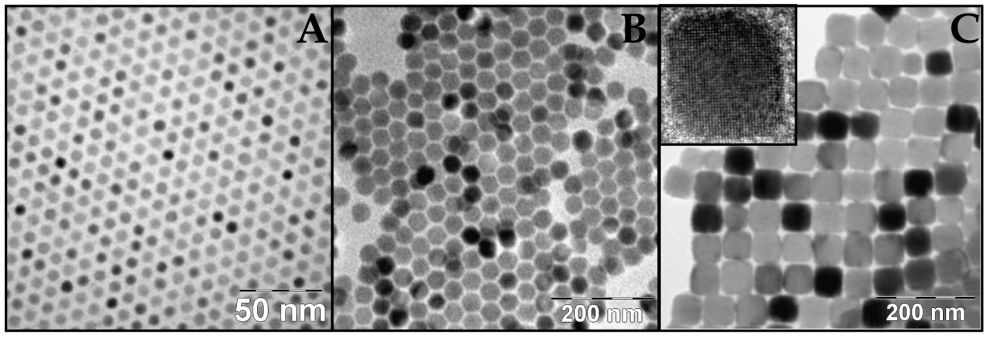

Figure 2.7. TEM images of PbSe nanocrystals showing a shape transition with increasing particles size. A) Quasi-spherical nanocrystals of 6.8 nm in diameter. B) Truncated octahedrons of 9.8 nm in diameter. C) Cubic nanocrystals of 11.1 nm in size.

was carefully dried under vacuum and we have only observed quasi-spherical NCs (see Figure 2.2C). It is important to note that adding 4.8 mmol of hexadecyl amine (HDA) does not result in an apparent change in NC size or shape, whereas the addition of 0.17 mmol acetic acid has a marked effect on both (see Figure 2.1B). Based on the observations reported here we propose that heating the precursor mixture to 150°C for 30 minutes under an argon stream leads to incomplete drying and the inherent presence of acetate at the surface of the synthesized NCs. We propose that this acetate is responsible for the high degree of oriented attachment and many of the resulting crystal shapes reported in the literature.[6, 7, 14]

2.4 Self-assembly of nanospheres, nanostars and nanocubes

This section considers the self-assembly of PbSe nanocrystals of different shapes. The synthesis of star-shaped nanocrystals was described in the previous section. In the absence of acetate one can synthesize very monodisperse quasi-spherical nanocrystals. The size of the NCs is determined by the growth temperature and growth time. It is well known that increasing the NC diameter leads to a gradual change in shape [9, 15] from nearly spherical (< 8 nm) to highly faceted truncated octahedrons (8-11 nm) to cubic (>11 nm). This transition is shown in Figure 2.7. The reason for this shape-transition is that the apolar {100} facets have a lower surface energy than higher index planes; a macroscopic PbSe crystal is always cubic. The edges and corners of a cube have a high energy, since the number of neighbours, and thus the total stabilizing lattice energy, is smaller than in the volume or at a surface plane. In addition, the entropy term in the Gibbs free energy is smaller for corners and edges as there are less microscopic configurations for a perfect corner than for a corner that is cut-off by a high-index plane. The balance between maximizing the relative amount of {100} surface and minimizing the corners, edges and total surface area determines the shape of the nanocrystals. For very small nanocrystals the latter effect dominates and the quasi-spherical shape results from a combination of many facets. Annealing quasi-spherical nanocrystals at 150ºC for 30 minutes does not change their shape; therefore, kinetic effects cannot explain the spherical shape. As the nanocrystals

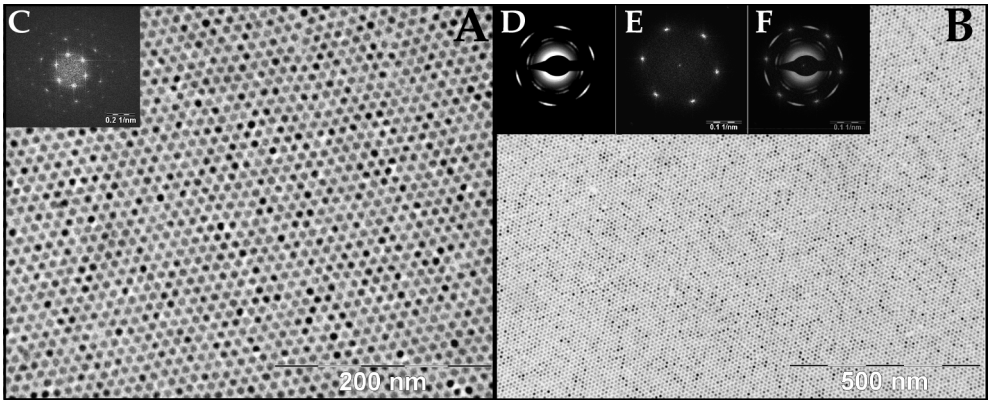

Figure 2.8. A and B are TEM images showing monolayers of quasi-spherical PbSe nanocrystals of 6.8 ± 0.3 nm in diameter on two different length scales, which exhibit nearly defect-free hexagonal order. C is a Fourier transform of the image illustrating again the high degree of order. D) WAED image of a 0.8 μm^2 subsection of the monolayer in B. E) Fourier transform of the image in B. F) The WAED image and Fourier transform overlaid on a single image.

grow the surface energy contribution becomes larger, finally resulting in a cubic shape that, however, still has rounded edges, as can be seen in Figure 2.7C. The star-shaped and octahedral NCs described in the previous section do not represent the thermodynamic most stable geometry. They result from the higher growth rate in the <100> direction.

Spheres

Monolayers of 6.8 nm quasi-spherical NCs are shown in Figure 2.8A and B, at different magnifications. The standard deviation in the diameter (of the inorganic core) of these nanocrystals is less than 5%, and the resulting monolayers are nearly defect-free and single-crystalline over areas of several μm^2. The Fourier transform of such a monolayer shows that the packing is fully hexagonal with an average distance of 8.8 nm between the nanocrystals. Figure 2.8D is a Wide-Angle Electron Diffraction (WAED) pattern of a 0.8 μm^2 subsection of the monolayer in Figure 2.8B. In WAED the diffraction of electrons is probed at angles corresponding to Bragg diffraction at atomic distances. Thus, WAED is sensitive to the crystal structure within the PbSe NCs and probes the crystal planes which are perpendicular to the electron beam (i.e. in the plane of the TEM image). The fact that the WAED pattern consists of discrete peaks instead of rings, shows that there is atomic alignment between the nanocrystals with the <111> axis of the rocksalt lattice toward the substrate (since six equidistant peaks are observed). The Fourier transform of the TEM image is shown in Figure 2.8E, while F shows the Fourier transform and WAED image overlaid. The first-order Fourier peaks fall exactly in between the second order WAED peaks, showing that the alignment of the nanocrystals in the monolayer is crystallographically defined.

The atomic alignment between spherical NCs is again illustrated in Figure 2.9. This figure shows a TEM image of 3D face-centered-cubic supercrystals of spherical nanocrystals with a 7.7 nm diameter, which self-assembled in a slightly

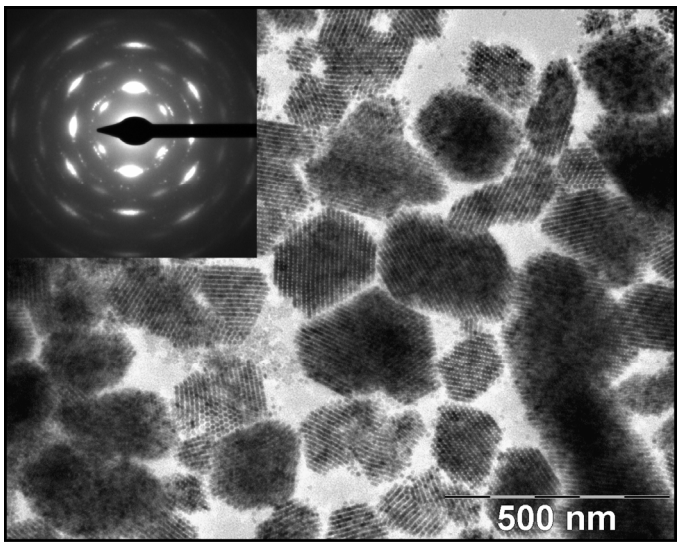

Figure 2.9. Three-dimensional fcc supercrystals formed by quasi-spherical PbSe nanocrystals with a 7.7 nm diameter. The insert shows a WAED pattern of one supercrystal, clearly illustrating atomic alignment.

destabilized dispersion. The insert is a WAED pattern of one of these supercystals clearly showing a strong alignment of the atomic lattices of the individual NCs, here in a <110> projection. This <110> projection is inferred from the observation of 4 peaks in the WAED pattern that are equidistant with respect to the center. The peaks form a rectangle with a $\sqrt{2}$:1 ratio of its sides. Such atomic alignment can be induced by the shape of the nanocrystals. Cubic nanocrystals for example exhibit cubic packing, where two {100} facets face one another. However, the nanocystals in Figure 2.9 and Figure 2.8 are almost completely spherical. The allignment of spherical particles implies a directive force between them, which is likely caused by dipolar interactions between the nanocrystals. This dipolar interaction will be discussed further below.

Stars

In the presence of small amounts of acetate (Pb:Ac ~ 5:1) the star-shaped NCs can be made very monodisperse. The narrow size-distribution results in a striking long range order in the 2D packing of star-shaped NCs. Figure 2.10 shows TEM images of self-assembled monolayers of star-shaped nanocrystals. Two different types of monolayers are encountered. Figure 2.10E shows a monolayer where the star-shaped NCs are in the <111> projection (“star of David”), A is a zoom-in and B is the Fourier transform of E. Figure 2.10F shows a monolayer of NCs in the <110> projection (“diamond”), with a zoom-in and the corresponding Fourier transform (C and D respectively).

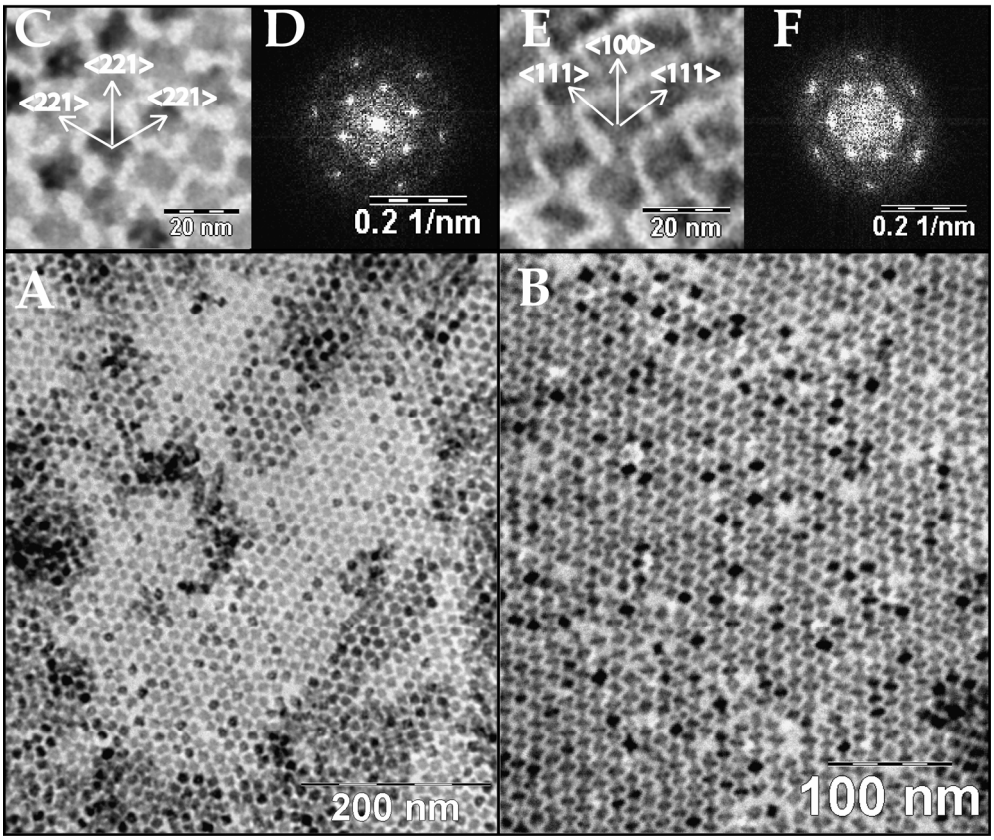

Figure 2.10. TEM images of self-assembled monolayers of star-shaped PbSe nanocrystals viewed along the <111> axis (i.e. the crystallographic <111> axis is perpendicular to the image) (A) and the <110> axis (B). C and E show the nanocrystal arrangement at higher magnification. The arrows indicate the crystallographic axes between neighbours. D and F are Fourier transforms of the images in A and B, respectively.

The Fourier transform of the <111> packing (Figure 2.10D) has threefold rotational symmetry. The peak-to-peak distance of the second-order peaks is 0.27 nm^{-1}, which corresponds to a 14.8 nm center-to-center distance in three directions, at angles of exactly 60°. Thus, the <111> packing of the star-shaped nanocrystals is hexagonal. This is in agreement with the crystallographic axes that connect the neighbours in the monolayer: three equivalent <221> axes (see Figure 2.10C). These axes are deduced from the shape of the NCs in the TEM images. In contrast, the Fourier transform of the <110> packing has lower symmetry. The second order peak to peak distances are 0.30 nm^{-1} (two times) and 0.27 nm^{-1}. The center-to-center distance in the <100> direction of the stars (vertical in Figure 2.10F) is longer than the center-to-center distance in the <111> directions (other two axes): 14.8 nm and 13.3 nm respectively. The packing is clearly not hexagonal. Neglecting the capping layer the expected ratio of the <111> to <100> centre-to-centre-distance is √3:2, very close to the ratio determined from the Fourrier transform. This supports the assignment of the crystallographic directions in the

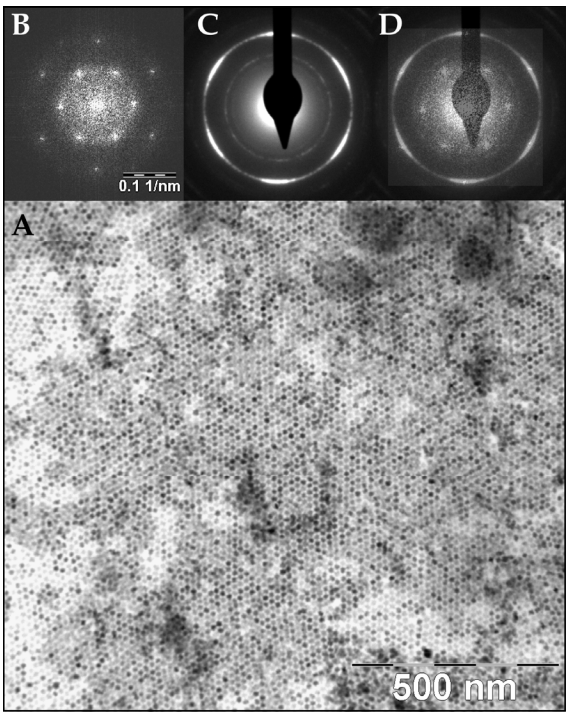

Figure 2.11. TEM image of a monolayer of star-shaped nanocrystals, self-assembled in the <111> projection (A). B and C are a Fourier transform and WAED image of the monolayer in A respectively. B and C are shown overlaid in D, to illustrate the direct correlation between atomic and nanocrystal alignment.

monolayers. The packing geometries in Figure 2.10A and B are, in fact, related by a 30° rotation of all NCs around a <110> axis.

Figure 2.11A shows a long-range ordered monolayer of star-shaped nanocrystals in the <111> projection. The long-range hexagonal order is obvious from the Fourier transform (Figure 2.11B), while the WAED pattern (Figure 2.11C) indicates atomic alignment by the occurrence of discrete peaks instead of rings. From the overlaid image (Figure 2.11D) it is clear that the peaks in the Fourier transform and WAED pattern occur at exactly the same angle. As in the case of spherical PbSe NCs, the self-assembly of star-shaped PbSe NCs is crystallographically defined. In the case of these star-shaped nanocrystals the alignment may be induced by the facets of the NC, by a dipole moment or by a combination of both.

The formation of self-assembled structures of anisotropic NCs with crystal alignment offers possibilities for the engineering of new functional NCs solids. The quantum-mechanical coupling between the NCs will be anisotropic in these systems and as a result, the optical and electrical properties are expected to depend strongly on the direction that is probed.

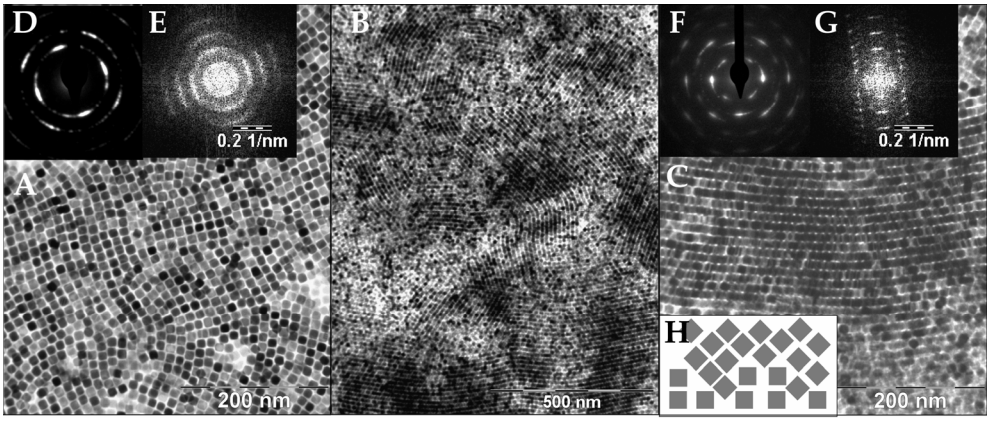

Figure 2.12. Self-assembled layers of 11.1 nm cubic PbSe nanocrystals. A) A bilayer, exhibiting short-range cubic packing. B) Extended region of ordered multilayers. C) Higher magnification of ordered multilayers. D) WAED image and E) Fourier transform of the image in A showing the atomic alignment in the <100> direction. F) WAED image and (G) Fourier transform of the image in C. The projection of the nanocrystals is in the <110> direction. A schematic of a possible arrangement of the nanocubes is shown in H.

Cubes

Finally, we have investigated the self-assembly of cubic PbSe nanocrystals. The cubic NCs self-assemble into a cubic arrangement. The degree of order we obtained was significantly lower than for the spherical and star-shaped nanocrystals. These NCs have a size dispersion of ~5%, comparable to the size dispersion of the star-shaped and spherical nanocrystals. Bilayers of cubic PbSe NCs, such as shown in Figure 2.12A, typically exhibit a higher degree of order than monolayers. We do not yet have a good explanation for this observation. The corresponding WAED pattern (Figure 2.12D) and Fourier transform (Figure 2.12E) clearly show that the nanocrystals have a cubic packing and are aligned in the atomic <100> direction.

Thicker layers of cubic NCs exhibit a different geometry. Figure 2.12B shows multilayers over several micrometers. A zoom-in on a crystalline part of these multilayers is shown in Figure 2.12C. The packing is still cubic, but as can be seen in the WAED pattern (F) and Fourier transform (G) the nanocrystals are in the <110> projection. This projection is apparently preferred for thicker layers of cubic NCs. A speculative explanation for this is given in Figure 2.12H. As a result of disorder in the first layer on the TEM substrate, some NCs in the second layer may get trapped in between the nanocrystals of the first layer. These trapped NCs would have a projection close to <110> and could induce this projection in subsequent layers. This would be a self-stabilizing growth mechanism.

Cryo-TEM

As explained in section 2.3 the synthesis of both star-shaped nanocrystals and wires via the mechanism of oriented attachments suggests that PbSe NCs possess a dipole moment.[6] The atomic alignment observed in monolayers and supercrystals of nanocrystals of several shapes again points in the direction of a

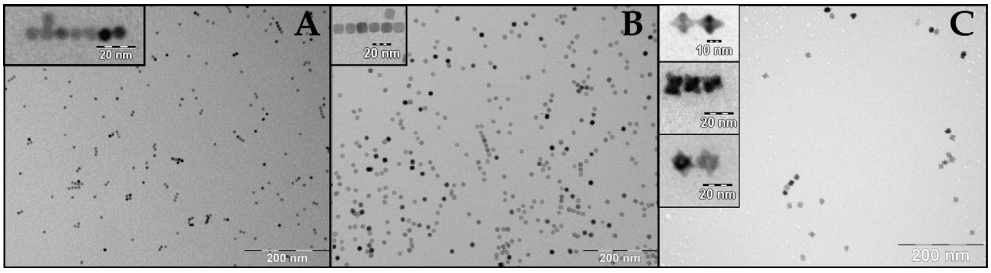

Figure 2.13. Cryo-TEM images of vitrified dispersions of (A) spherical (B) cubic and (C) star-shaped nanocrystals, insets show a mangnification. Linear aggregates can be observed for all three shapes and clearly indicate the presence of a directive force, irrespective of particle shape.

dipole moment. To investigate this possible dipole moment in a more direct way we performed Cryo-TEM measurements.

In Cryo-TEM a thin film of a dispersion of the nanocrystals is rapidly frozen in liquid nitrogen. This freezing process is fast enough to prevent significant diffusion of the nanocrystals and to avoid drying effects. The resulting TEM images correspond to the *in situ* arrangement in the dispersion. It has recently been shown by Cryo-TEM that magnetic nanocrystals, with a magnetic dipole moment, obey linear aggregation statistics and form chains in dispersion.[16-19] The length of these chains is determined by the balance between dipolar attraction and thermal motion. Nanocrystals with a sizable electric dipole moment are expected to behave very similarly to nanocrystals with a magnetic dipole moment.

Cryo-TEM images of PbSe nanocrystals with different shapes dispersed in decaline are shown in Figure 2.13. All nanocrystals with different shapes tend to form chains: PbSe spheres of 6.8 nm (± 0.3 nm), cubes of 11.1 (± 0.6 nm), and star-shaped nanocrystals of 12.8 nm (± 1.6 nm). The chains formed by spherical particles in particular are surprisingly straight. The formation of chains in dispersion indicates a directive attractive force on the particles, which we ascribe to the presence of a permanent electric dipole moment in PbSe nanocrystals. If a dipole moment is indeed responsible for chain-formation, it can be concluded from Figure 2.13 that this dipole moment is present in all different shapes of PbSe nanocrystals.

A more quantitative analysis of the cryo-TEM images was performed by tracking the particle positions in the snapshots using image analysis software developed earlier by Klokkenburg *et al*. for the analysis of chain formation of particles with a magnetic dipole moment.[16-19] Using this technique, the average cluster size and fraction of clusters with a certain size could be determined. We defined a cluster as having one end particle that serves as a starting point; all the nearest neighbors of this particle are assigned to be part of this cluster, including their nearest neighbors, etc., until no new neighbors are detected. We have checked that the chain formation is reversible, by investigating different concentrations of dispersions. As expected for a dynamic equilibrium, we found by the quantitative analysis that the average chain length decreases from 4.5 to 2 particles per cluster upon dilution of the same sample. We can also apply a one-dimensional aggregation model that was previously introduced to describe dipolar chain lengths

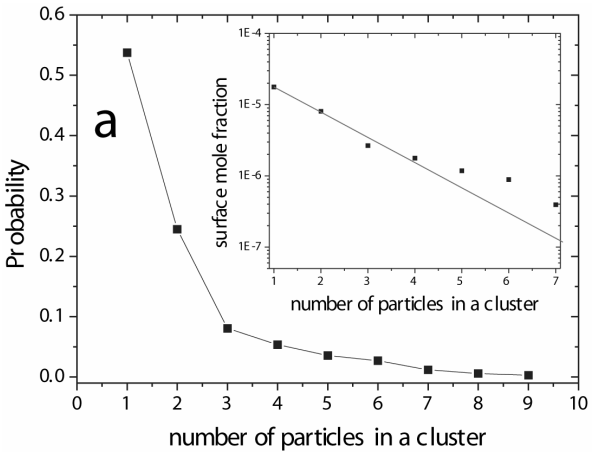

Figure 2.14. Cluster size distribution of spherical PbSe QDs (6.8 nm) in a vitrified dispersion analyzed by cryogenic TEM. Inset shows a fit of the data according to equation 2.2.

in colloidal dispersions of magnetic nanoparticles.[17] This model only takes into account the effective nearest neighbor interaction *V* and gives the following relation between the concentrations of dipolar chains with a certain length *q*:

$$x_q = x_1^q \exp(-(q-1)V) \qquad (2.2)$$

where x_1 is the surface mole fraction of single particles and *V* is scaled to the thermal energy. Figure 2.14 shows the fraction of chains with length *q* in a dispersion of spherical PbSe QDs (6.8 nm). It can be seen that the cluster-size distribution of these systems decays with increasing number of particles in a chain. The inset of Figure 2.14 shows that this decay is indeed exponential, as expected from equation (2.2). A fit to the initial decay yields a value for *V* of -8±1 and similar values were found for samples with a different concentration. Beyond 3-4 particles in a cluster, a more detailed description is required that takes into account chain curvature. We conclude that the spherical PbSe nanoparticles have a dipolar attraction of -8±1 k_BT (room temperature) at minimal contact. In a similar fashion we found a pair attraction (*V*) of -9±1 k_BT and -10±1 k_BT for cubic and star-shaped nanocrystals respectively.

If the model of Cho *et al*.[6] as explained in section 2.3 is correct, the size of the dipole moment is determined by the total surface area of the {111} facets. This should be largest for star-shaped nanocrystals, smallest for cubic nanocrystals (even 0 for perfect cubes) and intermediate for quasi-spherical nanocrystals. Surprisingly, the cubic NCs also clearly exhibit chain formation, and we find a pair attraction for cubic nanocrystals that is larger than for spherical nanocrystals. Therefore, we can conclude that the model of Cho *et al*.[6] cannot fully explain the dipole moment of PbSe nanocrystals.

2.5 Conclusions

We have shown that acetate, naturally present in insufficiently dried reaction mixtures, is a key factor in the growth mechanism and the final shape and size of PbSe nanocrystals. The controlled addition of acetate can be used to synthesize monodisperse star-shaped and octahedral nanocrystals over a wide range of sizes. By varying the reaction conditions in the absence of acetate, highly monodisperse (5%) spherical PbSe nanocrystals can be synthesized, as well as truncated octahedrons and cubic nanocrystals.

It was shown that it is possible to obtain self-assembled monolayers of star-shaped nanocrystals with crystalline domains of several μm^2. Two different structures were identified in the monolayers: a hexagonal packing with the NCs in the <111> projection and a hexagonal-like packing with the NCs in the <110> projection, which is distorted in the <100> direction. We have also demonstrated long-range nearly defect-free self-assembly of spherical nanocrystals in two and three dimensions. Monolayers and bilayers of cubic nanocrystals are observed in a cubic arrangement with the NCs in the <100> projection. Thicker layers of cubic NCs show a surprising preference for the <110> projection, possibly resulting from a self-stabilizing growth mechanism.

By performing wide angle electron diffraction measurements, we have shown that there is a high degree of atomic alignment in the self-assembled structures of spherical, cubic and star-shaped nanocrystals. The crystallographic alignment of cubic and star-shaped nanocrystals may be ascribed to geometric effects, which is not the case for spherical nanocrystals.

Both the directionality of oriented attachment in the synthesis of star-shaped nanocrystals and the atomic alignment of the spherical nanocrystals in self-assembled structures provide indirect evidence for the existence of a sizeable dipole moment in PbSe nanocrystals. Direct evidence for this dipole moment was obtained by Cryo-TEM analysis. Spherical, cubic and star-shaped PbSe nanocrystals were all shown to form chains in dispersions, as a result of a balance between dipolar interactions and thermal motion. Quantitative analysis of the cryo-TEM images yields a dipolar pair attraction of 8-10 k_bT at room temperature. The presence of a dipole moment in cubic nanocrystals is in contradiction with a model that was previously suggested to explain the dipole moment.[6]

2.6 References

1. F.W. Wise, *Acc. Chem. Res.*, **2000**. *33* (11): p. 773-780.
2. C.B. Murray, S.H. Sun, W. Gaschler, H. Doyle, T.A. Betley, and C.R. Kagan, *IBM J. Res. Dev.*, **2001**. *45* (1): p. 47-56.
3. B.L. Wehrenberg, C.J. Wang, and P. Guyot-Sionnest, *J. Phys. Chem. B*, **2002**. *106* (41): p. 10634-10640.
4. A.J. Nozik, *Next Generation Photovoltaics*, **2004**: p. 196-222.
5. V.I. Klimov, *Annu. Rev. Phys. Chem.*, **2007**. *58*: p. 635-673.
6. K.S. Cho, D.V. Talapin, W. Gaschler, and C.B. Murray, *J. Am. Chem. Soc.*, **2005**. *127* (19): p. 7140-7147.
7. W.G. Lu, J.Y. Fang, Y. Ding, and Z.L. Wang, *J. Phys. Chem. B*, **2005**. *109* (41): p. 19219-19222.
8. E. Lifshitz, M. Bashouti, V. Kloper, A. Kigel, M.S. Eisen, and S. Berger, *Nano Lett.*, **2003**. *3* (6): p. 857-862.
9. J.M. Pietryga, R.D. Schaller, D. Werder, M.H. Stewart, V.I. Klimov, and J.A. Hollingsworth, *J. Am. Chem. Soc.*, **2004**. *126* (38): p. 11752-11753.
10. D.V. Talapin and C.B. Murray, *Science*, **2005**. *310* (5745): p. 86-89.
11. E.V. Shevchenko, D.V. Talapin, N.A. Kotov, S. O'Brien, and C.B. Murray, *Nature*, **2006**. *439* (7072): p. 55-59.
12. E.V. Shevchenko, D.V. Talapin, S. O'Brien, and C.B. Murray, *J. Am. Chem. Soc.*, **2005**. *127* (24): p. 8741-8747.
13. F.X. Redl, K.S. Cho, C.B. Murray, and S. O'Brien, *Nature*, **2003**. *423* (6943): p. 968-971.
14. W.G. Lu, P.X. Gao, W. Bin Jian, Z.L. Wang, and J.Y. Fang, *J. Am. Chem. Soc.*, **2004**. *126* (45): p. 14816-14821.
15. J.J. Urban, D.V. Talapin, E.V. Shevchenko, and C.B. Murray, *J. Am. Chem. Soc.*, **2006**. *128* (10): p. 3248-3255.
16. M. Klokkenburg, B.H. Erne, J.D. Meeldijk, A. Wiedenmann, A.V. Petukhov, R.P.A. Dullens, and A.P. Philipse, *Phys. Rev. Lett.*, **2006**. *97* (18): p. -.
17. M. Klokkenburg, R.P.A. Dullens, W.K. Kegel, B.H. Erne, and A.P. Philipse, *Phys. Rev. Lett.*, **2006**. *96* (3): p. -.
18. M. Klokkenburg, B.H. Erne, and A.P. Philipse, *Langmuir*, **2005**. *21* (4): p. 1187-1191.
19. M. Klokkenburg, C. Vonk, E.M. Claesson, J.D. Meeldijk, B.H. Erne, and A.P. Philipse, *J. Am. Chem. Soc.*, **2004**. *126* (51): p. 16706-16707.

Chapter 3

Optical Investigation of Quantum Confinement in PbSe Nanocrystals at Different Points in the Brillouin Zone

This chapter is devoted to the unique optical properties of PbSe nanocrystals. The absorption spectra of monodisperse, quasi-spherical nanocrystals exhibit sharp features as a result of distinct optical transitions. To study the size-dependence, absorption spectra of nanocrystals ranging from 3.4 nm to 10.9 nm in diameter are analysed and a total of 11 distinct optical transitions is identified. The assignment of the various optical transitions is discussed and compared to theoretically calculated transition energies. By plotting all transitions as a function of nanocrystal size we find that the energy changes as $E \propto D^{-1.5}$ for the lowest energy transitions. The transition energy extrapolates to ~0.3 eV for infinite crystal size, in agreement with the bandgap of bulk PbSe at the L-point in the Brillouin zone. In addition, high energy transitions are observed which extrapolate to 1.6 eV for infinite crystal size, which is in good agreement with the bulk bandgap of PbSe at the Σ-point in the Brillouin zone. Tight binding calculations confirm that the high-energy transitions originate from the Σ-point in the Brillouin zone. The Σ-character of the high energy transitions may be of importance to explain the mechanism behind efficient Multiple Exciton Generation in PbSe nanocrystals.

3.1 Introduction

In recent years the interest in lead chalcogenide colloidal nanocrystals (NCs) has grown considerably. The bulk material is interesting, since it is a IV-VI compound with a Pb atomic configuration $[Xe]4f^{14}5d^{10}6s^{2}6p^{2}$. As a consequence of the high atomic number of Pb and the resulting high electron velocities, relativistic effects localize (lower) the 6s valence orbital, transforming the Pb cation into a $6p^2$ configuration (inert pair effect).[1] Another consequence of the high atomic number of Pb is the relatively large ratio of ionic radii ($r_{Pb,\ 2+}/r_{Se,\ 2-}$ = 0.59). As a result, the coordination number of PbSe (6) is higher than for e.g. CdSe (4). The PbSe rock-salt lattice leads to an electronic band structure that is different from that of the typical II-VI compounds (see also Chapter 1 of this thesis). An important consequence is that the valence-band maximum (VBM) and conduction-band minimum (CBM) are both situated at the L-point in the Brillouin zone (see Figure 3.1), which is four-fold degenerate (eight-fold including spin degeneracy).

As a result of the small effective mass of the charge carriers at the bottom of the valence band and top of the conduction band ($m^*_h \approx m^*_e$ = 0.1) and the large bulk exciton Bohr radius of 46 nm, the effect of quantum confinement is particularly strong in PbSe.[2, 3] Since the room temperature bandgap of the bulk material is only 0.278 eV, it is possible to tune the NC bandgap from 0.278 eV (~ 4400 nm) to over 1.1 eV (~ 1100 nm) by changing the size of the nanocrystal. Therefore, lead chalcogenide quantum dots are promising building blocks for a wide number of opto-electronic applications in the near infrared.[3-6] For example, PbSe QDs hold great promise in the field of photovoltaics, because of the recently observed Multiple Exciton Generation (MEG) in these nanocrystals. [7-10]

Here we report on detailed investigations of the optical absorption spectra of PbSe QDs. First, the assignment of the multiple features (up to 11) in the absorption spectrum of highly monodisperse PbSe QDs is discussed, and compared to calculated spectra of PbSe QDs that were recently published.[1, 11] Next, the size-dependence of the energy of the various transitions is analyzed for 16 different sizes of PbSe QDs ranging from 3.4 nm to 10.9 nm. It follows that the higher-energy transitions can be assigned to optical transitions at a different point in the Brillouin zone than the lower-energy transitions. We first use effective mass theory to qualitatively explain the differences observed in the optical transitions. Subsequently, we apply tight-binding calculations to quantitatively confirm the assignment of the different transitions to different points in the Brillouin zone. Finally, it is discussed how these observations may be relevant for the explanation of MEG, the mechanism of which is still under debate.

3.2 Experimental Section

The PbSe nanocrystals were synthesized inside an argon or nitrogen-purged glove box. All chemicals were stored inside this glovebox. A stock solution of lead acetate trihydrate (3.25 g, Aldrich, 99.999%) in diphenyl ether (10 ml DPE, Aldrich), oleic acid (7.5 ml, Aldrich, 90%) and trioctyl phosphine (40 ml TOP, Fluka, 90%) was prepared. The lead oleate precursor was prepared by heating the above mixture to over 70ºC under vacuum (<10^{-3} mbar) for 1 hour to remove trace amounts of water and acetate, a crucial step to obtain monodisperse spherical nanocrystals.[12] The solution was allowed to cool to room temperature. 11.5 ml of this solution was mixed with a solution of selenium (1.0 M, Alfa Aesar, 99.999%) in TOP (1.7 ml) and rapidly injected into DPE (10 ml) that was preheated to the desired injection temperature. In a typical synthesis the injection temperature was 180ºC, the temperature dropped upon injection to 125ºC and quickly reached the growth temperature of 135ºC. The size of the spherical nanocrystals was controlled by the growth time, which varied from 14 s (3.4 nm NCs) to 30 min (10.9 nm NCs). The crude products were cleaned by the addition of a small volume of butanol (Aldrich, anhydrous, 99.8%) , centrifugation, and dissolution of the precipitate in tetrachloroethylene (Aldrich, anhydrous, >99%). This cleaning procedure was repeated once. Transmission electron microscopy images were obtained with a Philips Tecnai 12, a Fei Tecnai 10 and a Fei Tecnai 20 FEG. Optical absorption spectra were recorded with a PerkinElmer Lambda 950 UV/VIS Spectrophotometer.

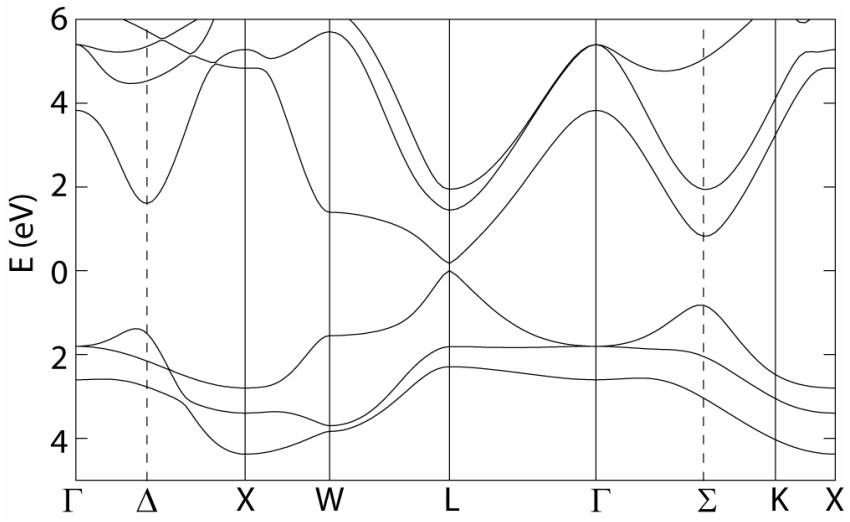

Figure 3.1 Band structure of bulk PbSe. The zero of energy is located at the top of the valence band.[11]

3.3 Results and Discussion

The absorption spectrum of a dispersion of nanocrystals with a diameter of 6.8 ± 0.3 nm, determined by TEM measurements, is shown in Figures 3.2A and 3.2B. The narrow size-distribution results in sharp optical transition features: the full-width at half-maximum of the lowest energy transition in Figure 3.2 is only 55 meV and many features can be distinguished in the spectrum. The second derivative of the absorption allows one to identify the different optical transitions, and the corresponding transition energies.[10] This is shown in Figures 3.2C and 3.2D. A minimum in the second derivative corresponds to the maximum of an absorption band (note that the second derivative is plotted with the minima upwards). Altogether, 11 minima can be distinguished in Figure 3.2.

One has to be careful in assigning optical transitions based on the second derivative. Noise in the absorption spectrum can create peaks in dA^2/d^2E. Absorption peaks caused by vibrational overtones of e.g. C-H or C=O vibrations in capping molecules or reagents can also interfere. To avoid the influence of noise we have only included features that were present in spectra of several nanocrystal

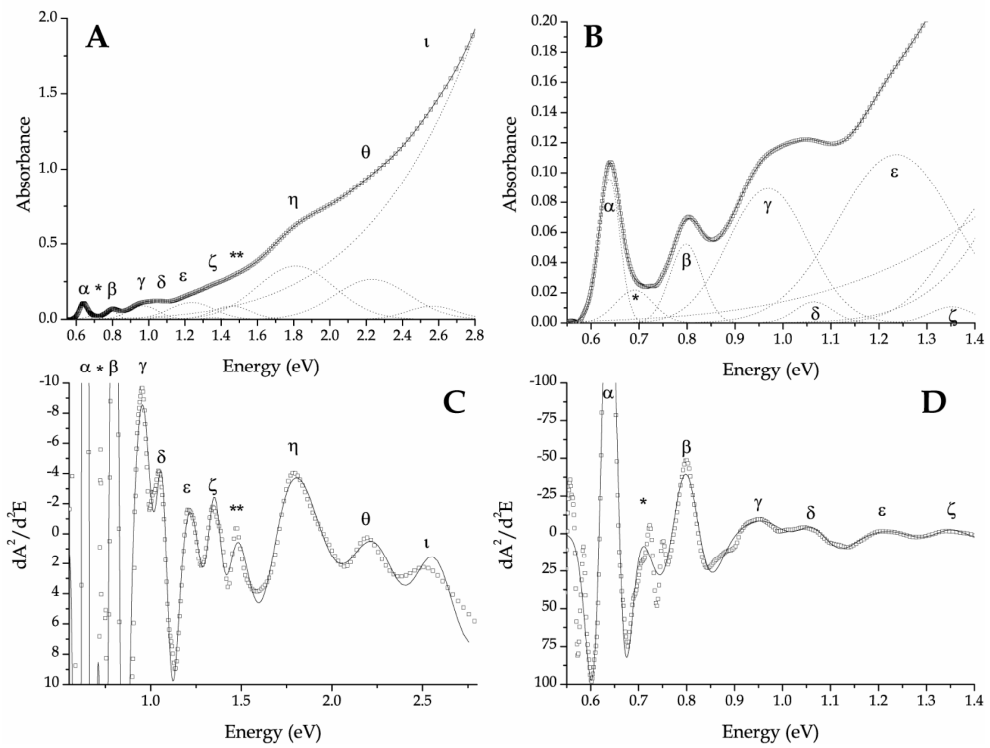

Figure 3.2. Optical absorption spectra of a dispersion of 6.8 nm quasi-spherical PbSe NCs in tetrachloroethylene. The open squares represent the experimental spectrum, the solid line is a fit to Gaussian components and a background that increases with E^4 (dotted lines). The low energy part of the same spectrum and fit are shown in (B). The second derivatives of the experimental spectrum and the fit are shown in (C) and (D) as the open squares and solid lines, respectively.

batches. To avoid optical transitions from organic material we have only included features that shift with particle size. Finally, one has to be aware that the second derivative itself can create artefacts. For example, the second derivative of two well-separated Gaussians has an additional minimum in between the two peaks. To analyze if the minima in the second derivative correspond to actual optical transitions, we have fitted the absorption spectrum in Figure 3.2A to multiple Gaussian functions. A background function that increases as $A \propto E^4$ was also included in the fit, corresponding to weak Rayleigh scattering by the nanocrystals. The multi-Gaussian fit of the absorption spectrum is plotted as a solid line in Figures 3.2A and 3.2B, and the 11 associated Gaussian functions and background function are shown as dotted lines. As can be seen in Figures 3.2A and 3.2B, there is an excellent agreement between the multi-Gaussian fit and the absorption spectrum. The second derivative of the multi-Gaussian fit is shown as a solid line in Figures 3.2C and 3.2D, and is in good agreement with the second derivative of the absorption spectrum. Importantly, we found that it is necessary to include all 11 Gaussians shown in the Figure 3.2A to obtain all the features in the second derivative. We conclude that they all correspond to optical transitions.

The optical transitions are labelled with Greek letters. Transitions that, to our knowledge, have not previously been reported are labelled with asterisks. The assignment of the optical transitions is subject to considerable debate in the literature.[1, 10, 11, 13, 14] This debate largely focuses on the assignment of the "second" peak in the absorption spectrum, labelled (β) here. Based on theoretical calculations of the energy levels and experimental work, this feature has previously been assigned to the $1S_h$-$1P_e$ (or $1P_h$-$1S_e$) transition.[11, 15] However, these transitions are optically forbidden and are expected to be very weak. Liljeroth et al. were able to measure the density-of-states of single PbSe nanocrystals directly using scanning tunnelling spectroscopy and suggested that transition (β) corresponds to the $1P_h$-$1P_e$ transition.[14] Below we will compare the experimental absorption spectra and their features with an absorption spectrum that we obtained by tight binding calculations, as well as an absorption spectrum that was recently calculated by An *et al.*[1] As will become clear, there are still important discrepancies between the experimental data and both theoretical calculations. The purpose of this comparison is to give an overview of the current understanding of the absorption spectrum of PbSe QDs, not to give a final answer on the correct assignment of the different transitions.

Using tight-binding calculations as reported earlier, the absorption spectrum of a PbSe QD of 6.1 nm in diameter was calculated.[11] The calculated spectrum is plotted together with the experimental spectrum of PbSe QDs with a diameter of 6.8 nm, see Figure 3.3. In energy, this is the best matching experimental spectrum that we have measured compared to the calculated spectrum. The second derivative of the experimental spectrum is shown as well, to identify the position of the different transitions more precisely. The first transition (α) of the calculated spectrum (a $1S_h$-$1S_e$ transition) is slightly blue-shifted with respect to the experimental spectrum, which is consistent with the smaller nanocrystal size. Transition (β) is not reproduced by the calculations, because the $1S_h$-$1P_e$ (or $1P_h$-$1S_e$) transition that is calculated for this energy has no oscillator strength. Nevertheless, transitions (γ) and (δ) are reproduced and have a $1P_h$-$1P_e$ character according to the tight binding calculations. Also transition (ε) is calculated, and

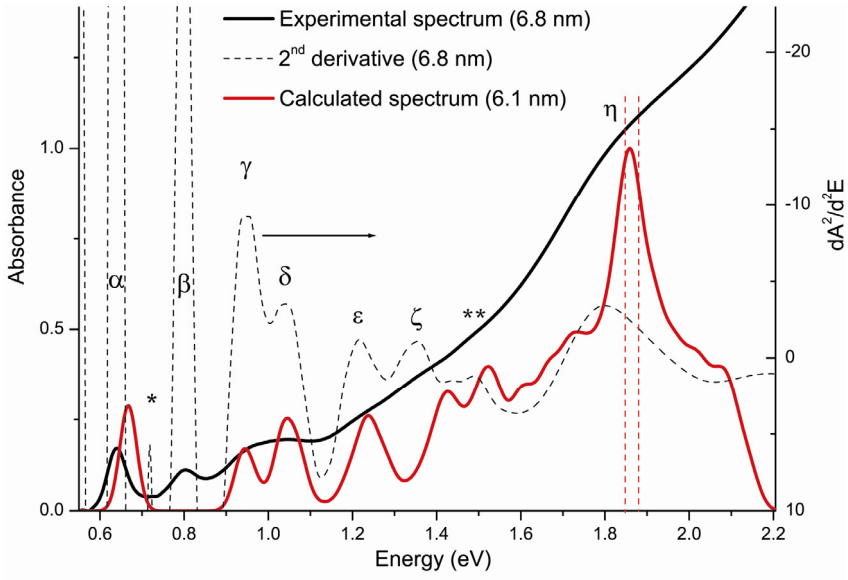

Figure 3.3. Experimental absorption spectrum of PbSe QDs with a diameter of 6.8 nm ± 0.3 nm (solid black line). For clarity, the second derivative of the experimental spectrum is plotted on a different scale (right y-axis). The absorption spectrum obtained by tight-binding calculations of a PbSe QD with a diameter of 6.1 nm is shown in red, scaled to an appropriate value for comparison with the experimental spectrum. The red dotted lines indicate the energy range that was used in the tight-binding calculations to determine from which points in the Brillouin zone these transitions originate. The decrease to zero of the theoretical spectrum above 2 eV is due to the limited number of eigenstates that we can calculate (here 1100 states).

transitions (ζ) and (**) show up in the theoretical spectrum as well (although slightly shifted). In addition, the relative oscillator strengths calculated for all these transitions are in good agreement with experiment. The tight binding calculations also reproduce the transition (η) at approximately 1.85 eV with a large oscillator strength. In summary, the tight-binding calculations reproduce the measured absorption spectrum of a nanocrystal with similar size, except for transition (β) which, according to these calculations, is the forbidden $1S_h$-$1P_e$ (or $1P_h$-$1S_e$) transition.

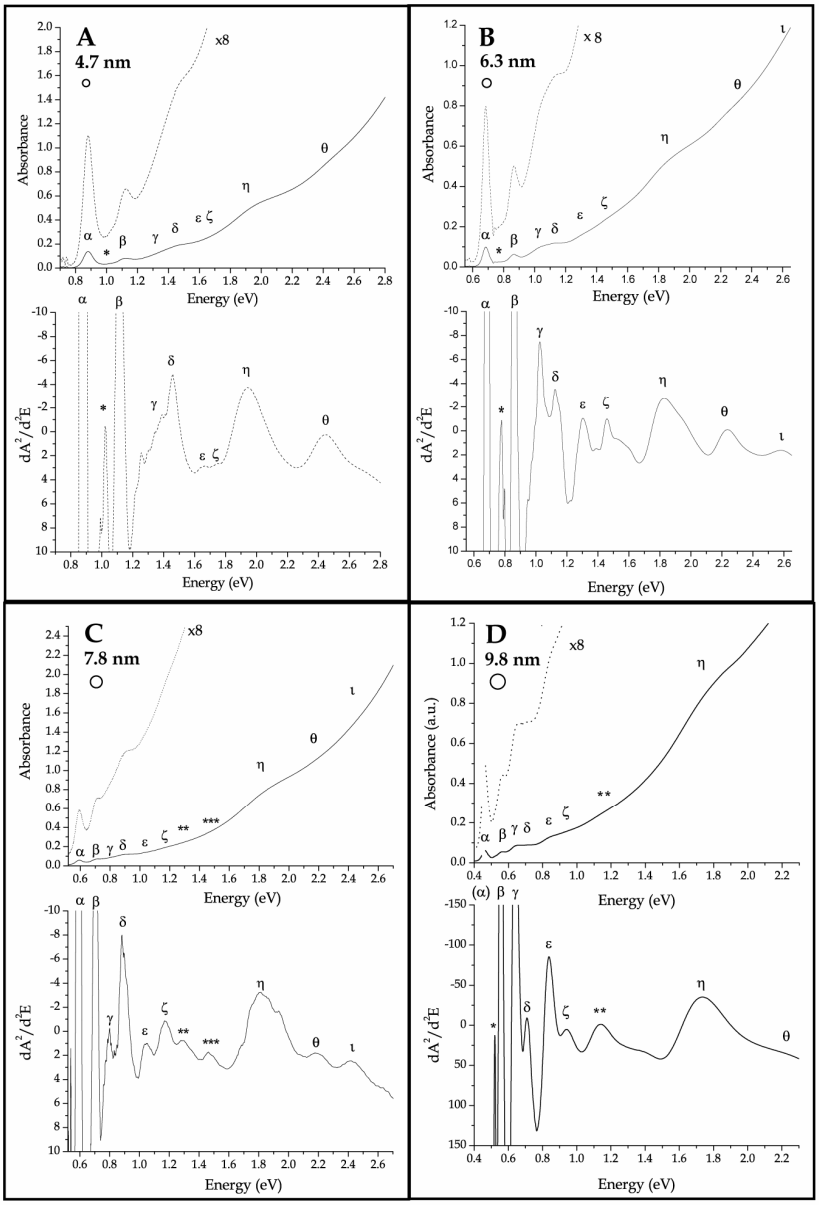

Figure 3.4. Absorption spectra and corresponding second derivative of PbSe QDs of 4.7 nm (A), 6.3 nm (B), 7.8 nm (C) and 9.8 nm (D) in diameter. The dotted absorption spectra are an 8-fold magnification of the original spectrum, shown for clarity.

A different approach for the assignment of the different transitions was recently reported by An *et al.*[1] Using pseudo-potential calculations, it was calculated that a PbSe nanocrystal with a $1S_h$-$1S_e$ transition (α) at 0.89 eV has a $1P_h$-$1P_e$ transition (β) that is 0.24 eV higher in energy, at 1.13 eV. We have measured and analyzed

the absorption spectrum of PbSe QDs that have a first transition (α) at 0.87 eV (see Figure 3.4A), allowing for a good comparison with the calculated spectrum by An *et al*. We find that PbSe QDs with transition (α) at 0.87 eV display a second transition (β) at 1.12 eV, which coincides nicely with the values calculated by An *et al*.[1] This suggests that the second peak in the absorption spectra of PbSe QDs is the $1P_h$-$1P_e$ transition, in line with the assignment by Liljeroth *et al.*,[14] but in contrast with the tight-binding calculations discussed above. Interestingly, An *et al.* calculate two additional transitions as a result of heavily mixed P and D-like states, located at 1.38 eV and ~1.48 eV respectively. The energies corresponding to the transitions (γ) and (δ) in the measured absorption spectrum are 1.39 eV and 1.46 eV, respectively (see Figure 3.4A), in good agreement with the calculated values of An *et al*. Furthermore, An *et al*. calculate a transition in between transitions (β) and (γ), originating from anisotropically asymmetric transitions with small oscillator strengths. We were not able to resolve this weak transition from the measured absorption spectra of PbSe QDs of various sizes. It is important to note that the calculated spectrum of An *et al*. is based on a nanocrystal with a diameter of 6.1 nm, whereas the corresponding absorption spectrum was measured for PbSe QDs with a diameter of 4.7 nm (± 0.4 nm), based on the analysis of TEM images. In other words, there is a striking difference of 220 meV between the calculated energy of the first transition (α) of a PbSe QD of 6.1 nm using tight binding calculations (0.67 eV) or pseudo-potential calculations (0.89 eV). As can be derived from Figure 3.5 (discussed below), we find an experimental value of 0.70 eV for the first transition of a PbSe QD of 6.1 nm.

Feature (*) in Figure 3.2 is not clearly observed in the absorption spectra. However, it does show up in the second derivative spectra we have studied (e.g. Figure 3.2D), and is situated in between the transitions (α) and (β). Several spectra from the literature also suggest an additional feature as a shoulder on the low energy side of peak (β). See, for instance, Figure 1 in the supporting information of ref. [16] or Figure 4 in ref. [4].[4, 16] This feature may be the $1S_h$-$1P_e$ (or $1P_h$-$1S_e$) transition, implying that transition (β) is the $1P_h$-$1P_e$ transition. A more definitive proof of the existence of feature (*) as a real optical transition will require measuring the absorption spectrum of a monodisperse sample at low temperature, or the use of excitation spectroscopy.[17]

To investigate the influence of quantum confinement on the various transitions, we have measured and analyzed the absorption spectra of quasi-spherical PbSe nanocrystals with diameters ranging from 3.4 nm to 10.9 nm. A few examples of absorption spectra of 4 different sizes of PbSe QDs are shown in Figure 3.4. The different transitions were assigned on the basis of the features in the second derivative spectra, in a similar way as discussed for the spectrum in Figure 3.2. Figure 3.5 shows the different transition energies of PbSe QDs as a function of the nanocrystal size. The x-axis has the dimension $D^{-1.5}$, because we found that the energy of the first transition in the absorption spectra is proportional to the diameter D as $E_{1st} \sim D^{-1.5}$. This is a somewhat stronger dependence on size than that reported by Yu *et al.*, who found an almost linear relation between diameter and wavelength of the first exciton, i.e. $E_{1st} \sim D^{-1.0}$.[18] The dotted lines in Figure 3.5 are linear fits for each transition (except for those labelled by asterisks) at varying nanocrystal size, and serve as a guide for the eye.

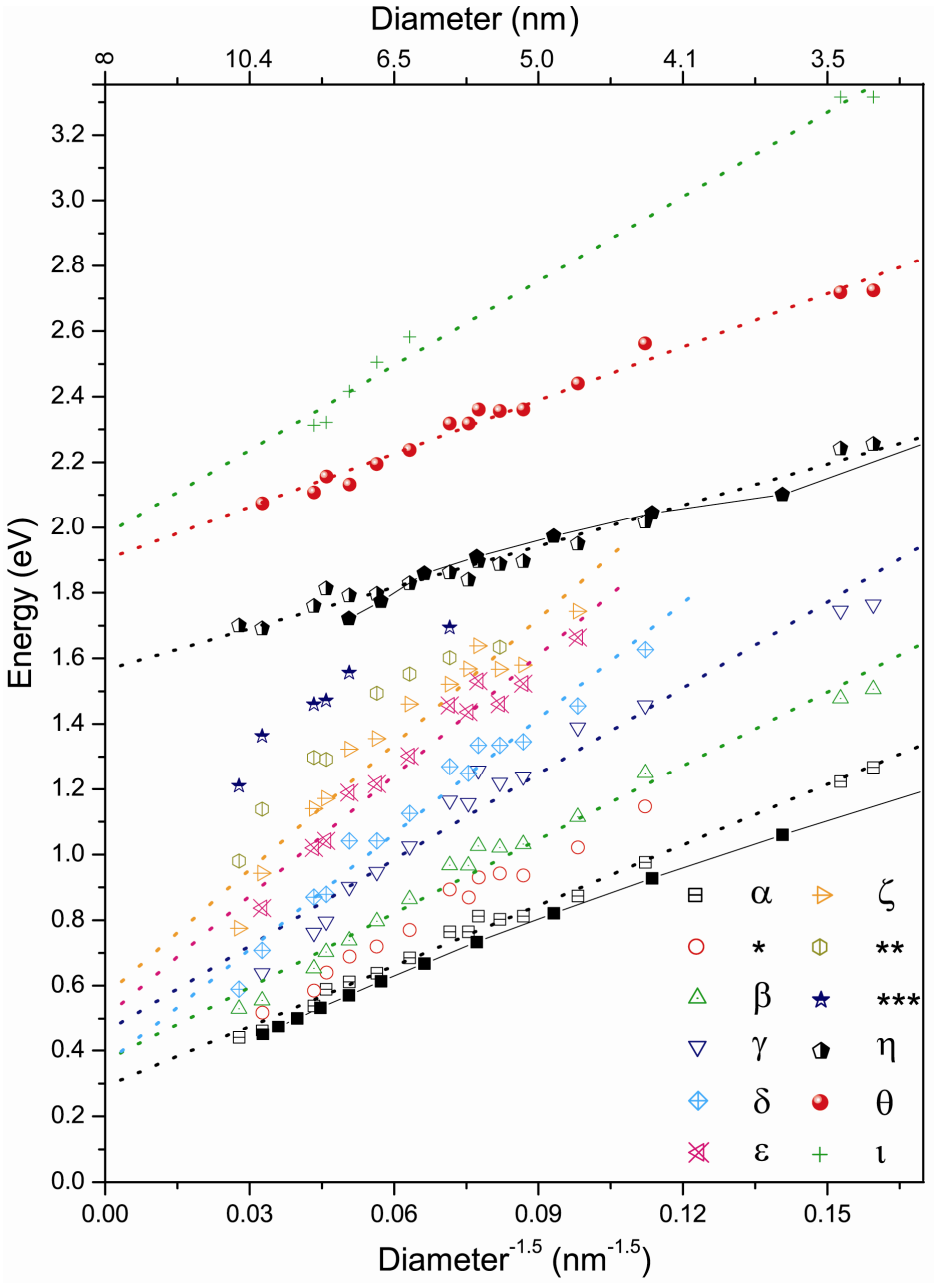

Figure 3.5. Energies of optical transitions as indicated in Figure 3.2 for PbSe nanocrystals of different sizes, ranging from 3.4 nm to 10.9 nm in diameter. The dotted lines are linear fits assuming a linear dependence between E and $D^{-1.5}$, and serve as a guide for the eye. The solid black symbols and interconnecting solid black lines show the results of the size-dependence using tight-binding calculations for the transition (α) and the first transition at the Σ-point of the Brillouin zone, transition (η).

The trends of the size-dependent energies of the transitions in Figure 3.5 are clear. The energy for the first transition (α) increases linearly with $D^{-1.5}$ and extrapolates to 0.29 eV for $D^{-1.5} = 0$ (i.e. infinite crystal size), in excellent agreement with the room temperature bandgap of bulk PbSe (0.278 eV) at the L-point of the Brillouin zone (see Figure 3.1). The higher lying transitions extrapolate to approximately the same value, and show a similar $D^{-1.5}$ dependence. Furthermore, the slope of the linear fits (dotted lines) increases gradually for the higher lying transitions. These observations can be explained with a simple effective mass approximation as will be shown below. The above described trend only holds up to transition (ζ). From transition (η) and higher, the slope of the linear fits abruptly changes to a lower value, and the transitions do not extrapolate to 0.29 eV for infinite crystal size. Transition (η) extrapolates to a value of 1.57 eV for $D^{-1.5} = 0$, and the higher lying transitions (θ) and (ι) again increase in slope and also extrapolate to a value relatively close to 1.6 eV. We propose that transitions (η), (θ) and (ι) in Figure 3.5 correspond to optical transitions at another point in the Brillouin zone of PbSe than the L-point. In the band structure of bulk PbSe, there is a second bandgap at the Σ-point in the Brillouin zone with an energy of 1.60 eV, in excellent agreement with our experimental value of 1.57 eV for the extrapolation of transition (η).[11, 19] We assign (η) to a direct transition between a hole at the Σ-point and an electron at the Σ-point, probably having S-symmetry envelope functions. Transitions (θ) and (ι) are assigned to transitions between higher energy envelope functions at the Σ-point. As can be seen from the multi-Gaussian fit in Figure 3.2A, the transition (η) has a large oscillator strength compared to the lower-energy transitions.

First, we will use effective mass theory to qualitatively explain the trends observed in Figure 3.5. As was mentioned above, the energies of transitions (α) to (ζ) increase (nearly) linearly with $D^{-1.5}$ and extrapolate to 0.29 eV, with an increasing slope for higher energy transitions. Effective mass theory yields the following expression[20-22] for interband transitions with electrons and holes in the same orbitals (e.g. $1S_h1S_e$, $1P_h1P_e$, …):

$$E_{nl}^{opt}(D) = E_g^0 + \frac{2\chi_{nl}^2\hbar^2}{D^2}\left(\frac{1}{m_e^*} + \frac{1}{m_h^*}\right) - \frac{0.9e^2}{\varepsilon_{in}D} \qquad (3.1)$$

where *nl* are the quantum numbers of the electron and hole orbitals and χ_{nl} are roots of the spherical Bessel function, which increase with increasing quantum number.[20] E_g^0, $\hbar$, e, and ε_{in} correspond to the fundamental bandgap, Planck's constant, the electronic charge, and the dielectric constant inside the nanocrystal, respectively. Neglecting the last term (due to the high ε_{in} of PbSe), we find the following slope of the energy with respect to D^{-2}:

$$dE/d\left(D^{-2}\right) \propto \left(\chi_{nl}^2\right)\left(\frac{1}{m_e^*} + \frac{1}{m_h^*}\right) \qquad (3.2)$$

Corrections to the above expressions (e.g. the use of a finite potential barrier) lead to a weaker dependence of energy on diameter.[20] However, it is clear that the slope of the curves in Figure 3.5 should increase with increasing quantum numbers of the orbitals involved, which is exactly what is observed. Furthermore, the slope of the different transitions is also determined by the effective masses of electrons and holes. The significantly smaller slope of transition (η) compared to transition (α) in Figure 3.5 is an indication that the effective masses are larger at the Σ-point than at the L-point. Although the size dependence of the lowest energy transition is $E \sim D^{-1.5}$ (and not D^{-2}), we estimate the ratios of the effective masses at the L and Σ-points from the slopes in Figure 3.5: $(1/m^*_e + 1/m^*_h)_\Sigma = 0.67 \times (1/m^*_e + 1/m^*_h)_L$. If we assume electron-hole symmetry we can deduce that $(m^*_e)_\Sigma = (m^*_h)_\Sigma = 1.5\ (m^*_e)_L = 0.15$. In view of the simplifying assumptions this should be regarded as a rough estimate.

As was shown in Figure 3.3, tight-binding calculations can reproduce the experimental absorption spectrum of PbSe QDs with a diameter of 6.8 nm to a large extent. We have calculated from which point in the Brillouin zone the different transitions of the calculated spectrum originate. Figure 3.6 shows a 2D-contour plot of the projection of the QD wave-functions on bulk states, weighted by the oscillator strength of the optical transitions within a certain energy range. The results are shown as a function of the wave-vector *k* of the bulk state in the (110) plane of the Brillouin zone, for both conduction and valence band states (upper and lower images respectively). Figures 3.6A and 3.6B show the distribution of all transitions within an energy range of 0.60 eV to 0.68 eV, corresponding to transition (α) in Figure 3.3. As expected, these transitions are centred exactly at the L-point in the Brillouin zone. Figures 3.6C and 3.6D show the oscillator strength-weighted distribution of all transitions within an energy range of 1.85 eV to 1.88 eV, corresponding to transition (η) in Figure 3.3 (range indicated by the red dotted lines). Interestingly, these transitions have a clear Σ-character, confirming the above interpretation that transition (η) originates from the Σ-point in the Brillouin zone. The tight-binding calculations find hundreds of different transitions (with Σ-character) around transition (η), indicating a high density of states around the Σ-point in the Brillouin zone. This explains the large optical density around 1.85 eV that is observed in both the calculated and experimental absorption spectra in Figure 3.3.

Furthermore, the size dependence of the energy of transitions (α) and (η) was calculated using the same tight-binding approach. The results are included in Figure 3.5. As can be seen, the calculated size-dependence of transition (α) nicely follows the experimentally obtained energies, although the dependence is not linear on this scale. The size dependence of the energy of transitions (η) is also reproduced by the tight binding calculations. The effective masses of both electrons and holes can be extracted from the tight binding calculations as well. The effective masses of the electrons (holes) are 0.167 (0.135) in the <110> direction, -2.11 (-1.53) in the <001> direction, and 0.098 (0.104) in the $<1\bar{1}0>$ direction. The negative effective mass in the <001> direction results from the fact that the Σ-point is not a valley, but a saddle point. On average, this results in an effective mass of approximately 0.19 for electrons ($1/m^*_e = 1/3*(1/m^*_{e,<110>} + 1/m^*_{e,<001>} + 1/m^*_{e,<1\bar{1}0>})$) and 0.18 for holes (in a similar fashion) at the Σ-point in the

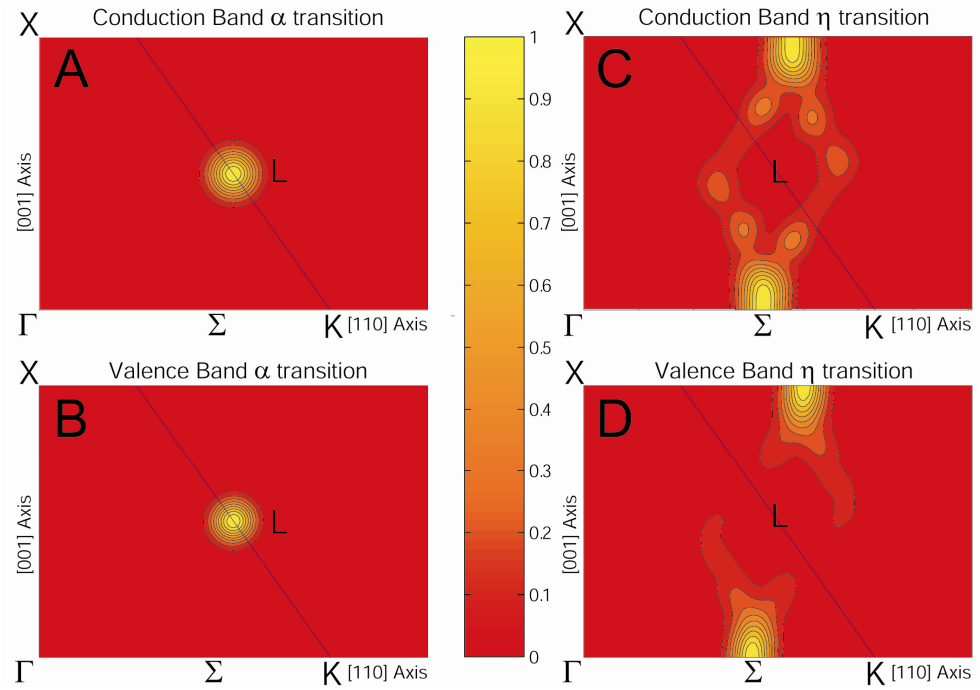

Figure 3.6. 2D-contour plot of the projection of the QD wave-functions ψ_i on bulk states ϕ_k, weighted by the oscillator strength of the optical transitions $\psi_i \rightarrow \psi_f$ within a certain energy range [$\propto \sum_{i,f} |\langle \psi_i | \psi_f \rangle|^2 |\langle \psi_i | r | \psi_f \rangle|^2$ with $E_{min} < E_f - E_i < E_{max}$]. The results are shown as a function of the wave-vector k on the bulk state ϕ_k in the (110) plane of the Brillouin zone. (A) and (B) show all calculated transitions (for conduction and valence band states ψ_i, respectively) in an energy range of E_{min} = 0.60 eV to E_{max} = 0.68 eV, corresponding to transition (α) in Figure 3.3. (C) and (D) show all calculated transitions in an energy range of E_{min} = 1.85 eV to E_{max} = 1.88 eV, corresponding to transition (η), as indicated by the dotted red lines in Figure 3.3.

Brillouin zone. This is in good agreement with the effective masses that were derived from the experimental data using effective mass theory.

Multiple Exciton Generation (MEG) in PbSe nanocrystals through excitation by a high energy photon has received considerable attention in the past few years.[7-10] The mechanism for MEG, however, is still under debate. Two theoretical papers used Impact Ionization (II) to explain the ultra fast carrier multiplication.[23, 24] In both cases, the II rate is calculated and compared to the rate of competing non-radiative decay mechanisms (i.e. phonon-assisted electron/hole cooling). Apart from II, a coherent superposition of multi-exciton and single-exciton states has also been proposed to explain MEG.[10, 25] In this case, the electron/hole cooling rate has to be slower than the multi-exciton thermalization rate and the rate of coupling between the single-and multi-exciton states.[25] Finally, another group proposed the instantaneous formation of multi-excitons through weak coupling with a virtual

single-exciton state to explain MEG, in which case the electron-hole cooling does not play a role.[7]

The threshold for MEG in PbSe QDs of 6.8 nm in diameter (E_g = 0.64 eV) was determined at 1.8 eV. [9] Here, we find that PbSe QDs of 6.8 nm (E_g = 0.64 eV) have the transition (η) at 1.9 eV. Similarly, Schaller *et al.* found that for smaller QDs (E_g = 0.94 eV)), the threshold for MEG is at 2.8 eV (~ three times the bandgap)[8], where we find the transition (η) at ~ 2 times the bandgap. However, Ellingson *et al.* found that for smaller PbSe QDs (3.9 nm -5.4 nm, E_g from 0.91 eV-0.73 eV), the threshold for MEG is in between 2.1-2.9 times the bandgap[10], which is in better agreement with the position of transition (η) that we find for these small nanocrystal sizes (between 2.2-2.6 times the bandgap). The observation that the experimentally obtained energy thresholds for MEG correspond with the energy of transition (η) indicates that excitation into the (η) state (at the Σ-point) may play a role in the mechanism of MEG. For example, electron/hole cooling to the L-valley may become significantly slower for an exciton at the Σ-point, compared to an exciton within the L-valley. As was mentioned above, slow electron/hole cooling is crucial to explain efficient MEG by (e.g.) Impact Ionization.

3.4 Conclusions

In conclusion, we have measured and analyzed the optical absorption spectra of quasi spherical PbSe nanocrystals ranging from 3.4 nm to 10.9 nm in diameter. We have identified in total 11 distinct optical transitions. Comparison with state-of-the-art calculated absorption spectra shows a good agreement for many of the features observed, but also demonstrates that there are still important discrepancies between experiment and theory. By plotting all transition energies as a function of nanocrystal size we find that the energy of the transitions changes as $E \propto D^{-1.5}$. Low energy transitions extrapolate to 0.29 eV, in good agreement with the bandgap of bulk PbSe in the L-valley. High-energy transitions extrapolate to 1.57 eV, in good accordance with the bandgap of bulk PbSe at the Σ-point in the Brillouin zone. These higher energy transitions are therefore ascribed to direct optical transitions at the Σ-point, and an estimate of the effective mass at this point of 0.15 for both electrons and holes is obtained. Tight binding calculations confirm that the high-energy transitions originate from the Σ-point, and an average effective mass of 0.19 (0.18) is calculated for electrons (holes), in good agreement with the experimentally derived value. It is shown that the reported threshold energy for Multiple Exciton Generation in PbSe nanocrystals coincides with the energy of the first direct transition at the Σ-point, suggesting a relation between the two.

3.5 References

1. J.M. An, A. Franceschetti, S.V. Dudiy, and A. Zunger, *Nano Lett.*, **2006**. *6* (12): p. 2728-2735.
2. A. Sashchiuk, L. Amirav, M. Bashouti, M. Krueger, U. Sivan, and E. Lifshitz, *Nano Lett.*, **2004**. *4* (1): p. 159-165.
3. C.B. Murray, S.H. Sun, W. Gaschler, H. Doyle, T.A. Betley, and C.R. Kagan, *IBM J. Res. Dev.*, **2001**. *45* (1): p. 47-56.
4. B.L. Wehrenberg, C.J. Wang, and P. Guyot-Sionnest, *J. Phys. Chem. B*, **2002**. *106* (41): p. 10634-10640.
5. F.W. Wise, *Acc. Chem. Res.*, **2000**. *33* (11): p. 773-780.
6. G. Konstantatos, I. Howard, A. Fischer, S. Hoogland, J. Clifford, E. Klem, L. Levina, and E.H. Sargent, *Nature*, **2006**. *442* (7099): p. 180-183.
7. R.D. Schaller, V.M. Agranovich, and V.I. Klimov, *Nat Phys*, **2005**. *1* (3): p. 189-194.
8. R.D. Schaller and V.I. Klimov, *Phys. Rev. Lett.*, **2004**. *92* (18): p. 186601.
9. R.D. Schaller, M. Sykora, J.M. Pietryga, and V.I. Klimov, *Nano Lett.*, **2006**. *6* (3): p. 424-429.
10. R.J. Ellingson, M.C. Beard, J.C. Johnson, P.R. Yu, O.I. Micic, A.J. Nozik, A. Shabaev, and A.L. Efros, *Nano Lett.*, **2005**. *5* (5): p. 865-871.
11. G. Allan and C. Delerue, *Phys. Rev. B*, **2004**. *70* (24): p. 245321.
12. A.J. Houtepen, R. Koole, D.L. Vanmaekelbergh, J. Meeldijk, and S.G. Hickey, *J. Am. Chem. Soc.*, **2006**. *128* (21): p. 6792-6793.
13. I. Kang and F.W. Wise, *J Opt Soc Am B*, **1997**. *14* (7): p. 1632-1646.
14. P. Liljeroth, P.A.Z. van Emmichoven, S.G. Hickey, H. Weller, B. Grandidier, G. Allan, and D. Vanmaekelbergh, *Phys. Rev. Lett.*, **2005**. *95* (8): p. 086801.
15. B.L. Wehrenberg and P. Guyot-Sionnest, *J. Am. Chem. Soc.*, **2003**. *125* (26): p. 7806-7807.
16. J.M. Pietryga, R.D. Schaller, D. Werder, M.H. Stewart, V.I. Klimov, and J.A. Hollingsworth, *J. Am. Chem. Soc.*, **2004**. *126* (38): p. 11752-11753.
17. D.J. Norris and M.G. Bawendi, *Phys. Rev. B*, **1996**. *53* (24): p. 16338-16346.
18. W.W. Yu, J.C. Falkner, B.S. Shih, and V.L. Colvin, *Chem. Mater.*, **2004**. *16* (17): p. 3318-3322.
19. E.A. Albanesi, C.M.I. Okoye, C.O. Rodriguez, E.L.P.Y. Blanca, and A.G. Petukhov, *Phys. Rev. B*, **2000**. *61* (24): p. 16589-16595.
20. S.V. Gaponenko, *Optical Properties of Semiconductor Nanocrystals*. 1998, Cambridge: Cambridge University Press. 245.
21. A. Franceschetti, A. Williamson, and A. Zunger, *J. Phys. Chem. B*, **2000**. *104* (15): p. 3398-3401.
22. L. Brus, *J. Phys. Chem.*, **1986**. *90* (12): p. 2555-2560.
23. A. Franceschetti, J.M. An, and A. Zunger, *Nano Lett.*, **2006**. *6* (10): p. 2191-2195.
24. G. Allan and C. Delerue, *Phys. Rev. B*, **2006**. *73* (20): p. 205423.
25. A. Shabaev, A.L. Efros, and A.J. Nozik, *Nano Lett.*, **2006**. *6* (12): p. 2856-2863.

Chapter 4

Exciton Energy Transfer in Cross-Linked CdTe Quantum Dots

Stable dispersions of aggregates of CdTe quantum dots are prepared by chemical cross-linkage. The CdTe nanocrystals are coated with the short ligand allylamine, and cross-linked by hexanedithiol molecules. Cryo-TEM images confirm the presence of cross-linked quantum dots, and show that the size of the small aggregates can be controlled by the amount of cross-linker added. Optical measurements reveal the presence of exciton energy transfer between neighboring quantum dots, which is studied for three different sizes of nanocrystals. Quantitative information on the energy transfer rates in the quantum-dot aggregates is obtained by photoluminescence lifetime measurements.

4.1 Introduction

World-wide efforts in the bottom-up synthesis of colloidal semiconductor quantum dots (QDs) by wet-chemistry have led to highly luminescent nanocrystals of II-VI and III-V compounds with excellent control over the nanocrystal size, shape and surface chemistry.[1] Concomitantly, optical and electron tunnelling spectroscopy, together with theoretical efforts has led to understanding of the energy level structure of nanocrystalline quantum dots.[2, 3] Strong confinement of the charge carriers in the nanocrystal host leads to discrete valence and conduction energy levels, and an optical gap which is strongly size-dependent. Highly efficient photoluminescence and a photon energy which can be tailored by the nanocrystal size promise applications of semiconductor nanocrystals in opto-electrical devices such as LEDs,[4, 5] lasers,[6, 7] solar cells,[8, 9] and as optical labels in biomedical applications.[10, 11]

Most of these applications are not based on isolated quantum dots, but on a molecular or solid-like assembly of nanocrystals. It is obvious that the collective opto-electrical properties of quantum dot materials will be influenced by mutual inter-dot interactions. Two important interactions, viz. exciton energy transfer and electronic coupling have been investigated extensively in extended arrays of colloidal quantum dots (quantum dot solids),[12-19] but much less in small molecular-like assemblies.[20-22] This is partly due to the fact that such systems are much more difficult to prepare than quantum dot solids. While chemically-blind dispersion forces are at work in the formation of nanocrystal superlattices, the formation of small quantum-dot aggregates from nanocrystal building blocks requires well-controlled chemical linking.[23] Small assemblies consisting of only a few nanocrystal building blocks are of great interest for fundamental research.

Exciton energy transfer in such small aggregates has been reported in a limited number of papers.[20, 22, 24] These aggregates were either formed by oppositely charged QDs[20] or bioconjugation of antigen/antibody complexes bound to the QDs[22, 24], and the experiments were all carried out in water. Electronic coupling between colloidal nanocrystals in small aggregates has not been reported up to date. However, it has been extensively studied in single pairs of epitaxially grown InAs/GaAs QDs.[25-27]

Here we present a study of dispersed aggregates of CdTe nanocrystals that are prepared by controlled cross-linking in hydrophobic dispersions. The structure of the aggregates is studied with Cryo-TEM and statistically analyzed. Exciton energy transfer in these aggregates is studied by absorption and fluorescence spectroscopy. Efficient energy transfer is studied by photoluminescence decay measurements, which show a clear distinction between single and cross-linked QDs in dispersion. A model is introduced to quantitatively analyze the time-resolved luminescence measurements.

4.2 Experimental Section

Red, yellow, and green emitting QDs (rQDs, yQDs and gQDs), were synthesized in a mixture of $Cd(Me)_2$ (ARC Technologies, 99.9%), tellurium-powder (Heraeus, 99.999%), trioctlyphosphine (TOP, Fluka, > 90%), and dodecylamine (DDA, Aldrich, 98%) that was slowly heated to the growth temperature.[28] The rQDs (Ø 5.1 nm) were grown for 3.5 hours at 185°C, the gQDs (Ø 3.4 nm) were grown at 146°C for 2.5 hours and the yQDs (Ø 3.8 nm) were grown at 185°C for 1.5 hours. Next, the DDA-capped gQDs and yQDs were re-capped by heating a mixture of 1 ml allylamine (AA, Aldrich, 98%) and 1 ml of the crude synthesis product for 4 hours at 50°C, followed by the evaporation of the excess AA. The rQDs were re-capped similarly, but now with the addition of 3 ml toluene, followed by a size-selective precipitation using methanol as a non-solvent. Subsequently, the precipitated rQDs were re-dispersed in 0.5 ml toluene. The AA-capped CdTe QDs thus obtained have a quantum yield > 50%, and the emission spectra of the gQDs and rQDs show a similar spectral distribution (FWHM = 0.14 eV). Concentrations of the AA-capped QDs were estimated using the absorbance and molar extinction coefficient at the first absorption peak. The extinction coefficient was calculated using the diameter of the QDs as determined by TEM, and the size dependent formula which was obtained by Yu *et al*.[29]

To cross-link the QDs 1,6 hexanedithiol (HdT, Fluka, > 97%) was used, since both thiol-groups of HdT can easily replace the allylamine capping molecules that have a weaker interaction with the cadmium surface atoms of the CdTe QDs. Since the QDs were capped with the short AA molecules, a relatively short cross-linker (i.e. HdT) could be used in order to minimize the distance between the cross-linked QDs. For the cross-linkage, 42 µl, 21.5 µl, and 7.2 µl of the concentrated dispersion of AA-capped rQDs, yQDs, and gQDs respectively was added to 0.5 ml of the linker HdT dissolved in toluene, varying the concentration HdT in such a way that a series was obtained with linker/QD ratios of 0.5:1 up to 32:1. We allowed each mixture to form clusters for 3 days at room temperature, after which the mixtures were diluted with toluene to 5 ml for the optical measurements.

Emission spectra were recorded using the monochromator of a Spex Fluorolog spectrometer (double-grating, 0.22 m, SPEX 1680) and a 450 W Xe lamp as the excitation source. The luminescence spectra were recorded by a Princeton Instrument CCD-camera and a 0.25 m Acton Research monochromator with a grating of 150 lines/mm blazed at 550 nm. Absorption spectra were measured on a double beam Perkin-Elmer Lambda 16 UV/vis spectrometer. Lifetime measurements were performed using a pulsed PicoQuant laser (2.5 MHz, λ_{ex}= 406 nm, pulse width = 55 ps) in combination with a 0.1 m monochromator (1350 lines/mm blazed at 500 nm), a Hamamatsu photo-multiplier tube (H5738P-01), and a Time Harp 200 computer card.[30] All measurements were performed at room temperature under Argon atmosphere. For cryo-TEM, 1 ml of the QD-dispersions as used for the optical measurements was diluted with 1ml of decaline. An aliquot of 3 µl of this dispersion was pipetted onto an untreated Quantifoil 2/2 grid in the environmental chamber of a Vitrobot. The sample was blotted once during 0.5 s and rapidly plunged into liquid nitrogen. The grid was transferred to a Gatan cryoholder Model 626. The TEM used was a Philips Tecnai 12 equipped with a Biotwin-lens and a LaB6 filament. Images were captured with a SIS Megaview II CCD-camera and processed with AnalySIS software.

4.3 Results and Discussion

Cryo-TEM on QD-aggregates

Allylamine capped CdTe QDs in dispersion were cross-linked by hexanedithiol (HdT) as decribed in the experimental section. A schematic representation of two cross-linked QDs is shown in Figure 4.2B. To obtain information about the size of the synthesized QD-aggregates, we performed cryo-TEM on the samples as used for the optical measurements. Regular TEM was ill-suited for this purpose, since it is difficult to discriminate between cross-linked QDs and QDs that self-assemble on the TEM-grid due to drying-effects. The cryo-TEM images of four samples of the gQDs with different linker/QD ratios are shown in Figure 4.1. As can be seen, mainly single QDs are present at a linker/QD ratio of 0:1, while aggregates of 2 and more QDs are visible at higher linker/QD ratios.

To obtain statistical information about the distribution in aggregate-size at a certain linker/QD ratio, the amount of QDs per aggregate was analysed from the cryo-TEM images. For each linker/QD ratio, between 150 and 350 QDs were counted and grouped into QDs present as single QDs and in aggregates of two, three, etc. QDs per QD-aggregate. Despite the relatively low resolution inherent to cryo-TEM images, a reasonable statistical analysis was possible, the result of which is shown in Figure 4.2A. As can be seen, the fraction of single QDs

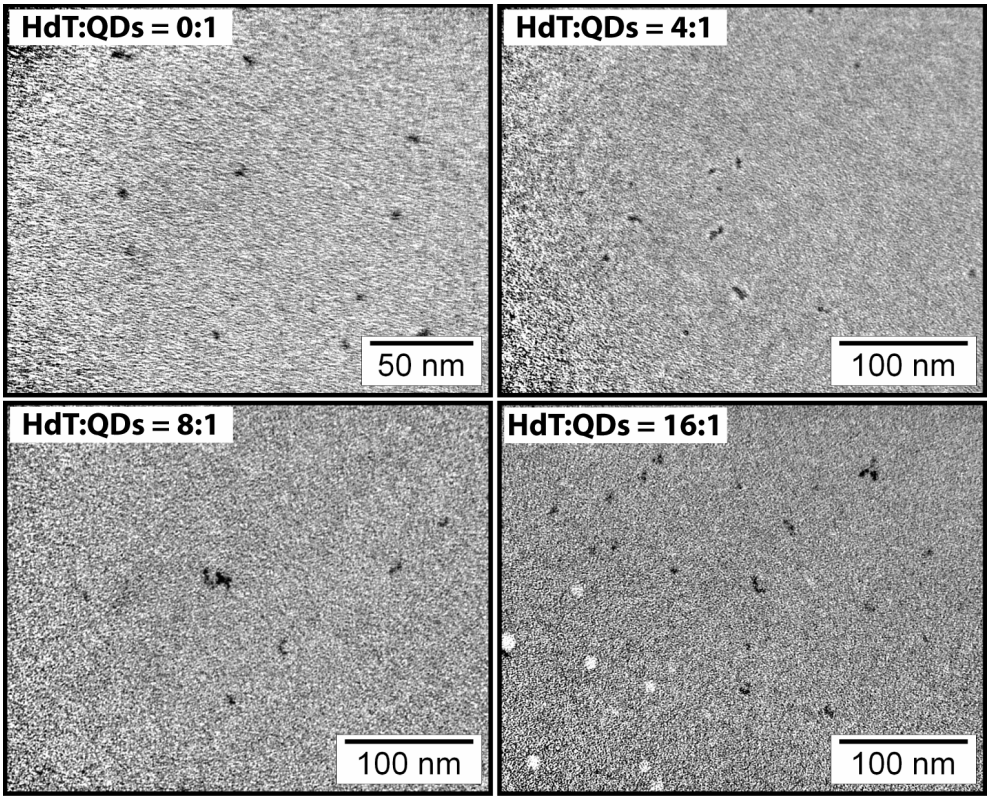

Figure 4.1. Cryo-TEM images of single gQDs (glinker/QD ratio 0:1), and of samples with a ratio of 4:1, 8:1, and 16:1.

decreases significantly with increasing linker concentration. Note that a small fraction of QD-aggregates is already formed in the system without cross-linker molecules. The fraction of QD-aggregates with 2 QDs per aggregate gradually increases up to the linker/QD ratio of 8:1, after which it slightly decreases. The fraction of QD-aggregates with 3 or more QDs per aggregate also increases at higher linker/QD ratios. For the highest linker/QD ratios (>8) the solutions are turbid due to the formation of larger clusters. Since these large clusters may not be incorporated in the cryo-TEM film the numbers obtained for these samples may not be representative for the dispersion. These results confirm the controllable cross-linkage of QDs by HdT, with an increase in both size and number of the aggregates at higher linker/QD ratios and give an estimate for the fraction of QDs present in QD-aggregates for different linker/QD ratios.

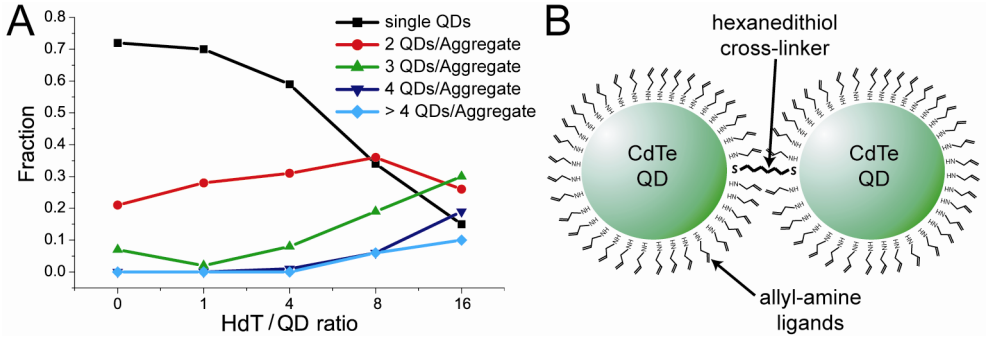

Figure 4.2. (A) Fraction of QDs present as single QDs or present in QD-aggregates of different sizes for 5 different linker/QD ratios. The lines serve as a guide for the eye. (B) Schematic representation of two cross-linked CdTe QDs by an HdT molecule.

Absorption and emission spectra

Figure 4.3A (4.3B) shows the normalized absorption spectra of dispersions of cross-linked rQDs (gQDs), for different linker/QD ratios. As can be seen in Figure 4.3A, the absorption spectra of the rQD-aggregates coincide after normalization. On the other hand, the gQD-aggregates show a clear, gradual red-shift for increasing linker/QD ratios (up to 40 meV). In addition, a broadening of the absorption spectrum is observed at the ratios 8:1 and 12:1, resulting in a less pronounced minimum at around 500 nm. At higher linker concentrations the dispersions of the QD-aggregates became turbid, and the absorption spectra were altered due to light scattering by these large aggregates (not shown).

Emission spectra of the same samples of rQDs and gQDs at different linker/QD ratios were also measured. To correct for the small variations in concentration within one series (less than 10%), the emission spectrum of each sample was corrected according to the absolute value of the first absorption peak. At increasing linker/QD ratios, the rQD-aggregates (Figure 4.4A) show a gradual decrease in emission intensity, a red-shift of the emission peak (see inset) up to 52 meV, and an increase in the relative intensity of the defect related emission at $\lambda > 675$ nm (see inset). Up to a linker/QD ratio of 8:1, the gQD-aggregates (Figure 4.4B) also show a gradual red-shift, but no decrease in emission intensity, while the defect related emission remains negligible (at $\lambda > 625$ nm). At ratios 16:1 and 32:1 (turbid

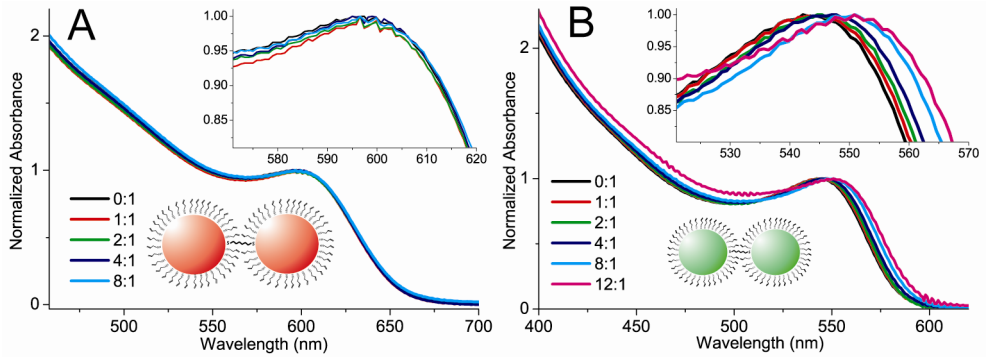

Figure 4.3. Normalized absorption spectra of cross-linked rQDs (A) and gQDs (B) in toluene at various linker/QD ratios. Insets show a magnification of the first absorption peak.

dispersions), a clear decrease in emission intensity, a further red-shift of the emission peak up to 74 meV, and an increase in defect related emission is observed. In addition to the rQD-aggregates and gQD-aggregates, we have also cross-linked intermediate sized yellow emitting QDs (yQDs, 3.8 nm, emission peak at 590 nm). The resulting yQD-aggregates show very similar results as compared to the gQD-aggregates; a red-shift in both absorption and emission spectra (up to 14 meV) is observed up to a linker/QD ratio of 12:1, without a decrease in emission intensity. At higher linker concentrations a decrease and further red-shift in emission spectra is observed.

The results described above for the rQD-aggregates can be explained by exciton energy transfer (ET) due to dipole-dipole interactions between the rQDs. ET has been reported before for QD-solids,[12-16] where the migration of an exciton from higher-bandgap QDs (donors) to smaller-bandgap QDs or defect states (acceptors) resulted in a red-shift and decrease of the excitonic emission peak, together with an increase in defect related emission. No significant changes in the absorption spectra of the rQD-aggregates are observed, which indicates that quantum mechanical coupling between the rQD-aggregates is weak. Therefore, we conclude that the changes observed in the emission spectra of the rQD-aggregates (Figure 4.4A) can be accounted for solely by energy transfer. Photoluminescence decay measurements confirm this interpretation (vide infra).

The gQD and yQD-aggregates also show a red-shift in the excitonic emission peak. In contrast to the rQD-aggregates, this is accompanied by a red-shift in the absorption. Figure 4.5 shows that the red-shift in absorption and emission upon cross-linkage of gQDs is approximately similar. These results, which we reproducibly measured on gQDs from separate syntheses, cannot be explained by ET. The observations could be qualitatively explained by a hybridization of the band edge orbitals (i.e. $1S_e$ and $1S_h$) of the individual QDs due to a strong electronic (tunnelling) coupling between neighboring gQDs. The resulting reduction of the confinement energy due to electron (and hole) delocalization could then explain the red-shift and broadening of the absorption spectra of the gQD-aggregates (Figure 4.3B).[31, 32]. As will be discussed in detail in the next chapter, (mono) thiols adsorbed to the QD-surface cause a red-shift in both absorption and emission spectra that is similar to what is observed in Figures 4.3 and 4.4. This shows that the red-shift is caused by capping exchange and not by electronic coupling. The red-shift in absorption and emission spectra upon addition of

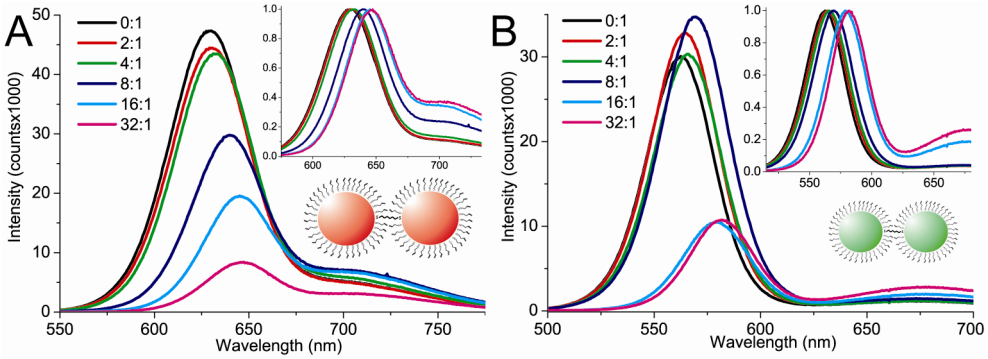

Figure 4.4. Emission spectra of cross-linked rQDs (A) and gQDs (B) in toluene at various linker/QD ratios. The inset shows the normalized spectra. Excitation is at 406 nm.

monothiols is size-dependent and decreases for increasing QD-size. This explains the absence of a red-shift in the absorption spectrum in the rQD-aggregates, and only a small red-shift in case of the yQD-aggregates (14 meV).

As mentioned above, no decrease in excitonic emission intensity is observed up to a linker/QD ratio of 8:1 for the gQD-aggregates (and yQD-aggregates), while the relative intensity of the defect related emission remains constant and very weak. Only at the linker/QD ratios 16:1 and 32:1 (turbid solutions), a significant quenching and further red-shift of the excitonic emission peak is observed, together with an increase in defect related emission (Figure 4.4B). It was reported earlier that the fluorescence of CdTe QDs can be enhanced by a capping-exchange of amines by thiols.[33] The total emission intensity upon addition of dithiol cross-linkers is therefore a balance between the enhancement due to capping-exchange, and reduction due to ET to QDs with defects (i.e. trapping). Apparently, the enhancement effect due to capping-exchange is dominant at low linker/QD ratios, while trapping due to ET dominates at linker/QD ratios of 16:1 and 32:1. The decrease in emission intensity in case of rQD-aggregates indicates that the enhancement effect due to capping exchange by thiols is weaker for the rQDs.

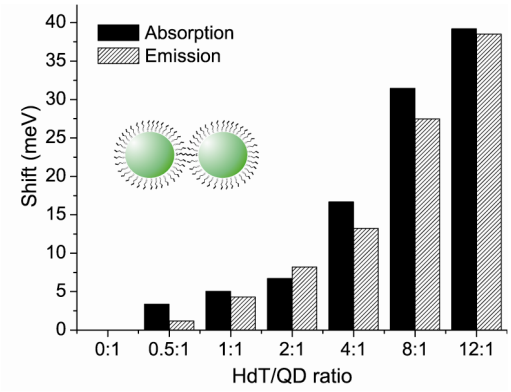

Figure 4.5. Comparison between the red-shift in first absorption peak (solid bars) and excitonic emission peak (striped bars) at various linker/gQD ratios.

Time resolved photoluminescence measurements

The photoluminescence decay curves of the single QDs and QD-aggregates were measured in order to investigate the exciton energy transfer process in more detail. The decay curves of the gQDs (Figure 4.6) were measured at a wavelength of 540 nm, which is on the far blue side of the emission spectrum. Consequently, the exciton lifetimes of the large-bandgap QDs in the gQD-aggregates, which should act as donors in the case of ET, were probed. As can be seen in Figure 4.6, the gQDs show a nearly mono-exponential decay up to a linker/QD ratio of 8:1. At higher linker/QD ratios, the decay-curves become non-exponential, with a rapid initial decay. The fast initial luminescence decays for these largest gQD-aggregates within the first ~2 ns is a clear signature of ET, and is observed only for those samples that show a decrease and red-shift of the excitonic emission peaks (see Figure 4.4B). As can be seen in Figure 4.7B, a similar bi-exponential decay and hence ET is also observed for the rQD-aggregates (probed at 580 nm, far blue side of the emission spectrum), at those linker/QD ratios where a clear decrease in intensity and a red-shift of the excitonic emission peak was observed (see Figure 4.4A). Further evidence for the presence of energy transfer is obtained from measurements of the decay curves as a function of wavelength. For systems in which energy transfer occurs (fast initial decay measured on the blue side of the spectrum) a feeding is observed for the decay curves measured for the acceptor emission on the red side of the spectrum due to energy transfer from the donors to the acceptors. It is well known that the ET rates in QD solids can range from 50 ps^{-1} up to ~2 ns^{-1}, depending on the spectral overlap between donor and acceptor, the inter-dot distance, and dipole moment of the transitions involved.[13, 14, 34]

In order to obtain more quantitative information on energy transfer rates from the lifetime measurements, we fitted the decay curves using a bi-exponential function. This implies a distinction between two radiative systems; QDs that are part of a QD-aggregate, and single QDs in dispersion. We ascribe the fast initial decay to the emission of those QDs that are part of a QD-aggregate, of which the total decay rate (Γ_a) is the sum of the radiative decay rate (Γ_{rad}) and the energy transfer rate (Γ_{ET}). The subsequent slow decay is attributed to the single QDs, since it has a similar decay in the long-time regime as measured for the QDs without cross-linker (0:1). In addition, a distribution function (σ) was introduced for the decay rates of the single QDs (σ_s) and QD-aggregates (σ_a), to allow for a variation in the decay rates within one system.[35] In practice, we first fitted the

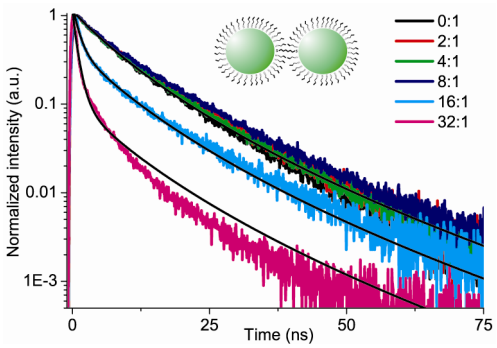

Figure 4.6. Photoluminescence decay curves of gQDs at various linker/QD ratios, measured at 540 nm. Solid black curves show the results of the fitting (see text).

nearly mono-exponential decay curves of the single QDs without cross-linker by using the following equation:

$$I(t) = A_0 \int_0^\infty \sigma(\Gamma) \exp(-\Gamma t) \mathrm{d}\Gamma \tag{4.1}$$

where *I(t)* is the PL intensity over time, A_0 a normalisation constant, and $\sigma(\Gamma)$ a log-Gaussian distribution function for the rate constant (Γ), which is defined as:

$$\sigma(\Gamma) = \exp\left[-\left(\frac{\ln \Gamma - \ln \Gamma_{max,s}}{\gamma} \right)^2 \right] \tag{4.2}$$

where $\Gamma_{max,s}$ is the most frequently found value for the decay rate of the single QDs, and γ is a width-related parameter. By introducing a distribution in the rate constants in this manner, we account for a variation in radiative decay rates between the individual QDs.[35] Using equation (4.1), the single rQDs and gQDs were found to have a radiative decay rate ($\Gamma_{max,s}$) of 0.08 ns^{-1} (τ = 13 ns) and 0.10 ns^{-1} (τ = 10 ns) respectively (γ = 0.5 and 0.7 respectively). Next, the non-exponential decay curves were fitted to an extended version of equation (4.1), adding an extra term to account for energy transfer for the QDs that are part of a QD-aggregate:

$$I(t) = A_a \int_0^\infty \sigma_a(\Gamma_a) \exp(-\Gamma_a t) \mathrm{d}\Gamma + A_s \int_0^\infty \sigma_s(\Gamma_s) \exp(-\Gamma_s t) \mathrm{d}\Gamma \tag{4.3}$$

where the subscript *a* stands for the QDs that are part of a QD-aggregate, and the subscript *s* for the single QDs. The physical meaning of the log-Gaussian distribution function $\sigma_a(\Gamma_a)$ is the distribution in ET rates due to a variation in the composition of the QD-aggregates. During the fitting procedure we allowed the parameters A_a, $\Gamma_{max,a}$, γ_a, and A_s to vary, while the rate constants for σ_s ($\Gamma_{max,s}$ and γ_s) were fixed at the values that were found for the mono-exponential decays of the

Table 4.1. Values obtained by fitting the decay curves of rQD-molecules and gQD-molecules at different QD:Linker ratios with equation (4.3). (See text for an explanation of the symbols)

	rQDs			gQDs	
QD:Linker	1:8	1:16	1:32	1:16	1:32
$\Gamma_{max,a}$ (ns^{-1})	0.8	0.9	1.0	0.9	1.1
γ_a	0.6	0.3	0.2	0.1	0.5
f_a (%)	43	82	94	61	90
f_s (%)	57	18	6	39	10

single QDs. In practice, this means that we fixed the parameters of the single QDs (except the normalisation constant) in order to find the parameters for energy transfer in the QD-aggregates. In this manner, the total decay rate of the QDs that are part of a QD-aggregate ($\Gamma_{max,a}$) was found, which is the sum of the energy transfer rate (Γ_{ET}) and the radiative decay rate (Γ_{rad}). The resulting fits of the decay curves for the gQD-aggregates and rQD-aggregates are depicted as solid black curves in Figure 4.6 and Figure 4.7B, respectively. A summary of the parameters obtained from fitting both gQD-aggregates and rQD-aggregates can be found in Table 4.1.

Figure 4.7A shows the normalized distribution functions obtained from fitting the decay curves of the rQD-aggregates (Figure 4.7B). For the plots of the distribution functions, and to obtain the fractions of single and cross-linked QDs, the summed areas of σ_s and σ_a at each linker/QD ratio were normalized. It can be seen that the distribution functions of the single rQDs (σ_s) and the rQD-aggregates (σ_a) are clearly separated, which confirms that they can be treated as two distinct systems. The total decay rate of the rQD-aggregates ($\Gamma_{max,a}$) increases at higher linker/QD ratios, and has an average value of about 1.0 ns^{-1} (see also Table 4.1). Since the total decay rate is the sum of the radiative rate (0.08 ns^{-1}) and ET rate, this implies an energy transfer rate (Γ_{ET}) of ≈ 0.9 ns^{-1}.The area of σ_s represents the fraction of single rQDs, and as can be seen in Table 4.1, the fraction of single rQDs decreases with increasing linker/QD ratio. Similarly, the fraction of QDs that are part of a QD-aggregate increases at increasing linker/QD ratios. For example, at a linker/QD ratio of 16:1, the fraction of single QDs is found to be 18%, so there is still a significant amount of single QDs present. The parameters obained from fitting the gQD-aggregates follow a similar trend as the rQD-aggregates; faster decay rates and larger fraction of QD-aggregates at higher linker concentrations (Table 4.1). It should be noted that a similar fitting procedure using a bi-exponential equation *without* a distribution function yielded almost identical values for the decay rates and fractions of the single QDs and QD-molecules, which shows the validity of the model used.

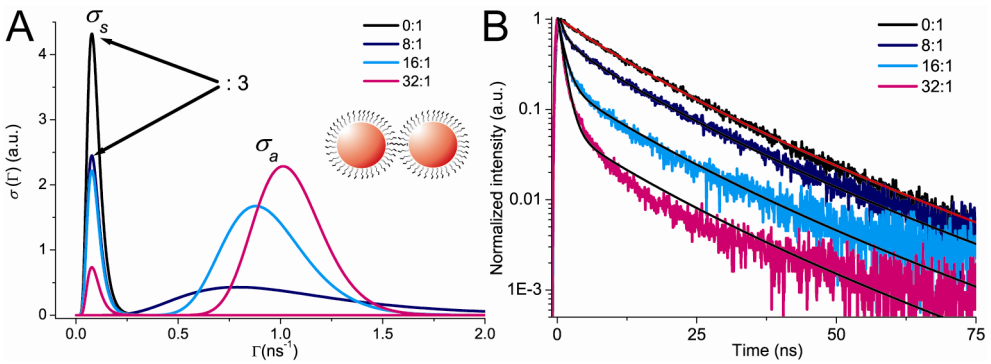

Figure 4.7. (A) Distribution functions of the decay rate of single rQDs (σ_s) and rQD-aggregates (σ_m) at different linker/QD ratios. Note that the curves of σ_s at ratios 0:1 and 8:1 were divided by three (B) Photoluminescence decay curves of rQDs at various linker/QD ratios, measured at 580 nm. Solid curves show the results of the fitting.

4.4 Conclusions

In conclusion, we have studied the optical properties of homonuclear QD-aggregates of green, yellow, and red emitting CdTe QDs. The aggregates were stable in dispersion and prepared by cross-linkage of QDs by hexanedithiol molecules. Cryo-TEM confirmed the presence of cross-linked QDs in dispersion. Statistical analysis of cryo-TEM images at different linker concentrations confirmed an increase in both the aggregate-size and fraction of aggregates.

The optical properties of the green, yellow, and red emitting QD-aggregates were investigated. Clear evidence for the presence of energy transfer was found, which causes the migration of excitons from higher to lower bandgap QDs within an aggregate. As a result, a red-shift in the emission spectra was observed upon cross-linkage, together with a decrease in emission intensity. The latter is explained by an increased probability of exciton-trapping when an exciton is migrating over several neighboring QDs. In line with this explanation, the defect related emission intensity increased at higher linker concentrations.

Time resolved photoluminescence measurements showed a clear bi-exponential decay of the QD-fluorescence upon cross-linkage. The fast initial decay was ascribed to emission of QDs that are part of an aggregate, and the subsequent slow decay to emission of single QDs. Quantitative information about the ET rates between neighboring QDs (≈ 0.9 ns^{-1}) and the fraction of single QDs versus QD-aggregates was obtained by a bi-exponential fit of the decay curves.

4.5 References

1. Y. Yin and A.P. Alivisatos, *Nature*, **2005**. *437* (7059): p. 664-670.
2. E.P.A.M. Bakkers, Z. Hens, A. Zunger, A. Franceschetti, L.P. Kouwenhoven, L. Gurevich, and D. Vanmaekelbergh, *Nano Lett.*, **2001**. *1* (10): p. 551-556.
3. U. Banin and O. Millo, *Annu. Rev. Phys. Chem.*, **2003**. *54*: p. 465-492.
4. N. Tessler, V. Medvedev, M. Kazes, S.H. Kan, and U. Banin, *Science*, **2002**. *295* (5559): p. 1506-1508.
5. S. Coe, W.K. Woo, M. Bawendi, and V. Bulovic, *Nature*, **2002**. *420* (6917): p. 800-803.
6. V.I. Klimov, A.A. Mikhailovsky, S. Xu, A. Malko, J.A. Hollingsworth, C.A. Leatherdale, H.J. Eisler, and M.G. Bawendi, *Science*, **2000**. *290* (5490): p. 314-317.
7. C.J. Wang, B.L. Wehrenberg, C.Y. Woo, and P. Guyot-Sionnest, *J. Phys. Chem. B*, **2004**. *108* (26): p. 9027-9031.
8. A.J. Nozik, *Physica E*, **2002**. *14* (1-2): p. 115-120.
9. I. Gur, N.A. Fromer, M.L. Geier, and A.P. Alivisatos, *Science*, **2005**. *310* (5747): p. 462-465.
10. X. Michalet, F.F. Pinaud, L.A. Bentolila, J.M. Tsay, S. Doose, J.J. Li, G. Sundaresan, A.M. Wu, S.S. Gambhir, and S. Weiss, *Science*, **2005**. *307* (5709): p. 538-544.
11. W.J.M. Mulder, R. Koole, R.J. Brandwijk, G. Storm, P.T.K. Chin, G.J. Strijkers, C. de Mello Donega, K. Nicolay, and A.W. Griffioen, *Nano Lett.*, **2006**. *6* (1): p. 1-6.
12. C.R. Kagan, C.B. Murray, M. Nirmal, and M.G. Bawendi, *Phys. Rev. Lett.*, **1996**. *76* (9): p. 1517-20.
13. S.A. Crooker, J.A. Hollingsworth, S. Tretiak, and V.I. Klimov, *Phys. Rev. Lett.*, **2002**. *89* (18): p. 186802.
14. M. Achermann, M.A. Petruska, S.A. Crooker, and V.I. Klimov, *J. Phys. Chem. B*, **2003**. *107* (50): p. 13782-13787.
15. T. Franzl, D.S. Koktysh, T.A. Klar, A.L. Rogach, J. Feldmann, and N. Gaponik, *Appl. Phys. Lett.*, **2004**. *84* (15): p. 2904-2906.
16. S.F. Wuister, R. Koole, C. de Mello Donegá, and A. Meijerink, *J. Phys. Chem. B*, **2005**. *109* (12): p. 5504-5508.
17. O.I. Micic, S.P. Ahrenkiel, and A.J. Nozik, *Appl. Phys. Lett.*, **2001**. *78* (25): p. 4022-4024.
18. M.V. Artemyev, A.I. Bibik, L.I. Gurinovich, S.V. Gaponenko, and U. Woggon, *Phys. Rev. B*, **1999**. *60* (3): p. 1504-1506.
19. H. Dollefeld, H. Weller, and A. Eychmuller, *J. Phys. Chem. B*, **2002**. *106* (22): p. 5604-5608.
20. R. Wargnier, A.V. Baranov, V.G. Maslov, V. Stsiapura, M. Artemyev, M. Pluot, A. Sukhanova, and I. Nabiev, *Nano Lett.*, **2004**. *4* (3): p. 451-457.
21. T. Ni, D.K. Nagesha, J. Robles, N.F. Materer, S. Mussig, and N.A. Kotov, *J. Am. Chem. Soc.*, **2002**. *124* (15): p. 3980-3992.
22. Q. Ma, X.G. Su, X.Y. Wang, Y. Wan, C.L. Wang, B. Yang, and Q.H. Jin, *Talanta*, **2005**. *67* (5): p. 1029-1034.
23. L.C. Brousseau, J.P. Novak, S.M. Marinakos, and D.L. Feldheim, *Adv. Mater.*, **1999**. *11* (6): p. 447.
24. S. Wang, N. Mamedova, N.A. Kotov, W. Chen, and J. Studer, *Nano Lett.*, **2002**. *2* (8): p. 817-822.
25. M. Bayer, P. Hawrylak, K. Hinzer, S. Fafard, M. Korkusinski, Z.R. Wasilewski, O. Stern, and A. Forchel, *Science*, **2001**. *291* (5503): p. 451-453.
26. H.J. Krenner, M. Sabathil, E.C. Clark, A. Kress, D. Schuh, M. Bichler, G. Abstreiter, and J.J. Finley, *Phys. Rev. Lett.*, **2005**. *94* (5).
27. S. Yamauchi, K. Komori, I. Morohashi, K. Goshima, and T. Sugaya, *J. Appl. Phys.*, **2006**. *99* (3).
28. S.F. Wuister, F. van Driel, and A. Meijerink, *Phys. Chem. Chem. Phys.*, **2003**. *5* (6): p. 1253-1258.

29. W.W. Yu, L. Qu, W. Guo, and X. Peng, *Chem. Mater.*, **2003**. *15* (14): p. 2854-2860.
30. S.F. Wuister, C. de Mello Donegá, and A. Meijerink, *J. Chem. Phys.*, **2004**. *121* (9): p. 4310-4315.
31. G.W. Bryant and W. Jaskolski, *Physica E*, **2002**. *13* (2-4): p. 293-296.
32. W. Jaskolski, G.W. Bryant, J. Planelles, and M. Zielinski, *Int. J. Quantum Chem.*, **2002**. *90* (3): p. 1075-1082.
33. S.F. Wuister, C. de Mello Donegá, and A. Meijerink, *J. Phys. Chem. B*, **2004**. *108* (45): p. 17393-17397.
34. T. Förster, *Naturwissenshaften*, **1946**. *33* (166): p. 166-175.
35. D.R. James and W.R. Ware, *Chem. Phys. Lett.*, **1986**. *126* (1): p. 7-11.

Chapter 5

Differences in Cross-link Chemistry between Rigid and Flexible Dithiol-molecules Revealed by Optical Studies of CdTe Quantum Dots

The cross-link chemistry of CdTe quantum dots (QDs) in dispersion is studied for different types of aliphatic (flexible) and aromatic (rigid) dithiol linker molecules. A remarkable difference in the cross-link efficiency is observed: the rigid dithiols are shown to form aggregates at much lower concentrations. Qualitative and quantitative information on the formation of aggregates is obtained from cryo-TEM images and photoluminescence decay measurements. The luminescence decay curves are analyzed with a model for energy transfer to neighboring QDs in aggregates. The analysis shows that the cross-link efficiency is four times higher for the rigid dithiols than for the flexible dithiols. The difference is attributed to the formation of loops for the flexible dithiols by attaching with both thiol groups to the same nanocrystal surface (preventing cross-linkage) whereas the rigid aromatic dithiols cannot form loops and the second thiol group is oriented away from the surface (enabling cross-linkage). The difference in conformation between flexible and rigid dithiols is confirmed by studies on the red-shift in the optical absorption spectra due to capping exchange of amines by monothiols or dithiols and by molecular simulations.

5.1 Introduction

To control the distance dependent interactions between two quantum dots (QDs), both lithographic and epitaxial growth techniques have been successfully applied. The opto-electronic properties of such a double quantum-dot structure have been studied in detail and it was shown that a precise tuning of the electronic coupling can be achieved by a careful design of the structure.[1-3] Alternatively, semiconductor QDs can be prepared by wet chemistry resulting in colloidal dispersions of semiconductor nanocrystals with well-defined shape and size. It is a challenge in current nanoscience to use these nanocrystals as building blocks for the assembly of new superstructures such as QD-molecules and superlattices, and to analyze the collective properties, which depend on the interactions between the individual QDs. Superlattices can be made by self-assembly of colloidal QDs on a substrate, and by choosing the right conditions, long-range ordering can be obtained, even with binary structures.[4] However, to study the interactions between neighboring QDs by optical spectroscopy, superlattices of colloidal QDs on a substrate are less suitable due to scattering processes and the relatively low signal from a monolayer of nanocrystals. Well-defined smaller clusters of only a few QDs in dispersion (QD-aggregates) are more promising to study the optical properties of interacting QDs. It is therefore important to have a high degree of control over the chemical cross-linkage of QDs in dispersion. Dithiol molecules have been used extensively to cross-link nanocrystals (i.e. Au nanocrystals), but the exact conformation of these cross-linkers on a nanocrystal surface is still under debate.[5, 6] There is an interesting connection of this topic to the field of self assembled monolayers (SAMS), where the conformation of dithiol molecules on a gold-substrate is still subject of extensive discussions.[7] The understanding of the conformation of these dithiols on a substrate or nanocrystal is of great importance, because thiol end-functionalized molecules hold promise for the field of molecular electronics. [6, 8-10]

Here, we report the effect of the rigidity of different dithiol cross-linker molecules on the cross-link chemistry of CdTe QDs. Information on the cross-linking is obtained from cryo-TEM studies, and the optical properties of the resulting QD-aggregates. Both aliphatic (flexible) and aromatic (rigid) dithiol molecules were used to cross-link green emitting CdTe QDs (gQDs) in dispersion. The three types of investigated rigid molecules are the same as Dadosh *et al.* used for single-molecule conductance measurements; 4,4'-biphenyldithiol (BPD), bis-(4-mercaptophenyl)-ether (BPE), and 1,4-benzenedimethanethiol (BdMT) (see insets Figure 5.4).[6] Triggered by their results on how the conjugation of the molecule determines the conductance, we aimed at a control over the degree of electronic coupling between CdTe QDs by using these three differently conjugated rigid cross-linker molecules. In addition, we used the flexible aliphatic molecules hexanedithiol (HdT) and nonanedithiol (NdT) to cross-link the QDs (see insets Figure 5.3).

Interestingly, we found that the aromatic rigid molecules (BPD, BPE, BdMT) act as very efficient linkers; at least 4 times more efficient than the flexible aliphatic cross-linkers (HdT, NdT). The distinct cross-link properties of the different dithiol-molecules reported and explained here are of interest for the field of molecular electronics, in which these molecules are also extensively investigated. No reduction of the optical gap is observed in the gQD-aggregates when BPD, BPE or

BdMT (rigid) is used as a cross-linker, in contrast to QDs cross-linked by HdT and NdT (flexible) as described in the previous chapter.[11] Finally, this chapter presents a detailed study on the influence of monothiols on the optical properties of CdTe and CdSe QDs, which shows that it is the exchange of native amine ligands bound to the QD surface by (mono- or di-) thiols that causes the reduction of the optical gap.

5.2 Experimental Section

Green (Ø 3.4 nm ± 0.5 nm), yellow (Ø 3.8 nm) and red (Ø 5.1 nm ± 0.7 nm) emitting CdTe QDs were synthesized in a mixture of $Cd(Me)_2$ (ARC Technologies, 99.9%), trioctylphosphine (TOP, Fluka, > 90%), tellurium-powder (Heraeus, 99.999%), and dodecylamine (DDA, Aldrich, 98%), as described in the previous chapter.[11, 12] Particle-sizes were determined by the analysis of TEM-images. The synthesis of the CdSe QDs used in this chapter is described in detail elsewhere.[13] The QDs were capped with allylamine (AA, Aldrich, 98%) by a ligand exchange; 1ml of crude QD-product was mixed with 1ml AA and heated for 4 hours at 50 °C. The concentration of AA-capped QDs was determined by the absorbance-value at the first absorption peak and the molar extinction coefficient, which was derived from the QD-size (TEM) and the size-dependent formula obtained by Yu *et al.*.[14] An accurately weighed amount of HdT (1,6-hexanedithiol, Fluka, > 97%), NdT (1,9-nonanedithiol, Aldrich), BPE (bis-(4-mercaptophenyl)-ether, Aldrich), BdMT (1,4-benzenedimethanethiol, Aldrich, 98%) or BPD (4,4'-biphenyldithiol, T.C.I. Europe) was dispersed in toluene and diluted to the various desired concentrations. Dispersions of different linker/QD ratios were prepared by adding a well-defined and constant quantity of AA-capped QDs to 0.5 ml toluene, in which the cross-linker was dissolved at varying concentrations. After 3 days, the dispersions were diluted to 5ml with toluene to perform the optical measurements. In a similar way, the samples with varying monothiol/QD ratios were prepared, starting with a stock solution of PT (propanethiol, 99%), HT (1-hexanethiol, 95%), NT (1-nonanethiol, 95%), BT (benzenethiol, > 99%), and PET (2-phenylethanethiol, 98%) (all purchased from Aldrich). All samples were prepared and stored in a nitrogen-purged glovebox. For optical measurements, the samples were transferred in the glovebox to quartz cuvettes that were tightly sealed. The excitation wavelength for all emission and photoluminescence decay measurements was 406 nm, using the experimental setups as described in the previous chapter. Samples for recording cryo-TEM images were prepared by first adding 1 ml of decaline to 1 ml of the QD-dispersions that were used for the optical measurements. An aliquot of 3 µl of this dispersion was pipetted onto an untreated Quantifoil 2/2 grid in the environmental chamber of a Vitrobot. The sample was blotted once during 0.5 s and rapidly plunged into liquid nitrogen. The grid was transferred to a Gatan cryoholder Model 626. The transmission electron microscope used was a Philips Tecnai12 equipped with a Biotwin-lens and a LaB6 filament. Images were captured with a SIS Megaview *II* CCD-camera and processed with AnalySIS software.

5.3 Results and Discussion

Cryo-TEM

QD-aggregates at various linker/QD ratios were synthesized by accurately varying the concentration of the cross-linker molecule in a dispersion of CdTe QDs (see Experimental Section). The QDs were capped with the short ligand allylamine (AA), to avoid sterical hindrance during cross-linkage and to enable an as small as possible inter-dot distance. To study the size of the aggregates obtained by the cross-linkage of the CdTe QDs at different linker/QD ratios, we performed cryo-TEM on two series of QD-aggregates: one using a flexible cross-linker (HdT) and the other using a rigid cross-linker (BPD). By counting between 100 and 500 QDs per sample, the composition of the aggregates (i.e. single QDs and number of QDs/aggregate) was analyzed (see Figure 5.1). Examples of cryo-TEM images of gQDs cross-linked by HdT or BPD are shown in Figure 5.2. In both series, the fraction of single QDs decreases with increasing linker/QD ratio, while the fraction of aggregates increases. It should be noted that even without a cross-linker molecule, dimers (2 QDs/aggregate) and a few trimers are present. Importantly, the results show a clear difference between the cross-link efficiency, which is higher for the rigid BPD molecules. For example, to reduce the fraction of single QDs to 0.2, about 10 times more HdT is needed compared to BPD. Furthermore, the concentration of dimers in the BPD-series clearly reaches a maximum at a linker/QD ratio between 0.25:1 and 0.5:1, which can be expected if each cross-linker binds to two QDs. For the flexible HdT molecules, the maximum concentration of dimers is reached at much higher concentrations (8:1). Clearly, BPD cross-links the QDs significantly more efficient than HdT.

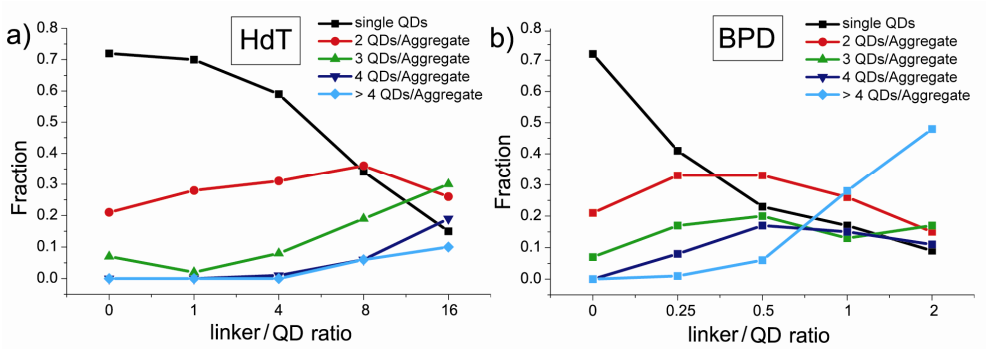

Figure 5.1. Fraction of QDs present as single QDs or as QD-molecules of different sizes as a function of the linker/QD ratio, using HdT (A) or BPD (B) as cross-linker molecule. Note the difference in scale for the x-axis in Figures (A) and (B).

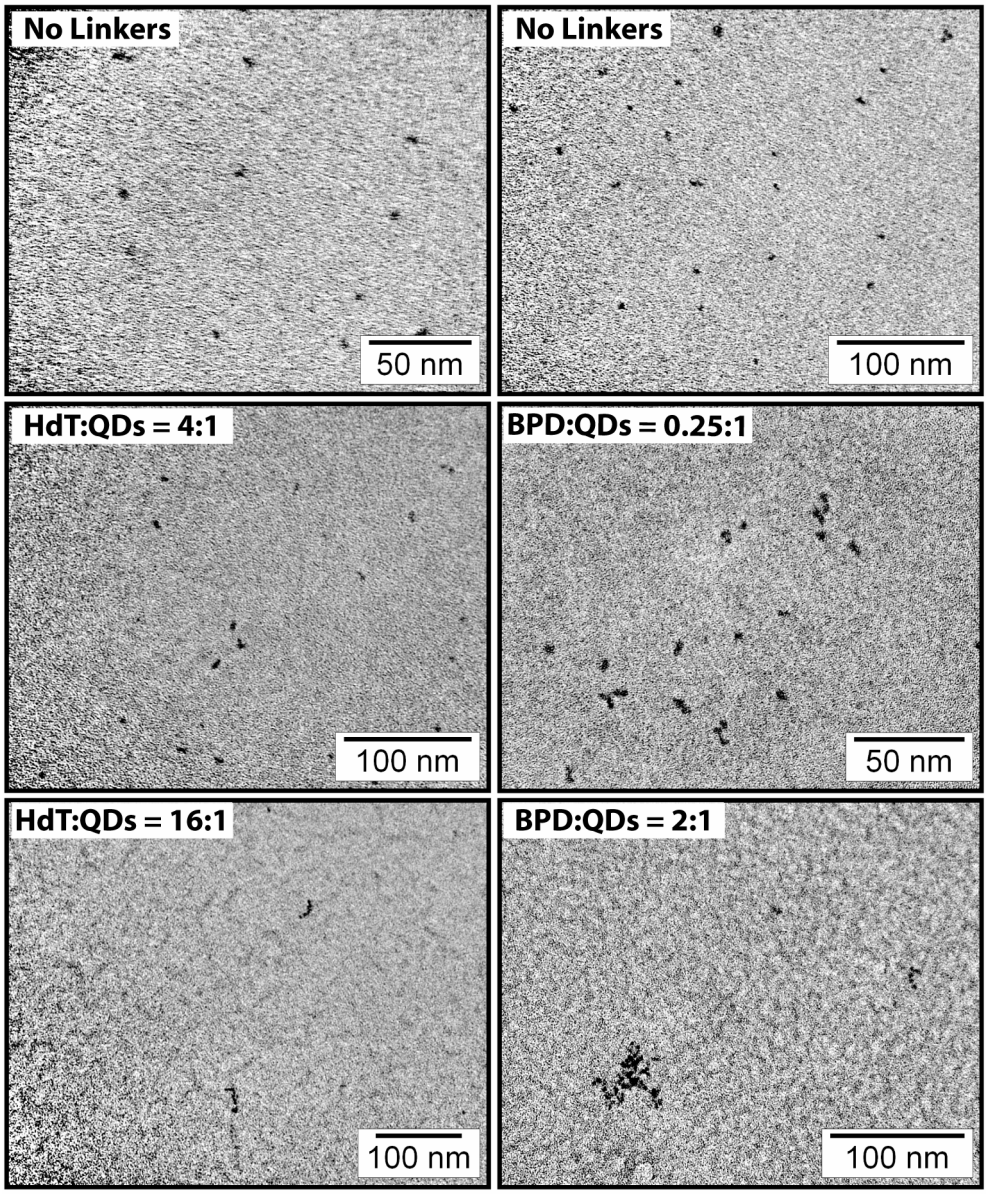

Figure 5.2. Cryo-TEM images of gQD-molecules at various linker/QD ratios, using HdT (left panels) and BPD (right panels) as the cross-linker molecule. Upper panels show cryo-TEM images of samples where no cross-linker was added. Note that (larger) aggregates are seen for BPD-cross-linked QDs at much lower linker/QD ratios.

Absorption and emission spectroscopy

Identification of single QDs and QD-aggregates from cryo-TEM images is not trivial and may not be representative for the aggregation of the ensemble of QDs in dispersion. To obtain further information on the aggregate-size and the interaction

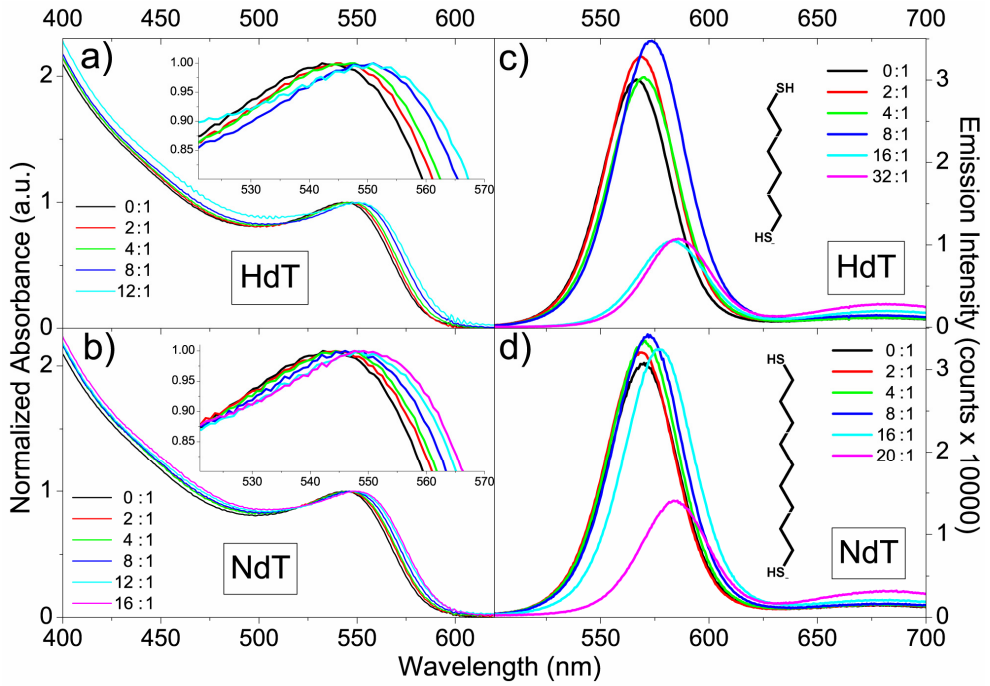

Figure 5.3. Absorption (A-B) and emission (C-D) spectra of gQD-molecules at different linker/QD ratios, using HdT or NdT as cross-linker molecule. Insets show a magnification of the first absorption peak. Absorption spectra are normalized at the first absorption peak(λ ≈ 550nm).

between QDs in the aggregates, we used optical spectroscopy: the absorption and emission spectra, and photoluminescence decay curves were measured. Absorption and emission spectra were measured for a series of linker/QD ratios for each of the five different cross-linker molecules (Figures 5.3 and 5.4). The difference in cross-link efficiency between HdT and BPD observed in cryo-TEM also appears in the absorption measurements, because scattering (non-zero absorption at λ > 650 nm) of the dispersions of both HdT and NdT cross-linked QDs consistently occurred at much higher linker/QD ratios (between 16:1 and 20:1) than for the BPD, BPE or BdMT cross-linked QDs (between 3:1 and 4:1). Individual QDs are too small to scatter light, but large clusters of QDs (in the size regime of tens of nm) can scatter light, which appears in the absorption spectrum as a background of decreasing transmission towards shorter wavelength. The scattering is most clearly observed in the wavelength region where the QDs in the dispersion do not absorb light (> 650 nm).[11] Because both HdT and NdT appeared to cross-link the QDs less efficiently than the other three molecules (BPD, BPE, BdMT), a different range of linker/QD ratios was chosen for the two groups of cross-linkers.

For the cross-linkers HdT and NdT, a behavior similar to that described in the previous chapter is observed.[11] Up to an HdT/QD ratio of 12:1 (16:1 for NdT), a gradual and similar red-shift up to 35 meV is seen in both absorption and emission spectra, without a decrease in the emission intensity (Figure 5.3). In the previous chapter it was suggested that this red-shift in absorption and emission could be due to electronic coupling between neighboring QDs, resulting in a decrease of the

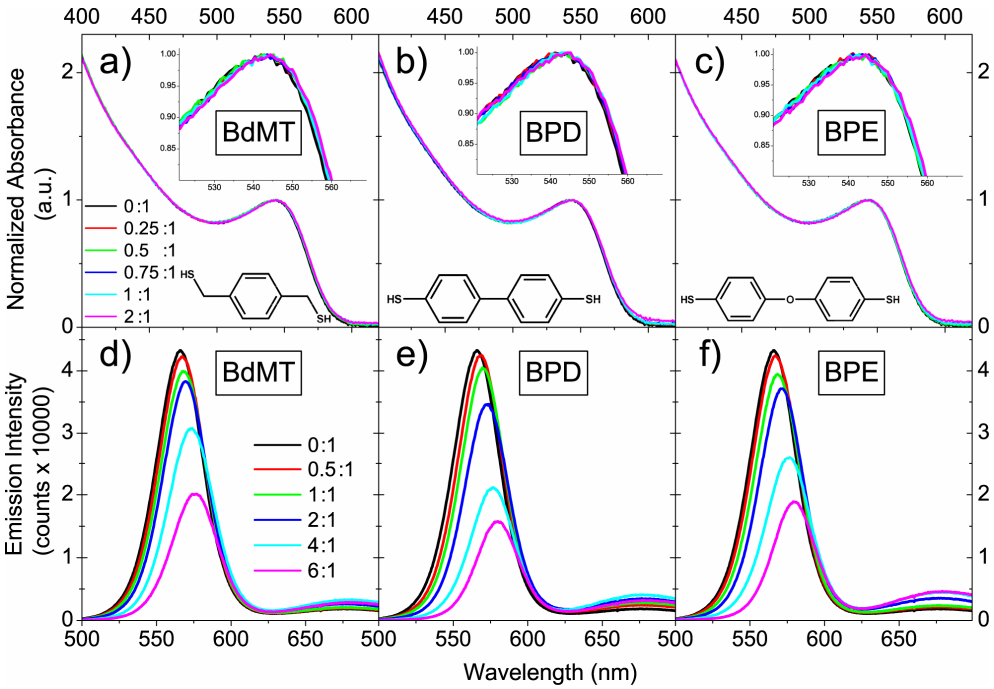

Figure 5.4. Absorption (A-C) and emission (D-F) spectra of gQD-molecules at different linker/QD ratios, using BPD, BPE, or BdMT as cross-linker molecule. Insets show a magnification of the first absorption peak. Absorption spectra are normalized at the first absorption peak.

optical gap, or due a change in the electronic structure related to capping exchange. At the end of this chapter it will be shown that the latter interpretation is correct. At higher linker/QD ratios, a decrease in emission intensity is observed, accompanied by an increase in the defect related emission (λ > 650 nm). These are signatures of (multi step) exciton energy transfer, which is confirmed by lifetime measurements (vide infra). Especially in the larger clusters, energy transfer between neighboring QDs results in trapping of the exciton on a QD with a defect, thus increasing the intensity of the defect related emission at the cost of the exciton emission intensity (Figure 5.3C and D).

When the QDs are cross-linked by BPD, BPE, or BdMT, the system behaves differently. Already at low concentrations of these rigid cross-linker molecules (linker/QD ratio between 0:1 and 2:1), the emission spectra (Figure 5.4D-F) show a gradual shift and decrease in emission intensity as the concentration of cross-linker increases. In addition, the defect related emission increases as a function of cross-linker concentration. For this concentration regime no red-shift in the absorption spectra is observed (Figure 5.4A-C). At higher cross-linker concentrations, scattering hampers the analysis of the absorption spectrum and therefore a red-shift can not be resolved. The gradual red-shift and decrease in emission intensity can be explained by exciton energy transfer, which was also seen for the CdTe-aggregates cross-linked by flexible molecules (Figure 5.3). Finally, it should be noted that the changes in emission spectra due to energy transfer are similar for all three rigid linker molecules (Figure 5.4D-F). This indicates that the differences in

molecular structure between the three cross-linkers do not significantly influence the energy transfer process. The fact that red-shifts are only observed in the emission spectra and not in the absorption spectra is discussed in more detail at the end of this paper.

As was mentioned above, both cryo-TEM and optical absorption measurements suggest that cross-linkage by the rigid dithiol molecules is more efficient than by flexible molecules. To provide additional evidence and to quantify the differences in cross-linking by the flexible and rigid dithiol molecules, we performed time-resolved photoluminescence measurements of CdTe gQDs at various linker/QD ratios with flexible and rigid cross-linkers. Two examples of the luminescence decay curves for CdTe gQDs cross-linked by HdT (flexible) and BPD (rigid) are shown in Figure 5.5. Without cross-linker (0:1), the gQDs display a nearly mono-exponential luminescence decay, indicating the high quality of the QDs and enabling a quantitative analysis. On the other hand, the gQD-aggregates cross-linked by HdT (32:1) and BPD (4:1 and 8:1) show a multi-exponential decay, which is ascribed to exciton energy transfer. The decay curves were measured at an emission wavelength of 535 nm, which is at the far blue side of the emission spectrum of the gQDs (see Figure 5.3C). QDs emitting at this wavelength will act as donors, and can transfer their energy to neighboring QDs that have a smaller bandgap (acceptors). The fast initial decay in the decay curves measured for QDs in the presence of cross-linkers is attributed to QDs that are part of an aggregate. The total decay rate (Γ_{tot}) of QDs in an aggregate is the sum of the radiative decay rate (Γ_{rad}, typically 0.1 ns^{-1}) and the energy transfer rate (Γ_{ET}), which is between 20 ns^{-1} and 0.5 ns^{-1} (transfer time between 50 ps – 2 ns) in QD solids.[15-18] The subsequent slow decay in these curves is attributed to single QDs that are not part of an aggregate, which display a radiative decay that is similar to the QDs without cross-linker (0:1).

Photoluminescence decay measurements

To obtain quantitative information about the cross-link efficiency of the different molecules, we fitted the decay curves to the following equation, the derivation of which is given in the appendix at the end of this chapter:

$$I(t) = I_0 \cdot e^{((-\Gamma_{rad} \cdot t) - n \cdot (1 - e^{(-\Gamma_{ET} \cdot t)}))} + y_0 \qquad (5.1)$$

Here I_0 is a normalization constant and y_0 is a constant that corrects for the background signal. The variable n is the average number of acceptor QDs cross-linked to a donor QD, and Γ_{ET} is defined as the energy transfer rate to one neighboring QD. This formula was developed earlier for a different system of emitting probes with neighboring quenchers.[19] In the present case, the model describes the luminescence decay kinetics of the dispersions of gQDs in the presence of cross-linkers, where the number of QDs cross-linked to another QD obeys a Poisson distribution. To connect n to a cross-link efficiency of the different molecules, we define z as the molar ratio of cross-linkers to QDs (i.e. linker/QD = 16:1 gives z = 16) and f as the fraction of cross-linkers that have a QD attached on both ends. Assuming that all linker molecules attach to the QDs, the variables z and f can be used to calculate m, which is the average number of linker molecules attached to a QD:

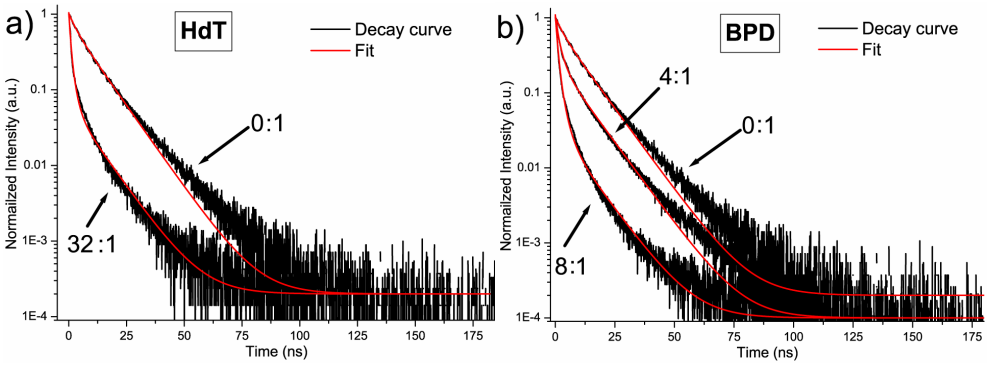

Figure 5.5. Decay curves of gQDs cross-linked with (A) HdT and (B) BPD at different linker/QD ratios. Red curves show the results of fitting the curves with equation (5.1). (Excitation wavelength = 406nm, emission wavelength = 535nm).

$$m = \frac{z}{(1-\frac{1}{2}f)} \tag{5.2}$$

The average number *n* of acceptor QDs cross-linked to a donor QD is the product of *m* and *f*, and can thus be expressed in terms of *z* and *f*:

$$n = mf = \frac{zf}{(1-\frac{1}{2}f)} \tag{5.3}$$

By fitting the decay curves using equation (5.1), the value for *n* could be extracted. Because the molar ratio of cross-linkers to QDs is known (*z*), the fraction of cross-linkers that has a QD attached on both ends (*f*) can be calculated for that particular system, which directly relates to the cross-link efficiency.

We fitted the decay curves by fixing the radiative rate (Γ_{rad}) to 0.1 ns^{-1}, and setting y_0 to a value equal to the background measured. The other parameters (*n* and Γ_{ET}) were fitted, and examples of the resulting fits are represented by red solid lines in Figure 5.5. As can be seen, the model describes the decay curves well. We found that Γ_{rad} varies between 0.09 ns^{-1} and 0.1 ns^{-1} for the different linker/QD ratios if this parameter is allowed to vary as well, close to the value that is found when the decay curve for the sample without cross-linkers (0:1) is fitted by a single-exponential fit. We fixed Γ_{rad} at 0.1 ns^{-1} because this gives the best fits for the decay curves with cross-linkers, from which the parameters *n* and Γ_{ET} were extracted. However, this value yields a lower quality fit for the decay curve without cross-linkers (0:1), which explains the deviation of the fit in the long time regime (>50 ns). We fitted all decay curves of gQDs cross-linked by HdT and BPD at different linker/QD ratios. In addition, we fitted the decay curves of red emitting CdTe QDs (rQDs) cross-linked by HdT. This was done to obtain additional information about the cross-link properties of flexible molecules, and to see if the cross-link behavior is independent of the nanocrystal size. An overview of the

Table 5.1: Overview of the values for Γ_{ET}, n, and f at different linker/QD ratios.

	gQDs with HdT			rQDs with HdT				gQDs with BPD		
HdT/QD	Γ_{ET} (ns^{-1})	n	f	Γ_{ET} (ns^{-1})	n	f	BPD/QD	Γ_{ET} (ns^{-1})	n	f
8:1	-	-	-	0.44	0.7	0.08	2:1	0.30	1.0	0.40
16:1	0.59	1.1	0.06	0.42	2.0	0.12	4:1	0.34	1.4	0.30
32:1	0.40	2.8	0.08	0.30	3.5	0.10	6:1	0.31	2.7	0.37
							8:1	0.28	3.5	0.36
							10:1	0.24	3.8	0.32
							12:1	0.25	3.9	0.28

values for n and Γ_{ET} that were extracted from the fitting curves, and the values of f are given in Table 5.1.

From Table 5.1 it can be seen that the average value of f is about 0.08 when HdT is used as cross-linker. Therefore, it can be concluded that about 1 out of 13 HdT molecules has a QD attached on both ends ($f \approx 0.08$; $1/f \approx 13$) when used to cross-link QDs. The values of f for gQDs and rQDs cross-linked with HdT are approximately the same. This indicates that the cross-linking efficiency is independent of the nanocrystal size. When gQDs are cross-linked with a rigid cross-linker (BPD), the average value of f is 0.34, which means that 1 out of 3 BPD molecules has a QD attached at both sides. This value is over 4 times higher than that for the flexible cross-linker HdT, confirming the above observations that the rigid molecules cross-link the QDs more efficiently than flexible molecules. Furthermore, the ET-rate (Γ_{ET}) was extracted from the fits. In our model, Γ_{ET} is defined as the rate at which an exciton is transferred to one neighboring QD, which is multiplied by n in equation (5.1) to obtain the total ET-rate due to all neighboring acceptors. Therefore, the value extracted for Γ_{ET} from the fits should be independent of the linker/QD ratio, as is indeed the case, especially for the gQD cross-linked with BPD (0.29 ns^{-1} ± 0.04). In the case of QDs cross-linked by HdT, there is a larger spread in the Γ_{ET} values, which we ascribe to experimental uncertainty. Note that up to the present day, the ET rates that have been reported in literature (20 ns^{-1}- 0.5 ns^{-1}) were measured in QD solids, where the inter-dot distance and amount of neighbors is not well defined.[15-18] Here we show that the energy transfer rate from one QD in dispersion to another single neighboring QD at a distance of about 1 nm (the size of BPD) is ~ 0.3 ns^{-1}.

The Γ_{ET} obtained for gQDs cross-linked with HdT (≈ 0.4 ns^{-1}) seems to be higher as compared to the Γ_{ET} of gQDs cross-linked by BPD (0.3 ns^{-1}). The slower ET rate in the latter case may be due to a longer (and fixed) inter-particle distance due to the rigid cross-linker, but may also be due to the uncertainty resulting from the analysis. It was reported earlier that the inter-particle distance between gold nanoparticles that were cross-linked by aromatic dithiols was consistent with the size of the molecule, confirming the rigidity of these dithiols.[6, 20, 21]

The optical analysis described above is a very sound tool to study a structural property of dithiol molecules on a nanocrystal surface. From the analysis of the decay curves (Table 5.1), it can be concluded that cross-linking of QDs by rigid molecules (BPD, BPE, BdMT) is at least 4 times more efficient than for the flexible molecules (HdT, NdT). To explain this difference we consider that both HdT and

NdT contain a single aliphatic chain which gives the molecules a high rotational freedom around the carbon-chain. We propose that flexible cross-linkers can therefore attach with both thiol groups to one single QD to form loops, whereas rigid molecules cannot. Because a significant fraction of the flexible molecules will form loops on one QD, a higher number of the flexible cross-linker molecules is needed compared to the rigid molecules to achieve a similar aggregation number. Further support for this explanation is provided by molecular simulations and optical absorption measurements for QDs in the presence of monothiols and dithiols, as explained below.

Molecular simulations

We performed molecular simulations showing that HdT indeed forms loops on a gold nanocrystal (Figure 5.6A), whereas more rigid molecules do not (Figure 5.6B). Although the simulations were performed on a gold nanocrystal, we consider the comparison to be legitimate, because in both systems a facetted nanocrystal with a high affinity for thiol groups dispersed in an apolar solvent is considered. For these simulations, the rigid aromatic molecules (i.e. BDT BPE, BdMT) were mimicked by HdT-molecules, where the torsional force constants along the carbon chain were increased by a factor of ten compared to the flexible HdT-molecules. In this manner, the energy-level of the gauche conformation increases from 2 kT to 20 kT at room temperature, ensuring that the molecule will stay in the anti-conformation (i.e. a rigid molecule). The conformational energy penalty for cross-linkage to the nanocrystal surface with both thiol groups is too large for the rigid HdT molecules. Hence, they attach with one thiol group to the nanocrystal surface and the (rigid) chains are oriented away from this surface (Figure 5.6B). On the other hand, a large fraction of the flexible HdT-molecules (5 out of 6 in Figure 5.6A) can form loops on the nanocrystal surface due to their conformational freedom, which is in qualitative agreement with our observations. A detailed description of the simulations can be found in the appendix of this chapter.

In the literature, there is a consensus that aromatic dithiols (and BdMT in particular) stand up-right on a gold surface.[22-25] In contrast, HdT was reported to

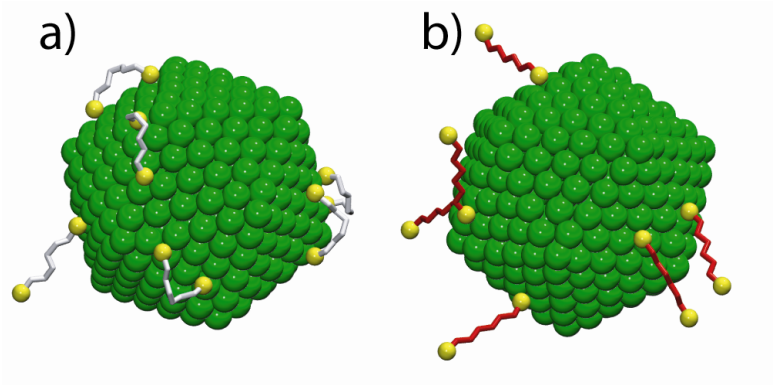

Figure 5.6. Snapshots from molecular simulations showing the configuration of (A) flexible hexanedithiol-molecules (grey bonds) and (B) rigid hexanedithiol-molecules (red bonds) on a gold nanocrystal (green), dispersed in hexane. The figure shows typical snapshots from well-equilibrated simulations. Note that, for clarity, the solvent molecules are not shown.

lie flat on gold substrates, and the formation of loops by HdT has been reported as well.[26, 27] On the other hand, the up-right orientation of HdT or octanedithiol molecules was also reported, and there is an extensive on-going debate about the orientation of these flexible dithiols on gold substrates.[7, 28, 29] In addition, it should be mentioned that a recent theoretical paper showed that benzene-1,4-dithiol lies almost flat on a gold surface at low coverage, although only one thiol group is bound to the surface in that case.[30] The present results show that there is indeed a difference in orientation between flexible and rigid dithiols on a nanocrystal surface: the high fraction *f* of 0.34 for BPD as cross-linker suggests that rigid dithiols bind with only one thiol to the nanocrystal in an up-right position, whereas flexible dithiols ($f \approx 0.08$) prefer to form loops and attach with both thiols to the surface.

Red-shifts

Further support for the binding of the dithiols with both thiol groups on the surface of the QDs is obtained from the analysis of the red-shift of the absorption (and emission) spectra upon the addition of either dithiols (flexible or rigid) or monothiols. In the previous chapter we suggested that the red-shift in both absorption and emission spectra of gQD-aggregates upon cross-linkage could be due to electronic coupling. To investigate the validity of this model, the optical properties of gQDs were studied after addition of monothiols. If the red-shift is indeed related to electronic coupling between cross-linked QDs, no red-shift is expected for this system, since no coupling occurs by the addition of monothiols. In a range of 1 to 4000 monothiols per QD, the shift in the first absorption peak was investigated for propanethiol (PT), hexanethiol (HT), nonanethiol (NT), benzenethiol (BT), and phenylethanethiol (PET), see Figure 5.7. The first absorption maximum of gQDs already shifts significantly in the range of 5 to 40 monothiols per QD, saturating at a level of 40 meV. The shift increases with increasing monothiol concentration and is independent of the type of monothiol used, indicating that it is an effect purely caused by the substitution of amine-groups by the thiol-groups. The reason for the decrease in absorption-shift in the particular case of gQDs cross-linked by BT at high concentrations is unclear. The

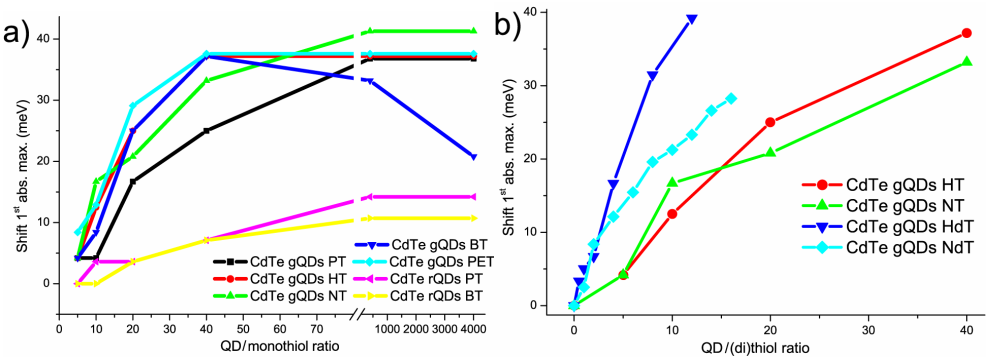

Figure 5.7. Red-shift of the first absorption maximum of green and red emitting AA-capped CdTe QDs (gQDs and rQDs), as a function of the thiol/QD ratio. (A) red-shift of gQDs and rQDs for 5 different monothiols (B) comparison of the red-shift of gQDs after addition of monothiols (HT and NT) or dithiols (HdT and NdT).

maximum shift of the first absorption peak of gQDs that were cross-linked by HdT was also 40 meV. Therefore, it can be concluded that the red-shift in absorption for gQD-aggregates is not due to strong electronic coupling, but an effect of thiol groups attaching to the nanocrystal surface. The absence of a red-shift in the case of rigid-cross-linkers is simply due to the low concentration of cross-linkers used in these experiments (linker/QD ratio up to 2:1).

In the range of 1 to 40 monothiols per QD, the red-shift depends approximately linearly on the molar thiol/QD ratio, i.e. the number of thiols attached to the nanocrystal surface. Importantly, Figure 5.7B shows that the red-shift of the first absorption peak increases faster as a function of the thiol/QD ratio when dithiols are used (HdT and NdT) as compared to monothiols (HT and NT). The slope of the red-shift as a function of the thiol concentration is about a factor of 2 steeper for the dithiols in comparison to the monothiols (see Figure 5.7B). These results from optical absorption measurements prove in a unique way that flexible cross-linkers attach with both thiol groups to the nanocrystal surface to form loops.

To study if the red-shift in the absorption spectrum after thiol-substitution is dependent on the nanocrystal size and/or type, CdTe and CdSe QDs of different sizes were prepared. Figure 5.8 shows the absorption spectra of green, yellow, and red emitting CdTe and CdSe QDs before and after the addition of an excess of hexanethiol (molar ratio thiol/QD > 25.000). For both CdTe and CdSe QDs, the smallest QDs (gQDs) show a significant red-shift of the first absorption maximum, whereas the larger QDs (yQDs and rQDs) show a small or no red-shift at all. The exciton emission peak of these samples all shifted in a similar way as the first absorption peak (not shown). The red-shift of red emitting CdTe QDs at various monothiol concentrations is plotted in Figure 5.7A, which also shows that the red-shift is much smaller as compared to the gQDs (10 meV versus 40 meV). This apparent size-dependent red-shift of the (first) absorption and emission peak due to the attachment of thiols can not be explained easily. Two tentative explanations for the size-dependent red-shift are given below.

In the first place, one might consider the replacement of amines by thiol-groups at Cd-terminated facets on the nanocrystal surface as an expansion of the (electronic) size of the QD. In that case, the confinement of the charge carriers is

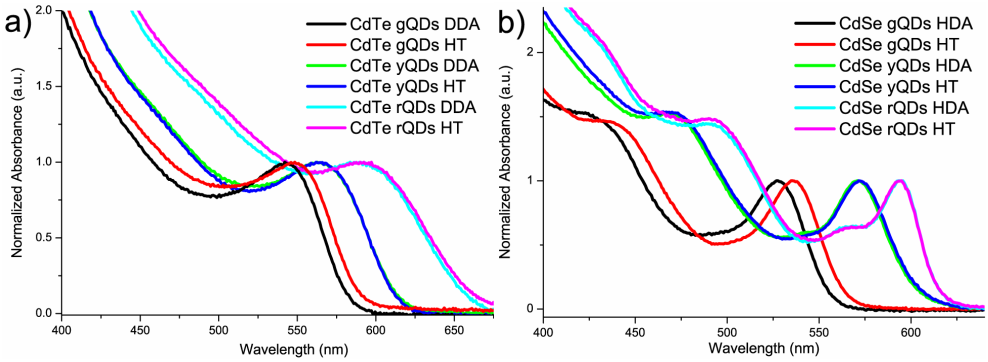

Figure 5.8. Normalized absorption spectra of green, yellow, and red emitting CdTe (A) and CdSe (B) QDs, dispersed in toluene with their original capping (DDA or HDA), and after addition of an excess of hexanethiol (HT) (HT/QD>25.000).

smaller, leading to a smaller optical gap. Qualitatively, this could explain why the red-shift is larger for the smallest QDs, for which quantum confinement is the largest. According to the formula of Sapra *et al.*, relating the confinement energy to the size of a nanocrystal, we calculate that the bandgap of the gQDs would decrease by 67 meV, after the attachment of a monolayer of thiols.[31] For this calculation, a gQD diameter of 3.4 nm, a Cd-S bond-length of 0.28 nm, and a 50% termination of the surface by Cd-ions are assumed. Furthermore, it is hypothesized that a monolayer of thiol-groups has a similar effect on the bandgap as the addition of a monolayer of Te-ions. It should be noted that a Cd-surface passivated by thiol ligands bond may not be regarded as an inorganic CdS shell, because the latter should result in an increase in the quantum yield of the CdSe QDs.[32, 33] Instead, we observe a decrease in the quantum yield upon addition of thiols to the CdSe QDs, which was reported earlier and ascribed to hole-trapping by the thiol ligands.[32, 33] A similar treatment for the rQDs (5.1 nm in diameter) in Figure 5.8A yields an expected decrease in bandgap of 29 meV. From experiments, a maximum red-shift of 40 meV and 10 meV was observed for the gQDs and rQDs, respectively (Figure 5.7A). Secondly, both an experimental and theoretical paper have shown that the Cd-thiol bond is significantly stronger for smaller CdTe and CdSe nanocrystals compared to larger QDs.[34, 35] It can be argued that a stronger Cd-thiol bond results in a larger influence of the thiol group on the electronic structure of the QD. This may be connected with the size-dependent red-shift that is observed upon the attachment of monothiols on the surface of CdSe and CdTe QDs (Figure 5.8).

5.4 Conclusions

In summary, we have investigated the cross-linkage of CdTe QDs by dithiol linker molecules. The results (cryo-TEM and optical spectroscopy) show that rigid dithiol molecules such as BPD (4,4'-biphenyldithiol) are more efficient cross-linkers than flexible dithiol molecules, such as HdT (hexanedithiol). Upon addition of dithiol linker molecules, the emission spectra shift to longer wavelengths, the relative intensity of the defect emission increases, and the luminescence decay curves show a fast initial decay due to exciton energy transfer to QDs with a smaller bandgap within the aggregate. These effects occur at much lower linker/QD ratios for the rigid linker molecules compared to the flexible dithiols. A quantitative analysis of the luminescence decay curves shows that the rigid dithiols cross-link the QDs at least 4 times more efficient than flexible cross-linkers. This is attributed to the formation of loops of the flexible dithiols on a QD surface by attaching with both thiol groups to the same QD, which is not possible for the rigid dithiols. Molecular simulations confirm the formation of loops by the flexible HdT on a nanocrystal with a strong affinity for thiol groups. Further experimental evidence for the formation of loops is obtained from the red-shift of the exciton emission band that is observed upon addition of both mono-and dithiols. The red-shift is induced by the exchange of amine capping molecules by thiols, and not by electronic coupling. For the flexible dithiols the same shift is observed as for monothiols at half the concentration, providing evidence that the dithiols bind with both thiol groups at the QD surface.

5.5 References

1. T.H. Oosterkamp, T. Fujisawa, W.G. van der Wiel, K. Ishibashi, R.V. Hijman, S. Tarucha, and L.P. Kouwenhoven, *Nature*, **1998**. *395* (6705): p. 873-876.
2. E.A. Stinaff, M. Scheibner, A.S. Bracker, I.V. Ponomarev, V.L. Korenev, M.E. Ware, M.F. Doty, T.L. Reinecke, and D. Gammon, *Science*, **2006**. *311* (5761): p. 636-639.
3. M. Bayer, P. Hawrylak, K. Hinzer, S. Fafard, M. Korkusinski, Z.R. Wasilewski, O. Stern, and A. Forchel, *Science*, **2001**. *291* (5503): p. 451-453.
4. E.V. Shevchenko, D.V. Talapin, S. O'Brien, and C.B. Murray, *J. Am. Chem. Soc.*, **2005**. *127* (24): p. 8741-8747.
5. L.C. Brousseau, J.P. Novak, S.M. Marinakos, and D.L. Feldheim, *Advanced Materials*, **1999**. *11* (6): p. 447-+.
6. T. Dadosh, Y. Gordin, R. Krahne, I. Khivrich, D. Mahalu, V. Frydman, J. Sperling, A. Yacoby, and I. Bar-Joseph, *Nature*, **2005**. *436* (7054): p. 1200-1200.
7. F. Schreiber, *Prog. Surf. Sci.*, **2000**. *65* (5-8): p. 151-256.
8. M.A. Reed, C. Zhou, C.J. Muller, T.P. Burgin, and J.M. Tour, *Science*, **1997**. *278* (5336): p. 252-254.
9. A. Nitzan and M.A. Ratner, *Science*, **2003**. *300* (5624): p. 1384-1389.
10. C. Joachim, J.K. Gimzewski, and A. Aviram, *Nature*, **2000**. *408* (6812): p. 541-548.
11. R. Koole, P. Liljeroth, C. de Mello Donega, D. Vanmaekelbergh, and A. Meijerink, *J. Am. Chem. Soc.*, **2006**. *128* (32): p. 10436-10441.
12. S.F. Wuister, F. van Driel, and A. Meijerink, *Phys. Chem. Chem. Phys.*, **2003**. *5* (6): p. 1253-1258.
13. C. de Mello Donega, M. Bode, and A. Meijerink, *Phys. Rev. B*, **2006**. *74* (8): p. 085320.
14. W.W. Yu, L. Qu, W. Guo, and X. Peng, *Chem. Mater.*, **2003**. *15* (14): p. 2854-2860.
15. S.A. Crooker, J.A. Hollingsworth, S. Tretiak, and V.I. Klimov, *Phys. Rev. Lett.*, **2002**. *89* (18): p. 186802.
16. M. Achermann, M.A. Petruska, S.A. Crooker, and V.I. Klimov, *J. Phys. Chem. B*, **2003**. *107* (50): p. 13782-13787.
17. T. Franzl, D.S. Koktysh, T.A. Klar, A.L. Rogach, J. Feldmann, and N. Gaponik, *Appl. Phys. Lett.*, **2004**. *84* (15): p. 2904-2906.
18. T. Franzl, A. Shavel, A.L. Rogach, N. Gaponik, T.A. Klar, A. Eychmuller, and J. Feldmann, *Small*, **2005**. *1* (4): p. 392-395.
19. M. Tachiya, *J. Chem. Phys.*, **1982**. *76* (1): p. 340-348.
20. L.C. Brousseau, J.P. Novak, S.M. Marinakos, and D.L. Feldheim, *Adv. Mater.*, **1999**. *11* (6): p. 447.
21. J.P. Novak and D.L. Feldheim, *J. Am. Chem. Soc.*, **2000**. *122* (16): p. 3979-3980.
22. D.L. Pugmire, M.J. Tarlov, R.D. van Zee, and J. Naciri, *Langmuir*, **2003**. *19* (9): p. 3720-3726.
23. J.M. Tour, L. Jones, D.L. Pearson, J.J.S. Lamba, T.P. Burgin, G.M. Whitesides, D.L. Allara, A.N. Parikh, and S.V. Atre, *J. Am. Chem. Soc.*, **1995**. *117* (37): p. 9529-9534.
24. H.M. Zareie, A.M. McDonagh, J. Edgar, M.J. Ford, M.B. Cortie, and M.R. Phillips, *Chem. Mater.*, **2006**. *18* (9): p. 2376-2380.
25. S. Hong, R. Reifenberger, W. Tian, S. Datta, J.I. Henderson, and C.P. Kubiak, *Superlattices Microstruct.*, **2000**. *28* (4): p. 289-303.
26. T.Y.B. Leung, M.C. Gerstenberg, D.J. Lavrich, G. Scoles, F. Schreiber, and G.E. Poirier, *Langmuir*, **2000**. *16* (2): p. 549-561.
27. C.D. Bain, E.B. Troughton, Y.T. Tao, J. Evall, G.M. Whitesides, and R.G. Nuzzo, *J. Am. Chem. Soc.*, **1989**. *111* (1): p. 321-335.
28. A.K.A. Aliganga, A.S. Duwez, and S. Mittler, *Organic Electronics*, **2006**. *7* (5): p. 337-350.
29. Y.C. Yang, Y.L. Lee, L.Y.O. Yang, and S.L. Yau, *Langmuir*, **2006**. *22* (11): p. 5189-5195.

30. R.B. Pontes, F.D. Novaes, A. Fazzio, and A.J.R. daSilva, *J. Am. Chem. Soc.*, **2006**. *128* (28): p. 8996-8997.
31. S. Sapra and D.D. Sarma, *Phys. Rev. B*, **2004**. *69* (12): p. 125304.
32. X.G. Peng, M.C. Schlamp, A.V. Kadavanich, and A.P. Alivisatos, *J. Am. Chem. Soc.*, **1997**. *119* (30): p. 7019-7029.
33. S.F. Wuister, C. de Mello Donegá, and A. Meijerink, *J. Phys. Chem. B*, **2004**. *108* (45): p. 17393-17397.
34. J. Schrier and L.W. Wang, *J. Phys. Chem. B*, **2006**. *110* (24): p. 11982-11985.
35. J. Aldana, N. Lavelle, Y.J. Wang, and X.G. Peng, *J. Am. Chem. Soc.*, **2005**. *127* (8): p. 2496-2504.

5.6 Appendix

Derivation of equation (5.1)

It can be assumed in a good approximation that the number *m* of QDs attached to one QD follows a Poisson distribution given by:

$$\varphi(m) = \left(\frac{n^m}{m!}\right) e^{(-n)} \tag{5.4}$$

where *n* is the average number of QDs attached to one QD. This assumes that the attachments of thiols to QDs are independent events that occur with a constant rate. When a QD is excited and has *m* QDs attached, the rate constant of the excited state decay for that QD is given by $\Gamma_{rad} + m\Gamma_{ET}$. Therefore, the ensemble averaged decay of the excited state is given by:

$$I(t) = I_0 \sum_m \varphi(m) e^{(-(\Gamma_{rad} + m\Gamma_{ET})t} \tag{5.5}$$

It can be seen from equation (5.5) that the decay of the excited state is essentially described by multi-exponentials. Equation (5.5) can be re-written as follows, resulting in equation (5.3), which was used in this chapter:

$$I(t) = I_0 \sum_m \varphi(m) e^{(-(\Gamma_{rad} + m\Gamma_{ET})t}$$

$$= I_0 \sum_m \left(\frac{n^m}{m!}\right) e^{(-n)} e^{(-(\Gamma_{rad} + m\Gamma_{ET})t}$$

$$= I_0 e^{(-\Gamma_{rad} t - n)} \sum_m \frac{(n \cdot e^{(-\Gamma_{ET} \cdot t)})^m}{m!}$$

$$= I_0 e^{(-\Gamma_{rad} t - n)} \cdot e^{(n \cdot e^{(-\Gamma_{ET} \cdot t)})}$$

$$= I_0 e^{((-\Gamma_{rad} t) - n(1 - e^{(-\Gamma_{ET} \cdot t)}))} \tag{5.3}$$

Molecular Simulations

The snapshots shown in Figure 5.6 are taken from Monte Carlo (MC) simulations at constant *NVT*, where *N* is the total number of molecules, *V* is the volume of the simulation box and *T* the temperature. Both simulations were performed at T = 300 K in a cubic box with V = 216 nm³, applying periodic boundary conditions. The systems consisted of one rigid nanocrystal of 561 Au atoms (radius R≈1 nm), 6 hexane dithiol molecules, and 940 hexane (solvent) molecules. This composition corresponds to experimental conditions (e.g. temperature, atmospheric pressure). The solvent and dithiol molecules are represented by a united atom model where the contributions of the atoms in each functional group (e.g. CH_2, CH_3 or SH) are incorporated in an effective pseudo atom. The intermolecular force field takes into account excluded volume and Van der Waals attraction. Within the chain molecules, we consider bond stretching, bond bending and torsional forces. The SH moieties interact stronger with the Au surface than other pseudo atoms. We performed two simulations: one where we used alkane-like torsional force constants for hexane dithiol (Figure 5.6A) and the other where we increased these constants for hexane dithiol by a factor of ten (Figure 5.6B). The latter should mimic rigid, aromatic dithiols. On average, one MC cycle consisted of 15 trial displacements, 15 trial rotations, 150 partial regrow trial moves and 750 full regrow trial moves. For both regrow moves we increased sampling efficiency by using the Configurational-bias Monte Carlo technique.

Chapter 6

Time-Dependent Photoluminescence Spectroscopy as a Tool to Measure the Ligand Exchange Kinetics on a Quantum Dot Surface

The exchange kinetics of native ligands that passivate CdSe quantum dots (hexadecylamine (HDA), trioctylphosphine oxide (TOPO), and trioctylphosphine (TOP)) by thiols is followed *in situ*. This is realized by measuring, in real time, the decrease in emission intensity of the QDs upon addition of hexanethiol (HT), which quenches the emission. The effect of adding an excess of native ligands prior to thiol addition on the ligand exchange is studied and provides insight in the bond-strength and exchange kinetics of the individual surfactants. Temperature dependent measurements reveal faster kinetics with increasing temperature. A kinetic model to fit the time-dependent measurements is introduced, taking into account the equilibrium between native ligands before thiol-addition, and describing the evolution of surface coverage by all ligands over time. The model allows us to extract the quenching rate for a single thiol ligand (0.004 ns^{-1}) and exchange rates, equilibrium constants, activation energies, and changes in Gibbs free energy for exchange of the different native surfactants by HT. The analysis reveals that the substitution half time of HDA by HT (72 s) is much shorter than for TOP (5h) or TOPO (2.5 h) under the same conditions. The temperature dependence of the kinetics shows that the activation energy for exchange of HDA/TOPO by hexanethiol (1.6 kJ/mol) is much smaller than for TOP (20.9 kJ/mol).

6.1 Introduction

Surface passivation of semiconductor nanocrystals by organic ligands strongly influences the properties of these so-called quantum dots (QDs). First of all, the organic ligands control the size and shape during synthesis, by accelerating or inhibiting crystal growth at certain facets.[1, 2] By varying the reaction conditions, in which the organic ligands play a dominant role, nanocrystals can now be synthesized in a wide variety of shapes, like spheres[3, 4], rods[5-7], rings[8], multipods[6, 7, 9, 10], stars and octahedrons[8, 11], cubes[6, 12], and so on. Next, stable dispersions of these colloids are a direct result of the capping molecules, avoiding irreversible aggregation and fusion of the nanocrystals due to van der Waals interactions. Most semiconductor nanocrystals are coated with hydrophobic ligands (mostly aliphatic chains) directly after synthesis, making them well soluble in apolar solvents. The nanocrystals can be transferred to more polar media like ethanol or water by simply exchanging the ligands by hydrophilic or even charged ligands[4, 13, 14], which is a crucial step for making QDs bioapplicable.[15-17] Finally, the fluorescence of quantum dots (QDs) is strongly dependent on the degree *and* type of surface passivation by organic ligands. For example, CdSe QDs synthesized in a trioctylphosphine/trioctylphosphineoxide (TOP/TOPO) mixture by the early synthesis route proposed by Murray et al.[4] results in QDs with a quantum yield (QY) ranging between 5-15%, while the addition of hexadecylamine (HDA) to the reaction mixture, as first reported by Talapin et al.[3], increases the QY to over 50% and can yield QDs with a QY near unity.[18, 19] In another example, closely related to the topic of this work, the fluorescence of CdSe QDs is shown to be quenched after exchanging the native ligands with thiol ligands[20-23], while the same thiol ligands enhance the fluorescence of CdTe QDs.[24, 25]

Despite the evident importance of capping molecules for both the fundamental understanding of QD properties and development towards applications, the number of detailed investigations on the surface passivation by organic ligands is limited. Early NMR and XPS studies on the surface coverage of CdSe QDs revealed that the majority of the surface was coated by TOPO ligands, but these QDs were synthesized by the early TOP/TOPO route without the presence of amines.[26, 27] Other groups have utilized the influence of ligands on the fluorescence properties of CdSe QDs to investigate the ligand exchange at the surface. It is generally found that primary amines enhance the QY of CdSe QDs, especially when the QDs have undergone several purification steps.[21-23, 28, 29] A quantitative study of the emission enhancement and quenching upon ligand exchange with amines and thiols respectively resulted in estimates for the binding constants for amines and thiols ranging between $2x10^4$ and $1x10^9$ M^{-1}.[21, 22, 29] In another study, the quenching of CdSe QDs by thiol adsorption was shown to be significantly smaller in case the surface is mainly terminated by Se, and these Se-rich QDs needed a sufficient coating by TOP to obtain a high QY (up to 50%).[30]

Molecular simulations provide another tool to study ligand adsorption. Some work has been done on gold NCs protected by alkyl thiols to determine the structure of the capping layer and adsorption properties of the capping molecules.[31-33] We are aware of only one paper that considers CdSe QDs capped by TOPO[34], in which surface packing and dipole moment of the cluster are considered. Moreover, it is known from simulations of a bare CdSe QD that a surface rearrangement takes place to minimize its dipole moment.[34, 35]

Previous work investigating the influence of ligand exchange on the emission of CdSe QDs focused on equilibrated samples, using steady-state measurements.[21-23] Little attention was paid to the exchange kinetics, which can be followed by measuring the change in emission of CdSe QDs upon ligand exchange *in situ*, as is shown in this work. In a recent publication the desorption and adsorption of alkylamines on CdSe QDs was followed over time by emission measurements.[29] The approach in that study differs from this work in the sense that the desorption kinetics of one type of ligand (amines) was studied by dilution experiments, making use of the fact that the emission intensity of CdSe QDs decreases when amine surfactants leave the surface.

In the present study, we have investigated the exchange kinetics of the three commonly used native ligands (HDA, TOP, and TOPO) on CdSe QDs by hexanethiol (HT), by measuring the decrease in emission intensity due to thiol adsorption as a function of time. The experimental conditions and timescale at which ligand exchange takes place allowed us to follow the exchange process with a high accuracy and reproducibility. By changing various parameters like native ligand concentration, hexanethiol concentration, and temperature, detailed information about the ligand exchange kinetics could be extracted. A self-consistent model was developed to extract the values for kinetic rates, equilibrium constants, and activation energies for ligand exchange.

This chapter is divided into four sections. First, the basic influence of adsorbed thiol ligands on the optical properties of CdSe QDs will be discussed. In this section, measurements on equilibrated samples will be considered, i.e. where the thiol ligands were added three days prior to the optical measurement. Secondly, we introduce a new approach to study the ligand exchange of thiols on CdSe QDs, by monitoring the emission of the QDs in real-time after addition of thiol ligands. These experiments were conducted with different concentrations of native ligands, and the results are discussed qualitatively. In the third section a model is introduced which allows for a quantitative analysis of the results from the second part. In the last section, temperature-dependent measurements are discussed and analyzed by the same model, to obtain the activation energies and changes in Gibbs free energy for the ligand exchange of native ligands by thiols.

6.2 Experimental Section

Anhydrous toluene (99.8%), trioctylphosphine (TOP, 90%), trioctylphosphine oxide (TOPO, 99%), hexadecylamine (HDA, 90%), and hexanethiol (HT, 95%) were purchased from Aldrich. Rhodamine B was supplied by Exciton. Dimethylcadmium ($Cd(Me)_2$, 99.99%) and selenium powder (99.99%, 200 mesh) were obtained from ARC Technologies and Chempur respectively.

The synthesis of CdSe nanocrystals was carried out by the high-temperature organometallic synthesis as reported in detail by de Mello Donegá et al.[19] In short, a solution of the precursor materials $Cd(Me)_2$ (0.28 g) and Selenium powder (0.79 g) in 10 ml TOP was quickly injected into a three-neck flask containing a pre-heated mixture (300 °C) of 10g HDA and 20g TOPO. Upon injection we allowed the temperature to drop to 165°C during 5 minutes, followed by 6 minutes heating time to 240°C, at which temperature it was kept for 4 minutes. After this the reaction mixture was allowed to cool down to room temperature. The resulting CdSe QDs were 2.8 nm in diameter (as determined from TEM) and had a QY of ~ 40%. The QY was determined by comparison of the integrated emission intensity of a reference dye (Rhodamine B in ethanol, QY = 90%) with the emission intensity of the CdSe QDs, correcting for the absolute absorbance value at the excitation wavelength (400nm). The raw product was diluted in a 1:1 ratio with anhydrous toluene to obtain what will be called the stock dispersion of QDs.

All samples were prepared in a nitrogen purged glovebox, and transferred to a sealed quartz cuvette for optical measurements. For the equilibrium measurements, 10 µl of the stock dispersion of CdSe QDs was added to 2.5 ml toluene, after which 0.5 ml of a solution with the desired quantity of HT in toluene was added. The samples were allowed to equilibrate for three days in the dark in the glovebox, after which the absorption and emission spectra were recorded. The size-dependent calibration curve of the extinction coefficient of CdSe QDs at the first absorption peak (empirically determined by Yu et al.[36]) was used to calculate the concentration of the QD dispersions. In this manner, we measured that the QD concentration of the samples thus obtained was ~ 0.7 µM (~ 2nmol QDs in 3ml toluene). This concentration was used to compute that the 0.5 ml solution corresponding to 2000 HT molecules per QD in the final mixture requires an HT concentration of 8 mM.

For the time-dependent measurements, a dispersion of 10 µl of CdSe stock dispersion in 2.5 ml toluene was transferred (in the glovebox) into a quartz cuvette that was tightly sealed by a septum. The cuvette was placed in the sample holder of a spectrofluorometer (see below), after which 0.5 ml of an HT solution in toluene was vigorously injected with a syringe (prepared in the glovebox) through the septum of the cuvette, into the QD dispersion. A few seconds before injection of the HT solution the recording of emission spectra was started. This was performed using a monochromator and CCD camera (see below) with a high repetition rate so that 10 emission spectra per second could be measured. During the first three minutes the emission spectra were recorded sequentially with a repetition rate of 10 spectra per second, directly followed by 2 hours (or 30 minutes) of measurements with a 10 s time interval, followed by a last series of measurements over 10 hours with a 100 s time interval. The reference measurements (injection of 0.5 ml of toluene containing no HT) were carried out in the exact same manner. The samples containing an excess of ligands were prepared by adding 10 µl of

CdSe stock dispersion to 1.25 ml of toluene, to which 1.25 ml of a toluene solution containing the desired quantity of HDA, TOP, or TOPO was added. The dispersion was allowed to equilibrate for at least three days in the dark (in the glovebox), after which the optical measurements were started upon injection of a 0.5 ml HT solution in toluene. From the amounts used in the synthesis, it can be calculated that 10 µl of the stock dispersion of CdSe QDs contains 5 µmol HDA, 3 µmol TOP, and 6.5 µmol TOPO, which corresponds to respectively 2500, 1400 and 3200 ligands per QD (in the standard dispersion). These numbers were used to calculate the amount of these native ligands that was needed to obtain a 10-or 100-fold excess compared to the concentrations in the standard dispersion.

For the temperature dependent (real-time) measurements, the sample holder of a Spex Fluorolog spectrofluorometer was replaced by a 1L glass beaker filled with ethanol. The element of a thermostat was placed in the beaker to obtain a constant temperature, tunable between -20 °C and +31 °C. The cuvette was partly plunged in the ethanol and tightly fixed, and the ethanol was gently stirred for an efficient heat exchange with the cuvette, but avoiding turbulence that would cause fluctuations in the excitation/emission intensity. The syringe containing the HT solution to be injected in the QD dispersion was brought to the same temperature as the cuvette prior to injection.

Emission spectra were recorded using a 450W Xe lamp as excitation source and a double grating 0.22 m SPEX monochromator (of a SPEX Fluorolog) to select the excitation wavelength of 406 nm. Emission was collected through an optical fiber leading to a 0.3 m monochromator (150 lines/mm, blazed at 550 nm) and detected by a liquid nitrogen cooled Princeton Instruments CCD-camera (1024x256 pixels). Absorption spectra were measured on a Perkin-Elmer Lambda 16 UV/VIS spectrofluorometer.

6.3 Results and Discussion

Equilibrium measurements

In this section, the basic changes in the optical properties of CdSe QDs upon addition of hexanethiol will be discussed. In all samples described in this section, thiols were added to the QD dispersion three days prior to the optical measurements. In this manner the ligand exchange had reached equilibrium, as will be shown in the next section. Figure 6.1A displays the absorption spectra of a dispersion of the as-synthesized CdSe QDs that were used for all experiments described throughout this paper. When an excess of effectively 2000 hexanethiol (HT) molecules per QD is added to the dispersion, a minor red-shift is observed in the absorption spectrum (inset Figure 6.1A). We refer to an earlier publication for a detailed discussion on the origin of these small spectral changes that are observed upon addition of thiol ligands to dispersions of CdTe or CdSe QDs.[37] The emission spectrum in Figure 6.1B shows a narrow emission band around 542 nm (full with at half maximum of 36 nm, or 150 meV). The quantum yield (QY) of the QDs is high (~ 40 %), which correlates with the absence of defect related emission that is often observed at the red tail of the (lower QY) QD emission spectrum. The high quality of the CdSe QDs allows for a detailed and sensitive study of the influence on the optical properties upon capping exchange with thiols. Removing excess of ligands from the CdSe QD dispersion by (multiple) washing steps usually decreases the QY significantly (up to a factor of 10), caused by the partial removal of passivating ligands. We have therefore used the as-synthesized QDs without any purification steps, which is an important difference between the present work and previous publications where ligand exchange on CdSe QDs was (quantitatively) studied.[21-23, 29] In case the decrease in emission due to the adsorption of thiols is to be studied, it is crucial to start with an as high as possible quantum yield (i.e. no purification steps). On the other hand, a low QY is required (i.e. multiple purification steps) in case the increase in emission intensity is monitored due to e.g. amine-adsorption.[29] By using a dilution of the unpurified as-synthesized QDs, we also take advantage of the fact that the concentration of native ligands (HDA, TOP, and TOPO) is accurately known (in contrast to a dispersion of purified QDs).

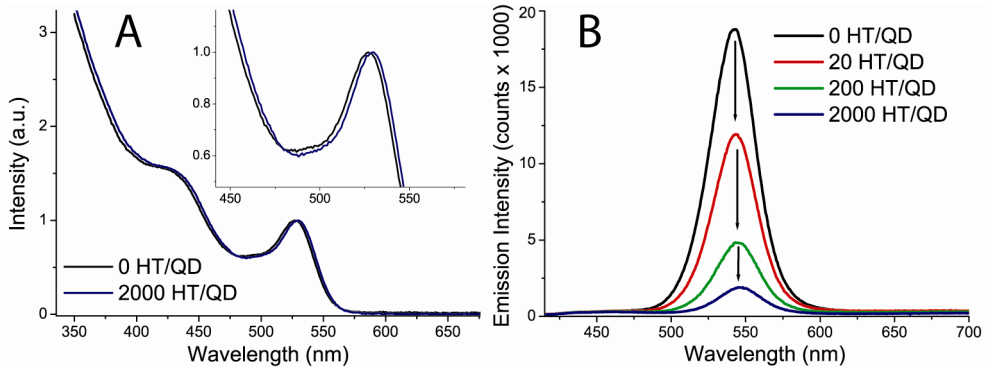

Figure 6.1. Absorption (A) and emission spectra (B) of CdSe QDs dispersed in toluene, after addition of a varying number of hexanethiol molecules per QD.

Figure 6.1B shows the effect on the fluorescence properties of the CdSe QDs upon addition of hexanethiols in a range between 0 and 2000 HT molecules per QD. Besides a minor red-shift, the emission spectra clearly show a quenching as a result of the HT addition, even at a concentration of effectively 20 HT/QD. Emission quenching of CdSe QDs as a result of the addition of thiol ligands has been studied extensively before[21-23], and the origin of this quenching was ascribed earlier to the trapping of photogenerated holes in the QD to a higher-lying HOMO level of thiol ligands.[25] This trapping induces an additional nonradiative recombination pathway for the exciton resulting in a lower overall emission QY:

$$QY(\theta_{thiol}) = QY(0) \bullet \frac{\Gamma_{rad}}{\Gamma_{tot}} = QY(0) \bullet \frac{\Gamma_{rad}}{\Gamma_{rad} + N_s \bullet \theta_{thiol} \bullet \Gamma_{trap}} \qquad (6.1)$$

where *QY(0)* is the quantum yield in the absence of thiols (~ 0.4), and (Γ_{tot}) is the total decay rate of the exciton, which can be written as the sum of the radiative decay rate of the exciton (Γ_{rad}) and the total trapping rate. The total trapping rate is defined here as the trapping rate of one adsorbed thiol molecule (Γ_{trap}) times the number of adsorbed thiols, which is the product of the total number of surface sites per QD (N_s) and the surface coverage by thiols (θ_{thiol}, $0 \leq \theta_{thiol} \leq 1$). In this definition it is assumed that the trapping rate of an adsorbed thiol ligand is constant and similar for different binding sites on the QD surface.

Emission spectra as shown in Figure 6.1B were recorded for a large series of dispersions with HT/QD ratios ranging between 0 and 2000, again after three days of equilibration time. Figure 6.2A shows the normalized emission intensity of the CdSe QDs as a function of the number of thiols per QD. The normalized emission intensity (I_{norm}) is defined as the integrated emission intensity of a sample, normalized to the integrated emission intensity of the dispersion without thiols (I_0). The emission intensity rapidly drops within the range of 0-100 HT/QD, after which it gradually decreases to a value of approximately 0.1. It is important for the modeling section to translate the emission intensity into surface coverage. Normalizing and rewriting equation (6.1) yields:

$$\alpha\theta_{thiol} = \frac{1}{I_{norm}} - 1 \qquad (6.2)$$

where α is a constant and defined as $\alpha = N_s\Gamma_{trap}/\Gamma_{rad}$. The data displayed in Figure 6.2A can now be plotted in terms of surface coverage as a function of the HT concentration, see Figure 6.2B. As in previous work[21, 22], the data can be well fitted by a Langmuir isotherm:

$$\alpha\theta_{\mathrm{Thiol}} = \alpha \frac{K_{\mathrm{L}} c_{\mathrm{Thiol}}}{1 + K_{\mathrm{L}} c_{\mathrm{Thiol}}} \qquad (6.3)$$

with the effective Langmuir constant K_L. The meaning of K_L will be discussed in more detail below. To illustrate the difference between equation (6.2) and the linear model used in previous work [21, 22], we compare for both methods the *titration*

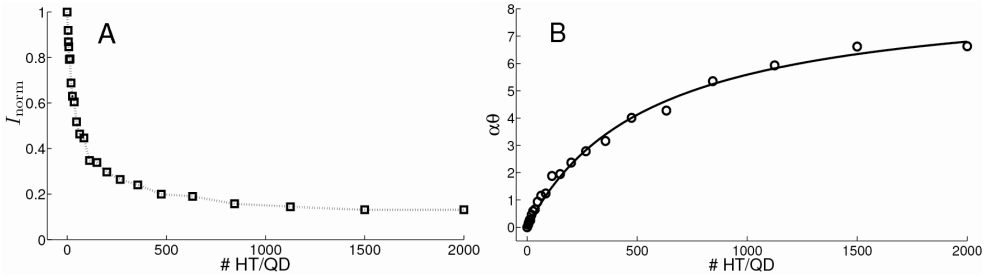

Figure 6.2. (A) Normalized integrated emission intensity (I_{norm}) of dispersions of CdSe QDs in toluene as a function of the number of added thiols per QD. Solid line connects data points and serves as a guide for the eye. (B) Surface coverage (θ_{thiol}) of thiols on a QD (times a constant α), as a function of the number of thiols/QD, extracted from the data displayed in (A). Solid line is a fit of the data by a Langmuir isotherm (see equation (6.3)), with fit parameters α = 8.7 and K_L = 0.0018 [-] (corresponding to K_L = 2600 (mol/l)$^{-1}$ in absolute units).

midpoint (*TM*): the thiol-coverage at which the emission intensity is half of the total decrease in emission intensity ($QY(\theta_{TM}) = 0.5(QY(0)+ QY(1))$. If a linear relation is assumed, then $\theta_{TM}=0.5$, whereas equation (6.2) yields $\theta_{TM}=0.09$ in our case (for $\alpha=8.7$).

The value for $\alpha\theta$ extrapolates to approximately 9 for infinite thiol concentration (or by simply filling in a value of 0.1 for I_{norm} in equation (6.2), when the surface coverage with thiols (θ_{thiol}) is approximately 1 (total surface coverage). Assuming a total number of cadmium surface sites (N_s) of ~ 125 per QD (based on 0.2 nm^2 per cadmium site[29] and a particle diameter of 2.8 nm), and taking a literature value for the radiative decay rate (Γ_{rad}) of 0.05 ns^{-1} ($\tau \approx 20$ ns)[38] for CdSe QDs emitting at 540 nm, it follows that the trapping rate per thiol ligand (Γ_{trap}) is in the order of 0.004 ns^{-1}.

Time-dependent measurements

All experiments described above involved equilibrated dispersions of CdSe QDs to which thiols were added three days prior to the optical measurements. In this section, the emission intensity of the QD dispersion upon addition of thiols is followed in real-time to obtain information on the ligand exchange kinetics. This was realized by sequentially measuring the emission spectra of the CdSe QDs before, during, and after the addition of thiols. In all experiments, 0.5 ml of a toluene solution containing the desired amount of HT molecules was rapidly injected (through a septum) into a dispersion of ~2 nmol of CdSe QDs in 2.5 ml toluene. In this manner, the decrease in emission intensity as a result of thiol addition could be recorded *in situ*, while the presence of oxygen was reduced to a minimum. To validate the experimental procedure, several control experiments were conducted by injecting pure toluene (without HT) into the QD dispersion. In the short time window, this dilution was measured to be highly reproducible within seconds (see Figure 6.9A in the appendix). The emission intensity decreases to 83% of the initial intensity, which is in excellent agreement with the dilution factor (2.5 ml/(2.5 ml + 0.5 ml) = 0.83). A sharp increase of 10-20 % is observed at the time of injection (set to t = -1 s), which is ascribed to scattering of the excitation

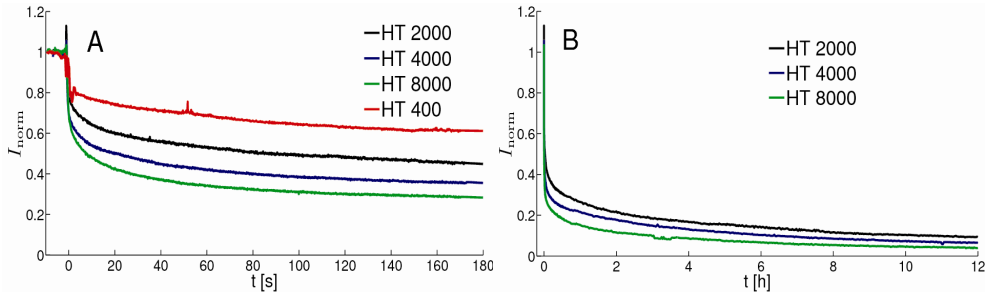

Figure 6.3. (A) Short time and (B) long time regime of the time-dependent decrease in emission intensity of CdSe QDs in toluene upon addition of thiol ligands with different concentrations. All emission spectra were recorded for 0.1s and the normalized (by the value before injection) integrated emission intensity is plotted as a function of time.

beam in the disturbed dispersion during injection. It can be seen that the injection and dilution process is very fast (1-2 seconds), and the subsequent emission intensity is constant over time in the short time window. These control experiments show that the decrease in emission intensities upon thiol addition (see below) can be directly ascribed to quenching by adsorbed thiols, even on very short time scales.

The evolution of emission intensity of the CdSe QDs upon addition of thiols is plotted in Figure 6.3. Four experiments were conducted in which effectively 400, 2000, 4000, and 8000 thiols per QD were added to the dispersion. In the short time window (Figure 6.3A), a sharp decrease in emission intensity is observed within the first minute. In the long time regime (Figure 6.3B), there is still a significant decrease in emission intensity between 1 and 12 hours. Clearly, the system needs at least 12 hours to equilibrate. Both in the short and long time regime, it is apparent that an increase in the concentration of added thiols results in a faster and eventually larger decrease in emission intensity. The experiment of 400 HT/QD was carried out for only 30 minutes and is therefore omitted in Figure 6.3B. These experiments show that there is a very fast initial ligand exchange with the native ligands, followed by a slower process that takes up to 12 hours.

In the reference measurements (no thiols added), there is also a very slow decrease in emission intensity observed in the long-time regime (Figure 6.9B in the appendix of this chapter). This decrease is ascribed to a slow photo-oxidation process due to the continuous illumination of the sample and the diffusion of a small amount of oxygen through the septum of the cuvette. To investigate the influence of photo-oxidation in the kinetic measurements, we checked the final emission intensity (after equilibration) of a sample where the thiols (2000 HT/QD) were added in the glovebox to prevent photo-oxidation and found a similar end-value of ~ 0.1 (see also Figure 6.2A). In a similar control experiment where the excitation beam was chopped during the experiment (to reduce photo-oxidation by limiting the exposure to light) showed a similar decrease in emission intensity compared to the curve of 2000 HT/QD in Figure 6.3A, also in the long time regime (not shown). Therefore we ascribe the decrease in emission intensity in the long time regime predominantly to a slow adsorption process of thiols, and not to photo-oxidation. Nevertheless, it should be noted that the photo-oxidation process may

slightly affect the outcome of the quantitative analysis that is described in the next section.

From the experiment displayed in Figure 6.3 it is apparent that the ligand exchange of the native ligands of CdSe QDs by thiol is not a simple first order process. This is not so surprising since the CdSe QDs are initially coated by a combination of ligands (HDA, TOP, TOPO), each of which will have a different binding constant and exchange kinetics. In addition, the exchange kinetics may also be dependent on the particular facet of the nanocrystal to which a ligand is bound. Therefore, it may be expected that the exchange of the native ligands by thiols is more complex. To obtain more insight in the exchange kinetics, several experiments were carried out where an excess of one of the native ligands was present. In each case, the kinetics of the exchange (i.e. the evolution of the emission intensity after thiol addition) was investigated after adding a 10 or 100 fold excess of one of the native ligands. The excess of ligands was added at least three

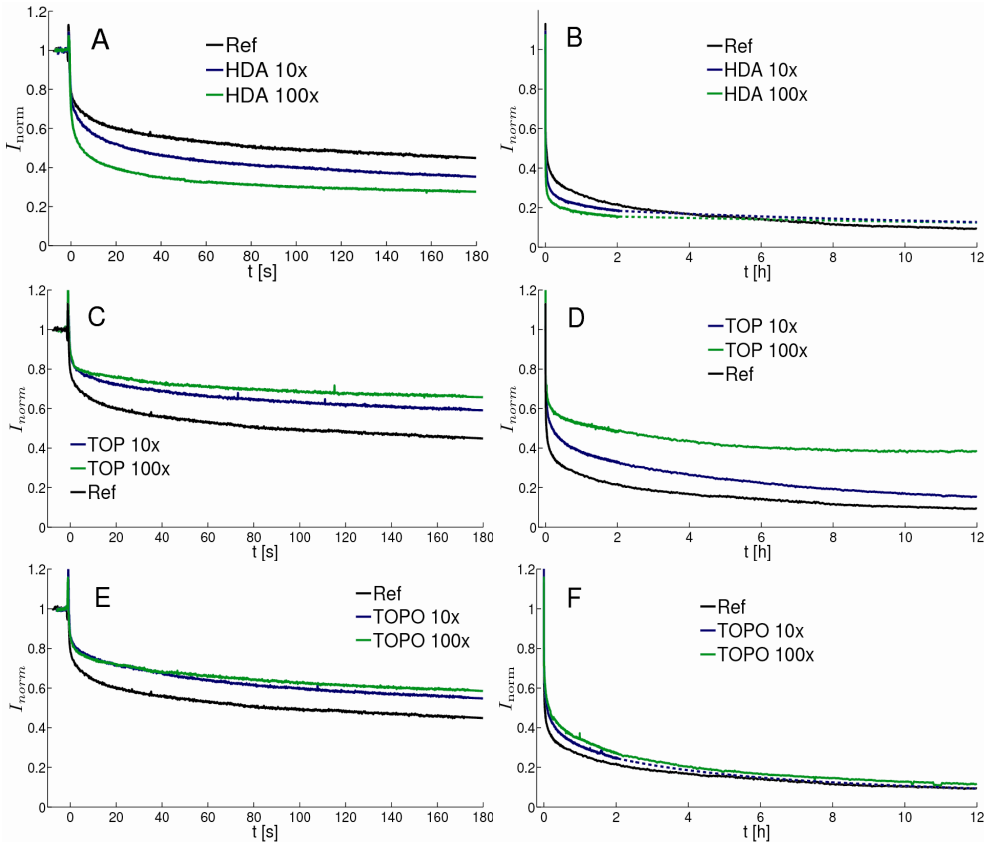

Figure 6.4. Time-dependent measurements of the emission intensity of CdSe QDs upon addition of 2000 HT/QD in all cases. The decrease in emission when a 10 or 100 fold excess of HDA (A and B), TOP (C and D), or TOPO (E and F) is compared to the standard experiment where no additional ligands were added prior to the injection of HT. Left and right panels show the evolution of the emission intensity on the short and long time scale respectively.

days prior to the thiol addition, to allow the system to equilibrate. It is stressed that the addition of excess ligands did *not* influence the initial QY of the QDs, in contrast with previous reports.[21-23] This is simply caused by the fact that in our case the QDs were not purified on forehand, maintaining the high QY of 40% which is not affected by the addition of excess native ligands. Figure 6.4 shows the decrease in emission intensity of these samples after addition of effectively 2000 HT molecules per QD, and the results are compared to the "standard" experiment where no excess ligands were added (but also addition of 2000 HT/QD). The measurements of 10 and 100 fold excess HDA and 10 fold excess TOPO was carried out for 2 hours only. For clarity, these curves are interpolated to the end-value measured after 12 hours (dotted lines).

In case an excess of amine ligands (HDA) is present in the QD dispersion, the decrease in emission intensity is significantly faster as compared to the standard experiment, especially on the short time scale (Figure 6.4A). On the long time scale, it can be seen that the final emission intensity in case of an excess of HDA is slightly higher compared to the standard experiment (Figure 6.4B). The faster decrease in emission in the case of excess HDA is counter-intuitive, because one would expect the ligand exchange by thiols to slow down in case more amines are present in the mixture. On the other hand, the slightly higher end-value of the emission intensity after 12 h is what one would expect at a higher concentration of competing ligands. When an excess of TOP is present, the decrease in emission intensity becomes significantly slower, especially in the short time regime (Figure 6.4C). Remarkably, the final emission intensity is largely influenced by the TOP ligands and up to a factor of five higher in case of a 100 fold excess (Figure 6.4D). Again, these results are somewhat surprising because TOP coordinates to Se surface sites of the quantum dot[27], and therefore should not directly influence the adsorption of thiols to QDs. Finally, the presence of additional TOPO slows down the ligand exchange with HT on the short time scale (Figure 6.4E) and results in a slightly higher end-value of the emission intensity. The effects of TOPO are smaller than the effects of HDA or TOP, but in line with an intuitive ligand exchange mechanism between TOPO and HT.

The surprising effects of HDA and TOP on the exchange rate of thiols as discussed above, in combination with the effect of TOPO, can be explained by the following qualitative model. First, TOP binds strongly to Se sites on the QD surface[27], and because of the bulky nature of this molecules (three octyl chains pointing sideways), it sterically prevents the adsorption of other ligands on neighboring surface sites. In case of a 100 fold excess of TOP, a higher coverage by TOP is expected which reduces the number of Cd-sites available for other ligands (HDA, TOPO or HT). Because of the large TOP-Se bond strength, a smaller number of HT will be coordinated to the QD surface after equilibration, explaining the higher emission end-value in case of a 10 or 100 fold TOP excess (Figure 6.4D). Next, it is clear from Figure 6.4A that amines are rapidly exchanged by thiols, which can be ascribed to the weaker bond strength of amines to Cd-sites[39] and faster kinetics due to the relatively small surface area occupied by HDA as compared to TOP or TOPO. Addition of a 100 fold excess of amines initially causes the replacement of both TOPO and TOP by HDA during the 3 days equilibration period. Considering that the exchange rates of both TOPO and TOP by HT are much slower compared to amines due to their bulky size, the higher initial surface coverage by amines in case of a 10 or 100 fold HDA excess explains

the faster decrease in emission intensity on a short time scale (Figure 6.4A). On the long time scale (in equilibrium) however, the excess of amines naturally causes a (slightly) reduced coverage of HT as compared to the standard experiment (Figure 6.4B). Returning to the case of an excess of TOP, the much slower decrease on the short time scale (Figure 6.4C) can now be explained by the removal of HDA (which would have been replaced rapidly by HT) by TOP (with much slower kinetics). As mentioned above, this removal of HDA by TOP is due to the sterical hindrance imposed by TOP ligands (bound to Se-sites) on HDA ligands that are attached to neighboring Cd-sites. A similar reasoning holds for the slower initial decrease in emission intensity in case of prior equilibration with an excess of TOPO (Figure 6.4E); it initially replaces the amines from the QD surface and is then slowly replaced by HT. However, the end-value of emission intensity after 12 hours in case of a 100 fold TOPO excess (Figure 6.4F) is much lower than that observed for an excess of TOP (Figure 6.4D). This indicates that the bond strength of TOP to the Se-sites (hindering thiol adsorption) is larger than the TOPO-Cd bond strength and competes with thiol adsorption.

Model

In order to obtain quantitative information from the kinetic experiments described in the previous section, a model for the ligand exchange is introduced in this section and shown to be able to explain the experimental observations. In our model the QD surface is assumed to be completely covered with capping molecules. This does not imply that ligands are fixed to the surface, but that the time between desorption of a ligand and adsorption of another one is much shorter than experimental time scales. Otherwise it would be impossible to accelerate the exchange of HT on a short time scale by increasing the concentration of another ligand (HDA). We therefore suggest a competition model consisting of three reactions:

$$\mathrm{HT+X*} \underset{k_X^-}{\overset{k_X^+}{\rightleftharpoons}} \mathrm{HT*+X} \qquad (6.4)$$

where X denotes a native ligand (HDA, TOP or TOPO); "*" describes the adsorbed state; and k_X^+ and k_X^- are the forward and backward substitution rates of X respectively. We do not take into account the differences between surface areas occupied by a small surface area (HT, HDA) and a bulky (TOP, TOPO) ligand, and all surface sites are assumed to be equal. We also neglect the dynamics of the exchange between native ligands during the experiment. However, the model does take in account the equilibrium between native ligands before thiol addition, and at the end of the experiment (because they are in equilibrium with HT).

Note that the exchange of HDA or TOPO follows a different path than the exchange of TOP. In the first case, a surfactant on a cadmium site is *exchanged* by another ligand with a stronger binding head group, whereas in the second case the TOP bound to selenium *leaves* the QD surface, creating space for an incoming thiol molecule to adsorb to an adjacent cadmium site.

The substitution constant is then given by $K_X = k_X^+ / k_X^-$, and large values of K_X imply a large final coverage with HT. For example, if a QD was initially coated only

by the native ligand X, then K_X would be the equilibrium constant between X and HT. It is apparent from Figure 6.4 that k^{+}_{HDA} is the largest forward rate, while K_{TOP} is the smallest substitution constant. The effective Langmuir constant in equation (6.3) can be derived from this model as (see equation (6.14) in the appendix):

$$K_{\mathrm{L}} = \frac{1}{K_{\mathrm{TOP}}^{-1} c_{\mathrm{TOP}} + K_{\mathrm{TOPO}}^{-1} c_{\mathrm{TOPO}} + K_{\mathrm{HDA}}^{-1} c_{\mathrm{HDA}}}, \tag{6.5}$$

where c_X is the concentration of the native ligand X. From the measurements in the long-time regime displayed in Figures 6.4B, 6.4D and 6.4F it becomes clear that TOP binds much stronger than TOPO or HDA. Therefore, the contribution of $K_{\mathrm{TOP}}^{-1} c_{\mathrm{TOP}}$ to the denominator of equation (6.5) is much larger than the other two. The value for K_L was determined to be 0.0018 from the equilibrium measurements in Figure 6.2B and equation (6.3). Thus, we obtain the first estimate $K_{\mathrm{TOP}} \approx K_{\mathrm{L}} c_{\mathrm{TOP}} = 2.51$ (assuming 1400 TOP molecules per QD, see experimental section).

Equation (6.2) was used to transform the normalized intensity I_{norm} into coverage $\theta_{\mathrm{HT,measured}}$. We have fitted the measured curves in Figure 6.5 to the following equation:

$$\Theta(t) = \exp(At) \cdot \Theta(0) \tag{6.6}$$

where A is a matrix containing the exchange rates and concentrations of all ligands involved, defined in equation (6.19); and $\Theta(t)$ is the vector containing the surface coverage by all ligands at a given time (t). The surface coverage $\Theta(0)$ before thiol injection ($t=0$) corresponds to the equilibrium of native ligands before HT addition, see equation (6.18). Equation (6.6) describes the collective time evolution of the surface coverage by all ligands after HT injection. Note that we can reduce the number of parameters in the model by setting the concentration of excluded components to zero. We refer to the appendix of this chapter for derivation of equation (6.6) and further details.

The fit was performed using a MATLAB script based on the deterministic derivative-free routine *fminsearch.* This routine was used to minimize the objective function:

$$F(\text{rates},\text{concentrations}) = \int_0^{t_{\max}} \left(\theta_{\mathrm{HT,model}}(t) - \theta_{\mathrm{HT,measured}}(t)\right)^2 dt \tag{6.7}$$

with respect to the rates, where $\theta_{\mathrm{HT,model}}(t)$ is the coverage computed using equation (6.6). A test for the quality of the fit is the agreement of the Langmuir constant obtained by filling in the values of the obtained substitution rates in equation (6.5), with the value for K_L obtained from Figure 6.2B and equation (6.3) (0.0018). The fitting range $t_{\max}$ is 1.5-2 hours. We did not use the full time range for

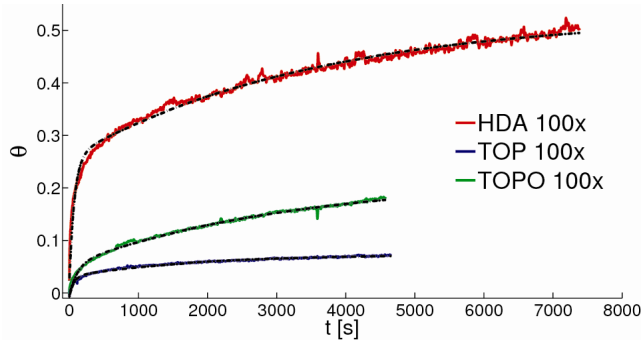

Figure 6.5. Fitting of the in situ measurements of 2000 fold HT addition to samples with 100 fold excess (compared to concentration after synthesis) of HDA, TOP and TOPO. Solid curves represent normalized intensities from Figure 6.4 transformed to coverage using equation (6.2) (α=8.7). Dashed lines represent the four-parameter fit to the model defined by equation (6.6).

two reasons: the measurements may be affected by photo-oxidation on longer time scales, and the signal-to-noise ratio becomes worse for high HT coverage due to the lower emission intensity.

The six parameters k_X^+ and k_X^- (X = TOP, TOPO or HDA) were fitted using equation (6.6) to the measured curves in three independent steps. To avoid over-fitting, we only used four parameters in each step. The equilibrium between native surfactants before thiol injection is accounted for in equations (6.5) and (6.18). During the first step, we fitted the curve with the 100-fold excess of TOP to obtain values for k_{TOP}^+ and k_{TOP}^-, while the other two rates are a combination of the exchange rates of the other ligands (TOPO, HDA) by HT. Next, we fitted the curve with the 100-fold excess of TOPO, neglecting the presence of HDA (*i.e.* by setting its concentration to 0). However, the presence of TOP was accounted for. As a result, we obtain k_{TOPO}^+ and k_{TOPO}^-; the fitted rates for TOP are in the same order as those obtained by fitting the 100-fold TOP excess curve. Similarly, we obtained the rates for HDA, assuming no TOPO present. Also in this case the rates for TOP were similar to those obtained previously. Figure 6.5 shows the surface coverage by HT as a function of time together with the individually fitted curves. As one can see, the latter nicely reproduce experimental data. The rates obtained from fitting can be found in the Table 6.1.

Table 6.1. Substitution rates and constants and substitution half-times (at 2000 HT/QD) for different native ligands obtained from fitting the corresponding measurement with 100-fold excess.

X	k_X^+ [(s·mol/l)$^{-1}$]	k_X^- [(s·mol/l)$^{-1}$]	K_X [-]	$t_{1/2}$
HDA	7.5	0.017	445	72s
TOP	0.03	0.005	5.6	5.0h
TOPO	0.06	0.001	49.3	2.5h

The values for k_X^+ support the conclusion of the previous section: the exchange of linear amines by HT is two orders of magnitude faster than the exchange of branched TOP and TOPO. To give a feeling for time scales, we provide substitution half-times $t_{1/2} = \frac{\ln(2)}{k_X^+ c_{\mathrm{HT}}}$ at the "standard" thiol concentration of 2000 HT/QD. These are the times required to replace half of the ligand X from the QD surface by HT when no further surfactants are present and the reverse reaction does not take place. We see that while the replacement of the amine goes very fast (within minutes), the replacement of branched surfactants TOP and TOPO can last hours and days. Interestingly, the half-time for amine replacement is close to the desorption half-time for octylamine (70s) as was recently determined by another group.[29]

The values for K_X support the conclusion that TOP binds stronger than HDA and TOPO, and indicate that TOPO binds stronger than HDA. This suggests that the rates for HDA might be even underestimated due to TOPO present on QDs in the experiment with 100-fold amine excess, while TOPO was neglected during fitting. An estimate $K_{HDA}>300$ (calculated as the ratio between the Langmuir constants for thiols and amines) from a previous publication[22] is in a good agreement with our value of 445. The value $K_{HDA}\approx 2$ reported by Bullen *et al.*[21] is inconsistent with our observations (Figure 6.3A,B) since for such a small value the replacement of HDA by thiols would be negligible in the 100-fold HDA excess measurement, which is not in line with the observed large drop in emission intensity.

We assessed the quality of the model and the fitting procedure by generating the curves using six parameters from Table 6.1 for the "standard" measurement where no excess ligands were present. It is important to note that these experimental data were not used for fitting, and thus provide a suitable tool to test if the parameters obtained from fitting the 100-fold excess curves can reproduce the emission decay curves under "standard" conditions (no excess of native ligands). The results are shown in Figure 6.6. The reasonable agreement between the generated and measured curves supports the model. Deviations on the short time scale indicate that the forward substitution rate of amines is indeed underestimated, as explained above.

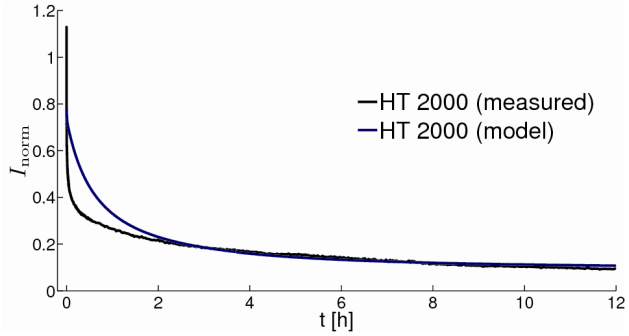

Figure 6.6. Time-dependent decrease in emission intensity upon thiol addition (2000HT/QD) measured (black) and reproduced (blue) for the experiment without excess ligands. The curve $\theta_{HT,model}(t)$ was calculated using the corresponding ligand concentrations and rates from Table 6.1, and transformed into normalized intensity using equation (6.2).

Temperature dependent measurements

To determine the activation energies for ligand adsorption and desorption, time-dependent measurements of the ligand exchange were conducted at various temperatures, by adding 2000 HT molecules per QD at T = -10°,-2°,5°,12°,21°,31°C. The results are shown in Figure 6.7. As expected, the ligand exchange is slower with decreasing temperature. The initial intensity increases with decreasing temperature from 31° to -10° by ca. 30% (not shown).

We used again equation (6.2) to calculate surface coverage θ from the intensity I_{norm}. Equation (6.1) shows that the temperature dependent term in QY(θ) is QY(0), which cancels by normalization. Each of the curves was then fitted with only four parameters to the model described in the previous section. The first rates k_X^+ and k_X^- describe the exchange of TOP ("slow" component), while the other two combine the exchange of HDA and TOPO ("fast" component). The starting parameters for the fit were created by fitting the "standard" measurement (at room temperature) on a long time scale. Because of the short time range (30 minutes) of the measurements, the long-term properties of the system must be accounted for in a different way: the term $(K_L - K_{L,measured})^2$ was added to the objective function (equation (6.7)). Here K_L is the Langmuir constant from equation (6.5), and $K_{L,measured}$ the value obtained from Figure 6.2B and equation (6.3) (0.0018).

Recall the Arrhenius equation that relates a reaction rate k and the activation energy E_{act}:

$$k = k_0 e^{-E_{act}/RT} \tag{6.8}$$

where k_0 is the kinetic pre-factor and R the universal gas constant. Similarly, the equilibrium constant K is related to the change in Gibbs free energy $\Delta G°$ by

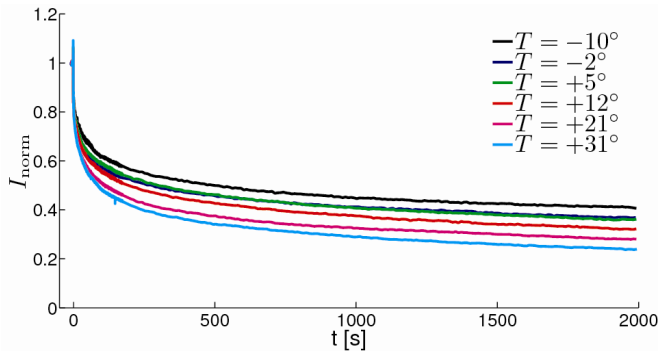

Figure 6.7. Time-dependent measurements of the emission intensity of CdSe QDs upon addition of 2000 HT/QD at different temperatures. All emission spectra were recorded for 0.1s and the normalized (by the value before injection) integrated emission intensity is plotted as a function of time.

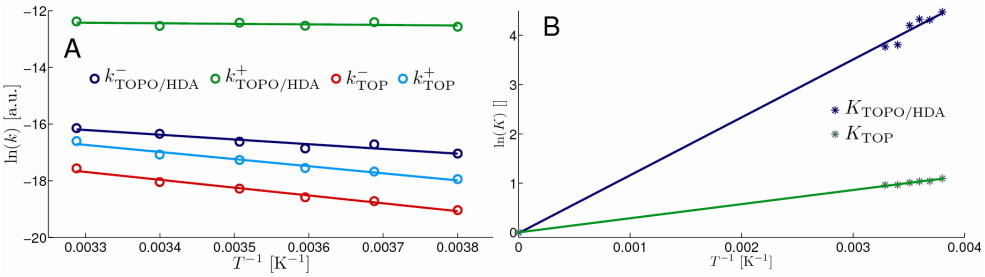

Figure 6.8. Arrhenius plots of the substitution rates (A) and substitution constants (B) from the temperature dependent measurements. The point 0 in 6B has been extrapolated. Solid lines are linear fits. Regression slopes are summarized in Table 6.2.

$$K = e^{-\Delta G^\circ / RT}. \qquad (6.9)$$

In Figure 6.8A we plot logarithms of the four rates versus inverse temperature, while Figure 6.8B shows the equilibrium constants. The excellent linear correlation of the data is another justification of our model and fitting procedure. Note that the logarithm of the measured equilibrium constants K_X extrapolates to 0 when the inverse temperature goes to 0. This is in good agreement with equation (6.9), meaning that all equilibrium constants go to 1 at infinite temperature.

The activation energies E_{act} and enthalpy changes $\Delta G°$ are summarized in Table 6.2. E^+_{act} is the activation energy for the forward reaction while E^-_{act} is the activation energy for the reverse reaction. It should be noted that all values lie in the order of thermal fluctuations at room temperature. The activation energy is low for the "fast" exchange of HDA/TOPO by HT. The activation energy for the reverse process can be interpreted as the energy required for removing a thiol from the QD surface, i.e. the dissociation energy of a single thiol. For the exchange of TOP, E_{act} is larger than the one for HDA/TOPO, which makes it to be a "slow" process. It was discussed above that TOP binds stronger than the other native ligands, which is consistent with a higher dissociation energy. As expected, the activation energy for the exchange of HT by TOP is similar to the one for HDA/TOPO, since both are dominated by the dissociation of a single HT molecule. The estimate of 14-21 kJ/mol is in the same order as the one determined for binding of thiolates in aqueous solution.[40]

Table 6.2. Gibbs free energy changes and activation energies the substitution reactions as regression slopes from Figure 6.8.

X	$\Delta G°$ [kJ/mol]	E^+_{act} [kJ/mol]	E^-_{act} [kJ/mol]
HDA/TOPO	-9.9	1.6	13.9
TOP	-2.4	20.9	23.0

6.4 Conclusions

By recording the decrease in emission intensity of CdSe QDs upon addition of thiols *in situ* with a high time resolution, we were able to follow the kinetics of the ligand exchange of the native ligands (HDA, TOP, and TOPO) by hexanethiol (HT). From the relation between the emission intensity of CdSe quantum dots and the number of alkyl thiol ligands adsorbed at their surface the surface coverage by thiols can be calculated. The quenching rate per adsorbed hexanethiol molecule was found to be 0.004 ns^{-1}. Adding an excess of HDA to the QD dispersion prior to HT addition results in faster exchange kinetics, whereas the addition of TOP or TOPO has the reverse effect. We conclude that the exchange of amines by thiols is very fast compared to TOPO. The addition of amines prior to thiol injection results in a QD-surface that is predominantly covered by amines, leading to a faster overall ligand exchange. TOP binds very strong to selenium sites and sterically prevents the attachment of thiols to cadmium sites. TOP thereby slows down the ligand exchange and causes a significant shift in the equilibrium. The conclusions are confirmed by a kinetic model that takes into account the equilibrium between ligands before thiol addition and describes the surface coverage over time. The strong affinity of the bulky TOP molecule to the QD surface may be an important factor in controlling the growth kinetics of CdSe (and related) QDs. The exchange of HDA by HT is found to be two orders of magnitude faster than for TOPO or TOP. An equilibrium constant of ~ 500 is found for amine-exchange by thiols (i.e. a highly forward reaction), whereas a 10 and 100 fold smaller value is obtained for the equilibrium constants of TOPO and TOP, respectively. Temperature dependent *in situ* measurements display slower kinetics with decreasing temperature. The data were fitted using the same model, from which the activation energies for the exchange of HDA/TOPO (1.6 kJ/mol) and TOP (20.9 kJ/mol) by thiols could be extracted. The binding energy of thiols to the QD surface can de estimated between 14 and 23 kJ/mol. The changes in Gibbs free energy are -9.9 kJ/mol and -2.4 kJ/mol for the thiol-exchange of HDA/TOPO and TOP respectively. The results provide insight in binding and kinetics of ligands at the QD surface for some of the commonly used ligands for surface passivation of CdSe and CdTe QDs. In view of the prominent role of ligands on the (opto-electronic) properties and stability of QDs, the results are important for a better understanding and control in the synthesis of QDs and for tailoring their properties by ligand exchange.

6.5 References

1. Y.W. Jun, J.W. Seo, S.J. Oh, and J. Cheon, *Coordin Chem Rev*, **2005**. *249* (17-18): p. 1766-1775.
2. Y. Yin and A.P. Alivisatos, *Nature*, **2005**. *437* (7059): p. 664-670.
3. D.V. Talapin, A.L. Rogach, A. Kornowski, M. Haase, and H. Weller, *Nano Lett.*, **2001**. *1* (4): p. 207-211.
4. C.B. Murray, D.J. Norris, and M.G. Bawendi, *J. Am. Chem. Soc.*, **1993**. *115* (19): p. 8706-15.
5. X.G. Peng, L. Manna, W.D. Yang, J. Wickham, E. Scher, A. Kadavanich, and A.P. Alivisatos, *Nature*, **2000**. *404* (6773): p. 59-61.
6. E. Lifshitz, M. Bashouti, V. Kloper, A. Kigel, M.S. Eisen, and S. Berger, *Nano Lett.*, **2003**. *3* (6): p. 857-862.
7. L. Manna, E.C. Scher, and A.P. Alivisatos, *J. Am. Chem. Soc.*, **2000**. *122* (51): p. 12700-12706.
8. K.S. Cho, D.V. Talapin, W. Gaschler, and C.B. Murray, *J. Am. Chem. Soc.*, **2005**. *127* (19): p. 7140-7147.
9. X.G. Peng, *Adv. Mater.*, **2003**. *15* (5): p. 459-463.
10. L. Manna, D.J. Milliron, A. Meisel, E.C. Scher, and A.P. Alivisatos, *Nat. Mat.*, **2003**. *2* (6): p. 382-385.
11. A.J. Houtepen, R. Koole, D.L. Vanmaekelbergh, J. Meeldijk, and S.G. Hickey, *J. Am. Chem. Soc.*, **2006**. *128* (21): p. 6792-6793.
12. W.G. Lu, J.Y. Fang, Y. Ding, and Z.L. Wang, *J. Phys. Chem. B*, **2005**. *109* (41): p. 19219-19222.
13. S.F. Wuister, I. Swart, F. van Driel, S.G. Hickey, and C. de Mello Donegá, *Nano Lett.*, **2003**. *3* (4): p. 503-507.
14. D.V. Talapin, A.L. Rogach, I. Mekis, S. Haubold, A. Kornowski, M. Haase, and H. Weller, *Colloid Surface A*, **2002**. *202* (2-3): p. 145-154.
15. X. Michalet, F.F. Pinaud, L.A. Bentolila, J.M. Tsay, S. Doose, J.J. Li, G. Sundaresan, A.M. Wu, S.S. Gambhir, and S. Weiss, *Science*, **2005**. *307* (5709): p. 538-544.
16. H. Mattoussi, J.M. Mauro, E.R. Goldman, G.P. Anderson, V.C. Sundar, F.V. Mikulec, and M.G. Bawendi, *J. Am. Chem. Soc.*, **2000**. *122* (49): p. 12142-12150.
17. W.C. Chan and S. Nie, *Science*, **1998**. *281* (5385): p. 2016-8.
18. L. Qu and X. Peng, *J. Am. Chem. Soc.*, **2002**. *124* (9): p. 2049-2055.
19. C. de Mello Donega, S.G. Hickey, S.F. Wuister, D. Vanmaekelbergh, and A. Meijerink, *J. Phys. Chem. B*, **2003**. *107* (2): p. 489-496.
20. M. Kuno, J.K. Lee, B.O. Dabbousi, F.V. Mikulec, and M.G. Bawendi, *J. Chem. Phys.*, **1997**. *106* (23): p. 9869-9882.
21. C. Bullen and P. Mulvaney, *Langmuir*, **2006**. *22* (7): p. 3007-3013.
22. A.M. Munro, I.J.L. Plante, M.S. Ng, and D.S. Ginger, *J. Phys. Chem. C*, **2007**. *111* (17): p. 6220-6227.
23. G. Kalyuzhny and R.W. Murray, *J. Phys. Chem. B*, **2005**. *109* (15): p. 7012-7021.
24. N. Gaponik, D.V. Talapin, A.L. Rogach, K. Hoppe, E.V. Shevchenko, A. Kornowski, A. Eychmuller, and H. Weller, *J. Phys. Chem. B*, **2002**. *106* (29): p. 7177-7185.
25. S.F. Wuister, C. de Mello Donegá, and A. Meijerink, *J. Phys. Chem. B*, **2004**. *108* (45): p. 17393-17397.
26. J.E.B. Katari, V.L. Colvin, and A.P. Alivisatos, *J. Phys. Chem.*, **1994**. *98* (15): p. 4109-4117.
27. L.R. Becerra, C.B. Murray, R.G. Griffin, and M.G. Bawendi, *J. Chem. Phys.*, **1994**. *100* (4): p. 3297-3300.
28. J.A. Gaunt, A.E. Knight, S.A. Windsor, and V. Chechik, *J. Colloid Interface Sci.*, **2005**. *290* (2): p. 437-443.
29. X. Ji, D. Copenhaver, C. Sichmeller, and X. Peng, *J. Am. Chem. Soc.*, **2008**. *130* (17): p. 5726-5735.

30. J. Jasieniak and P. Mulvaney, *J. Am. Chem. Soc.*, **2007**. *129* (10): p. 2841-2848.
31. P. Schapotschnikow, R. Pool, and T.J.H. Vlugt, *Comput Phys Commun*, **2007**. *177* (1-2): p. 154-157.
32. R. Pool, P. Schapotschnikow, and T.J.H. Vlugt, *J. Phys. Chem. C*, **2007**. *111* (28): p. 10201-10212.
33. W.D. Luedtke and U. Landman, *J. Phys. Chem. B*, **1998**. *102* (34): p. 6566-6572.
34. E. Rabani, *J. Chem. Phys.*, **2001**. *115* (3): p. 1493-1497.
35. B.J. Morgan and P.A. Madden, *Phys. Chem. Chem. Phys.*, **2007**. *9* (19): p. 2355-2361.
36. W.W. Yu, L.H. Qu, W.Z. Guo, and X.G. Peng, *Chem. Mater.*, **2004**. *16* (3): p. 560-560.
37. R. Koole, B. Luigjes, M. Tachiya, R. Pool, T.J.H. Vlugt, C. de Mello Donegá, A. Meijerink, and D. Vanmaekelbergh, *J. Phys. Chem. C*, **2007**. *111* (30): p. 11208-11215.
38. A.F. van Driel, G. Allan, C. Delerue, P. Lodahl, W.L. Vos, and D. Vanmaekelbergh, *Phys. Rev. Lett.*, **2005**. *95* (23): p. 236804 1-4.
39. D.K. Breitlinger, *Cadmium and Mercury*, in *Comprehensive Coordination Chemistry II*, J.A. McCleverty and T.J. Meijer, Editors. 2004, Elsevier: Amsterdam. p. 1253.
40. J. Aldana, N. Lavelle, Y.J. Wang, and X.G. Peng, *J. Am. Chem. Soc.*, **2005**. *127* (8): p. 2496-2504.

6.6 Appendix

Reference measurements

Figure 6.9 displays the time-dependent emission intensity of CdSe QDs upon dilution with pure toluene. In the short time-window (Figure 6.9A), these measurements are highly reproducible, and the decrease in emission intensity corresponds exactly to the dilution factor $0.83 = \frac{2.5\text{ml}}{2.5\text{ml} + 0.5\text{ml}}$. It can be observed in Figure 6.9A that the dilution at t = 0 is very fast, in the order of seconds, after which the emission intensity is constant. This allows for an accurate interpretation and fitting of the data in case thiols are added to the dispersion of CdSe QDs.

In the long time regime (Figure 6.9B), a very slow and gradual decrease in emission intensity is observed upon dilution with pure toluene. This is ascribed to photo-oxidation due to the continuous excitation with UV-light and slow diffusion of oxygen into the cuvette.

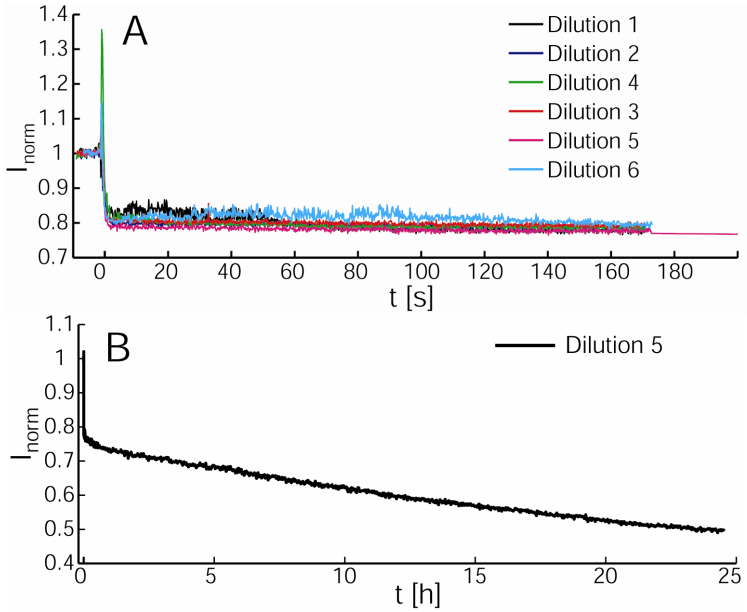

Figure 6.9. Evolution of emission intensity of CdSe QDs upon dilution with pure toluene (no HT) in the short time window, performed six times (A) and long time window, displaying only one measurement (B).

Mathematical formulation of the model

The chemical reaction described by equation (6.4) suggests the following model. The (time-dependent) relative coverage θ_X of the QD surface by the ligand X (HT,HDA,TOP or TOPO), is defined by the number of molecules of type X on a QD surface divided by the total number of binding sites, so that $0 \leq \theta_X \leq 1$. Note

that time dependence of θ_X is suppressed in our notation. The temporal change of the variables θ_X can be described by the set of differential equations:

$$\begin{aligned}\dot{\theta}_{\mathrm{HT}} = &-k^{-}_{\mathrm{HDA}} c_{\mathrm{HDA}} \theta_{\mathrm{HT}} - k^{-}_{\mathrm{TOP}} c_{\mathrm{TOP}} \theta_{\mathrm{HT}} - k^{-}_{\mathrm{TOPO}} c_{\mathrm{TOPO}} \theta_{\mathrm{HT}} \\ &+ k^{+}_{\mathrm{HDA}} c_{\mathrm{HT}} \theta_{\mathrm{HDA}} + k^{+}_{\mathrm{TOP}} c_{\mathrm{HT}} \theta_{\mathrm{TOP}} + k^{+}_{\mathrm{TOPO}} c_{\mathrm{HT}} \theta_{\mathrm{TOPO}}\end{aligned} \tag{6.10}$$

$$\dot{\theta}_{\mathrm{HDA}} = k^{-}_{\mathrm{HDA}} c_{\mathrm{HDA}} \theta_{\mathrm{HT}} - k^{+}_{\mathrm{HDA}} c_{\mathrm{HT}} \theta_{\mathrm{HDA}} \tag{6.11}$$

$$\dot{\theta}_{\mathrm{TOP}} = k^{-}_{\mathrm{TOP}} c_{\mathrm{TOP}} \theta_{\mathrm{HT}} - k^{+}_{\mathrm{TOP}} c_{\mathrm{HT}} \theta_{\mathrm{TOP}} \tag{6.12}$$

$$\dot{\theta}_{\mathrm{HDA}} = k^{-}_{\mathrm{TOPO}} c_{\mathrm{TOPO}} \theta_{\mathrm{HT}} - k^{+}_{\mathrm{TOPO}} c_{\mathrm{HT}} \theta_{\mathrm{TOPO}}\,, \tag{6.13}$$

where the dot denotes the derivative with respect to time and c_X the concentration of the ligand X. Adding the four equations together shows that the total coverage does not change during the exchange process, as suggested by equation (6.4).

The steady-state coverages $\overline{\theta}_X$ are found by setting the left hand-side of (6.10-6.13) to zero, i.e. when all θ_X do not change. In addition, we require the total coverage to be constant and equal to 1 ($\overline{\theta}_{\mathrm{HT}} + \overline{\theta}_{\mathrm{HDA}} + \overline{\theta}_{\mathrm{TOP}} + \overline{\theta}_{\mathrm{TOPO}} = 1$). Then the solution of the linear system of equations becomes:

$$\overline{\theta}_{\mathrm{HT}} = \frac{c_{\mathrm{HT}}}{c_{\mathrm{HT}} + K^{-1}_{\mathrm{HDA}} c_{\mathrm{HDA}} + K^{-1}_{\mathrm{TOP}} c_{\mathrm{TOP}} + K^{-1}_{\mathrm{TOPO}} c_{\mathrm{TOPO}}} \tag{6.14}$$

$$\overline{\theta}_{\mathrm{HDA}} = \frac{K^{-1}_{\mathrm{HDA}} c_{\mathrm{HDA}}}{c_{\mathrm{HT}} + K^{-1}_{\mathrm{HDA}} c_{\mathrm{HDA}} + K^{-1}_{\mathrm{TOP}} c_{\mathrm{TOP}} + K^{-1}_{\mathrm{TOPO}} c_{\mathrm{TOPO}}} \tag{6.15}$$

$$\overline{\theta}_{\mathrm{TOP}} = \frac{K^{-1}_{\mathrm{TOP}} c_{\mathrm{TOP}}}{c_{\mathrm{HT}} + K^{-1}_{\mathrm{HDA}} c_{\mathrm{HDA}} + K^{-1}_{\mathrm{TOP}} c_{\mathrm{TOP}} + K^{-1}_{\mathrm{TOPO}} c_{\mathrm{TOPO}}} \tag{6.16}$$

$$\overline{\theta}_{\mathrm{TOPO}} = \frac{K^{-1}_{\mathrm{TOPO}} c_{\mathrm{TOPO}}}{c_{\mathrm{HT}} + K^{-1}_{\mathrm{HDA}} c_{\mathrm{HDA}} + K^{-1}_{\mathrm{TOP}} c_{\mathrm{TOP}} + K^{-1}_{\mathrm{TOPO}} c_{\mathrm{TOPO}}} \tag{6.17}$$

with the substitution constants $K_X = k^{+}_X / k^{-}_X$. The equilibrium *before* addition of HT is found by setting c_{HT} in (equations (6.14)-(6.17)) to 0. The equilibrium between native ligands is correctly defined by the model (equations (6.10)-(6.13)) also in absence of thiols, but it does not describe how the equilibrium is reached. We define the time scale with 0 corresponding to the injection of thiols. Since all concentrations are defined as number of ligands per QD, their values do not change during the dilution. Because of the large excess of surfactants we can also

assume that the total coverage remains 1 after dilution. Therefore, the values of θ_X at t=0 coincide with the equilibrium without thiols:

$$\theta_{\mathrm{X}}(0) = \frac{K_{\mathrm{X}}^{-1} c_{\mathrm{X}}}{K_{\mathrm{HDA}}^{-1} c_{\mathrm{HDA}} + K_{\mathrm{TOP}}^{-1} c_{\mathrm{TOP}} + K_{\mathrm{TOPO}}^{-1} c_{\mathrm{TOPO}}}; \quad \theta_{\mathrm{HT}}(0) = 0 \tag{6.18}$$

After addition of HT, the equilibrium described by equations (6.14)-(6.17) changes, and the system moves towards the new equilibrium obeying the differential equations (6.10)-(6.13).

To solve the initial value problem (i.e. the set of differential equations together with an initial value) we define the vector $\Theta = (\theta_{HT}, \theta_{HDA}, \theta_{TOP}, \theta_{TOPO})$ and the matrix:

$$A = \begin{pmatrix} -k_{\mathrm{HDA}}^{-} c_{\mathrm{HDA}} - k_{\mathrm{TOP}}^{-} c_{\mathrm{TOP}} - k_{\mathrm{TOPO}}^{-} c_{\mathrm{TOPO}} & k_{\mathrm{HDA}}^{+} c_{\mathrm{HT}} & k_{\mathrm{TOP}}^{+} c_{\mathrm{HT}} & k_{\mathrm{TOPO}}^{+} c_{\mathrm{HT}} \\ k_{\mathrm{HDA}}^{-} c_{\mathrm{HDA}} & -k_{\mathrm{HDA}}^{+} c_{\mathrm{HT}} & 0 & 0 \\ k_{\mathrm{TOP}}^{-} c_{\mathrm{TOP}} & 0 & -k_{\mathrm{TOP}}^{+} c_{\mathrm{HT}} & 0 \\ k_{\mathrm{TOPO}}^{-} c_{\mathrm{TOPO}} & 0 & 0 & -k_{\mathrm{TOPO}}^{+} c_{\mathrm{HT}} \end{pmatrix} \tag{6.19}$$

Now the system (equations (6.10)-(6.13)) can be compactly written as

$$\dot{\Theta} = A \cdot \Theta \tag{6.20}$$

The solution of the initial value problem (equations (6.18) and (6.20)) is formally given by the matrix exponential:

$$\Theta(t) = \exp(At) \cdot \Theta(0) \tag{6.21}$$

We remark without going into detail that it is better not to use the vector $\Theta(t)$ in the implementation, but its deviation from the equilibrium $\Theta(t) - \overline{\Theta}$ for a better numerical accuracy and computational efficiency. This way the solution $\theta_X(t)$ is obtained as a function of the four ligand concentrations and six exchange rates. One can easily verify that if the concentration of a component X is 0, then the rates k_X^+ and k_X^- do not influence the solution of equations (6.18) and (6.20). Hence, we can effectively restrict our model to less components (e.g. HT, TOP, TOPO) by setting the concentration of the excluded component(s) (HDA) to 0.

Chapter 7

Quantum Dots with a Paramagnetic Coating as a Bimodal Molecular Imaging Probe

MRI detectable and target-specific quantum dots were developed. To that aim, quantum dots were coated with paramagnetic and pegylated lipids, which resulted in a relaxivity r_1 of nearly 2000 $mM^{-1}s^{-1}$ per quantum dot. The paramagnetic quantum dots were functionalized by covalently linking αvβ3-specific RGD peptides and the specificity was assessed and confirmed on cultured endothelial cells. The bimodal character, the high relaxivity, and the specificity of this nanoparticulate probe make it an excellent contrast agent for molecular imaging purposes.

7.1 Introduction

A rapidly growing field in experimental diagnostic radiology is molecular imaging, aiming to image biological processes *in vivo* and non invasively at the cellular and molecular level.[1] Magnetic resonance imaging (MRI) has become one of the most important imaging modalities in both clinical and research settings[2], because of its fast scan times, its capacity to produce excellent quality and high resolution images, lacking the need for radiochemicals. The MRI signal arises from the excitation of the magnetic moments of hydrogen nuclei of mainly water and lipids, placed in a strong magnetic field. MR images are known for their excellent soft tissue contrast. The most important contrast mechanisms are based on differences in the transverse (T_2) and longitudinal (T_1) relaxation times. These relaxation times can be manipulated by the use of paramagnetic contrast agents, *e.g.* Gd-DTPA, which efficiently shorten T_1, and therefore give rise to signal enhancement in T_1-weighted images.[3] The introduction of MRI as a molecular imaging modality has been hampered by its low sensitivity compared to nuclear methods like PET and SPECT.[4] With recent developments in chemistry and the synthesis of powerful, innovative[4], specific, and multimodal contrast agents, *e.g.* by introducing fluorescent properties as well[5-7], MRI is becoming increasingly important for molecular imaging.

Quantum dots have gained much interest the last few years for biological imaging purposes[8], especially because of their bright fluorescence, broad absorption band, photo-stability, and narrow and tuneable emission spectrum. The *in vivo* use requires the quantum dots to be water soluble and biocompatible.[9] Efforts have been undertaken to achieve these goals and quantum dots have successfully been used for imaging studies of live cells[9-11] and animal models[12-14], mainly in combination with 2 photon fluorescence microscopy.

Angiogenesis, the formation of new blood vessels, is a key process in many pathological processes, including cancer and atherosclerosis.[15] The identification of angiogenesis with molecular imaging methods is important for early screening and for following the effect of anti-angiogenesis therapy. As a targeting ligand for angiogenesis the RGD peptidic sequence was used. The arginine-glycine-aspartic acid (RGD) peptide sequence is present in many extracellular matrix proteins[16] and is recognized by αvβ5- and αvβ3-integrins[17], of which the latter is over expressed on the surface of angiogenic endothelial cells and tumor cells.[15, 18, 19]

This chapter reports on the synthesis of pegylated and paramagnetic quantum dots (pQDs) with high relaxivity to make them detectable by both MRI and fluorescence microscopy. Specificity for angiogenic blood vessels was introduced by conjugating the pQDs with cyclic RGD peptides. The contrast agent was characterized in terms of relaxation and optical properties, and was tested *in vitro* on cultured human umbilical vein endothelial cells (HUVEC).

7.2 Experimental Section

Materials

Trioctylphosphine (TOP, tech. Grade 90%), trioctylphosphine oxide (TOPO, 98%), selenium powder 200 mesh (99,99%), and stearic acid were purchased from Aldrich. Hexadecylamine (HDA 99 %) and cadmium acetate (>99,999%) were purchased from Aldrich and Strem, respectively. Toluene, methanol and all other solvents were anhydrous, of analytical grade and purchased from Aldrich. 1,2-Distearoyl-sn-glycero-3-phosphocholine (DSPC), 1,2-distearoyl-sn-glycero-3-phosphoethanolamine-N-[methoxy(polyethylene glycol)-2000] (PEG2000-DSPE), 1,2-distearoyl-sn-glycero-3-phosphoethanolamine-N-[maleimide(polyethylene glycol)2000] (Mal-PEG2000-DSPE) were obtained from Avanti Polar Lipids (Albaster, AL). Gd-DTPA-bis(stearylamide) (Gd-DTPA-BSA) was purchased from Gateway Chemical Technology (St. Louis, MO). HEPES was obtained from Merck (Darmstadt, Germany). The cyclic 5mer RGD (c(RGDf(-S-acetylthioacetyl)K)) was synthesized at a purity of 95% by Ansynth Service BV (Roosendaal, The Netherlands).

Synthesis of TOPO/HDA capped CdSe/ZnS core/shell QDs

The CdSe QDs were synthesized under a flow of argon with less than 1 ppm of water and oxygen. The reaction was performed in a mixture of 4 g of hexadecylamine (HDA) and 8 g of trioctylphosphine oxide (TOPO). The precursor solution consisted of cadmium acetate (0.1078 g) and elemental selenium (0.159 g) dissolved in 3 ml of trioctylphosphine, which was rapidly injected into the HDA/TOPO mixture at 280 ºC under vigorous stirring. The nanocrystal growth was stopped immediately after the injection by cooling the reaction mixture with 7 ml toluene. After further dilution with 10 ml toluene the QDs were precipitated by adding 20 ml methanol. The precipitate was separated by centrifugation. The washed QDs were dissolved in 2 ml toluene and added to a reaction mixture containing 8 g TOPO, 4g HDA, 2.09 g zinc stearate and 2.98 g stearic acid. Elemental sulphur (0.093 g) dissolved in 5ml oleylamine was added dropwise over one hour to the reaction mixture at 200 ºC. After the shell growth the reaction mixture was diluted in chloroform, followed by the addition of the same volume of methanol to precipitate the CdSe/ZnS core/shell QDs. The precipitate was centrifuged, dried under vacuum overnight and stored in a glovebox under nitrogen. The procedure that was used to apply a lipidic coating around the QDs is described in the next section.

In vitro targeting experiments

Human umbilical vein derived endothelial cells (HUVEC) were cultured in gelatin (0.2 % in PBS) coated tissue culture flasks (Costar, Cambridge, MA) in culture medium, RPMI-1640 (Life Technologies, Breda, The Netherlands), containing 20 % human serum (HS; University Hospital Maastricht, The Netherlands), 2 mM glutamine (Life Technologies), 100 U/ml penicillin and 0.1 mg/ml streptomycin (ICN Biomedicals, Aurora, OH). For all experiments cells of passage 2-3 were used. Next, ~1.5 x 10^6 HUVEC were incubated with either RGD-pQDs, pQDs, or without contrast agent for 2 hours at 37 ºC. After the incubation the cells were washed, and either used for fluorescence microscopy or put in small

Eppendorf-cups and fixed with 40 μl of 4 % paraformaldehyde solution. MR imaging was performed on preparations of 1.5 x 10^6 packed cells.

MRI experiments

Cell pellets were measured with MRI in a 6.3 T horizontal 9.5 cm bore magnet. A 3 cm send and receive birdcage coil was used. T_1- and T_2-weighted imaging was performed on cell pellets that were placed in a home build sample holder, capable of containing four cups. For absolute quantification of the T_1 and T_2 relaxation times an MRI inversion recovery experiment and a multi-echo experiment were performed, respectively. From these data the T_1 and T_2 relaxation times of the different cell pellets were calculated. From the images, a T_1-map or a T_2-map was calculated using Mathematica (Wolfram Research, Inc.). T_1 and T_2 of the different cell pellets were determined in regions-of-interest and averaged for the independent experiments (n=2). Since the concentration of a paramagnetic agent is proportional with the relaxation rate R_1 ($1/T_1$) and R_2 ($1/T_2$) these values of these parameters were calculated for the different cell pellets.

7.3 Results and discussion

High-quality CdSe/ZnS core/shell QDs were synthesized as described in the experimental section, following methods reported in the literature[20]. A micellular and paramagnetic coating was applied to the QDs in order to make them MR detectable, water soluble, and biocompatible.[9, 21] This micellular coating was comprised of a pegylated phospholipid (PEG-DSPE) and a paramagnetic lipid (Gd-DTPA-BSA). PEG-lipids are commonly used to stabilize liposomes for pharmaceutical applications, since the PEG chains form a hydrophilic coating at the liposomal surface. *In vivo* this results in enhanced circulation half lives, because pegylated liposomes are protected from interactions with plasma proteins and are less rapidly cleared by the liver.[22] Incorporation of a large quantity of PEG-lipids in a lipid mixture leads to the formation of micelles[23], required for obtaining a monolayer lipid coating around the hydrophobic QDs. The method used in this study has been described previously[9], but we further extended it by incorporating magnetically labelled lipids, for the simultaneous detection with magnetic resonance imaging of these water soluble QDs. A schematic representation of this procedure is given in Figure 7.1. First, the lipids were dissolved in chloroform/methanol (20/1) in a 1/1 ratio. For functionalization of the QDs with a target-specific group, 10% of PEG lipids terminated by a maleimide group (Mal-PEG-DSPE) was added as well (see also Figure 7.4). The lipid mixture was added to the purified QDs in chloroform and the solvents were evaporated gently until a dry film of lipids and QDs was obtained. Thereafter, the lipid film was heated to 70° C, and hydrated with a HEPES buffer (pH 6.7) of the same temperature. This suspension was heated and vigorously stirred until a clear suspension was obtained (Figure 7.2A). Empty micelles were separated from the micelles containing QDs (pQDs) by ultracentrifugation for 1 hour at 500000 g. The supernatant with empty micelles was discarded and the pellet was suspended in HEPES buffer. The luminescence of the resulting suspension was verified by excitation with 365 nm UV light (Figure 7.2B). The absorption and emission spectra of the pQDs, depicted in Figure 7.2C, are comparable to the spectra of the original QDs in chloroform, before applying the lipid coating.

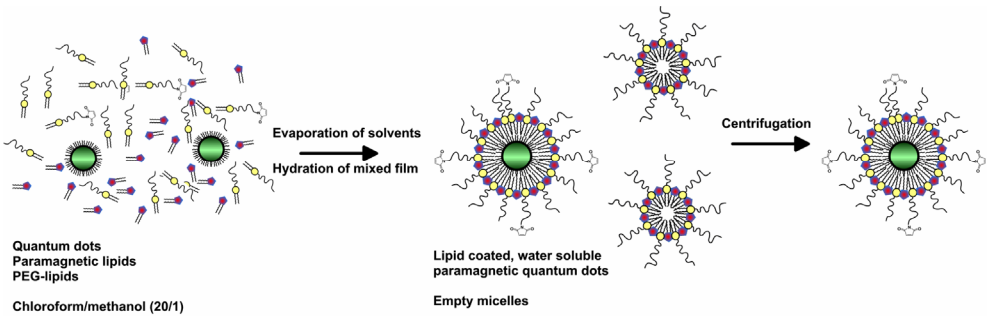

Figure 7.1. Schematic representation of the preparation of QDs with a paramagnetic micellular coating. Lipids with a red dot represent the paramagnetic lipids, and lipids with yellow dots represent the pegylated lipids, some of which have a maleimide group attached.

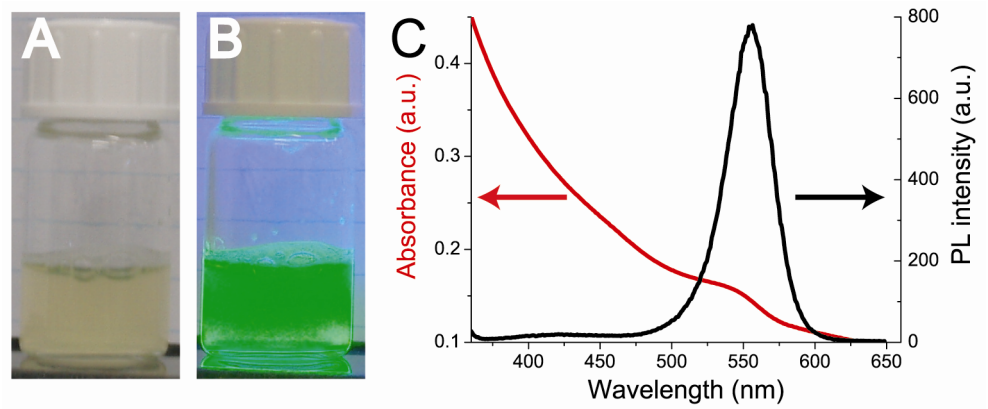

Figure 7.2. Optical properties of pQDs in HEPES buffer. (A) Under weak day light illumination; (B) photoluminescence under 365 nm excitation; (C) UV-Vis absorption (red) and PL (black) spectra.

The relaxivities r_1 and r_2, the potency to shorten the T_1 and T_2 relaxation time of water (and thus the potency to generate contrast in MRI), of an MRI contrast agent can be determined from the following equation:

$$\frac{1}{T_{1,2,obs}} = \frac{1}{T_{1,2,dia}} + r_{1,2} \cdot [\mathrm{CA}]$$

which shows that the inverse of the relaxation time T_1 and T_2 (*i.e.* $1/T_1$ and $1/T_2$) depends linearly on the contrast agent concentration [CA] and that r_1 and r_2 can be obtained by determining the slope of a plot of [CA] versus $1/T_{1,2}$. $1/T_{1,2,\mathrm{dia}}$ represents the inverse of the intrinsic T_1 or T_2, without contrast agent. Such plots, measured on a 60 MHz NMR spectrometer (Mini Spec, Bruker) are presented in Figure 7.3. For comparison nonparamagnetic quantum dots (npQDs), *i.e.* QDs without Gd-DTPA-BSA in the micellular coating, were prepared in parallel. Since

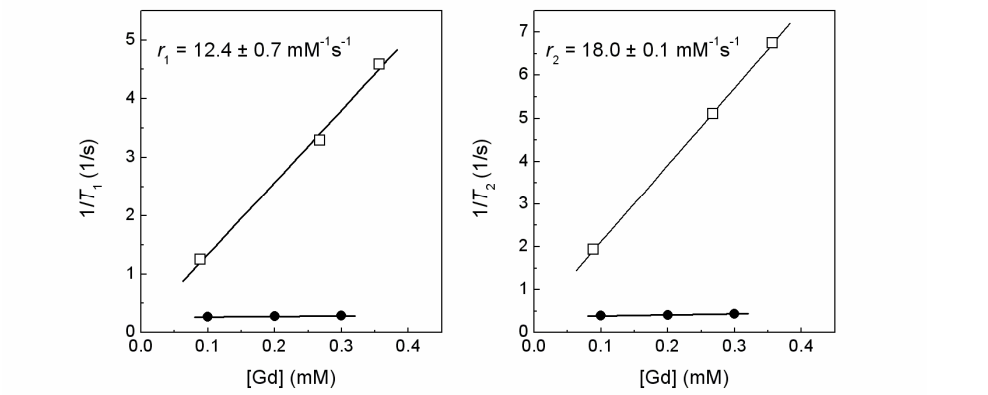

Figure 7.3. The longitudinal (left) and transverse (right) relaxivity of lipid coated quantum dots with (squares) and without (circles) paramagnetic lipids in the micellular coating.

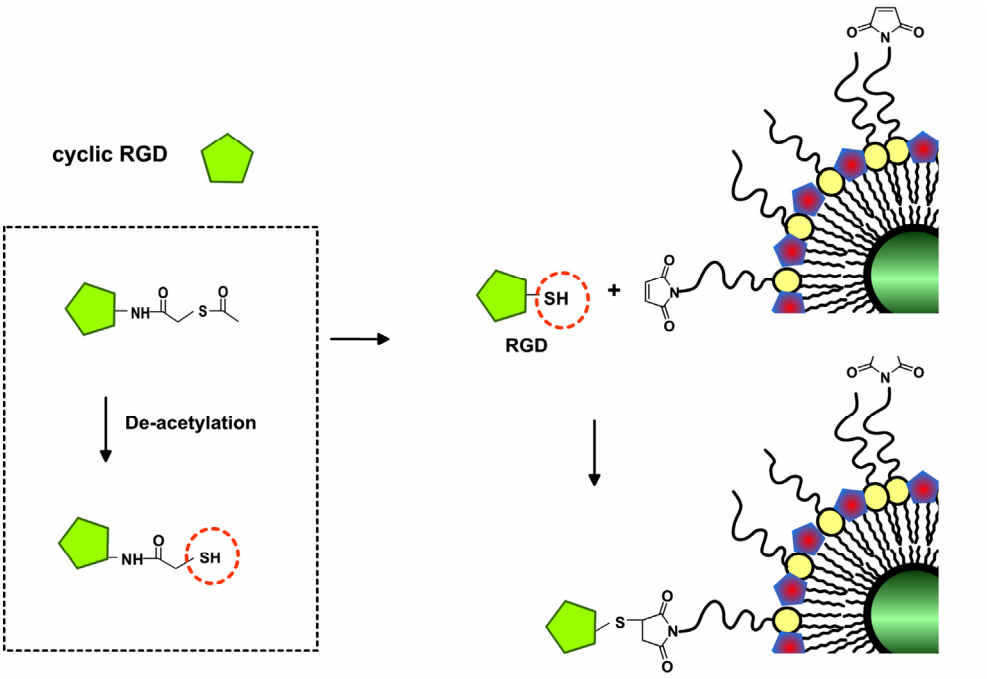

Figure 7.4. Schematic representation of coupling RGD to maleimide incorporated in the micellular coating after activation of the peptide.

the npQDs did not contain Gd, both Gd and Cd were determined with ICP, to make a direct comparison of the pQDs and the npQDs possible. The value for the ionic r_1 of the pQDs at this clinically relevant field strength was more than 12 $mM^{-1}s^{-1}$, which is 3 times higher than that of free Gd-DTPA in solution.[3] The ionic r_2 value was 18 $mM^{-1}s^{-1}$, and the r_2/r_1 ratio of ~ 1.5 indicates that the pQDs are well suited as T_1 contrast agent. As expected, there was hardly any effect on the relaxation rates for the npQDs with increasing concentration. Since the pQDs contain approximately 300 lipids, half of which is Gd-DTPA-BSA, the relaxivity per pQD was estimated to be circa 2000 $mM^{-1}s^{-1}$. This high relaxivity makes the pQD contrast agent an attractive candidate for molecular MRI purposes.

Next, the pQDs were conjugated to cyclic RGD to make them specific for activated and angiogenic vascular endothelium. Angiogenesis, the formation of new blood vessels, is a key process in many pathological processes, including cancer and atherosclerosis.[15] The identification of angiogenesis with molecular imaging methods is important for early screening and for following the effect of anti-angiogenesis therapy. The conformation of the peptide sequence used in this study has been optimized for the αvβ3-integrin previously.[24] It was shown that a cyclic conformation has favorable binding properties for this integrin as compared to *e.g.* the αvβ5-integrin.[25] The cyclic 5mer RGD was synthesized with a thioacetyl group at the lysine residue for coupling. After deacetylation of the peptide the thiol group was used to form a thioether bond between maleimide functionalized PEG-lipids, present in the micellular coat of the QDs, and cRGD (Figure 7.4).

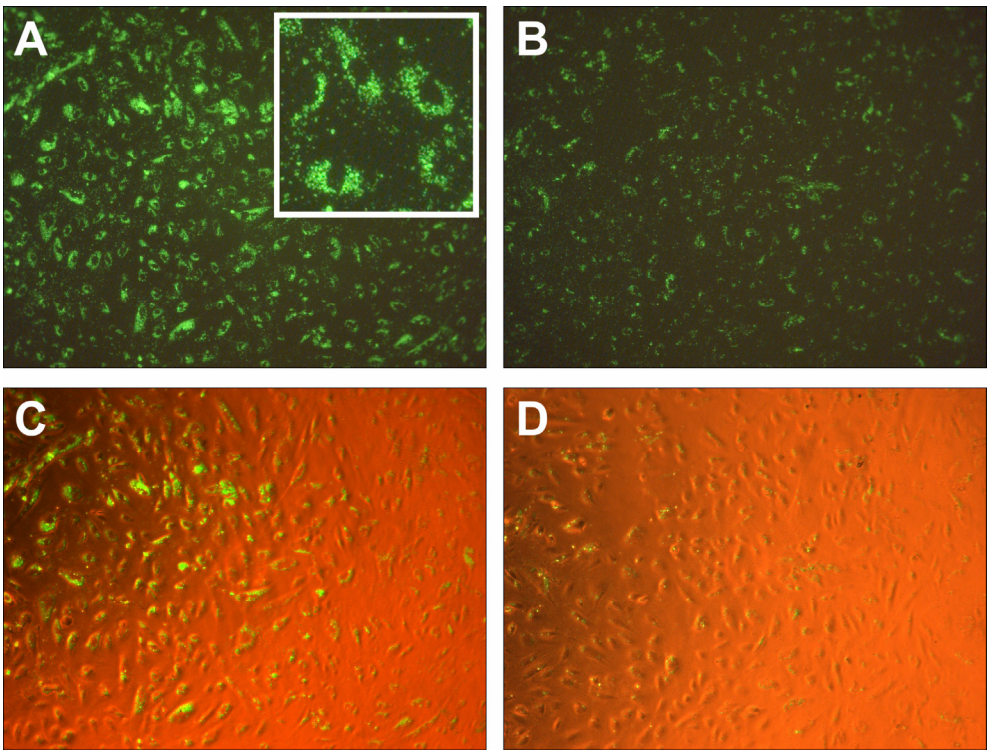

Figure 7.5. Fluorescence microscopy of HUVEC incubated with (A) RGD-pQDs and (B) bare pQDs. The corresponding phase contrast images of (A) and (B) are depicted in (C) and (D), respectively.

Human Umbilical Vein Endothelial Cells (HUVEC) were used as an *in vitro* test system to assess the biological specificity of the RGD conjugated pQDs. Proliferating HUVEC express cell surface receptors, including the αvβ3-integrin, which are also expressed at angiogenic blood vessels. Therefore RGD conjugates target to HUVEC as well and inhibit the proliferation of the cells.[26] To assess specificity of the contrast agent HUVEC were incubated with the αvβ3 targeted pQDs (RGD-pQDs) at 37° C for two hours. As a control pQDs that were not conjugated with RGD were used. After the incubations cells were washed twice. In Figure 7.5A a fluorescence microscopy image of HUVEC that had been incubated with green emitting RGD-pQDs is depicted. The RGD-pQDs were clearly associated with the cells and were found internalized, at a perinuclear location (inset). Fluorescence images of HUVEC incubated with bare pQDs showed much less green fluorescence (Figure 7.5B). This can be explained by a nonspecific cellular uptake of the pQDs, also observed when HUVEC are incubated with liposomes.[5] Both microscopy scans were made with the same settings for laser power and photomultiplier sensitivity, allowing direct comparison between different incubations. For clarity the corresponding phase contrast images, which were simultaneously excited with a laser, are depicted in Figure 7.5C and D. The cell density for both incubations is comparable and therefore the difference in fluorescence intensity arose from the difference in the level of association of pQDs.

These results demonstrate that RGD conjugated pQDs were actively taken up by the cells.

Lastly, ~1.5 x 10^6 HUVEC were incubated with either RGD-pQDs, pQDs, or without contrast agent for 2 hours at 37° C. After the incubation the cells were washed, put in small Eppendorf-cups, and fixed with 40 µl of 4 % paraformaldehyde solution. A T_1-weighted image, in which cells with a high content of Gd appear brighter than cells with a low content of Gd or no Gd, was made of cell pellets of the three incubations (Figure 7.6, left). The MR image of a cell pellet that was incubated with RGD-pQDs was much brighter than those that were incubated with pQDs and that were not incubated with contrast agent. Furthermore the T_1 and T_2 relaxation times of the different cell pellets were determined (Figure 7.6, right). The T_1 of the pellet of HUVEC incubated with RGD-pQDs was 1123 ± 33 ms, while the cells incubated with pQDs had a T_1 of 1673 ± 26 ms. Cells that were not incubated with liposomes had a T_1 of 1966 ± 19 ms. The same trend was found for T_2 relaxation times (Figure 7.6, right). These data show that the level of association of RGD-pQDs sufficed to be detected by MRI.

Molecular imaging mainly relies on the development of potent, innovative, and specific contrast agents.[4] Intravital microscopy, *e.g.* two-photon laser scanning microscopy, is capable of visualizing multiple species at the subcellular level, but with a relatively low penetration depth and a small scanning window. QDs, in combination with intravital microscopy, have shown potential *in vivo.*[8, 12-14] MRI is a non invasive *in vivo* imaging modality capable of visualizing opaque, intact tissue at resolutions down to 50 µm^2. Recent developments have led to more potent and more specific MRI contrast agents. This makes both imaging modalities highly complementary and therefore the development of a bimodal contrast agents, based on QDs, which can be detected with both MRI and fluorescence microscopy, may greatly enhance the opportunities of molecular imaging. Furthermore, QDs have been shown to be useful in guided surgery[27], and recently the combination of an optical and MR detectable probe has been proposed to be useful in this field.[28]

The RGD peptide has been proven useful in drug and gene targeting *in vivo*[29, 30], and in the field of molecular imaging. Conjugates of RGD have been used for the identification of angiogenesis with PET[25], while paramagnetic perfluorcarbon nanoparticles carrying RGD mimetics[31] and paramagnetic bimodal liposomes[5]

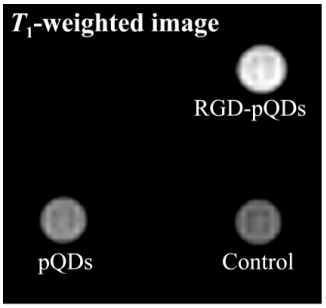

HUVEC incubated with (n=2)	T_1 (ms)	T_2 (ms)
RGD-pQDs	1123 ± 33	24.3 ± 0.3
pQDs	1673 ± 26	60.1 ± 0.6
-	1966 ± 19	87.3 ± 0.8

Figure 7.6. T_1-weighted image of cells that were incubated with RGD-pQDs, pQDS, or without contrast agent (left). The T_1 and T_2 relaxation times of the different cell pellets (n=2) are depicted right.

conjugated to cyclic RGD peptides[6] have shown their potential for the *in vivo* detection of the αvβ3-integrins with MRI. Furthermore, this approach might be useful to evaluate the effect of anti-angiogenesis therapy. Next to the targeting ligand used in this study, other ligands can also be conjugated to the pQDs for multimodality imaging of other markers of angiogenesis, but also for imaging processes like inflammation[5], atherosclerosis[32], and apoptosis[33]. The pQDs without targeting-ligand may be used to study vascular permeability with both MRI and fluorescence microscopy.[12, 13, 34]

7.4 Conclusions

In conclusion, we have shown the synthesis of quantum dots with a water soluble and paramagnetic micellular coating as a molecular imaging probe for both fluorescence microscopy and MRI. The quantum dots preserve their optical properties and have a very high relaxivity. Targeting ligands can be coupled to these pQDs via maleimide or other functional groups. In this study the paramagnetic quantum dots were functionalized by conjugating them with cyclic RGD peptides and were successfully targeted to human endothelial cells *in vitro*. We infer that this nanoparticulate bimodal contrast agent may be of great use for the detection of (tumor) angiogenesis.

7.5 References

1. R. Weissleder and U. Mahmood, *Radiology*, **2001**. *219* (2): p. 316-333.
2. P. Caravan, J.J. Ellison, T.J. McMurry, and R.B. Lauffer, *Chem. Rev.*, **1999**. *99* (9): p. 2293-2352.
3. S. Aime, M. Botta, M. Fasano, and E. Terreno, *Chem. Soc. Rev.*, **1998**. *27* (1): p. 19-29.
4. S. Aime, W. Dastru, S.G. Crich, E. Gianolio, and V. Mainero, *Biopolymers*, **2002**. *66* (6): p. 419-428.
5. W.J. Mulder, G.J. Strijkers, A.W. Griffioen, L. van Bloois, G. Molema, G. Storm, G.A. Koning, and K. Nicolay, *Bioconjug. Chem.*, **2004**. *15* (4): p. 799-806.
6. W.J. Mulder, G.J. Strijkers, J.W. Habets, E.J. Bleeker, D.W. van der Schaft, G. Storm, G.A. Koning, A.W. Griffioen, and K. Nicolay, *Faseb J.*, **2005**. *19* (14): p. 2008-10.
7. M.M. Huber, A.B. Staubli, K. Kustedjo, M.H.B. Gray, J. Shih, S.E. Fraser, R.E. Jacobs, and T.J. Meade, *Bioconjug. Chem.*, **1998**. *9* (2): p. 242-249.
8. X. Michalet, F.F. Pinaud, L.A. Bentolila, J.M. Tsay, S. Doose, J.J. Li, G. Sundaresan, A.M. Wu, S.S. Gambhir, and S. Weiss, *Science*, **2005**. *307* (5709): p. 538-544.
9. B. Dubertret, P. Skourides, D.J. Norris, V. Noireaux, A.H. Brivanlou, and A. Libchaber, *Science*, **2002**. *298* (5599): p. 1759-1762.
10. J.K. Jaiswal, H. Mattoussi, J.M. Mauro, and S.M. Simon, *Nat. Biotechnol.*, **2003**. *21* (1): p. 47-51.
11. X.Y. Wu, H.J. Liu, J.Q. Liu, K.N. Haley, J.A. Treadway, J.P. Larson, N.F. Ge, F. Peale, and M.P. Bruchez, *Nat. Biotechnol.*, **2003**. *21* (4): p. 452-452.
12. M. Stroh, J.P. Zimmer, D.G. Duda, T.S. Levchenko, K.S. Cohen, E.B. Brown, D.T. Scadden, V.P. Torchilin, M.G. Bawendi, D. Fukumura*, et al.*, *Nat. Med.*, **2005**. *11* (6): p. 678-682.
13. X.H. Gao, Y.Y. Cui, R.M. Levenson, L.W.K. Chung, and S.M. Nie, *Nat. Biotechnol.*, **2004**. *22* (8): p. 969-976.
14. D.R. Larson, W.R. Zipfel, R.M. Williams, S.W. Clark, M.P. Bruchez, F.W. Wise, and W.W. Webb, *Science*, **2003**. *300* (5624): p. 1434-1436.
15. A.W. Griffioen and G. Molema, *Pharmacol. Rev.*, **2000**. *52* (2): p. 237-268.
16. E. Ruoslahti and M.D. Pierschbacher, *Cell*, **1986**. *44*: p. 517-518.
17. V. Pedchenko, R. Zent, and B.G. Hudson, *J. Biol. Chem.*, **2004**. *279* (4): p. 2772-2780.
18. R. Pasqualini, E. Koivunen, and E. Ruoslahti, *Nat. Biotechnol.*, **1997**. *15* (6): p. 542-546.
19. S. Zitzmann, V. Ehemann, and M. Schwab, *Cancer. Res.*, **2002**. *62* (18): p. 5139-5143.
20. C. de Mello Donega, S.G. Hickey, S.F. Wuister, D. Vanmaekelbergh, and A. Meijerink, *J. Phys. Chem. B*, **2003**. *107* (2): p. 489-496.
21. H.Y. Fan, E.W. Leve, C. Scullin, J. Gabaldon, D. Tallant, S. Bunge, T. Boyle, M.C. Wilson, and C.J. Brinker, *Nano Lett.*, **2005**. *5* (4): p. 645-648.
22. V.P. Torchilin, *Nat. Rev. Drug. Discov.*, **2005**. *4* (2): p. 145-60.
23. M. Johnsson and K. Edwards, *Biophys. J.*, **2003**. *85* (6): p. 3839-3847.
24. R. Haubner, R. Gratias, B. Diefenbach, S.L. Goodman, A. Jonczyk, and H. Kessler, *J. Am. Chem. Soc.*, **1996**. *118* (32): p. 7461-7472.
25. R. Haubner, H.J. Wester, W.A. Weber, C. Mang, S.I. Ziegler, S.L. Goodman, R. Senekowitsch-Schmidtke, H. Kessler, and M. Schwaiger, *Cancer. Res.*, **2001**. *61* (5): p. 1781-1785.
26. R.J. Kok, A.J. Schraa, E.J. Bos, H.E. Moorlag, S.A. Asgeirsdottir, M. Everts, D.K.F. Meijer, and G. Molema, *Bioconjug. Chem.*, **2002**. *13* (1): p. 128-135.
27. S. Kim, Y.T. Lim, E.G. Soltesz, A.M. De Grand, J. Lee, A. Nakayama, J.A. Parker, T. Mihaljevic, R.G. Laurence, D.M. Dor*, et al.*, *Nat. Biotechnol.*, **2004**. *22* (1): p. 93-97.
28. O. Veiseh, C. Sun, J. Gunn, N. Kohler, P. Gabikian, D. Lee, N. Bhattarai, R. Ellenbogen, R. Sze, A. Hallahan*, et al.*, *Nano Lett.*, **2005**. *5* (6): p. 1003-1008.
29. R.M. Schiffelers, A. Ansari, J. Xu, Q. Zhou, Q.Q. Tang, G. Storm, G. Molema, P.Y. Lu, P.V. Scaria, and M.C. Woodle, *Nucleic Acids Res.*, **2004**. *32* (19): p. 149.

30. R.M. Schiffelers, G.A. Koning, T.L.M. ten Hagen, M.H.A.M. Fens, A.J. Schraa, A.N.P.C.A. Janssen, R.J. Kok, G. Molema, and G. Storm, *J. Control Release*, **2003**. *91* (1-2): p. 115-122.
31. P.M. Winter, S.D. Caruthers, A. Kassner, T.D. Harris, L.K. Chinen, J.S. Allen, E.K. Lacy, H.Y. Zhang, J.D. Robertson, S.A. Wickline*, et al.*, *Cancer. Res.*, **2003**. *63* (18): p. 5838-5843.
32. K.A. Kelly, J.R. Allport, A. Tsourkas, V.R. Shinde-Patil, L. Josephson, and R. Weissleder, *Circ. Res.*, **2005**. *96* (3): p. 327-336.
33. G.A.F. van Tilborg, W.J.M. Mulder, P.T.K. Chin, G. Storm, C.P. Reutelingsperger, K. Nicolay, and G.J. Strijkers, *Bioconjug. Chem.*, **2006**. *17* (4): p. 865-868.
34. H. Dafni, A. Gilead, N. Nevo, R. Eilam, A. Harmelin, and M. Neeman, *Magn. Reson. Med.*, **2003**. *50* (5): p. 904-914.

Chapter 8

On the Incorporation Mechanism of Hydrophobic Quantum Dots in Silica Spheres by a Reverse Microemulsion Method

In this chapter, strong experimental evidence is presented in favor of a proposed incorporation mechanism of hydrophobic semiconductor nanocrystals (or quantum dots, QDs) in monodisperse silica spheres (diameter ~ 35 nm) by a water-in-oil (W/O) reverse microemulsion synthesis. Fluorescence spectroscopy is used to investigate the rapid ligand exchange that takes place at the QD-surface upon addition of the various synthesis reactants. It is found that hydrolyzed TEOS has a high affinity for the QD surface and replaces the hydrophobic amine-ligands, which enables the transfer of the QDs to the hydrophilic interior of the micelles where silica growth takes place. By hindering the ligand exchange using stronger binding thiol-ligands, the position of the incorporated QDs can be controlled from centred to off-centre, and eventually to the surface of the silica spheres. The proposed incorporation mechanism explains how we can have high control over the incorporation of single QDs exactly in the middle of silica spheres. It is likely that the proposed mechanism also applies to the incorporation of other hydrophobic nanocrystals in silica using the same method. In conjunction with our findings, we were able to make QD/silica particles with an unprecedented quantum efficiency of 35%.

8.1 Introduction

In the past decade, the incorporation of metal[1, 2], semiconductor[3, 4] or insulating[5, 6] nanoparticles into silica spheres has been studied extensively.[7, 8] Silica coated nanocrystals have several advantages over their bare counterparts, especially regarding their end-use in applications. In the first place, silica may provide both chemical and physical shielding from the direct environment, thereby improving the stability. For example, it can prevent aggregation of the nanocrystals, reduce the release of (cytotoxic) ions, or prevent photo-oxidation in the case of quantum dots (QDs).[9-12] Furthermore, the surface chemistry of colloidal silica is well developed and therefore facilitates the solubilization in water or other hydrophilic solvents, enhances the bio-applicability, and allows modifications of the composite particles for further use.[3, 13-18] At present, the main application of silica coated nanoparticles (< 50 nm) is their use as biomarkers, where the reduced cytotoxicity, size tuneability, and enhanced surface control are the most important features. In addition, silica spheres can contain multiple and different nanocrystals per particle (e.g. gold, magnetite, QDs), which is an ideal starting point for a multi-modality contrast agent.[19-21] However, silica coated nanoparticles may also be used for (opto-) electronic devices, as building blocks for photonic crystals, or fundamental single-particle research. In these cases, the robustness, (photo) chemical stability, and high control over the particle size are the most important advantages. For example, silica-coated QDs could be a very suitable starting point for the integration in fluorescent solar concentrators.

The incorporation of QDs in silica spheres has been accomplished using two different methods. The first method is an adapted “Stöber” approach[22], where QDs act as seeds for silica growth in an ethanol/water mixture. Typically, the hydrophobically coated QDs have to undergo a ligand exchange to render the QDs hydrophilic, for which MPS (3-mercaptopropyl-trimethoxysilane) is frequently used.[3, 4, 23] This method yields single or multiple QDs per silica sphere, but the size and size dispersion of the QD/silica particles are not well controlled. The second method uses a water-in-oil (W/O) reverse microemulsion system, where small water droplets are stabilized by a non-ionic surfactant (e.g. NP-5, see Figure 8.1 for an overview of some of the molecules discussed in this article) in a hydrophobic continuous phase (e.g. cyclohexane).[24] Hydrolysis and condensation of the silica precursor (e.g. TEOS) takes place at the W/O interface or in the water phase, resulting in highly monodisperse silica particles even at small sizes (>25 nm). This system was previously used for the *in-situ synthesis* of CdS QDs in silica spheres.[25] Recently, the microemulsion system was also used to *incorporate* both hydrophilic CdTe QDs [12, 26] and hydrophobic CdSe/ZnS [9, 27] or PbSe [28, 29] QDs in silica particles. In comparison with the “Stöber” approach, this method is clearly advantageous because it is less complicated (e.g. no prior ligand exchange is required) and the control over particle size and size dispersion is higher.[27] Hydrophilic CdTe QDs coated with TGA (thioglycolic acid) or MPA (mercaptopropionic acid) are expected to transfer easily into the small water droplets, where silica growth takes place. The silica growth mechanism for this system was studied in detail, and colloidal stability resulting from the repulsion between the negatively charged QDs explained why only one QD per silica sphere was observed.[12, 26] For the hydrophobically coated CdSe or PbSe QDs, the subject of this paper, it is puzzling how the hydrophobic particles end up in the

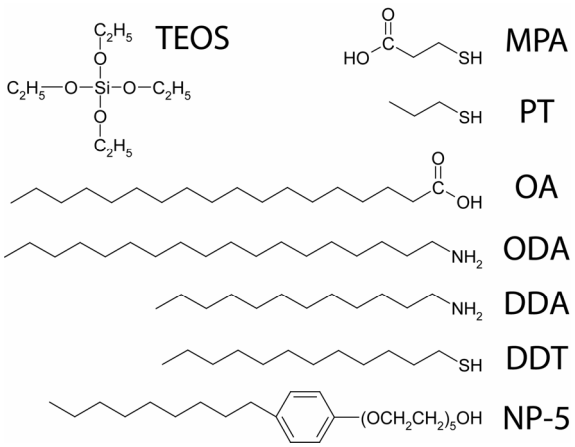

Figure 8.1. Structural formulas of some of the molecules discussed throughout the article.

water phase of the microemulsion, and are incorporated exactly in the middle of highly monodisperse hydrophilic silica spheres (see Figure 8.2). Selvan *et al.* have suggested a ligand exchange of the hydrophobic capping molecules (trioctylphosphine oxide, hexadecylamine, oleic acid) by the non-ionic surfactant (NP-5), resulting in a transfer of the QDs to the water phase, but provide no direct evidence for this mechanism.[9] Nann and co-workers have suggested two possible mechanisms for the transfer of hydrophobic QDs to the aqueous phase.[27] The first mechanism assumes an "inverse" bilayer of the surfactants (e.g. NP-5) around the hydrophobic ligands of the QDs, where the silica growth occurs within the bilayer. The second mechanism assumes a ligand exchange, but in this case the hydrophobic ligands (TOPO or oleic acid) are exchanged by TEOS molecules. From their results, no conclusions could be obtained on which of the mechanisms is operative.

It is the aim of this work to elucidate the incorporation mechanism of hydrophobic QDs in silica spheres using the mentioned reverse microemulsion system. Three different types of QDs (CdSe, CdTe and PbSe) are used to study how the silica shell grows around the QD. The unique advantage of QDs over iron oxide or metal nanoparticles is that changes at the nanocrystal surface frequently affect the optical properties of the QDs. We have therefore used steady state and time-resolved fluorescence spectroscopy to probe the interaction of the QDs with the precursors in the reaction mixture at different stages of the silica synthesis. A ligand exchange mechanism is found to be responsible for the transfer of the hydrophobic QDs into the aqueous phase. Based on these results, we were able to control the position of the QD from centred to off-centre, and eventually to the surface of the silica sphere. Furthermore, we found that the ligand exchange is also responsible for the luminescence quenching that is generally observed when QDs are incorporated in silica. In connection with these findings we were able to obtain a quantum efficiency (QE) of 35% for silica coated QDs which, to the best of our knowledge, is the highest value reported in literature. It is likely that the incorporation mechanism proposed here also applies to the silica coating of hydrophobically coated iron oxide[30] or metal[31] nanoparticles by the reverse

micelle method, for which the mechanism has not been resolved yet. In addition, the new insights will facilitate the incorporation of other hydrophobic nanocrystals in silica spheres. Understanding the incorporation mechanism of nanocrystals in silica by this reverse microemulsion method is crucial for further research that has the aim to improve the quality (QE, stability) or control over the final composite particles, or to synthesize even more complex architectures based on nanocrystals and silica chemistry.

8.2 Experimental Section

Acetone (p.a.), chloroform (p.a.), ammonia (25 wt% in water, p.a.), cadmium oxide (>99%) and zinc oxide (> 99%) were purchased from Merck. Tetraethyl orthosilicate (TEOS, 99%) was obtained from Johnson Matthey GMBH Alfa Products. Toluene (anhydrous, 99.8%), methanol (anhydrous, 99.8%), cyclohexane (≥ 99%) poly(5)oxyethylene-4-nonylphenyl-ether (NP-5), oleic acid (OA, 90%), dodecylamine (DDA, 98%), octadecylamine (ODA, 97%), propanethiol (PT, 99%), dodecanethiol (DDT, > 98%), octadecanol (ODO, 99%), mercaptopropionic acid (MPA, > 99%), ultra pure TEOS (99.999%), butanol (anhydrous, 99.8%), and octadecene (ODE, 90%) were purchased from Aldrich. Sulphur powder (99.999%) was obtained from Alfa Aesar, and ethanol (> 99.8%) from Riedel de Haën.

CdTe[32], CdSe[33] and PbSe[34] QDs were synthesized by organometallic syntheses using standard literature procedures. CdTe QDs were purified once by adding 150 µl methanol to 50 µl of the crude reaction mixture, followed by centrifugation, and redispersing the precipitate in 50 µl chloroform. To this, 50 µl of DDA, or 25 µl PT or DDT was added to re-coat the purified QDs. For MPA coated QDs, 50 µl of the crude CdTe reaction mixture was dispersed in 2.5 ml chloroform, after which 50 µl of 0.1M MPA in methanol was added. For transfer to water, 100 µl of a 0.1 M KOH solution in methanol was added, after which 1.5 ml deionised water (Millipore, 15 MΩ cm) was added. Upon shaking the mixture formed, the MPA coated QDs were transferred to the water phase.[35] The 1.5 ml aqueous dispersion was separated and partly evaporated to obtain the desired volume for addition to the reverse microemulsion system.

The CdSe QDs were washed by a similar procedure as the CdTe QDs but redispersed in ODE. The CdSe QDs were coated with 7 monolayers of inorganic shells (2 x CdS, 3 x $Cd_{0.5}Zn_{0.5}S$, 2 x ZnS) by a SILAR procedure.[36] Addition of these shells was performed by adding pre-calculated amounts of a 0.1 M precursor solution (Cd oleate, CdZn oleate, Zn oleate, and sulphur in ODE) to CdSe QDs dispersed in ODE at 230°C. Each monolayer was allowed to grow for ten minutes before the next precursor solution was added. The CSS QDs were purified by precipitation in a chloroform/acetone mixture followed by redispersion in chloroform for 2 times, after which they were dispersed in cyclohexane. The ligand exchange by DDT was performed by mixing an appropriate volume of a 1:100 DDT/cyclohexane (v/v) solution (0.042 M)) or pure DDT to 1.8 nmol of CdSe CSS QDs in 1 ml cyclohexane. Addition of 650 DDT molecules per QD was assumed to be equivalent to one monolayer coverage. The mixture was allowed to stand for 24 hours, after which it was added to the reverse microemulsion system. The PbSe

QDs were purified by precipitation and redispersed in a toluene/butanol mixture for two times. For incorporation in silica, PbSe QDs were dispersed in chloroform.

For a typical reverse microemulsion synthesis, 1.3 ml of NP-5 was dispersed in 10 ml cyclohexane and stirred for 15 minutes (850 rpm). Subsequently, 1-2 nmol of QDs dispersed in either chloroform (100 µl), cyclohexane (1 ml), or water (50 µl) was added, after which 80 µl of TEOS and 150 µl ammonia were added. Between the additions, the reaction mixture was stirred for 15 minutes (850 rpm). The order in which the chemicals were added was varied for the experiments described in Figure 8.6. After the last step, the mixture was stirred for one minute, after which it was stored in the dark at room temperature for one week. Finally, the QD/silica particles were purified by adding 3 ml ethanol to the reaction mixture and centrifuging this for 10 minutes at 1800 *g*. After removal of the supernatant, 10 ml of ethanol was added and the silica particles were sedimented again by centrifugation at 1800 *g* for twenty minutes. This was repeated once more for 40 minutes after which the QD/silica particles were redispersed in ethanol. The purified QD/silica samples were used for making TEM-images, or ODO-coating (see below).

To determine the QE of the silica coated QDs, the particles were coated by octadecanol (ODO). This was performed in a nitrogen-purged glovebox by adding 2.5 g of ODO dispersed in 5 ml of ethanol to a dispersion of 1.8 nmol of QD/silica particles in 5 ml ethanol. After heating this mixture to 100°C for 1 hour to evaporate all ethanol, the temperature was increased to 170°C for 3 hours to covalently link the ODO to the silica spheres by a condensation reaction.[37] The ODO coated particles were purified by precipitation and centrifugation in a cyclohexane/ethanol mixture (repeated 2-3 times), and redispersed in chloroform. To quantify the QE, the integrated emission of the QDs was compared with that of both Rhodamine 6G (QE = 90%) and Rhodamine 101 (QE = 95%).

Emission spectra were recorded using the monochromator of a Spex Fluorolog spectrometer (double-grating, 0.22 m, SPEX 1680) and a 450 W Xe lamp as the excitation source. The luminescence spectra were recorded by a Princeton Instruments CCD-camera (liquid nitrogen cooled) and a 0.25 m Acton Research monochromator with a grating of 150 lines/mm blazed at 550 nm. Photoluminescence decay curves were obtained by time-correlated single-photon counting. The setup consisted of a pulsed PicoQuant laser (2.5 MHz, λ_{ex}= 406 nm, pulse width = 55 ps) in combination with a monochromator (1350 lines/mm blazed at 500 nm), a Hamamatsu photo-multiplier tube (H5738P-01), and a Time Harp 200 computer card.[33, 38]

8.3 Results and discussion

Following a synthesis procedure adapted from Nann and co-workers (see experimental section for details), we have incorporated 6.4 nm CdSe core/shell/shell (CSS) QDs in silica spheres by the reverse microemulsion method.[27] The resulting silica particles of 37.2 nm are highly monodisperse (4% size dispersion) and have one QD incorporated exactly in the centre of the sphere (Figure 8.2A and insert). The control over the number of QD per silica particle is high: 96% of the particles contains a single QD in the centre, 3% is empty, and only 1% contains two QDs per particle. The CSS QDs were coated with octadecylamine (ODA) and dispersed in chloroform or cyclohexane before addition to the microemulsion system. The amount of CSS QDs that was added (1.8 nmol), was estimated from the initial amount of CdSe core QDs before shell growth. The number of initial CdSe QDs was determined by using the experimentally determined size-dependent extinction coefficient of CdSe QDs.[39] For comparison, the number of silica particles can be calculated, given the final size of the particles, the size of the incorporated QDs, and the amount of TEOS molecules used (assuming that all TEOS has reacted). For the QD/silica particles shown in Figure 8.2A this calculation yields 1.1 nmol of QD/silica particles (or slightly more when a lower density for porous silica is assumed)[40], which is in fair agreement with the 1.8 nmol mentioned above.

To investigate the general applicability of the method, also oleic acid (OA) coated PbSe QDs (6.8 nm) were incorporated in silica spheres using the same method. This resulted in 47.0 nm silica spheres with one PbSe QD incorporated in the middle (Figure 8.2B). The final particles are 10 nm larger than the CdSe CSS QDs in silica, which is explained by the lower amount of PbSe QDs that was used for the synthesis. We did not encounter problems regarding the dissolution of the PbSe QD using ammonia as base catalyst, as was reported earlier.[28] The quality of our silica coated PbSe QDs is unprecedented, particularly regarding the size dispersion and homogeneity (single QD per particle) of the samples.[28, 29] Cubic

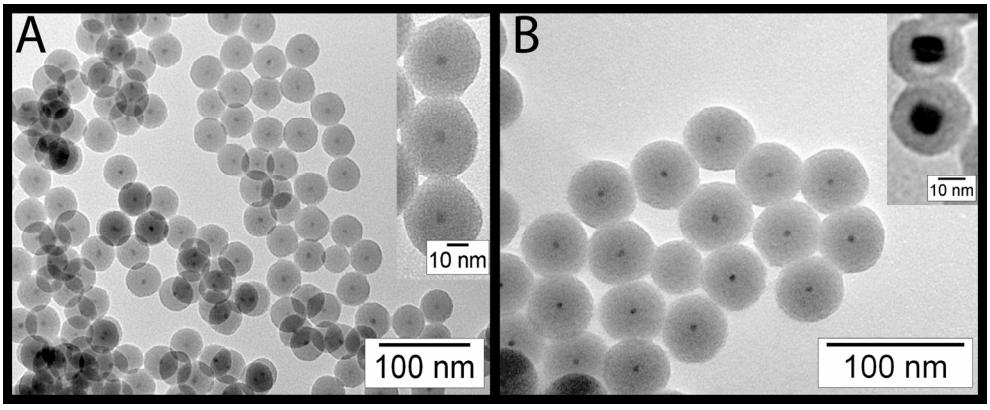

Figure 8.2. TEM images of (A) CdSe CSS QDs (6.4 ± 0.8 nm, ODA coated) in silica spheres of 37.2 ± 1.5 nm in diameter, insert shows a magnification of the same sample (B) PbSe QDs (6.8 ± 0.3 nm, OA coated) in silica spheres of 47.0 ± 3 nm. Insert in panel (B) shows a TEM image of cubic PbSe QDs (11.1 ± 0.6 nm, OA coated) coated with a thin layer of silica (6.4 ± 1.0 nm).

shaped PbSe QDs (11.1 nm) were also incorporated in silica spheres, as is illustrated in the inset of Figure 8.2B. In this case, the reaction was stopped after 2 hours, which resulted in a thin but homogeneous shell (6.4 nm) around the PbSe QDs.

The size of the final QD/silica particles changed if the amount of CdSe CSS-QDs added to the reaction mixture was varied within a certain range. Smaller (25 nm), and thus more silica spheres resulted when twice the amount of CSS-QDs (3.5 nmol) was used, whereas the number of silica spheres with two or more QDs per silica spheres increased with only 10%. Vice versa, larger silica particles (> 40nm) were formed when less QDs were used, without the number of empty silica spheres changing significantly. These observations together with their central position in the silica spheres indicate that the QDs act as efficient nucleation sites for silica growth. Below this range (1.3 nmol), the amount of empty silica particles increased (see for example Figure 8.5A), whereas an excess of QDs (>3.5 nmol) resulted in predominantly multiple QDs per silica particle. Figure 8.3A and 3B show TEM images of silica particles with multiple QDs incorporated, as a result of adding 7.2 nmol or 9 nmol QDs to the reaction mixture respectively (four and six times the quantity used for the particles shown in Figure 8.2A). At these high concentrations of QDs the micellar system becomes unstable, resulting in an aggregation of the QD/silica nuclei. Aggregation at an early stage of the silica growth results in little or no spacing in between the QDs, whereas aggregation at a later stage causes a certain distance between the QDs. Both small and larger inter-dot distances are observed in Figure 8.3A. The latter is particularly interesting because it may open up a new route to co-localize different types of nanocrystals within one silica sphere (to study for instance exciton-plasmon coupling), by adding a second type of nanocrystals at a later stage of the silica synthesis. When even more QDs are added (Figure 8.3B), the QDs clearly form chains within the silica particles. This suggests a directional force on the particles during aggregation, which may be explained by the presence of a permanent dipole moment in semiconductor nanocrystals.[41-43]

As is shown in Figure 8.2, the incorporation of hydrophobically coated QDs in

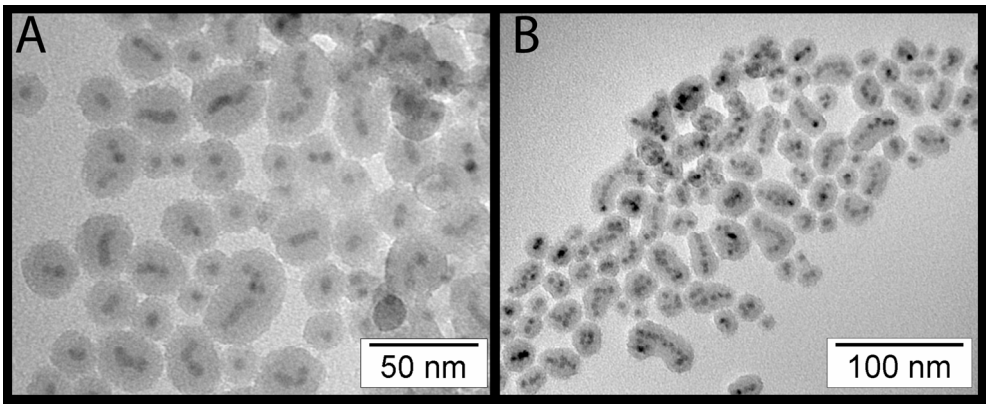

Figure 8.3. TEM images of silica particles with multiple CdSe CSS QDs (ODA coated) incorporated. The particles were obtained by adding (A) four times (7.2 nmol) or (B) six times (9 nmol) the number of CdSe CSS QDs used for the particles shown in Figure 8.2A.

silica spheres by the reverse microemulsion method gives a high degree of control and indicates that the QDs act as nucleation centres. This control is surprising since the silica nucleation and growth occurs within the small water droplets of the microemulsion, where one would expect the hydrophobic QDs to agglomerate or not to be present at all. To study the influence of the hydrophobic nature of the capping layer in more detail, we have also used CdTe QDs with different ligand coatings for the incorporation in silica. Figure 8.4A shows the result for dodecylamine coated CdTe QDs. These were incorporated, albeit in more polydisperse silica spheres with a larger spread in the number of QDs per silica particle. When the same CdTe QDs were coated with an excess of propanethiol (see experimental section), the nanocrystals were not incorporated in silica spheres, as is clearly illustrated in Figure 8.4B. We have performed the same experiment with dodecanethiol coated CdTe QDs, which gave a similar result (no incorporation). In addition, the CdTe QDs were coated with mercaptopropionic acid (MPA) and transferred to water as described previously.[35] When the water soluble MPA coated QDs were added to the standard microemulsion system, no incorporation was observed (Figure 8.4C). The same experiment was conducted for MPA coated CdTe QDs that were not transferred to water but still dispersed in chloroform (not deprotonated), which did not result in incorporation in silica either (not shown). It has been reported earlier that hydrophilic coated CdTe QDs dispersed in water do incorporate in silica using the same procedure, but we were not able to reproduce these results.[12, 26]

The results described above indicate that CdTe QDs coated with either hydrophobic or hydrophilic thiolated ligands are not incorporated in silica spheres using the reverse microemulsion method, whereas the incorporation of amine coated CdTe QDs is successful. We have therefore systematically investigated the influence of thiol-coating of CdSe CSS QDs on their incorporation in silica spheres. A variable amount of dodecanethiol (DDT) was added to the CSS QDs, 24 hours before addition to the microemulsion system. For these experiments, a significantly smaller amount of QDs was used (1.3 nmol), to avoid multiple QDs per particle. This explains the higher number of empty silica spheres in the case no DDT was added (Figure 8.5A) as compared to Figure 8.2A. When an amount of DDT corresponding to a tenfold excess of the number of molecules that is required for one monolayer (assuming 650 DDT molecules per QD, see Table 1 in the appendix at the end of this chapter) is added, the QDs are still incorporated into silica, but are positioned off-centre (Figure 8.5B). When an amount corresponding

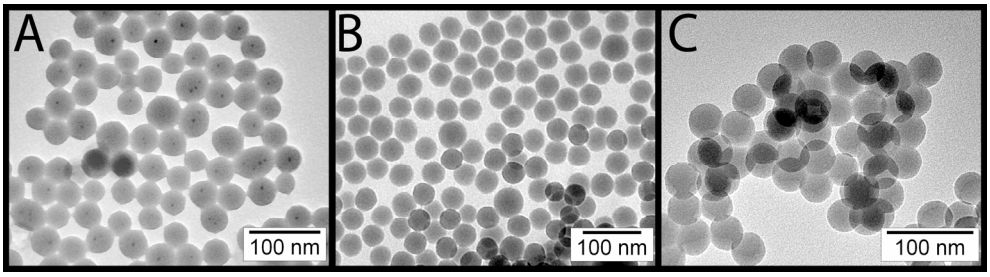

Figure 8.4. TEM images of resulting silica spheres when (A) DDA coated and (B) propanethiol coated CdTe QDs in chloroform, or (C) MPA coated CdTe QDs in water are added to the microemulsion system.

to 100 monolayers of DDT is added, some QDs are incorporated off-centre, but most of the QDs are attached to the surface of the silica spheres (Figure 8.5C). In the case of an amount for 500 monolayers DDT, the QDs are also attached to the outside of the silica particles, and the number of QDs associated with silica spheres decreases significantly (Figure 8.5D). TEM images of samples where concentrations corresponding to 1 or 50 monolayers of DDT were used are in line with the trend that the CSS QDs are "pushed" to the outside of the silica spheres when more thiolated ligands are added. These results show that the position of the QD in the silica sphere can be controlled by varying the amount of DDT molecules.

In the experiment described above, the relative number of DDT molecules compared to TEOS or NP-5 is low. The number of DDT molecules at 10 monolayers is still a factor 50 and 410 lower as compared to the number of TEOS and NP-5 molecules respectively (an overview of the relative amount of molecules present in the microemulsion system is given in Table 8.1 in the appendix). Therefore, we assume that the relatively low number of DDT molecules does not significantly influence the actual microemulsion system, which is confirmed by the fact that the shape or size of the silica spheres themselves is not changed upon addition of DDT. Nevertheless, the effect on the incorporation of the QDs is clearly visible already at 10 monolayers of DDT.

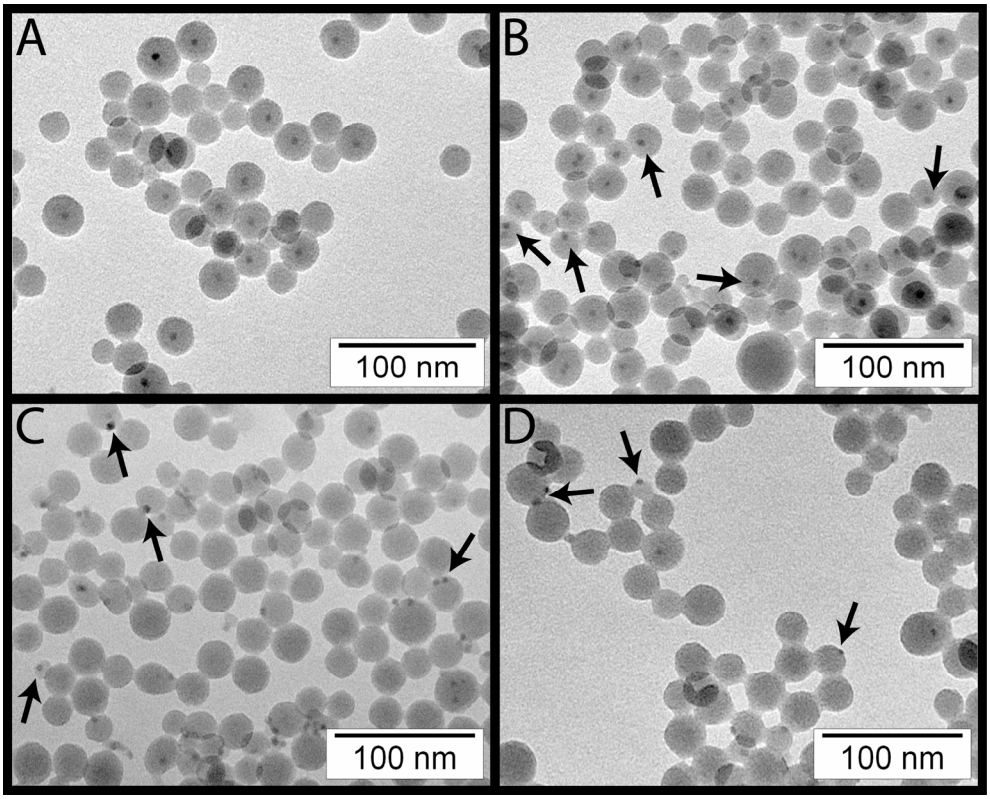

Figure 8.5. TEM images of silica particles when an amount of DDT corresponding to (A) 0 (B) 10 (C) 100 or (D) 500 monolayers is added to the CdSe CSS QDs (originally ODA coated), 24 hours before addition to the microemulsion system.

The original ODA coating of the CdSe CSS QDs is easily replaced by the DDT molecules, because the thiolated ligands bind much stronger to the QD surface than the amine groups of ODA.[35, 44] The observation that DDT coated QDs are not incorporated in silica cannot be explained by the first mechanism proposed by Nann and co-workers, where silica growth takes place in a bilayer of NP-5 molecules around the hydrophobic QDs.[27] This mechanism should still be possible when ODA ligands are replaced by DDT, because both coatings result in a hydrophobic coating of the QDs. On the other hand, the observations in Figure 8.5 do support a ligand exchange mechanism, where ODA or DDT is replaced by either NP-5 or TEOS, enabling the transfer of the QDs to the small water droplets.[26, 27] The stronger binding of DDT to the QD surface reduces this ligand exchange and hinders the incorporation of the QDs, explaining the trend observed in Figure 8.5. Without any DDT present, the QDs are coated by ODA which is easily replaced by TEOS and/or NP-5 (Figures 8.2A and 8.5A) resulting in a central incorporation in silica. At a relatively low amount of DDT molecules, an incomplete or delayed ligand exchange can still result in incorporation in silica spheres, albeit off-centre. At higher DDT concentrations, ligand exchange occurs only locally (or not at all), resulting in QDs that are attached to the outer surface of the silica spheres (or not associated at all).

To provide additional evidence for the ligand exchange mechanism, (time resolved) fluorescence spectroscopy experiments were performed on the reaction mixture at different stages of the silica synthesis. The optical spectroscopy elucidates by which ligands (and to what extent) the ODA is exchanged, allowing us to propose a detailed picture of the incorporation mechanism. The emission spectra of CdSe CSS QDs (initial QE of 60%) at different stages of the reverse microemulsion synthesis are shown in Figure 8.6. To 10 ml of a QD dispersion in cyclohexane, NP-5, TEOS and ammonia were added in different sequences. After each addition, the reaction mixture was stirred for 15 minutes, directly followed by the optical measurement. Figure 8.6A shows a decrease to 81% of the initial emission intensity upon addition of NP-5, followed by a decrease to 32% and 10% upon addition of TEOS and ammonia respectively. After 1 week, the emission intensity had decreased to approximately 2% of the initial intensity. When TEOS is added first (Figure 8.6B), a drastic decrease in emission intensity is observed (to 16%), followed by an intriguing increase to 35% upon addition of NP-5. Finally, the emission decreased to 19% of the initial intensity when ammonia was added. Figure 8.6C shows that addition of ammonia in the absence of TEOS does not cause a significant decrease in emission intensity. However, the emission intensity drastically decreases to 14% when TEOS is subsequently added.

Figures 8.6A and 8.6C clearly show that both NP-5 and TEOS (in a hydrolyzed form, as will be shown below) have affinity for the QD surface, as is concluded from the quenching of the QD emission. This provides direct evidence for the ligand exchange mechanism, that is, the replacement of ODA ligands by hydrolyzed TEOS and/or NP-5 molecules. If TEOS is added after NP-5 (Figure 8.6A), the NP-5 is partly replaced by TEOS, as can be concluded from the drastic additional decrease in emission intensity. The fact that (hydrolyzed) TEOS quenches the QD emission significantly stronger than NP-5 can be attributed to a higher affinity of TEOS for the QDs (i.e. more TEOS molecules attached), to an intrinsic higher quenching efficiency of TEOS, or both. In this context, it is important to note that there is approximately 8 times more NP-5 present in the reaction mixture than

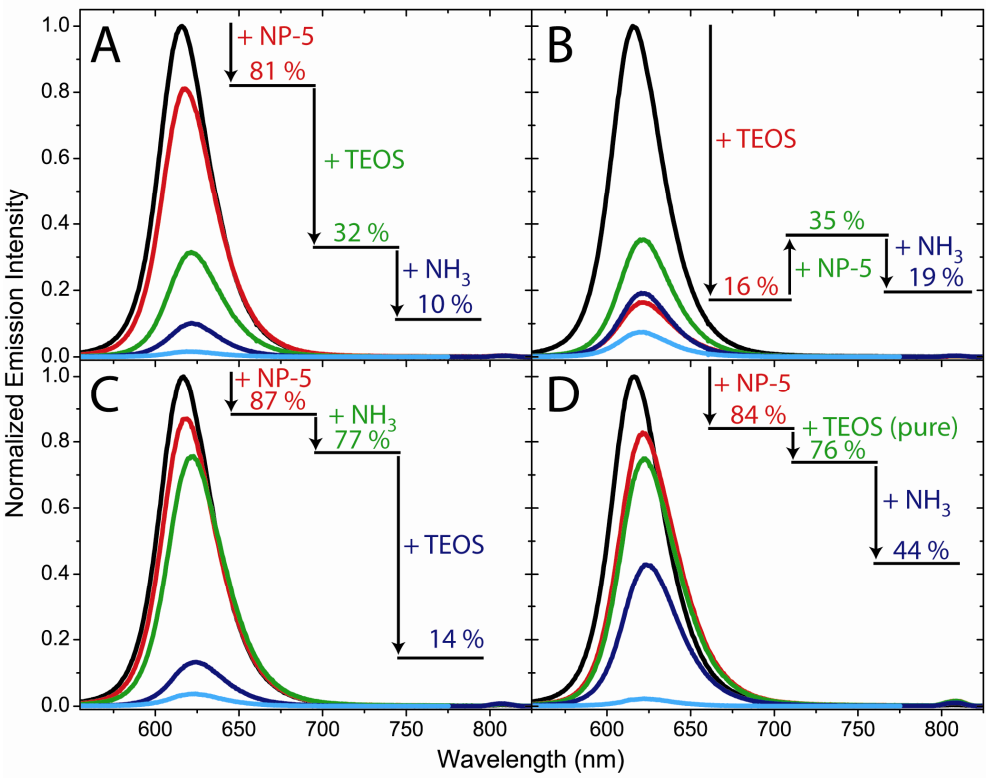

Figure 8.6. Emission spectra of CdSe CSS QDs (ODA coated) at different stages of the reverse microemulsion synthesis (λ_{exc} = 406 nm). In panels (A) to (C), NP-5, TEOS and NH_3 were added in different orders, as indicated by the arrows in each panel. The synthesis shown in panel (D) was identical to the synthesis in panel (A), except for the use of ultra pure and water-free TEOS. The emission spectra are corrected for the significant dilution factor upon addition of NP-5, and percentages represent the integrated emission intensity. The emission spectra in 'cyan' were measured 1 week after the synthesis.

TEOS (see Table 8.1 in the appendix). Importantly, the increase in emission intensity in Figure 8.6B after addition of NP-5 can be explained by an exchange of TEOS attached to the QD surface by NP-5, implying that NP-5 quenches the QD emission less efficiently than TEOS. The values of 32% and 35% after addition of both NP-5 and TEOS (Figures 8.6A and 8.6B) indicate that a similar equilibrium is reached, regardless of the order in which they were added.

In a simplified model, the relative quenching efficiency and binding affinity of NP-5 and (hydrolyzed) TEOS molecules can be (roughly) quantified. Because the number of NP-5 and TEOS molecules per QD is rather high ($3.6x10^5$ and $2.1x10^6$ respectively, see Table 8.1 in the appendix), we assume that 100% of the QD surface sites is occupied by TEOS or NP-5 molecules after addition to the QDs in cyclohexane. When NP-5 is added only, the quenching is 16% on average, while the quenching is 84% when the QDs are fully covered by TEOS. It can thus be calculated that TEOS quenches the QD emission a factor of 28 more efficiently than NP-5 (see appendix for the calculation). When NP-5 is added to TEOS coated

QDs (Figure 8.6B), the emission intensity increases from 16% to 35%. It can be calculated that this is due to the replacement of 64% of the TEOS molecules by NP-5 (see appendix). This means that in the equilibrium situation, 64% of the QD surface is coated by NP-5, while 36% of the surface is coated by TEOS. Taking into consideration that there is an 8-fold excess of NP-5 with respect to TEOS, it may be concluded that TEOS has a factor of four to five times higher affinity for the QD surface than NP-5. It must be stressed that this calculation assumes a 100% (or at least equal) coverage of the QD surface when TEOS or NP-5 is added only, for which we cannot provide direct evidence. The calculated values must therefore be regarded as rough estimates.

Figure 8.6D shows the emission spectra measured on a QD/silica synthesis similar to the synthesis depicted in Figure 8.6A, except for the fact that ultra pure and water-free TEOS (99.999%, stored in glove-box) was used. As can be seen, there is a clear difference in the degree of quenching upon addition of ultra pure water-free TEOS (decrease of 8%) as compared to the 99%-pure TEOS used in the other experiments (decrease of 49%). The 99%-pure TEOS was stored outside the glovebox and therefore contained more hydrolyzed TEOS as compared to the ultra pure and water-free TEOS. The difference in degree of quenching between Figures 8.6A and 8.6D therefore implies that it is hydrolyzed TEOS in particular that attaches to the QDs, and causes the emission quenching. When TEOS is (partly) hydrolyzed, the resulting Si–OH or $Si–O^-$ groups can bind to the QD surface. The calculated affinity of TEOS relative to NP-5 (vide supra) should therefore be regarded as the lower limit, because only a (small) fraction of the TEOS molecules will be initially hydrolyzed. The further decrease in emission intensity upon addition of ammonia (Figures 8.6A, B, and D) can now be explained by the enhanced hydrolysis of TEOS, which leads to a shift in the NP-5/TEOS

Scheme 8.1. Schematic representation of the incorporation mechanism of hydrophobic CSS QDs (in orange) in silica spheres by the reverse microemulsion method. (a) Illustrates the ODA coated CSS QDs dispersed in cyclohexane. Upon addition of TEOS or NP-5 the ODA is largely replaced, resulting in TEOS (b_1) or NP-5 (b_2) coated QDs. When subsequently NP-5 or TEOS is added, the same equilibrium is obtained (c), where the QDs is coated by (hydrolyzed) TEOS and NP-5. Upon addition of ammonia, TEOS is further hydrolyzed, and replaces all NP-5 (d). Water and ammonia molecules are present in between the TEOS coated QD and the micelle that is formed by NP-5.

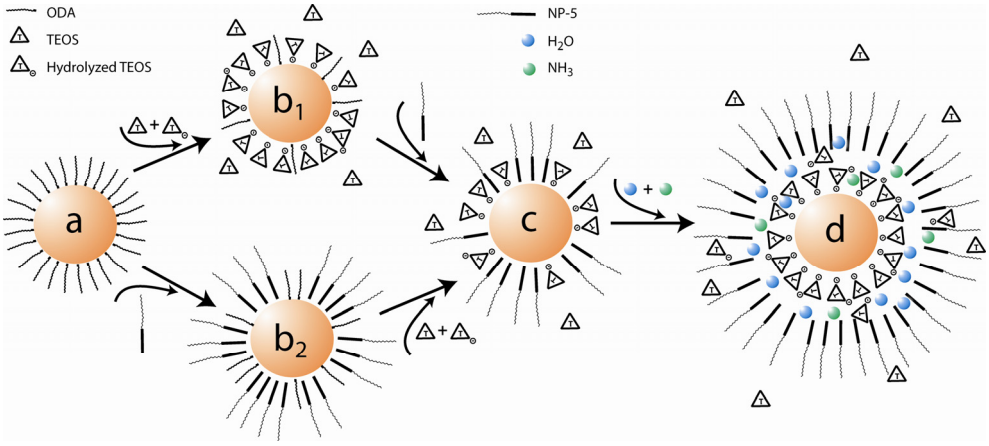

equilibrium. That is, the increased number of hydrolyzed TEOS molecules will eventually replace all NP-5 molecules that are attached to the QD surface, and thereby even further decrease the emission intensity. After 1 week, the emission intensity in Figure 8.6D has decreased to approximately 2%, similar to the result in Figure 8.6A. The initial smaller decrease in emission intensity upon addition of the ultra pure TEOS has apparently no effect on the final emission intensity, which can be explained by the fact that eventually all TEOS will be hydrolyzed due to the presence of ammonia. The similar final emission intensities in Figures 8.6A and D also suggest that possible other impurities in the 99%-pure TEOS do not play an important role. The mechanism described above is illustrated in Scheme 8.1.

Fluorescence decay curves for the CdSe CSS QDs were measured at the different stages of the silica synthesis (Figures 8.7A and B). The QDs dispersed in cyclohexane display a nearly single-exponential decay (τ = 22 ns), in good agreement with the high initial QE (60%). When NP-5 is added, no significant change in the decay curve is observed (Figures 8.7A and B), even when this is followed by the addition of ammonia (Figure 8.7B). However, when TEOS is added, the fluorescence decay becomes significantly faster and non-exponential. This effect is stronger when ammonia is present (Figure 8.7B), as compared to the situation where ammonia is absent (Figure 8.7A). Faster fluorescence decay indicates the presence of additional non-radiative recombination pathways of the exciton, resulting in a lower overall QE. These results are in good agreement with the changes in emission intensities observed in the spectra of the same samples in Figures 8.6A and 8.6C. It can be concluded that the attachment of hydrolyzed TEOS molecules to the QD surface causes quenching and corresponding faster decay of the QD emission.

To follow the kinetics of the ligand exchange, we have followed the emission intensity of the CdSe CSS QDs over time, upon addition of TEOS (Figure 8.7C). When TEOS is added to the QDs dispersed in cyclohexane, the emission decreases rapidly to 18% of the initial intensity, which is in good agreement with the decrease to 16% in Figure 8.6B upon addition of TEOS only. The fast decrease

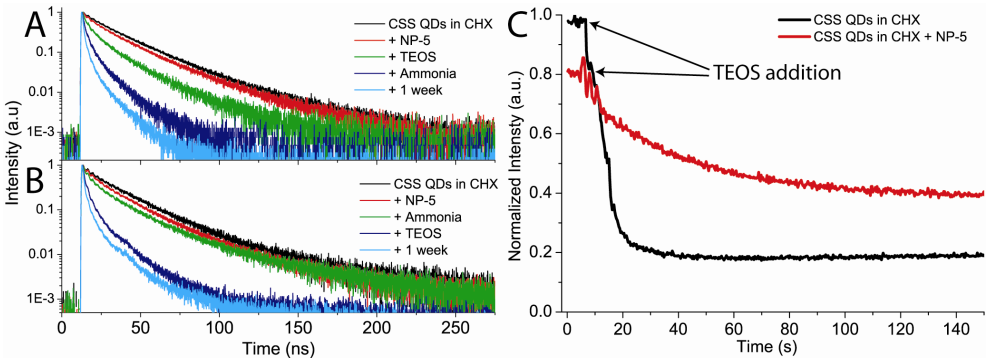

Figure 8.7. (A) and (B) Fluorescence decay curves of CdSe CSS QDs (ODA coated) at different stages of the reverse microemulsion synthesis (λ_{exc} = 406 nm, λ_{em} = 620 nm). The order in which the precursors were added (indicated from top to bottom) differs for the two panels. (C) Evolution of the emission intensity of CdSe CSS QDs as a function of time, after addition of TEOS (at time = 0). Ten spectra per second were recorded, and the intensity at the emission maximum (620 nm) was plotted as a function of time.

demonstrates the rapid association of hydrolyzed TEOS to the QDs. The emission intensity of a dispersion where NP-5 is present before TEOS addition was initially 19% lower compared to the cyclohexane dispersion, which is in good agreement with the decrease observed upon addition of NP-5 in Figure 8.6A. When TEOS is added to this mixture, a significantly slower decrease in emission intensity is observed. The final emission intensity is 39%, again in good agreement with the emission decrease in Figure 8.6A and 6B when both TEOS and NP-5 are added.

The slower decrease in emission intensity when NP-5 is present provides additional evidence for the partial replacement of NP-5 by TEOS, which is hindered due to the large excess of NP-5 (see Table 8.1). However, it still takes only about two minutes before the NP-5/TEOS equilibrium on the QD-surface is reached. This rapid exchange and equilibration of the TEOS and NP-5 can explain the exact central incorporation of the QDs in the silica spheres. It is well known that the silica nucleation and growth in the reverse microemulsion system (and even in the Stöber approach) is relatively slow (slower than minutes) and rate limited by the (first) hydrolysis of TEOS.[45, 46] Because this process is much slower than the complete TEOS exchange and subsequent TEOS/NP-5 equilibration time, systems (c) and (d) as depicted in Scheme 8.1 will act as effective and isotropic nucleation sites for the growth of silica. If, due to the presence of DDT, the ligand exchange is hindered and therefore not complete or delayed, the QDs are incorporated off-centre (as illustrated in Figure 8.5B) due to anisotropic silica growth. In the presence of an excess of DDT, only a fraction of the ligands will be eventually exchanged, which will force the hydrophobic QDs to reside at the interface of the micelle. In this case, silica growth takes place only on a part of the QD surface, which results in QDs attached to the outside of silica spheres, as illustrated in Figures 8.5C and 8.5D.

The emission intensity of the final QD/silica particles after 1 week of silica growth is typically only a few percent of the initial intensity (Figure 8.6). This dramatic decrease in QE is ascribed to the attachment of fully hydrolyzed and subsequently condensed TEOS (i.e. silica) to the QD surface causing emission quenching. We observed that this decrease is partly reversible, although only

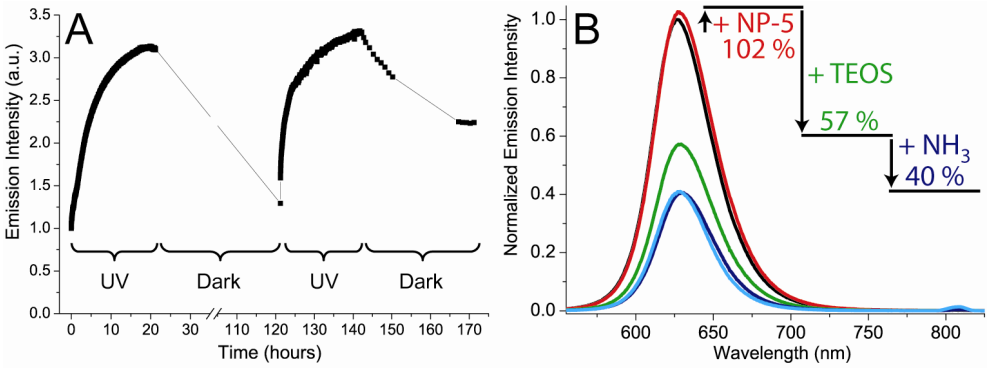

Figure 8.8. (A) Evolution of the emission intensity of CSS-QD/silica particles dispersed in ethanol as a function of time, under UV-illumination and in the dark. Note the time-break between 35 and 95 hours. (B) Emission spectra of CSS CdSe QDs (ODA coated) with a thicker inorganic shell (7.7 ± 0.9 nm in diameter), at different stages of the reverse microemulsion synthesis.

temporarily, by illumination of the samples after synthesis. Figure 8.8A shows the evolution of the emission intensity over time, when the sample is illuminated with an intense 406 nm light source (450 W Xe lamp, slits of the spectrometer fully opened). An increase in emission intensity by a factor of three is observed within 24 hours, which decreases to the initial intensity when the sample is stored in the dark. When exposed to the light source again, a similar photo-activation is observed.

The quenching-mechanism when hydrolyzed TEOS attaches to the QD surface remains unclear, but we can think of two possibilities. First, the hydrolyzed TEOS can act as an efficient hole or electron acceptor, which introduces new non-radiative decay pathways for the exciton. This would increase the total fluorescence decay rate, as observed in Figures 8.7A and B. Another explanation may be the presence of charges such as $Si\text{-}O^-$ groups, hydroxyl ions, or ammonium ions which are likely to be found in the close vicinity of the QD. It is known that the presence of a single charge close to the QD surface can generate an electric field that is sufficiently large to cause significant quenching[47] and/or a red-shift[48] of the QD emission, as observed in Figure 8.6. Photo-activation has been reported for QDs in organic or aqueous solvents[49], monolayers in air[50], films[51], polymers[52], or physiological conditions.[53] Surface passivation by water, or photo-activated rearrangement of the surface and/or surfactants are proposed as possible mechanisms responsible for the enhanced luminescence upon UV-illumination. Because the quenching-mechanism by the silica layer is unclear, it is difficult to assign the photo-activation that is observed for the QDs to one of the explanations mentioned above.

Regardless of the mechanism, the quenching by hydrolyzed TEOS and its condensed form, silica, will be dependent on the distance between the luminescent CdSe core, and the quenching groups. To reduce the quenching in order to obtain more efficiently luminescing QDs in silica, we have incorporated CSS QDs with a thicker inorganic shell (7.7 ± 0.9 nm in diameter) in silica spheres using the same method. The decrease in the emission intensity at the different stages of the silica synthesis was significantly lower using these QDs (see Figure 8.8B). As can be seen, NP-5 no longer influences the emission intensity, and subsequent addition of TEOS to the reaction mixture results in a decrease to 57%, as compared to 32% in Figure 8.6A. Addition of ammonia leads to a reduction to 40%, which is maintained after one week. This decrease in intensity is much lower than that observed for CdSe CSS QDs with thinner shells (to 10% and 2% respectively, see Figure 8.6A). The final emission intensity of the QD/silica particles directly after synthesis was 40% of the initial intensity, which implies a final QE of approximately 24% (the initial QE was 60%). The QD/silica particles were subsequently coated with octadecanol (ODO, see experimental section) to render them hydrophobic. The hydrophobic QD/silica particles could be dispersed in chloroform, of which the refractive index is well matched to that of octadecanol coated silica.[37, 54] The scattering-free dispersions allow a reliable determination of the QE of the QDs in silica when a dye is used as a reference, in contrast to QD/silica particles dispersed in for example ethanol. We observed that the hydrophobic coating increases the QE of the QD/silica particles, which may be ascribed to the heating step to 170 °C that is involved in this procedure. In this manner, we have measured a final QE of the QDs in hydrophobic silica spheres dispersed in chloroform of 35%, which to the best of our knowledge is the highest value reported.

8.4 Conclusions

In conclusion, we have found strong experimental evidence in favor of the proposed incorporation mechanism of hydrophobic QDs in silica spheres by a reverse microemulsion system based on a non ionic surfactant (NP-5) in hexane, in addition with TEOS and ammonia that are used to cover the QDs with silica. We show by (time resolved) fluorescence spectroscopy that hydrolyzed TEOS molecules (and initially also NP-5 molecules) replace the original hydrophobic amine-ligands of QDs in this reverse microemulsion system. The replacement facilitates the transfer of the QDs into the hydrophilic interior of the micelles, where silica growth takes place. For QDs coated with (stronger binding) thiol-ligands, the replacement by TEOS or NP-5 is hindered, which results in QDs that are incorporated off-centre, attached to the outer surface of the silica spheres or not incorporated at all, depending on the fraction of thiol-ligands at the QD-surface. Based on these results, we can now explain the highly controlled incorporation of hydrophobic CdSe CSS and PbSe QDs exactly in the middle of monodisperse silica spheres by this reverse microemulsion synthesis. In conjunction with these findings, we were able to make QD/silica particles with a final QE of 35%. It is likely that the mechanism proposed here also applies to the incorporation of other hydrophobic nanoparticles in silica (such as iron oxide, gold, or iron-platinum nanocrystals) by a reverse microemulsion method. Multiple QDs per silica can be achieved by increasing the QD concentration, which implies the possibility of co-localizing different types of nanocrystals in silica at a tuneable distance.

8.5 References

1. C. Graf, D.L.J. Vossen, A. Imhof, and A. van Blaaderen, *Langmuir*, **2003**. *19* (17): p. 6693-6700.
2. L.M. LizMarzan, M. Giersig, and P. Mulvaney, *Langmuir*, **1996**. *12* (18): p. 4329-4335.
3. D. Gerion, F. Pinaud, S.C. Williams, W.J. Parak, D. Zanchet, S. Weiss, and A.P. Alivisatos, *J. Phys. Chem. B*, **2001**. *105* (37): p. 8861-8871.
4. T. Nann and P. Mulvaney, *Angew. Chem. Int. Ed.*, **2004**. *43* (40): p. 5393-5396.
5. S. Santra, R. Tapec, N. Theodoropoulou, J. Dobson, A. Hebard, and W.H. Tan, *Langmuir*, **2001**. *17* (10): p. 2900-2906.
6. A.P. Philipse, M.P.B. Vanbruggen, and C. Pathmamanoharan, *Langmuir*, **1994**. *10* (1): p. 92-99.
7. P. Mulvaney, L.M. Liz-Marzan, M. Giersig, and T. Ung, *J. Mater. Chem.*, **2000**. *10* (6): p. 1259-1270.
8. B.L. Cushing, V.L. Kolesnichenko, and C.J. O'Connor, *Chem. Rev.*, **2004**. *104* (9): p. 3893-3946.
9. S.T. Selvan, T.T. Tan, and J.Y. Ying, *Adv. Mater.*, **2005**. *17* (13): p. 1620-+.
10. T.T. Zhang, J.L. Stilwell, D. Gerion, L.H. Ding, O. Elboudwarej, P.A. Cooke, J.W. Gray, A.P. Alivisatos, and F.F. Chen, *Nano Lett.*, **2006**. *6* (4): p. 800-808.
11. C. Kirchner, T. Liedl, S. Kudera, T. Pellegrino, A.M. Javier, H.E. Gaub, S. Stolzle, N. Fertig, and W.J. Parak, *Nano Lett.*, **2005**. *5* (2): p. 331-338.
12. Y.H. Yang, L.H. Jing, X.L. Yu, D.D. Yan, and M.Y. Gao, *Chem. Mater.*, **2007**. *19* (17): p. 4123-4128.
13. F.Q. Chen and D. Gerion, *Nano Lett.*, **2004**. *4* (10): p. 1827-1832.
14. J.H. Lee, Y.W. Jun, S.I. Yeon, J.S. Shin, and J. Cheon, *Angew. Chem. Int. Ed.*, **2006**. *45* (48): p. 8160-8162.
15. H.S. Yang, S. Santra, G.A. Walter, and P.H. Holloway, *Adv. Mater.*, **2006**. *18* (21): p. 2890-+.
16. C. Graf, S. Dembski, A. Hofmann, and E. Ruhl, *Langmuir*, **2006**. *22* (13): p. 5604-5610.
17. V. Salgueiriño-Maceira, M.A. Correa-Duarte, M. Spasova, L.M. Liz-Marzán, and M. Farle, *Adv. Funct. Mater.*, **2006**. *16* (4): p. 509-514.
18. S. Santra, H.S. Yang, P.H. Holloway, J.T. Stanley, and R.A. Mericle, *J. Am. Chem. Soc.*, **2005**. *127* (6): p. 1656-1657.
19. S.T. Selvan, P.K. Patra, C.Y. Ang, and J.Y. Ying, *Angew. Chem. Int. Ed.*, **2007**. *46* (14): p. 2448-2452.
20. J. Kim, S. Park, J.E. Lee, S.M. Jin, J.H. Lee, I.S. Lee, I. Yang, J.S. Kim, S.K. Kim, M.H. Cho*, et al.*, *Angew. Chem. Int. Ed.*, **2006**. *45* (46): p. 7754-7758.
21. D.K. Yi, S.T. Selvan, S.S. Lee, G.C. Papaefthymiou, D. Kundaliya, and J.Y. Ying, *J. Am. Chem. Soc.*, **2005**. *127* (14): p. 4990-4991.
22. W. Stöber, A. Fink, and E. Bohn, *J. Colloid Interface Sci.*, **1968**. *26*: p. 62.
23. A.L. Rogach, D. Nagesha, J.W. Ostrander, M. Giersig, and N.A. Kotov, *Chem. Mater.*, **2000**. *12* (9): p. 2676-2685.
24. K. Osseo-Asare and F.J. Arriagada, *Colloid Surface*, **1990**. *50*: p. 321-339.
25. S.Y. Chang, L. Liu, and S.A. Asher, *J. Am. Chem. Soc.*, **1994**. *116* (15): p. 6739-6744.
26. Y.H. Yang and M.Y. Gao, *Adv. Mater.*, **2005**. *17* (19): p. 2354-+.
27. M. Darbandi, R. Thomann, and T. Nann, *Chem. Mater.*, **2005**. *17* (23): p. 5720-5725.
28. M. Darbandi, W.G. Lu, J.Y. Fang, and T. Nann, *Langmuir*, **2006**. *22* (9): p. 4371-4375.
29. T.T. Tan, S.T. Selvan, L. Zhao, S.J. Gao, and J.Y. Ying, *Chem. Mater.*, **2007**. *19* (13): p. 3112-3117.
30. C.W. Lu, Y. Hung, J.K. Hsiao, M. Yao, T.H. Chung, Y.S. Lin, S.H. Wu, S.C. Hsu, H.M. Liu, C.Y. Mou*, et al.*, *Nano Lett.*, **2007**. *7* (1): p. 149-154.
31. C.H. Yu, N. Caiulo, C.C.H. Lo, K. Tam, and S.C. Tsang, *Adv. Mater.*, **2006**. *18* (17): p. 2312-2314.

32. S.F. Wuister, F. van Driel, and A. Meijerink, *Phys. Chem. Chem. Phys.*, **2003**. *5* (6): p. 1253-1258.
33. C. de Mello Donega, M. Bode, and A. Meijerink, *Phys. Rev. B*, **2006**. *74* (8): p. 085320.
34. A.J. Houtepen, R. Koole, D.L. Vanmaekelbergh, J. Meeldijk, and S.G. Hickey, *J. Am. Chem. Soc.*, **2006**. *128* (21): p. 6792-6793.
35. S.F. Wuister, I. Swart, F. van Driel, S.G. Hickey, and C. de Mello Donegá, *Nano Lett.*, **2003**. *3* (4): p. 503-507.
36. R.G. Xie, U. Kolb, J.X. Li, T. Basche, and A. Mews, *J. Am. Chem. Soc.*, **2005**. *127* (20): p. 7480-7488.
37. A.K. van Helden, J.W. Jansen, and A. Vrij, *J. Colloid Interface Sci.*, **1981**. *81* (2): p. 354-368.
38. S.F. Wuister, C. de Mello Donegá, and A. Meijerink, *J. Chem. Phys.*, **2004**. *121* (9): p. 4310-4315.
39. W.W. Yu, L. Qu, W. Guo, and X. Peng, *Chem. Mater.*, **2003**. *15* (14): p. 2854-2860.
40. A. van Blaaderen and A.P.M. Kentgens, *J Non-Cryst Solids*, **1992**. *149* (3): p. 161-178.
41. M. Klokkenburg, A.J. Houtepen, R. Koole, J.W.J. de Folter, B.H. Erne, E. van Faassen, and D. Vanmaekelbergh, *Nano Lett.*, **2007**. *7* (9): p. 2931-2936.
42. K.S. Cho, D.V. Talapin, W. Gaschler, and C.B. Murray, *J. Am. Chem. Soc.*, **2005**. *127* (19): p. 7140-7147.
43. S.A. Blanton, R.L. Leheny, M.A. Hines, and P. GuyotSionnest, *Phys. Rev. Lett.*, **1997**. *79* (5): p. 865-868.
44. S.F. Wuister, C. de Mello Donegá, and A. Meijerink, *J. Phys. Chem. B*, **2004**. *108* (45): p. 17393-17397.
45. K. Osseo-Asare and F.J. Arriagada, *J. Colloid Interface Sci.*, **1999**. *218* (1): p. 68-76.
46. A. van Blaaderen, J. van Geest, and A. Vrij, *J. Colloid Interface Sci.*, **1992**. *154* (2): p. 481-501.
47. L.W. Wang, *J. Phys. Chem. B*, **2001**. *105* (12): p. 2360-2364.
48. S.A. Empedocles and M.G. Bawendi, *Science*, **1997**. *278* (5346): p. 2114-2117.
49. M. Jones, J. Nedeljkovic, R.J. Ellingson, A.J. Nozik, and G. Rumbles, *J. Phys. Chem. B*, **2003**. *107* (41): p. 11346-11352.
50. S.R. Cordero, P.J. Carson, R.A. Estabrook, G.F. Strouse, and S.K. Buratto, *J. Phys. Chem. B*, **2000**. *104* (51): p. 12137-12142.
51. B.C. Hess, I.G. Okhrimenko, R.C. Davis, B.C. Stevens, Q.A. Schulzke, K.C. Wright, C.D. Bass, C.D. Evans, and S.L. Summers, *Phys. Rev. Lett.*, **2001**. *86* (14): p. 3132-3135.
52. A.Y. Nazzal, X.Y. Wang, L.H. Qu, W. Yu, Y.J. Wang, X.G. Peng, and M. Xiao, *J. Phys. Chem. B*, **2004**. *108* (18): p. 5507-5515.
53. J. Silver and W. Ou, *Nano Lett.*, **2005**. *5* (7): p. 1445-1449.
54. A. van Blaaderen and A. Vrij, *J. Colloid Interface Sci.*, **1993**. *156* (1): p. 1-18.

8.6 Appendix

Calculation of the relative affinity and quenching rate of TEOS versus NP-5

For the calculations it is assumed that in case NP-5 or TEOS is added only, the QDs are fully (or at least equally) covered by these ligands because of the large excess as compared to the original coating. The initial QE of the QDs (QE_I) before addition of NP-5 or TEOS can be written as:

$$QE_I = \frac{\Gamma_{rad}}{\Gamma_{rad} + \Gamma_{nonrad}} = \frac{\Gamma_{rad}}{\Gamma_{tot}} \tag{8.1}$$

where Γ_{rad} and Γ_{nonrad} are the radiative and non-radiative decay rates respectively, and Γ_{tot} is the total decay rate. It is further assumed that the quenching rate per TEOS or NP-5 molecule is constant, and that the total quenching rate is thus the product of the quenching rate per molecule and the number of molecules attached. The total QE of the QDs (QE_T) after addition of TEOS can then be written as:

$$QE_T = \frac{\Gamma_{rad}}{\Gamma_{tot} + n \cdot \Gamma_{TEOS}} \tag{8.2}$$

where n is the number of TEOS molecules (in percentage, 100 is full coverage), and Γ_{TEOS} is the quenching rate per percent TEOS coverage. Since the emission intensities in Figure 8.4 of the article are relative emission intensities (compared to the initial intensity), we define the relative QE (QE_R) as:

$$QE_R = \frac{QE_T}{QE_I} = \frac{\Gamma_{tot}}{\Gamma_{tot} + n \cdot \Gamma_{TEOS}} \tag{8.3}$$

Similarly, the relative QE of the QDs (QE_T) after addition of NP-5 can be written as:

$$QE_R = \frac{QE_T}{QE_I} = \frac{\Gamma_{tot}}{\Gamma_{tot} + n \cdot \Gamma_{NP-5}} \tag{8.4}$$

When TEOS or NP-5 are added only, the coverage is assumed to be 100 %, hence n = 100. The QE_R in those cases are 0.16 and 0.84 respectively. Filling in these numbers in equations (8.3) and (8.4), yields that:

$$\Gamma_{tot} = 19 \cdot \Gamma_{TEOS} = 525 \cdot \Gamma_{NP-5} \tag{8.5}$$

This implies that the quenching rate per TEOS molecule is 525/19 = 28 times higher than for NP-5. When both TEOS and NP-5 are added, the relative QE (QE_R) is defined as:

$$QE_R = \frac{QE_T}{QE_I} = \frac{\Gamma_{tot}}{\Gamma_{tot} + n \cdot \Gamma_{TEOS} + (100 - n) \cdot \Gamma_{NP-5}} \quad (8.6)$$

It was found that QE_R is 0.34 on average when both TEOS and NP-5 are added (Figure 8.4A and 4B). Filling in this number in equation (8.6) and by defining Γ_{NP-5} and Γ_{tot} as a function of Γ_{TEOS} (equation (8.5)), the value for n can be calculated. In this manner we obtain a value of 36 for n, which means that 36 % of the surface is covered by TEOS, and 64 % by NP-5.

Table 8.1. Number of molecules X (upper row) relative to molecule Y (left column) in a standard reverse microemulsion system. 1 ML DDT stands for 1 monolayer of DDT molecules. It is estimated that one monolayer DDT around a 6.4 nm QD contains approximately 650 DDT molecules assuming a surface area of 20 $Å^2$ per DDT molecule. One can also calculate the number of thiols that may attach to the QD surface by calculating the number of ZnS unit cells on the surface of a 6.4 nm QD, which gives approximately the same number (540).

	1 ML DDT	TEOS	NH_3	NP-5	H_2O
QDs	650	$3.6x10^5$	$2.1x10^6$	$2.9x10^6$	$5.6x10^6$
1 ML DDT	1	550	3200	4500	8600
TEOS		1	6	8.2	16
NH_3			1	1.4	2.7
NP-5				1	1.9

Chapter 9

Paramagnetic Lipid-coated Silica Nanoparticles with a Fluorescent Quantum Dot Core: a New Contrast Agent Platform for Multimodality Imaging

Silica particles as a nanoparticulate carrier material for contrast agents have received considerable attention the past few years, since the material holds great promise for biomedical applications. A key feature for successful application of this material *in vivo* is biocompatibility, which may be significantly improved by appropriate surface modification. In this study we report a novel strategy to coat silica particles with a dense monolayer of paramagnetic and PEGylated lipids. The silica nanoparticles carry a quantum dot in their centre and are made target-specific by the conjugation of multiple αvβ3-integrin-specifc RGD-peptides. We demonstrate their specific uptake by endothelial cells *in vitro* using fluorescence microscopy, quantitative fluorescence imaging and magnetic resonance imaging. Biodistribution tests *in vivo* show an enhanced blood circulation half-time of lipid coated silica particles compared to bare silica particles. The lipid coated silica particles introduced here represent a new platform for nanoparticulate multimodality contrast agents. As a proof-of-principle, an example of a trimodal particle based on the concept of a lipid coated silica particle is given.

9.1 Introduction

Nanoparticles have been explored for a few decades now as vehicles to deliver therapeutic agents.[1] Traditionally, nanoparticles composed of naturally occurring molecules, such as bilayered vesicles composed of phospholipids, have been utilized.[2] The revolution in nanoscience has resulted in the development of a tremendous amount of new materials, that hold great potential for biomedical applications.[3] In the field of diagnostic imaging nanoparticles also create new possibilities. Examples are iron oxide nanoparticles (for magnetic resonance imaging, MRI),[4] carbon nanotubes (for MRI),[5] or gold nanoparticles (for computed tomography, CT).[6] Semiconductor nanocrystals, also known as quantum dots (QDs), have been recognized as an optical contrast agent due to their outstanding fluorescent properties.[7] A major advantage in the use of nanoparticles for biomedical purposes is the option of integrating multiple properties in a single carrier particle. The possibilities for surface modification create additional flexibility for a large range of applications and has resulted in the synthesis of nanoparticles that are suitable for both therapeutic and diagnostic purposes,[8] but also the synthesis of a single type of nanoparticle that can be employed for different imaging modalities.[9]

Silica as a nanoparticulate carrier material has received considerable attention the past few years. The incorporation of nanoparticles in silica has been reported for semiconductor[10, 11], metallic[12, 13], and magnetic nanocrystals.[14] In addition, the simultaneous incorporation of magnetic nanoparticles and QDs in silica nanospheres has been reported recently.[15-18] Doping of silica particles with dye molecules is well-established[19-21], and combinations of dyes with other functionalities within one silica sphere have also been reported.[22-24] The use of these silica coated nanoparticles and/or dyes as contrast agents for bio-imaging applications benefits from the high versatility and well-known surface chemistry of silica nanospheres.[25] The possibility of combining multiple properties within one silica nanosphere as well as the control over the final particle size over a broad range (20 nm – 5 μm) make these composite particles especially suitable as carriers for multiple (molecular imaging) contrast agents. However, a key feature for successful application of this material *in vivo* is biocompatibility, which may be significantly improved by appropriate surface modification.

Two distinct surface modifications to enhance the bio-applicability of silica nanospheres have been reported to date, which both depend on the use of silane coupling agents. The first method is by terminating the silica spheres by an amine or thiol groups using APS or MPS (aminopropyltrimethoxysilane and mercaptopropylmethoxysilane), to which bio-functional groups can be covalently linked.[24, 26-30] The second method involves the modification of the silica surface by molecules that have a silane-group already integrated within the molecule. [24, 28, 30, 31] Most of the aforementioned reports use both strategies simultaneously to attach functional groups (e.g. antibodies or paramagnetic molecules) through an amide bond, and PEG-silane molecules (PEG = polyethelyneglycol) to enhance solubility of the silica nanospheres. Although they allow for some variation in surface functionalization, there are several serious drawbacks for these methods. Firstly, it is not clear to what extent (and in what ratio) the silica surface is covered by the pegylated molecules and biofunctional groups (due to sterical hindrance and differences in reactivity with coupling agents). Secondly, the density of the

(pegylated) coating around the silica spheres is not well-defined, which limits the optimal use of the surface area (payload of contrast agents or antibodies) and bio-compatibility. In addition, depending on the pH, this methodology results in the presence of negatively (positively) charged hydroxyl (amine) groups, which may unfavorably affect the stability under physiological conditions. Thirdly, the flexibility of these methods is limited to molecules with reactive groups for the covalent linking step.

In the current study we report a novel strategy to coat silica particles with a dense monolayer of lipids without the usage of (silane) coupling agents. First the silica particles are rendered hydrophobic, after which they are coated with both paramagnetic and PEGylated lipids. This highly flexible and widely applicable coating method of silica particles also allows for the conjugation of target-specific molecules at the surface of the nanoparticle. In the present case, we use highly monodisperse silica particles that have a single core-shell-shell (CSS) QD incorporated in the centre (for fluorescence imaging) and Gd-DTPA-DSA in the lipid coating (for MRI). As a proof-of-principle we demonstrate target-specific uptake and multimodality imaging (MRI and fluorescence) of αvβ3-integrin expression on cultured endothelial cells using our lipid-coated QD/silica nanoparticles.

9.2 Experimental Section

Materials

1,2-distearoyl-*sn*-glycero-3-phosphoethanolamine-*N*-[methoxy(poly(ethylene glycol))-2000] (PEG-DSPE) and 1,2-distearoyl-*sn*-glycero-3-phosphoethanolamine-*N*-[maleimide(poly(ethylene glycol))2000] (Mal-PEG-DSPE) were purchased from Avanti Polar Lipids. Gd-DTPA-bis(stearylamide) (Gd-DTPA-DSA) was obtained from Gateway Chemical Technology. Methanol (anhydrous, 99.8%), Octadecanol (99%), Igepal (CO-520), Oleic acid (90%), octadecylamine (ODA, 97%) and octadecene (ODE, 90%) were purchased from Aldrich. Tetraethyl orthosilicate (TEOS, 99%) was obtained from Johnson Matthey. Acetone (p.a.), chloroform (p.a.), Ammonia (25% in water, p.a.), Cadmium Oxide (>99%), Zinc oxide (>99%), and HEPES ($C_8H_{18}N_2O_4S$, >99%) were purchased from Merck. The HEPES buffer contained 2.38 g/l HEPES and 8.0 g/l NaCl (99.8%, Baker), and the pH was adjusted to 6.7 by addition of a NaOH solution. Sulphur powder (99.999%) was obtained from Alfa Aesar, and ethanol (>99.8%) from Riedel de Haën. The cyclic 5mer RGD (c(RGDf(-S-acetylthioacetyl)K)) was synthesized at a purity of 95% by Ansynth Service BV (The Netherlands).

Synthesis silica-coated QDs

CdSe (core) QDs (3.4 nm in diameter) were synthesized by the conventional organometallic synthesis route, described in detail elsewhere.[32] The CdSe QDs were coated with 7 monolayers of inorganic shells (2xCdS, 3x$Cd_{0.5}Zn_{0.5}S$, 2xZnS) according to a SILAR method that was recently published by Xie *et al.*[33]. Addition of these shells was performed by adding pre-calculated amounts of a 0.1M precursor solution (Cd oleate, CdZn oleate, Zn oleate, and sulphur in ODE) to 200 nmol CdSe QDs dispersed in a mixture of 4.5 ml ODE and 1.5 ml ODA at 230 °C. Each monolayer was allowed to grow for ten minutes before the next precursor solution was added. The CSS-QDs were purified by precipitation and redispersion

in a chloroform/acetone mixture for 3 times. The resulting core-shell-shell (CSS) QDs increased in size to 7.7 nm (± 0.9 nm) and were photostable in air for months, with a QY of 60%. The CSS-QDs were incorporated in silica spheres by a reverse micro-emulsion method.[10] In short, 1.3 ml Igepal was added to 10 ml cyclohexane and stirred for 15 minutes (850 rpm). Subsequently, 2 nmol of QDs (in 100 µl cyclohexane), 80 µl TEOS, and 150 µl ammonia was added with 15 minutes of stirring in between the additions. After the last addition the mixture was stirred for 1 minute, after which it was placed in the dark for 1 week. The resulting silica-coated QDs were centrifuged and re-dispersed in ethanol for at least 3 times to remove excess reactants from the silica synthesis (i.e. Igepal, TEOS, ammonia, and water).

Lipid coating of silica particles

The silica-coated QDs were subsequently capped with a hydrophobic ligand, by adding an excess of octadecanol (ODOH, 2.5 g in 5 ml of EtOH) to a dispersion of 2 nmol of silica-coated QDs in 5 ml ethanol. This mixture was first heated to 100 °C for 1 hour to remove the ethanol, after which the temperature was raised to 170 °C for 3 hours to covalently link the ODOH to the silica spheres by a condensation reaction.[34] The QY of the CSS QDs and ODOH coated QD/silica particles was determined by integrating the emission spectra of these samples (in chloroform) and comparing it to the integrated emission of both Rhodamine 6G and Rhodamine 101 (assuming a QY of 90% and 95% for these dyes respectively). Each emission spectrum was corrected for the relative absorbance of the sample at the excitation wavelength (497 nm in case of Rhodamine 6G and 528 nm in case of Rhodamine 101). Next, the ODOH-coated silica nanoparticles (with a QD incorporated) were dispersed in chloroform/methanol (20/1, v/v). PEG-DSPE, Mal-PEG-DSPE, Gd-DTPA-DSA were added in a molar ratio of 0.4/0.1/0.5. The amount of lipids was 25 times higher than the calculated amount of lipids for a monolayer on all nanoparticles. This solution was added to a mildly basic HEPES buffer (20 mM HEPES, 135 mM NaCl, pH 6.7) under vigorous stirring, which led to the formation of an emulsion that was subsequently heated to 110 °C to evaporate chloroform. Upon evaporation of chloroform, the milky suspension converted into a clear dispersion indicative of the total removal of chloroform and the formation of lipid-coated QD/silica nanoparticles. The excess of lipids was removed by centrifugation (3000 rpm) of the lipid coated QD/silica particles, which were redispersed in HEPES buffer. The cyclic 5mer RGD (c(RGDf(-S-acetylthioacetyl)K)) was conjugated to Mal-PEG-DSPE included in the lipid layer as described previously.[35] In short, acetyl protected-peptide was deacetylated in 0.05 M Hepes/0.05 M hydroxylamine-HCl/0.03 mM ethylenediamine tetraacetic acid (pH 7.0) for 1 hour at room temperature. The activated peptide was added to the Mal-PEG2000-DSPE containing particles. This preparation was stored at 4 ºC under N_2 overnight.

TEM and Dynamic Light Scattering (DLS)

A Tecnai 10 (FEI Company) transmission electron microscope, operated at an acceleration voltage of 100 kV, was used to take TEM images. Samples were prepared for negative staining by exchanging the buffer for a 0.125 M ammonium acetate and 0.26 mM EDTA adjusted to pH 7.4. This solution was then mixed in a 1:1 ratio with a 2% sodium phosphotungstate negative stain solution (pH 7.4). Formvar coated nickel grids were dipped in this solution and imaged shortly afterwards. The TEM micrographs were processed using TIA software (Tecnai

imaging and analysis software). Measurement of the size distribution of the ODOH coated QD/silica particles in chloroform and the Q-SiPaLCs suspended in deionized water was performed with a Malvern HPPS DLS (dynamic light scattering) instrument equipped with a He-Ne laser operating at 633 nm.

In vitro targeting experiments

Human umbilical vein derived endothelial cells (HUVEC) were cultured on gelatin (0.2% in PBS) coated tissue culture flasks (Costar, Cambridge, MA) in culture medium, RPMI-1640 (Life Technologies, Breda, The Netherlands), 10% human serum and 10% fetal calf serum (HS and FCS; University Hospital Maastricht, The Netherlands), 2 mM glutamine (Life Technologies), 50 U/ml penicillin and 50 ng/ml streptomycin (ICN Biomedicals, Aurora, OH). For all incubations 1.5 x 10^6 cells of passage 2-3 were used for experiments (at least n=2). The cells were incubated for 7 hours with RGD conjugated nanoparticles or control nanoparticles at a concentration of 0.07 nmol particles per ml medium. Association of the different nanoparticles to endothelial cells was assessed using fluorescence microscopy and magnetic resonance imaging. A Leica DMIL phase contrast fluorescence microscope (Leica Microsystems, Rijswijk, The Netherlands) equipped with a 20 Watt G4 HXL64250 Xenophot Halogen lamp (Leica) was used. Parallel phase contrast and red fluorescence (using a BP645-675 filter, Leica) images of the endothelial cell monolayers were taken at 200 times magnification. All fluorescence microscopy scans were made with the same settings for laser power and detector sensitivity, allowing direct comparison between different incubations. The cell density for both incubations in Figure 9.2 was comparable and therefore the difference in fluorescence intensity arises from the difference in the level of association.

Fluorescence imaging and MRI

Fluorescence imaging of cell pellets was performed using the Xenogen IVIS-200 small animal imaging system. A continuous external light source of 365 nm and an emission filter 610-630 nm were used. MRI experiments were performed on a 6.3 Tesla horizontal bore magnet (Oxford Instruments, England) interfaced to a Bruker (Bruker, Ettlingen, Germany) MR Imaging console. A 3 cm quadrature-driven birdcage coil was used. The cups containing cell pellets were placed in a custom-made sample holder, capable of carrying 4 Eppendorf-cups. For absolute quantification of T_1 an inversion recovery fast T_1-mapping sequence was used with 80 different inversion times. In the experiment TR was 20 s, TE was 9 ms, and the slice thickness was 0.7 mm. For absolute quantification of T_2 a multi spin echo sequence was used with TR 2000 ms and 32 echos that had a 9 ms echo spacing. A T_1-weighted image of cell pellets of the three incubations was generated with a TR of 1500 ms. In this image cells with a high content of Gd appear brighter than cells with a low content of Gd or no Gd. In all the MRI experiments the FOV was 3 cm^2, the matrix size 128 x 128 voxels and the slice thickness 0.7 mm.

9.3 Results and discussion

Highly photo-stable and luminescent CdSe/CdS/$Cd_{0.5}Zn_{0.5}S$/ZnS core-shell-shell (CSS) QDs were synthesized according to a SILAR procedure reported by Xie *et al.*[33] Subsequently, a reverse micelle method reported earlier[10, 11] was used to incorporate QDs in the centre of highly monodisperse silica particles of 31 nm (± 4 nm), see Figure 9.1A. The synthesis involved the dispersion of hydrophobic QDs in cyclohexane, to which a non-ionic surfactant (Igepal), a silane precursor (TEOS, tetraethyl orthosilicate), and catalyst (ammonia) were added. The exact incorporation mechanism and details on the synthesis are published elsewhere.[36] In short, hydrolyzed TEOS present in the initial reaction mixture (before adding ammonia) replaces the hydrophobic ligands on the QDs. The TEOS-coated QDs are then transferred to the hydrophilic interior of the reverse micelles, where subsequent silica growth takes place. The majority of the silica particles contained a single QD in the centre, while only a small fraction of the silica particles contained 2 or more QDs per particle (Figure 9.1A). Although the QD/silica particles thus obtained are well-soluble in ethanol or water, the pharmacokinetics of charged

Scheme 9.1. Overview of the multi-step synthesis of Q-SiPaLCs. (a) Incorporation of CSS-QDs in silica spheres by the reverse micelle method. (b) Hydrophobic coating of silica by ODOH, after which they can be dispersed in chloroform. (c) Addition of the different lipids to the QD/silica particles in chloroform, which is subsequently added to a HEPES buffer. (d) Vigorous stirring results in an emulsion, with the chloroform and nanoparticles enclosed in a lipid monolayer. (e) Chloroform is evaporated by heating the mixture, resulting in water soluble Q-SiPaLCs. See experimental section for details. The lower panel displays the structural formulas of the lipids.

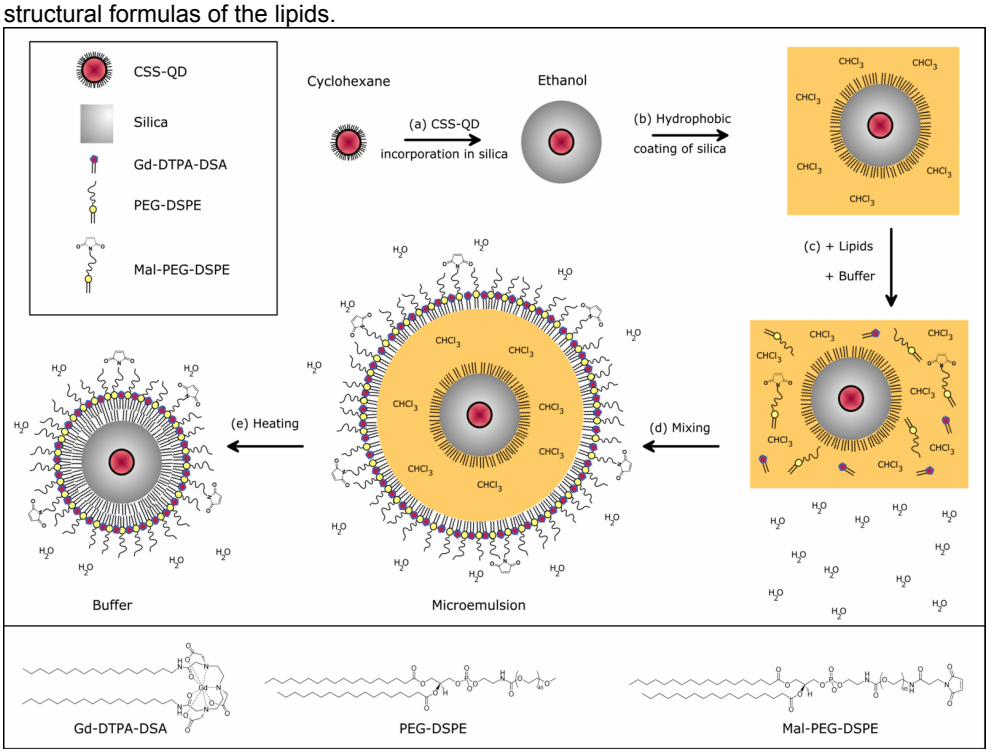

surface particles are unfavorable, typically due to a short circulation half-life and/or accumulation in the lungs.[37, 38] In order to obtain bio-applicability by a dense lipid coating, the QD/silica particles were first made hydrophobic by an octadecanol (ODOH) coating. This was achieved using a well-known condensation reaction[34], where the alcohol group of ODOH reacts with the hydroxyl groups at the silica surface to form a covalent bond, neutralizing the surface charges. The hydrophobic QD/silica particles were subsequently coated with a dense monolayer of lipids using a simple and fast procedure reported earlier for hydrophobic nanocrystals.[35, 39] The procedure involves the addition of lipids and water to the hydrophobic QD/silica particles in chloroform, followed by the evaporation of chloroform, leaving behind a clear suspension of well-dispersed, uncharged silica particles in lipidic micelles. The total synthesis procedure is schematically summarized in Scheme 9.1. The lipid coating is versatile, because in principal any (functional) amphiphile may be incorporated in this lipid layer. As an example, we have used a combination of Gd-DTPA-based lipids to introduce paramagnetic properties for MRI, pegylated lipids to improve biocompatibility, and maleimide-terminated (pegylated) lipids for conjugation of a biofunctional group. We will refer to the synthesized QDs in Silica with a Paramagnetic Lipidic Coating as Q-SiPaLCs.

The nanoparticles were characterized in terms of their size, optical and magnetic properties. We performed TEM and negative staining TEM (Figure 9.1A) as well as dynamic light scattering (DLS) measurements to determine the morphology and size of the silica particles before and after applying the lipid coating. Negative stain TEM (which allows the visualization of hydrophobic substances) images were analyzed, revealing a hydrophobic layer of 3.9 nm (± 0.5 nm) around individual particles, illustrated by the bright corona around the silica particle (Figure 9.1A, inset). This 4 nm thick hydrophobic layer confirms the presence of both the ODOH coating around silica (~ 2nm), and the stearyl-chains of the lipids (~ 2nm) around the particles. DLS measurements show an average diameter of 50 nm for ODOH coated QD/silica particles, increasing to 58 nm after the application of the lipid coating (Figure 9.1B). We note that DLS is not the most appropriate method to obtain an absolute value for the sizes of the particles, because the technique generally over-estimates the size of small colloidal particles. This may explain the difference between the size of ODOH-coated particles as determined by DLS (50 nm), and what one would expect based on the size of the bare silica particles as determined by TEM (35 nm, another, slightly larger batch of QD/silica particles was used for these DLS experiments) and the increase in size due to ODOH (2 x 2 nm). However, the increase in diameter after lipid coating was reproducibly measured by DLS, and is in the order of 8-9 nm. This increase is in reasonable agreement with what one may expect in case a single silica nanoparticle is coated with both paramagnetic lipids (~2 nm), and pegylated lipids (~10 nm).

Figure 9.1C displays the absorption and emission spectra. The emission spectrum is shown for the final Q-SiPaLCs in HEPES buffer. The absorption spectrum in Figure 9.1C was measured for the QDs in silica with an octadecanol coating, dispersed in chloroform. The latter system is refractive-index matched (in contrast to the Q-SiPaLCs in water), allowing for a scattering-free absorption measurement and reliable determination of the quantum yield (QY). The absorption spectrum displays multiple absorption features as a result of discrete excitonic transitions in the CSS-QDs, which can be observed due to the high quality and

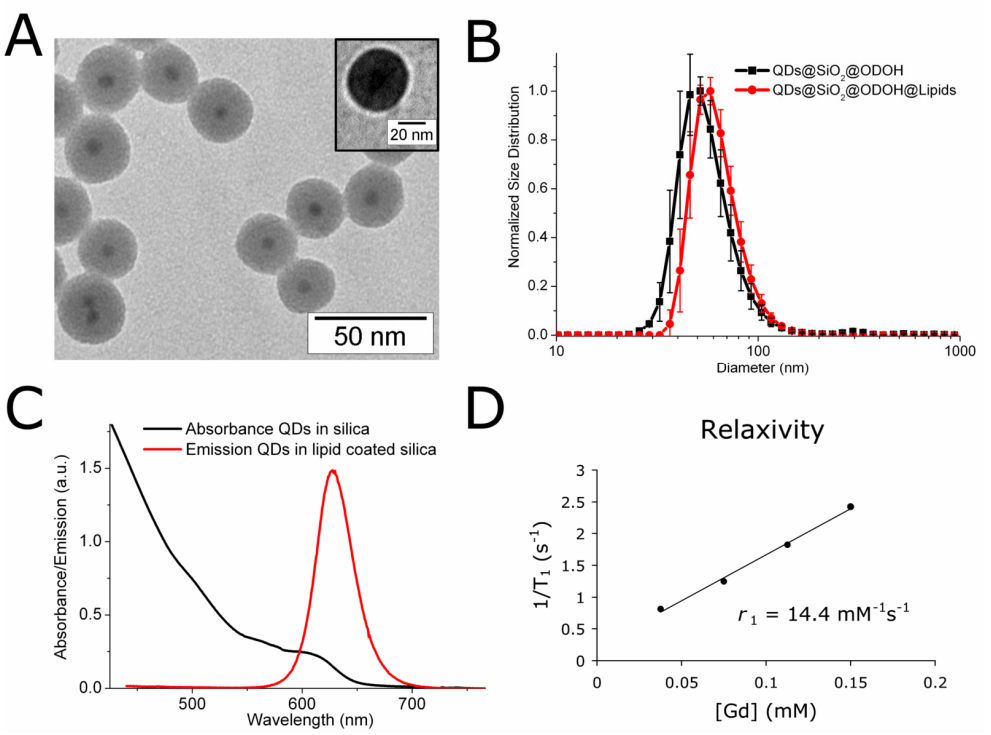

Figure 9.1 (A) TEM image of monodisperse QD/silica particles of 31 nm (± 4 nm) with a single QD (7.7 nm, black spots) incorporated in the centre. Inset shows an image from negative staining TEM, where the bright corona illustrates the hydrophobic layer around the silica particle. (B) DLS of ODOH capped QD/silica nanoparticles and ODOH capped QD/silica nanoparticles encapsulated in lipids. (C) Absorption and emission spectra of the CSS-QDs in silica. (D) Relaxation rates of the Q-SiPaLCs as a function of the concentration of Gd^{3+} ions (determined by ICP-MS).

monodispersity of the QDs. The initial QY of the CSS-QDs was 60%, but decreased as a result of the silica coating. This decrease is difficult to measure due to the scattering of the silica particles in ethanol, but it is estimated that the QY after silica coating is 25%. Coating the QD/silica particles with ODOH increased the QY to 35%, which could be accurately determined because of the scattering-free dispersion of the hydrophobic particles in chloroform. The QY of the lipid coated QD/silica particles in water was slightly lower (by eye), which was again difficult to quantify due to scattering. It should be noted that a significant QY-enhancement of the silica coated QDs is observed upon UV-illumination (which was avoided here when determining the QY, to obtain the lower-limit). The silica coating and further coating steps did not change the shape of absorption or emission spectra of the QDs. A detailed discussion on the evolution of the QY of the QDs upon incorporation in silica and photo-activation is published elsewhere.[36] The emission maximum of the CSS QDs lies at 630 nm. This relatively long wavelength is favourable for *in vivo* fluorescence imaging because of the lower autofluorescence levels of tissue for longer wavelength excitation and the longer penetration depth into tissue of light with this wavelength.

To make the particle also suitable as an MRI contrast agent, Gd-DTPA-DSA was included in the lipidic coating of the Q-SiPaLCs. This paramagnetic amphiphile consists of Gd-DTPA, a clinically used contrast agent for MRI, and two saturated acyl chains with a chain length of 18 carbon atoms. To evaluate the performance as an MRI contrast agent, the longitudinal relaxation rates R_1 of a dilution series were determined at 60 MHz, and Gd contents of these samples were determined by ICP-MS. From these data the longitudinal relaxivity r_1 of the Gd^{3+} ions was calculated to be 14.4 $mM^{-1}s^{-1}$ (Figure 9.1D), which is a factor of 3-4 higher than free Gd-DTPA molecules in solution. This difference is ascribed to the lower tumbling rate of the Gd-lipids in the micelle compared to free Gd-DTPA molecules, enhancing the molar relaxivity.[31, 35, 40]

As mentioned above, the number of Gd ions was determined by ICP-MS for a dispersion of Q-SiPaLCs. The concentration of Q-SiPaLCs in this dispersion was estimated from the initial number of QDs used for the silica synthesis at 0.24 µM. We found with ICP-MS that the concentration of Gd in the same dispersion was 0.60 mM, which gives a number of 2500 Gd-lipids per silica particle. The estimated maximum number of lipids in a densely packed lipid layer surrounding a 31 nm silica particle is approximately 5000, using a literature value of 60 A^2/lipid.[41] Since half of the lipids consisted of Gd-DTPA-DSA, the estimated (2500) and experimentally determined (2500) number of Gd-lipids are in excellent agreement, confirming a dense coating of lipids around the Q-SiPaLCs. This is further confirmed by the number of Cd ions that was determined for the same dispersion using ICP-MS, which was found to be 0.50 mM. The number of Cd ions per CSS QD can be estimated to be approximately 2200, by assuming an average wurtzite unit cell volume of 1.1E-28 m^3 (for CdSe, CdS and CdZnS) with Z=2, and taking into account the presence of Zn ions in the outer shells. Assuming a number of 2200 Cd ions per QD, the concentration of QDs in the dispersion is estimated to be 0.23 µM, which correlates well with the estimation above.

Taking into consideration that the 31 nm Q-SiPaLCs thus carry approximately 2500 Gd-DTPA-DSA lipids per particle (average between calculated and experimentally determined value), the r_1 relaxivity per particle was estimated to be 36000 $mM^{-1}s^{-1}$. The relaxivity of the Q-SiPaLCs per particle is thereby a factor of 21 higher than for our previously reported lipid coated QDs[35], and a factor of 8-12 higher than Gd-wedge-coated QDs that were recently reported.[42] In another recent report, the relaxivity of Gd-DOTA covalently attached to silica was determined to be 23 $mM^{-1}s^{-1}$, and apart from the lower tumbling rate the very high relaxivity was ascribed to a higher water density close to the Gd-DOTA complexes due to the absence of lipids.[31] However, their maximum relaxivity per particle was still a factor of 3 lower compared to the Q-SiPaLCs due to a lower payload of the paramagnetic complexes per particle. Similarly, the relaxivity per particle of Q-SiPaLCs is a factor of 40 higher than Mn-doped QDs that were recently reported, despite their high molar relaxivity of 18 $mM^{-1}s^{-1}$.[43] Other lipid-based particles, such as liposomes[44, 45] or microemulsions[46], are capable of carrying a much higher payload of Gd-chelates (typically 25,000 to 100,000 molecules) and therefore exhibit a higher relaxivity per particle. On the other hand, such particles are considerably larger (100 to 250 nm). Apart from r_1, we also determined the transverse relaxivity r_2. The r_2/r_1 ratio determines whether a contrast agent is more suitable for T_1-weighted or for T_2-weighted MRI. This value was determined to be

1.6 for our nanoparticulate contrast agent and therefore can be considered an effective T_1 contrast agent.

The characterization of the Q-SiPaLCs shows that they form a very promising particle for dual modality imaging. A crucial aspect for application however, is their ability to be targeted to specific cell types. The targeting potential of this nanoparticle was demonstrated on serum activated human umbilical vein endothelial cells (HUVEC) *in vitro*. Nanoparticles can be targeted to these cells by conjugation of multiple RGD-peptides to the maleimide exposing PEG-lipids. These tri-peptides specifically bind to αvβ3-integrin, an adhesion molecule that is expressed by proliferating HUVEC.[47] This receptor is also predominantly present at angiogenically activated blood vessels, such as those present in tumors,[48] and has been used for identification of angiogenesis with molecular imaging.[47] We conjugated ~650 RGD-peptides per particle using a method described previously.[35] In short, thiol exposing peptides were covalently linked to the distal ends of maleimide functionalized PEG lipids incorporated in the outer lipid layer of the particle. To assess the specificity of the contrast agent, HUVEC were incubated with either RGD-functionalized nanoparticles (targeted), non-functionalized nanoparticles (untargeted, no RGD), or they were not incubated with nanoparticles (control). We first established the optimal incubation time on a limited number of

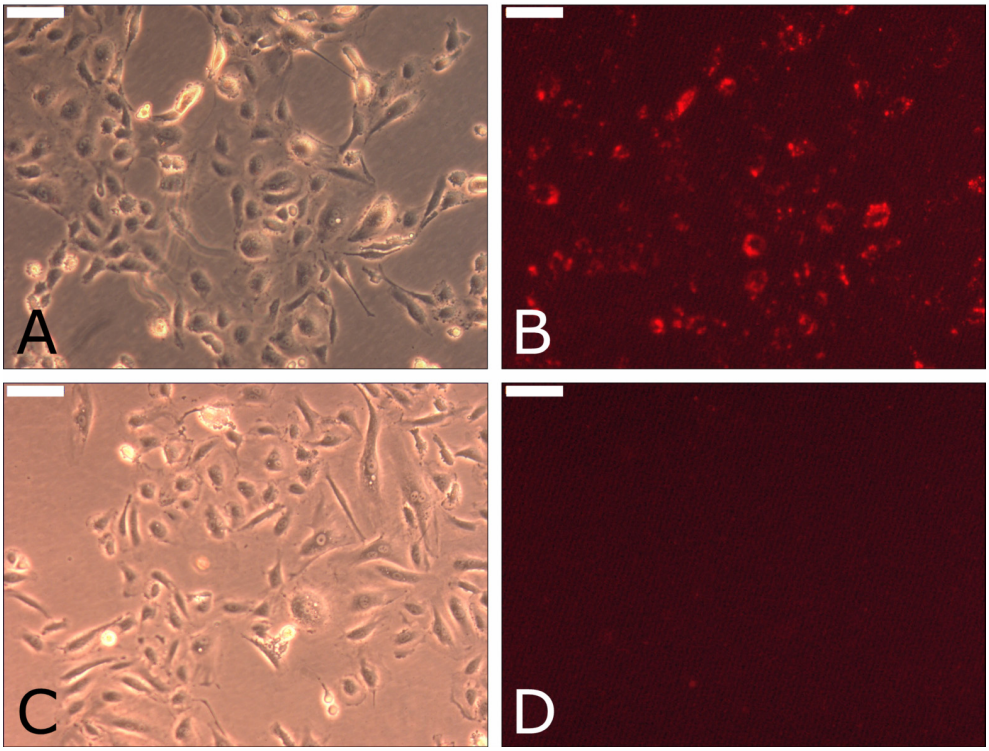

Figure 9.2 (A, C) Bright-field microscopy images and (B, D) fluorescence microscopy images of HUVEC incubated with (A, B) RGD-conjugated nanoparticles or (C, D) non-conjugated (untargeted) nanoparticles. The scale bars correspond to 100 µm.

cells. Thereafter, incubations were done in duplo for 7 hours at 37 °C in tissue culture flasks containing ~1.5 x 10^6 HUVEC. Subsequently, cells were washed twice with PBS and fixed with 4% paraformaldehyde solution. In Figure 9.2A and 2B bright-field and fluorescence microscopy images are shown of HUVEC that were incubated with RGD-conjugated nanoparticles. The Q-SiPaLCs are clearly associated with the cells and were found to be internalized, at a perinuclear location. Fluorescence images of HUVEC incubated with untargeted Q-SiPaLCs (no functionalization by RGD) showed marginal or no fluorescence (Figure 9.2C and 2D), similar to the untreated control cells (not shown). These results demonstrate that lipid-coated QD/silica particles conjugated with RGD peptides are actively taken up by the activated endothelial cells, and that nonspecific uptake (even after 7 hours of incubation) is negligible.

Next, the cells were collected and transferred into small Eppendorf cups. In daylight there is no visual difference between the different loosely packed cell pellets (Figure 9.3A). Under UV illumination (365 nm) only the cells that had been incubated with RGD conjugated Q-SiPaLCs exhibit a bright red fluorescence, and could clearly be distinguished from the two other cell pellets (Figure 9.3B). In addition, we performed quantitative fluorescence imaging on the different cell pellets (Figure 9.3C) using the Xenogen IVIS-200. An external illumination source of 365 nm was used, while the photon count was acquired using a spectral imaging filter of 620 nm. In Figure 9.3D the mean photon counts of cell pellets incubated with targeted particles, cell pellets incubated with untargeted particles, and control cell pellets are depicted. A ~25-fold and ~50-fold difference in photon count were found between the targeted and untargeted cell pellets, and the targeted and control pellets, respectively.

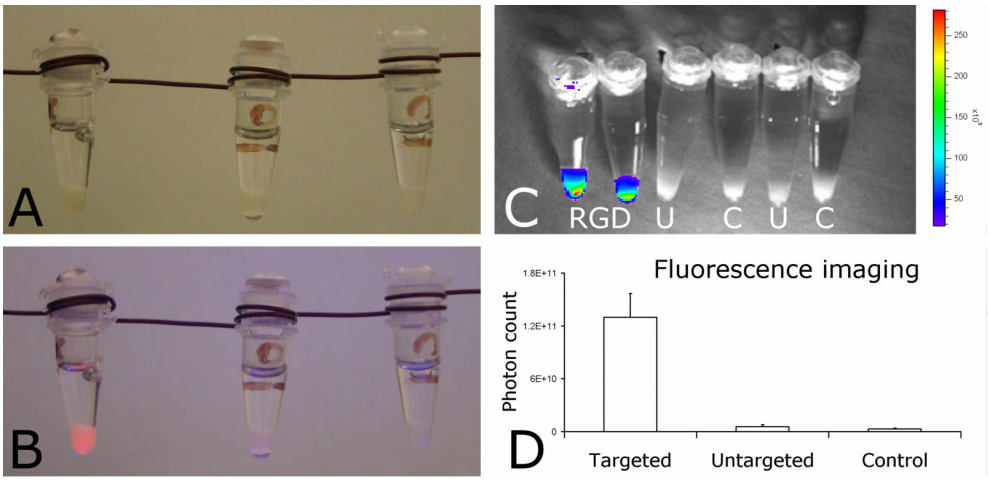

Figure 9.3 Pellets of cells incubated with RGD-conjugated targeted Q-SiPaLCs (left), non-conjugated untargeted Q-SiPaLCs (middle), and untreated control cells (right) (A) in daylight and (B) illuminated with 365 nm UV. (C) Overlay of a black/white photograph and quantitative fluorescence image of the different cell pellets under UV illumination at 365 nm (RGD=targeted, U=untargeted, C=control cells). The emission intensity from U and C is too low (less than 20 x 10^9 counts) to be displayed by one of the colours in the scalebar. (D) Mean photon counts of the different cell pellets.

Subsequently, MRI was performed on these cell pellets. A T_1-weighted image of the different cell pellets is depicted in Figure 9.4A and clearly demonstrates higher signal intensity for the pellet of cells incubated with the RGD conjugated Q-SiPaLCs (the bright white circle) as compared to the control cell pellets (grey circles). In addition, T_1 relaxation times were determined in order to allow a more quantitative evaluation of Q-SiPaLCs as a MRI contrast agent. The mean values were 1706 ms, 2189 ms, and 2460 ms, for cells incubated with the targeted particles, cells incubated with untargeted particles, and untreated cells, respectively. The differences in relaxation rate R_1 (1/ T_1) between control cell pellets and cell pellets that were incubated with the nanoparticles correlate with the concentration of contrast agent in the cell pellets. Therefore, we calculated these differences in mean relaxation rates between the control cell pellets and the targeted or untargeted cell pellets. The values clearly demonstrate the effective and specific targeting of this nanoparticulate agent to angiogenically activated endothelial cells (Figure 9.4B). (Scan parameters are in the experimental section).

The Q-SiPaLCs reported here demonstrate the integration of multiple imaging properties in a single bio-applicable nanoparticle and the specific uptake by living cells. This nanoparticulate probe has several advantages over existing agents in terms of detection sensitivity (contrast) due to the high fluorescence quantum yield (35%) and high relaxivity. In addition, it presents a new and versatile platform for a wide range of contrast agents suitable for multimodality imaging. In biomedical research the two main applications of nanoparticles are their use as carriers for drugs and diagnostic active materials. Their size varies from a few nanometers (QDs, iron oxide nanoparticles, micelles)[35, 49, 50] up to hundred nanometers (liposomes)[2] and even several hundred nanometers (microemulsions)[46] to micrometers (microbubbles).[51] Depending on the application, and importantly, the targeted site (vascular versus extravascular), the size may dictate effectiveness. For example in a study by Stroh et al. it was shown that QD containing silica particles of different sizes (100 nm versus 500 nm) extravasate from the

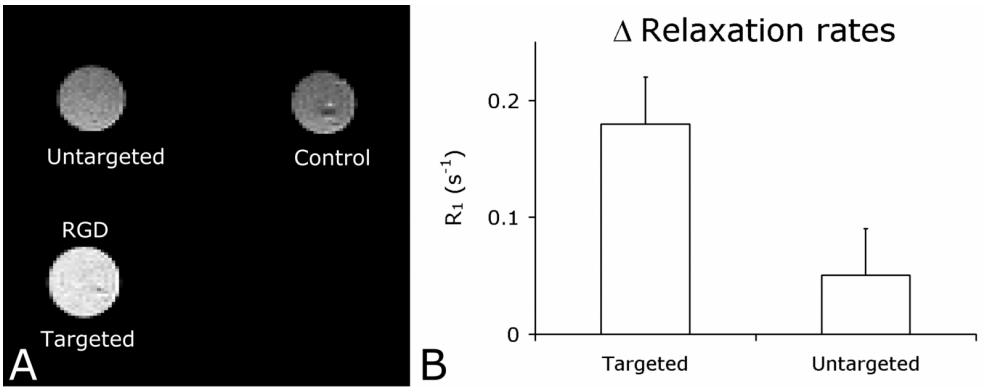

Figure 9.4 (A) T_1-weighted MRI of the different cell pellets (same pellets as displayed in Figure 9.3) revealed specific uptake of the targeted nanoparticles. (B) Difference in relaxation rates (R_1) of the targeted and untargeted cell pellets compared to the relaxation rate of the control cell pellet (set to zero). The differences in relaxation rate reflect the concentration of contrast agent in the untargeted and targeted cell pellets.

vasculature into the tumor to differing extents.[52] Our particles are highly monodisperse, as a result of the reverse micelle method used to grow a silica shell of a well-defined thickness. As compared to other nanoparticles such as micelles or liposomes, a great advantage of our particles is that they can be easily and accurately tuned to any desired size from ~20 nm to over one micron, by increasing the diameter of the silica spheres. The silica shell is also expected to prevent leaking of Cd and thus reduce the cytotoxicity due to the Cd-containing quantum dots. In addition, any desired fluorescence colour or a combination of colours can be chosen to allow for multiplexing or "bar-coding"[53], by inserting different kinds of QDs in the silica spheres. Furthermore, due to the high surface area of the Q-SiPaLCs, a high payload of Gd-DTPA-DSA lipids can be integrated per particle. Therefore, the relaxivity per particle is high, and can even be increased significantly by increasing the size of the silica particle. Target-specificity can be introduced using PEG-lipids with a functional moiety, like maleimide used in this study. The number of functional groups can be varied, which allows the creation of a particle with multiple ligands. This can increase the targeting efficiency of the particle due to multivalent interactions. This is an important issue, since it was recently reported that the target-specificity of maleimide-targeted QDs may be poor when a single QD contains less that 1 target peptide per QD, making the uptake highly nonspecific, especially due to the small size of a single QD.[54] The design of our Q-SiPaLCs solves this problem, because of the possibility to attach multiple ligands per particle. Furthermore, the nonspecific uptake of the Q-SiPaLCs by HUVEC is shown to be negligible in this study. The nanoparticles as designed in the present report can be applied for imaging of ongoing angiogenesis as a diagnostic tool in the management of cancer. Next to the RGD-peptides used in this study, other ligands, such as antibodies[55], antibody fragments[56], or proteins[57] may be conjugated in a similar fashion. The PEG-lipids that surround the Q-SiPaLCs ensure good pharmacokinetics and an improved biocompatibility of the nanoparticles.

The presently reported contrast agent design offers numerous possibilities to integrate a wide range of properties for multimodality imaging. We have successfully demonstrated a general and effective pathway for making silica (nano)spheres bio-applicable and target-specific. Recently, we have carried out *in vivo* experiments to investigate the biodistribution properties of the Q-SiPaLCs. To study the pharmacokinetics, mice were intravenously injected with either Q-SiPaLCs (untargeted) or bare QD-silica particles. The bare silica particles were not coated by ODOH or lipids, and as a results, these particles were simply terminated by Si-OH or SiO^- groups. After injection, small blood-samples were taken from the mice at different time-points, and analyzed by quantitative fluorescence imaging (Figure 9.5A and B) and ICP-MS (on Cd-content, Figure 9.5B). Without going into further experimental details, the preliminary data of both techniques reveal an enhanced circulation half-life of the Q-SiPaLCs (165 ± 30 minutes) compared to the bare silica particles (16 ± 3 minutes). Note that the results from both techniques (quantitative fluorescence imaging and ICP-MS) for the same type of particle are in in good agreement with each other. These results confirm that the Q-SiPaLCs have favourable bio-distribution properties compared to bare silica particles, and the long circulation half-life of almost three hours is promising for targeted *in vivo* studies using the lipid-coated silica particles reported in this chapter.

In the future, the lipid coating can be applied to any combination of contrast agents incorporated in silica to make them suitable for biomedical applications. For example, magnetite nanoparticles (for MRI detection), gold or bismuth nanoparticles (for CT or EM detection), or fluorescent materials (QDs, dyes, phosphor nanocrystals) can readily be integrated in silica, and can be made bio-applicable through the procedure reported here. Additional properties may be added to the particle by inserting paramagnetic or fluorescent amphiphiles in the

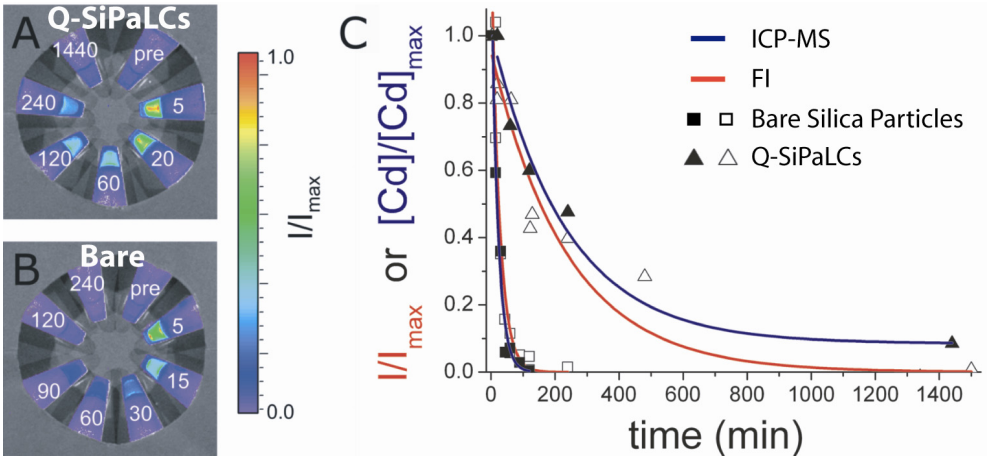

Figure 9.5. Determination of Q-SiPaLC and bare-silica blood circulation half-life values. Fluorescence intensity (FI), resulting from the quantum dots in Q-SiPaLC (A) and bare silica particles (B), was quantified in blood plasma taken at different time points (indicated in minutes) post injection. (C) As another measure for the relative particle concentrations, cadmium determination with ICP-MS was done on blood samples and both sets of results were plotted and fitted (blue fit of closed symbols for ICP-MS; red fit of open symbols for FI) to determine the half-life values of Q-SiPaLCs (triangles) and bare silica particles (squares).

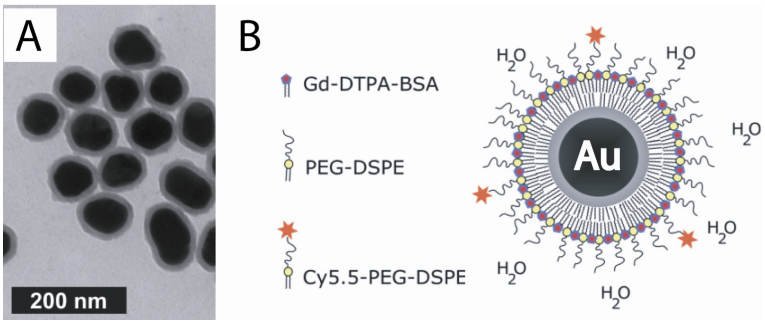

Figure 9.6 (A) TEM image of 65 nm gold nanocrystals coated by a thin layer of silica. (B) Schematic representation of the Au-SiFluPaLC: a Au nanocrystal in a Silica sphere with a Fluorescent (Cy5.5-PEG-DSPE) and Paramagnetic (Gd-DTPA-BSA) Lipidic coating. Pegylated lipids (PEG-DSPE) are incorporated as well in the lipid coating.

lipidic coating, for example. Drug delivery and gene targeting may also be functionalities that can be accomplished using this biocompatible silica nanoparticle platform. As a proof-of-principle, we have developed a tri-modal particle based on the lipid-coated silica particle concept. Gold nanocrystals of 65 nm were coated by a thin layer of silica (Figure 9.6A), and made hydrophobic by ODOH. Subsequently, the hydrophobic gold-silica particles were coated by a combination of paramagnetic (Gd-DTPA-BSA), fluorescent (Cy5.5-PEG-DSPE)), and PEGylated lipids (PEG-DSPE), using the procedure as described in the experimental section. A schematic representation of the particles is given in Figure 9.6B. The resulting Au particles in Silica with a Fluorescent and Paramagnetic Lipid Coating (Au-SiFluPaLC) can be detected by fluorescence (confocal) microscopy, MRI, and CT. This was assessed by incubating macrophage cells (which are known for their high aspecific uptake) with the Au-SiFluPaLCs for 24 hours, after which they were washed and collected in small Eppendorf-cups. Confocal Microscopy, MRI, and CT on these cells (Figure 9.7 A-C) confirm that the Au-SiFluPaLCs can be detected by these three imaging techniques.

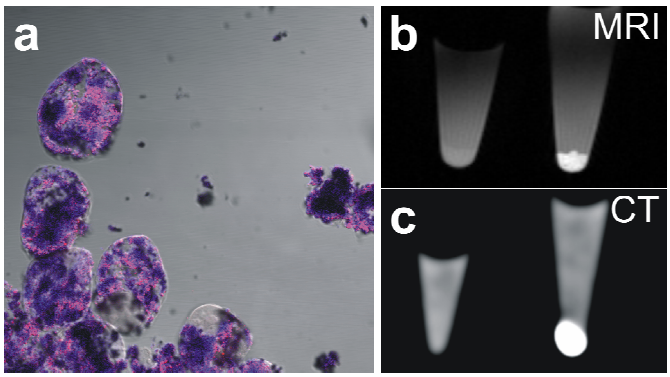

Figure 9.7. Confocal Microscopy (A), MRI (B), and CT (C) on macrophage cells incubated with trimodal Au-Si-FluPaLC particles. The blue colour in (A) results from DAPI-staining, the red colour represents the Cy5.5 fluorescence. In panels (B) and (C), control and incubated cells are displayed left and right respectively, to illustrate the difference in contrast.

9.4 Conclusions

In summary, we have developed a new method for making bio-applicable silica nanoparticles that can serve as a contrast agent for target-specific multimodality imaging. The nanoparticle is comprised of a QD incorporated in a silica sphere of 31 nm. First the silica surface is made hydrophobic and subsequently it is surrounded by pegylated, paramagnetic, and biofunctional lipids. This results in a highly monodisperse, fluorescent, and paramagnetic contrast agent suitable for both fluorescence imaging and MRI studies, and it shows a highly specific uptake by HUVEC. The use of the presently reported method for creating biocompatible and target specific silica nanoparticles opens a new platform for multimodality imaging contrast agents by integrating any desired combination of contrast agents in the silica nanoparticle, and inserting (combinations of) functional amphiphiles in the lipidic coating. Preliminary *in vivo* biodistribution studies show an enhanced circulation half-time of lipid coated silica particles compared to their bare counterparts. Finally, the broad applicability of the concept described in this chapter is illustrated by an example of a trimodal particle that was developed (for fluorescence imaging, MRI, and CT), comprised of a gold nanocrystal in silica, surrounded by a fluorescent and paramagnetic lipidic coating.

9.5 References

1. R. Sinha, G.J. Kim, S. Nie, and D.M. Shin, *Mol. Cancer. Ther.*, **2006**. *5* (8): p. 1909-17.
2. V.P. Torchilin, *Nat. Rev. Drug. Discov.*, **2005**. *4* (2): p. 145-60.
3. S.M. Moghimi, A.C. Hunter, and J.C. Murray, *Faseb J.*, **2005**. *19* (3): p. 311-30.
4. J.W. Bulte and D.L. Kraitchman, *NMR Biomed.*, **2004**. *17* (7): p. 484-99.
5. B. Sitharaman, K.R. Kissell, K.B. Hartman, L.A. Tran, A. Baikalov, I. Rusakova, Y. Sun, H.A. Khant, S.J. Ludtke, W. Chiu*, et al.*, *Chem Commun*, **2005** (31): p. 3915-3917.
6. D. Kim, S. Park, J.H. Lee, Y.Y. Jeong, and S. Jon, *J. Am. Chem. Soc.*, **2007**. *129* (24): p. 7661-7665.
7. X. Michalet, F.F. Pinaud, L.A. Bentolila, J.M. Tsay, S. Doose, J.J. Li, G. Sundaresan, A.M. Wu, S.S. Gambhir, and S. Weiss, *Science*, **2005**. *307* (5709): p. 538-544.
8. S.A. Wickline, A.M. Neubauer, P.M. Winter, S.D. Caruthers, and G.M. Lanza, *J. Magn. Reson. Imaging*, **2007**. *25* (4): p. 667-80.
9. W.J.M. Mulder, A.W. Griffioen, G.J. Strijkers, D.P. Cormode, K. Nicolay, and Z.A. Fayad, *Nanomedicine*, **2007**. *2* (3): p. 307-324.
10. M. Darbandi, R. Thomann, and T. Nann, *Chem. Mater.*, **2005**. *17* (23): p. 5720-5725.
11. S.T. Selvan, T.T. Tan, and J.Y. Ying, *Adv. Mater.*, **2005**. *17* (13): p. 1620-+.
12. C. Graf, D.L.J. Vossen, A. Imhof, and A. van Blaaderen, *Langmuir*, **2003**. *19* (17): p. 6693-6700.
13. L.M. Liz-Marzan, M. Giersig, and P. Mulvaney, *Langmuir*, **1996**. *12* (18): p. 4329-4335.
14. A.P. Philipse, M.P.B. Vanbruggen, and C. Pathmamanoharan, *Langmuir*, **1994**. *10* (1): p. 92-99.
15. T.R. Sathe, A. Agrawal, and S.M. Nie, *Anal. Chem.*, **2006**. *78* (16): p. 5627-5632.
16. J. Kim, J.E. Lee, J. Lee, J.H. Yu, B.C. Kim, K. An, Y. Hwang, C.H. Shin, J.G. Park, and T. Hyeon, *J. Am. Chem. Soc.*, **2006**. *128* (3): p. 688-689.
17. D.K. Yi, S.T. Selvan, S.S. Lee, G.C. Papaefthymiou, D. Kundaliya, and J.Y. Ying, *J. Am. Chem. Soc.*, **2005**. *127* (14): p. 4990-4991.
18. V. Salgueiriño-Maceira, M.A. Correa-Duarte, M. Spasova, L.M. Liz-Marzán, and M. Farle, *Adv. Funct. Mater.*, **2006**. *16* (4): p. 509-514.
19. A. Vanblaaderen and A. Vrij, *Langmuir*, **1992**. *8* (12): p. 2921-2931.
20. A. Burns, H. Ow, and U. Wiesner, *Chem. Soc. Rev.*, **2006**. *35* (11): p. 1028-1042.
21. H. Ow, D.R. Larson, M. Srivastava, B.A. Baird, W.W. Webb, and U. Wiesner, *Nano Lett.*, **2005**. *5* (1): p. 113-117.
22. C.-W. Lu, Y. Hung, J.-K. Hsiao, M. Yao, T.-H. Chung, Y.-S. Lin, S.-H. Wu, S.-C. Hsu, H.-M. Liu, C.-Y. Mou*, et al.*, *Nano Lett.*, **2007**. *7* (1): p. 149-154.
23. W.J. Rieter, J.S. Kim, K.M.L. Taylor, H.Y. An, W.L. Lin, T. Tarrant, and W.B. Lin, *Angew. Chem. Int. Ed.*, **2007**. *46* (20): p. 3680-3682.
24. T.J. Yoon, K.N. Yu, E. Kim, J.S. Kim, B.G. Kim, S.H. Yun, B.H. Sohn, M.H. Cho, J.K. Lee, and S.B. Park, *Small*, **2006**. *2* (2): p. 209-215.
25. L. Wang, K.M. Wang, S. Santra, X.J. Zhao, L.R. Hilliard, J.E. Smith, J.R. Wu, and W.H. Tan, *Anal. Chem.*, **2006**. *78* (3): p. 646-654.
26. F.Q. Chen and D. Gerion, *Nano Lett.*, **2004**. *4* (10): p. 1827-1832.
27. D. Gerion, F. Pinaud, S.C. Williams, W.J. Parak, D. Zanchet, S. Weiss, and A.P. Alivisatos, *J. Phys. Chem. B*, **2001**. *105* (37): p. 8861-8871.
28. N.R. Jana, C. Earhart, and J.Y. Ying, *Chem. Mater.*, **2007**. *19* (21): p. 5074-5082.
29. S.T. Selvan, P.K. Patra, C.Y. Ang, and J.Y. Ying, *Angew. Chem. Int. Ed.*, **2007**. *46* (14): p. 2448-2452.
30. A. Wolcott, D. Gerion, M. Visconte, J. Sun, A. Schwartzberg, S.W. Chen, and J.Z. Zhang, *J. Phys. Chem. B*, **2006**. *110* (11): p. 5779-5789.
31. D. Gerion, J. Herberg, R. Bok, E. Gjersing, E. Ramon, R. Maxwell, J. Kurhanewicz, T.F. Budinger, J.W. Gray, M.A. Shuman*, et al.*, *J. Phys. Chem. C*, **2007**. *111* (34): p. 12542-12551.
32. C. de Mello Donega, M. Bode, and A. Meijerink, *Phys. Rev. B*, **2006**. *74* (8): p. 085320.

33. R.G. Xie, U. Kolb, J.X. Li, T. Basche, and A. Mews, *J. Am. Chem. Soc.*, **2005**. *127* (20): p. 7480-7488.
34. A.K. van Helden, J.W. Jansen, and A. Vrij, *J. Colloid Interface Sci.*, **1981**. *81* (2): p. 354-368.
35. W.J.M. Mulder, R. Koole, R.J. Brandwijk, G. Storm, P.T.K. Chin, G.J. Strijkers, C. de Mello Donega, K. Nicolay, and A.W. Griffioen, *Nano Lett.*, **2006**. *6* (1): p. 1-6.
36. R. Koole, M.M. van Schooneveld, J. Hilhorst, C. de Mello Donega, D.C.t. Hart, A. van Blaaderen, D. Vanmaekelbergh, and A. Meijerink, *Chem. Mater.*, **2008**. *20* (7): p. 2503-2512.
37. V.D. Awasthi, D. Garcia, R. Klipper, B.A. Goins, and W.T. Phillips, *J. Pharmacol. Exp. Ther.*, **2004**. *309* (1): p. 241-248.
38. D.C. Litzinger, J.M. Brown, I. Wala, S.A. Kaufman, G.Y. Van, C.L. Farrell, and D. Collins, *BBA-Biomembranes*, **1996**. *1281* (2): p. 139-149.
39. B. Dubertret, P. Skourides, D.J. Norris, V. Noireaux, A.H. Brivanlou, and A. Libchaber, *Science*, **2002**. *298* (5599): p. 1759-1762.
40. S. Aime, M. Botta, M. Fasano, and E. Terreno, *Chem. Soc. Rev.*, **1998**. *27* (1): p. 19-29.
41. H.I. Petrache, S.W. Dodd, and M.F. Brown, *Biophys. J.*, **2000**. *79* (6): p. 3172-3192.
42. L. Prinzen, R.J.J.H.M. Miserus, A. Dirksen, T.M. Hackeng, N. Deckers, N.J. Bitsch, R.T.A. Megens, K. Douma, J.W. Heemskerk, M.E. Kooi*, et al.*, *Nano Lett.*, **2007**. *7* (1): p. 93-100.
43. S. Wang, B.R. Jarrett, S.M. Kauzlarich, and A.Y. Louie, *J. Am. Chem. Soc.*, **2007**. *129* (13): p. 3848-3856.
44. W.J.M. Mulder, G.J. Strijkers, A.W. Griffioen, L. van Bloois, G. Molema, G. Storm, G.A. Koning, and K. Nicolay, *Bioconjug. Chem.*, **2004**. *15* (4): p. 799-806.
45. W.J.M. Mulder, G.J. Strijkers, G.A.F. van Tilborg, A.W. Griffioen, and K. Nicolay, *NMR Biomed.*, **2006**. *19* (1): p. 142-164.
46. G.M. Lanza, P.M. Winter, S.D. Caruthers, M.S. Hughes, T. Cyrus, J.N. Marsh, A.M. Neubauer, K.C. Partlow, and S.A. Wickline, *Nanomedicine*, **2006**. *1* (3): p. 321-329.
47. W.J. Mulder, G.J. Strijkers, J.W. Habets, E.J. Bleeker, D.W. van der Schaft, G. Storm, G.A. Koning, A.W. Griffioen, and K. Nicolay, *Faseb J.*, **2005**. *19* (14): p. 2008-10.
48. P.C. Brooks, R.A.F. Clark, and D.A. Cheresh, *Science*, **1994**. *264* (5158): p. 569-571.
49. G.A.F. van Tilborg, W.J.M. Mulder, N. Deckers, G. Storm, C.P.M. Reutelingsperger, G.J. Strijkers, and K. Nicolay, *Bioconjug. Chem.*, **2006**. *17* (3): p. 741-749.
50. W.J.M. Mulder, G.J. Strijkers, K.C. Briley-Saboe, J.C. Frias, J.G.S. Aguinaldo, E. Vucic, V. Amirbekian, C. Tang, P.T.K. Chin, K. Nicolay*, et al.*, *Magn. Reson. Med.*, **2007**. *58* (6): p. 1164-1170.
51. B.A. Kaufmann, J.M. Sanders, C. Davis, A. Xie, P. Aldred, I.J. Sarembock, and J.R. Lindner, *Circulation*, **2007**. *116* (3): p. 276-284.
52. M. Stroh, J.P. Zimmer, D.G. Duda, T.S. Levchenko, K.S. Cohen, E.B. Brown, D.T. Scadden, V.P. Torchilin, M.G. Bawendi, D. Fukumura*, et al.*, *Nat. Med.*, **2005**. *11* (6): p. 678-682.
53. H.X. Xu, M.Y. Sha, E.Y. Wong, J. Uphoff, Y.H. Xu, J.A. Treadway, A. Truong, E. O'Brien, S. Asquith, M. Stubbins*, et al.*, *Nucleic Acids Res.*, **2003**. *31* (8): p. e43 1-10.
54. S. Pathak, M.C. Davidson, and G.A. Silva, *Nano Lett.*, **2007**. *7* (7): p. 1839-1845.
55. W.J. Mulder, G.J. Strijkers, A.W. Griffioen, L. van Bloois, G. Molema, G. Storm, G.A. Koning, and K. Nicolay, *Bioconjug. Chem.*, **2004**. *15* (4): p. 799-806.
56. H.W. Kang, L. Josephson, A. Petrovsky, R. Weissleder, and A. Bogdanov, Jr., *Bioconjug. Chem.*, **2002**. *13* (1): p. 122-7.
57. G.A. van Tilborg, W.J. Mulder, P.T. Chin, G. Storm, C.P. Reutelingsperger, K. Nicolay, and G.J. Strijkers, *Bioconjug. Chem.*, **2006**. *17* (4): p. 865-8.

Samenvatting in het Nederlands

De letterlijke vertaling van de term “Quantum Dots” in het Nederlands is “Kwantum Punten”, maar daarmee wordt voor een breed publiek niet meteen duidelijk waar dit proefschrift over gaat. Het doel van deze samenvatting is om zo eenvoudig mogelijk uit te leggen wat er in de negen voorgaande hoofdstukken beschreven is. Zo kan de lezer een indruk krijgen van wat Quantum Dots (QDs) zijn, hoe je ze kunt maken en bestuderen en wat je er mee kunt. Zoals de titel doet vermoeden, bestaat het gepresenteerde werk uit zowel fundamenteel onderzoek aan QDs (hoofdstukken 2 t/m 6), als de toepassing ervan in biomedisch onderzoek (hoofdstukken 7, 8, en 9).

Het aantal atomen waaruit bijvoorbeeld een schroefje (metaal), de chip in een mobiele telefoon (halfgeleider), een glazen fles (isolator), of een appel (organisch materiaal) is opgebouwd is nagenoeg ontelbaar. Zelfs wanneer je deze voorwerpen steeds kleiner en kleiner maakt tot een paar micrometer (een haar is ongeveer dertig micrometer dik), dan nog bestaat het uit ongeveer honderd miljard atomen. Pas als je dat nogmaals duizend keer zo klein maakt, dan is het aantal atomen waaruit je objectje (kristal) bestaat te tellen: ongeveer honderd tot duizend. Het metalen of halfgeleider voorwerpje is dan nog maar een paar nanometer groot, en wordt daarom ook wel een *nanokristal* genoemd. Een quantum dot is een voorbeeld van zo’n nanokristal, gemaakt van halfgeleider materiaal zoals zinkoxide, cadmiumtelluride, of loodselenide.

De eigenschappen van een materiaal veranderen normaal gesproken niet als je ze kleiner maakt. Zo zijn het smeltpunt en de kleur van een goudstaafje dezelfde als die van een korreltje goud. Dit gaat niet langer op als het object slechts een paar nanometer klein is. Het feit dat het kristalletje nog maar uit een paar honderd atomen bestaat, zorgt ervoor dat de eigenschappen van het deeltje ineens wél afhankelijk zijn van de grootte. Maar welke eigenschappen veranderen? In het geval van QDs is dat onder andere de kleur. Het licht wat kan worden opgenomen (geabsorbeerd) door een materiaal hangt af van de energie die elektronen in een materiaal kunnen hebben. In een halfgeleider is een met elektronen gevulde band gescheiden van een lege band (bij hogere energie) door de zogenaamde bandafstand. Licht met een energie (kleur) kleiner dan de bandafstand kan niet worden geabsorbeerd, licht boven die energie wel. Het licht dat niet wordt geabsorbeerd wordt weerkaatst (gereflecteerd), en dat bepaalt de kleur die wij als mens waarnemen.

De energiestructuur van de halfgeleider verandert als het uit nog maar een paar honderd atomen bestaat: de bandafstand wordt groter naarmate de deeltjes kleiner worden. Dit betekent ook dat de kleur licht die de QDs kunnen absorberen verandert, evenals de kleur die quantum dots kunnen uitstralen (fluorescentie). Dit zorgt er voor dat QDs van één materiaal alle kleuren van de regenboog kunnen aannemen door eenvoudigweg de grootte te variëren. Zo stralen cadmiumselenide (CdSe) QDs met een grootte van 6 nanometer rood licht uit, van 5 nanometer oranje licht, van 4 nanometer geel licht, van 3 nanometer groen licht en van 2 nanometer blauw licht. Door deze unieke eigenschap van QDs wordt gespeculeerd dat ze in de toekomst voor veel verschillende toepassingen gebruikt gaan worden, bijvoorbeeld voor displays, LEDs, zonnecellen, lasers en biomarkers. Daarvoor zijn

echter nog wel wat drempels te nemen; de meest gebruikte en best ontwikkelde QDs zijn gebaseerd op giftige componenten zoals cadmium of lood, en zijn nog steeds gevoelig voor zuurstof en water.

Hoe worden QDs gemaakt? Door bij een hoge temperatuur (250 °C) de losse chemische uitgangsstoffen van QDs heel snel samen te voegen in een oplosmiddel ontstaan er kleine kiemkristalletjes. Deze kiemkristallen worden onmiddellijk omringd door een schilletje van moleculen die sterk binden aan het oppervlak van deze minuscule QDs. Binnen het schilletje groeit de QD langzaam verder doordat soms een molecuul van het oppervlak afgaat en er nieuw materiaal voor de kristalgroei kan worden aangevoerd. Door de temperatuur en de moleculen in het oplosmiddel te veranderen kan de grootte en de vorm van de QDs worden beïnvloed. In hoofdstuk 2 van het proefschrift wordt uitgelegd hoe een kleine verontreiniging van azijnzuur in het synthesemengsel voor loodselenide (PbSe) QDs zorgt voor stervormige, in plaats van ronde nanodeeltjes. Door de temperatuur en duur van de synthese te variëren kunnen ook kubische PbSe nanodeeltjes gemaakt worden. Na synthese kunnen de deeltjes met een elektronenmicroscoop bestudeerd worden. Het blijkt dat de bolletjes, sterretjes en kubusjes zich automatisch ordenen in hele mooie gelijkmatige roosters. Vervolgens is de energiestructuur van deze PbSe QDs bestudeerd door alle details in het licht absorptie spectrum van een oplossing van deze deeltjes te analyseren. Hoofdstuk 3 beschrijft hoe dit voor QDs variërend van 3 tot 11 nanometer is onderzocht. Dit heeft tot nieuw inzicht geleid met betrekking tot de grootteafhankelijkheid van de energiestructuur en absorptie van hoogenergetisch (UV) licht in PbSe QDs.

Hoofdstuk 4 en 5 beschrijven wat er gebeurt met de lichtgevende eigenschappen van QDs als je ze zó dicht bij elkaar brengt dat ze elkaar kunnen “voelen”. Door deze interactie tussen QDs kan de energie van het geabsorbeerde licht in de ene QD worden overgedragen naar een naburige QD. Met behulp van optische spectroscopie, waarbij naar de licht absorptie en tijdsafhankelijke fluorescentie van de QDs wordt gekeken, is deze energieoverdracht aangetoond en kon de snelheid waarmee energieoverdracht plaatsvindt worden vastgesteld. Daartoe zijn eerst cadmiumtelluride (CdTe) QDs gemaakt, en in oplossing aan elkaar gekoppeld door middel van moleculen die aan twee kanten sterk aan een QD binden. De structuur en lengte van deze zogenaamde koppelmoleculen is gevarieerd om te kijken naar de afstandsafhankelijkheid van de energieoverdracht. Hoewel de energieoverdracht tussen in oplossing gekoppelde QDs duidelijk is aangetoond, was er geen verschil te zien tussen de verschillende koppelmoleculen. Wel bleek dat de mate waarin de koppelmoleculen daadwerkelijk QDs aan elkaar verbinden afhangt van de stijfheid van het betreffende koppelmolecuul; flexibele moleculen kunnen loops vormen op één QD door met beide kanten aan dezelfde QD te binden en koppelen daardoor veel minder efficiënt dan stijve moleculen.

De moleculen aan het oppervlak van QDs zorgen ervoor dat de deeltjes oplosbaar zijn en niet meteen samenklonteren. Deze moleculen (ook wel liganden genoemd) kunnen worden uitgewisseld door andere moleculen, waardoor de QDs bijvoorbeeld oplosbaar worden in water, in plaats van een hydrofoob oplosmiddel zoals tolueen. De uitwisseling van oppervlakteliganden kan ook de lichtgevende eigenschappen van QDs beïnvloeden. In hoofdstuk 6 staat beschreven hoe deze uitwisseling nauwkeurig gevolgd kan worden, door tijdens het toevoegen van het vervangende ligand (thiolen) de fluorescentie van de CdSe QDs te meten. De

intensiteit van de fluorescentie van de QDs gaat drastisch omlaag als de originele liganden (amines, phosphines, en phosphineoxides) vervangen worden door thiolen. Door deze verandering *in situ* te meten bij verschillende temperaturen en ligandconcentraties, is er een gedetailleerd inzicht verkregen in de snelheid van uitwisseling van oppervlaktemoleculen, de sterkte waarmee ze op het QD-oppervlak binden, en de ligging van het chemisch evenwicht tussen de verschillende moleculen.

De enige bestaande commerciële toepassing van QDs is als fluorescerend label voor bio-imaging. QDs lichten fel op en kunnen zo als contrastmiddel worden gebruikt om ziektebeelden in beeld te brengen door bijvoorbeeld specifiek aan een tumor te laten binden. Hoofdstuk 7 beschrijft de synthese van QDs die niet alleen zichtbaar zijn door middel van hun fluorescentie, maar ook te zien zijn in een MRI scanner. Hiertoe zijn de QDs ingekapseld in een dunne laag van vetmoleculen (een micel van lipiden), die verschillende functionaliteiten kunnen bevatten. Zo zijn de QDs ingekapseld in een combinatie van magnetische lipiden (voor contrast in de MRI scanner), lichaamseigen lipiden (zodat het deeltje niet meteen wordt afgebroken), en biofunctionele lipiden (zodat ze specifiek aan bijvoorbeeld een tumor kunnen binden). Hoofdstuk 7 laat zien dat de multifunctionele QDs inderdaad te zien zijn met fluorescentie microscopie en MRI en dat ze specifiek door cellen die rondom tumoren zitten worden opgenomen. Zulke deeltjes die met twee technieken detecteerbaar zijn worden ook wel bimodale contrastmiddelen genoemd.

Om bovenstaand idee uit te breiden, is er gekeken of “dragerdeeltjes” gebruikt kunnen worden om nog eenvoudiger de verschillende functionaliteiten te combineren. Als dragermateriaal zijn kleine glasbolletjes (silicadeeltjes) van ongeveer 40 nanometer gebruikt. Om te beginnen zijn hiertoe eerst luchtstabiele QDs gesynthetiseerd, en vervolgens in silica nanodeeltjes ingebouwd. Hoofdstuk 8 onthult hoe het komt dat de QDs precies in het midden van de silicadeeltjes terecht komen. Door middel van optische spectroscopie kon worden aangetoond dat de moleculen die reageren tot glas heel snel aan het oppervlak van de QDs binden, en zo de oorspronkelijke liganden vervangen. Dit proces is vele malen sneller dan de aangroei van het glas zelf, waardoor de QDs met daarop de silica precursor-moleculen als groeikernen dienen. Hierdoor bevat uiteindelijk ieder silica nanodeeltje precies één QD, exact in het midden.

Hoofdstuk 9 beschrijft hoe de silica nanodeeltjes met ingebouwde QDs zijn gebruikt als multimodaal contrast middel. Om de glasdeeltjes biotoepasbaar te maken is eerst een hydrofobe laag om het silica aangebracht, waarna ze omringd kunnen worden met een laag van functionele vetmoleculen, vergelijkbaar met de laag omschreven in hoofdstuk 7. Ook deze deeltjes geven dus licht, zijn te detecteren met een MRI scanner, en binden specifiek aan cellen die rondom een tumor zitten. Het voordeel is echter dat er nog meer functies in en rondom de silicadeeltjes kunnen worden toegevoegd. Zo kunnen er naast QDs ook ijzeroxide of goud nanodeeltjes worden toegevoegd, die zichtbaar zijn in een MRI of CT scanner. Verder is de hoeveelheid contrastmiddel per deeltje groter, eenvoudigweg doordat de glasbolletjes groter zijn. Een ander voordeel is dat de grootte van de glasbolletjes heel nauwkeurig gevarieerd kan worden tussen de 40 nanometer tot wel een paar micrometer. Daarnaast wordt gedemonstreerd dat de glasbolletjes mét lipide-laag veel langer in de bloedbaan van muizen blijven circuleren dan bolletjes zonder deze coating. Dit laat zien dat de lipide-laag om de glasbolletjes

daadwerkelijk bijdraagt aan een betere bio-compatibiliteit, en dat de deeltjes veelbelovend zijn als een nieuw platform voor multimodale contrast middelen. Om de flexibiliteit van dit concept te illustreren, wordt aan het slot van hoofdstuk 9 een deeltje beschreven dat niet alleen detecteerbaar is met een MRI scanner en fluorescentie microscopie, maar ook contrast geeft in een CT scanner. Dit trimodale deeltje is gebaseerd op een goud nanodeeltje in een glasbolletje, dat omgeven is door een laag van lichtgevende, magnetische, en lichaamseigen vetmoleculen.

Acknowledgements

A persistent prejudice about doing a PhD project is that it would be so specialized that the student becomes isolated and “is the only one who really knows what his research is about”. I would like to thank my supervisors Andries Meijerink and Daniel Vanmaekelbergh for showing that this statement can be very wrong. One of the first things that will occur to the careful reader of this thesis is the wide variety in research topics. I am grateful to my supervisors for giving me so much freedom in which direction to go with my research, and for continuously being up to date and interested in the different projects that were running. Also personally it was a great pleasure to have worked for you the past four years. Daniel, our numerous tennis games are memorable, and I will never forget your fanatic and perseverant way of playing. Andries, I truly enjoined our trip to the Nanax 2 conference in Grenoble, not to mention the unforgettable days in Chateau St. Gerlach. I would like to thank both of you for the professional, pleasant, and close supervision.

Apart from the luxury of two complementary promotores, I was lucky to have Celso de Mello Donegá as my co-promotor. Your close, hands-on supervision was always useful and also prevented me from doing useless or silly experiments in the lab. The extensive discussions we had were always interesting and instructive, and especially your chemical input was valuable to me.

The multidisciplinary work described in this thesis could never have been accomplished without the help of collaborators. Special thanks go out to three persons. First of all, I would like to thank Arjan Houtepen for all the black magic we did together with the PbSe materials. I have experienced our collaboration as highly complementary and learned a lot from your thorough and meticulous scientific approach. Next, I would like to thank Peter Liljeroth for everything he taught me since he supervised me as a Master student. This supervision has never really stopped and you are responsible for an important part of my scientific development, more than you may think. Arjan and Peter, I am happy that our pseudo-intellectual discussions haven’t stopped so far, and I hope we will continue to do so in the future. Besides all the alcoholic consumptions we shared, I have special memories to the three bottles of champagne that we have opened together. Last but not least, many thanks go out to Willem Mulder for the exciting and rather successful collaboration we had. I will never forget your first sentence you spoke to me on the telephone: “jij bent toch die jongen die van die quantum dots maakt?”. A week later we were together in the lab, and two weeks later I was sitting in a hospital (in between umbilical cords) looking through a microscope at my QDs in cells. Only a few months later we published our first paper that became the most cited Nano Letters of that year. The collaboration after that has been at least as exciting, and I can’t thank you enough for letting us stay in your apartment in New York.

I have had the luxury and great pleasure to supervise four excellent Master students who have all made an important contribution to this thesis. Stefan, it was exciting to supervise you so early in my PhD project, and admire your persistence in making dozens of McFarland cells. Bob, I will not forget the precision, discipline, and enthusiasm you used to perform all your cross-link experiments. Your hard

work also resulted in a serious scientific disappointment that we experienced together, which I think was instructive for the both of us. Jan, I have enjoined your unique and silent, yet highly efficient and independent way of working. Your work has resulted in at least two chapters of this thesis, and sometimes I doubted if it was really necessary to supervise you. Matti, I think there are only a few students that have been so productive during their Master research. Your broad scientific talent has resulted in an excellent piece of work and many papers, and it was both exciting and challenging to supervise you. I also thank Pepijn for his enthusiastic contribution during his Bachelor research.

I would like to thank all the members of the CMI group for the nice and pleasant working atmosphere they have created during the past years. Special thanks go out to my roommate Dennis for providing me with a daily dose of humour, and for being patient enough to deal with my busy presence. Technical assistance from Hans is greatly appreciated, as well as our numerous cups of coffee and relaxing conversations. Many thanks to Sander Wuister for getting me started with the QD work in the beginning of my PhD. I would like to thank Stephan for his work at the TEM and adequate help with the IT-related problems. I have enjoined and learned a lot from the instructive and complementary lectures from Cees Ronda and Harold de Wijn.

In addition I would like to thank the following collaborators who have scientifically contributed to this thesis: Christophe Delerue and Guy Allan from France for the tight binding calculations; Masanori Tachiya from Japan for his spontaneous and fruitful suggestion; Hans Meeldijk for his patience and excellent work at the TEM; Stephen Hickey from Germany for teaching us how to make PbSe QDs; Philipp Schapotschnikow, René Pool, and Thijs Vlugt for performing various calculations; Dannis ‘t Hart and Alfons van Blaaderen for showing us around in the world of silica colloids; Mark Klokkenburg and Ben Erné for the short but efficient collaboration; Zahi Fayad, Klaas Nicolay, Arjan Griffioen, Gustav Strijkers, and all others that have contributed to the bio-related work described in this thesis; and of course all the partners within Fullspectrum for the interesting and pleasant meetings and various projects.

Finally, I would like to thank all the people that have supported me during my PhD in a non-scientific way. Resetting my mind by means of social activities, music, and sports was crucial and I would like to thank everybody who has entertained me in any of these ways. I am more than grateful for the unconditional support from my parents and brothers. Finally, I would like to thank Chantal for keeping me from work once in a while when necessary, taking care during busy times, and your interest in my work (you even understand the definition of a bandgap!). And Daan, you just made it in time so that I can also mention you in my thesis. Wonderful.

List of Publications

This thesis is based on the following publications:

Chapter 1:

- R. Koole, W.J.M. Mulder, M.M. van Schooneveld, G.J. Strijkers, A. Meijerink and K. Nicolay, *Magnetic Quantum Dots for Multimodal Imaging.* Wiley Interdisciplinary Reviews: Nanomedicine **2008**.

Chapter 2:

- A.J. Houtepen, R. Koole, D.L. Vanmaekelbergh, J. Meeldijk and S.G. Hickey, *The Hidden Role of Acetate in the PbSe Nanocrystal Synthesis.* J. Am. Chem. Soc. **2006**. *128* (21): p. 6792-6793.
- M. Klokkenburg, A.J. Houtepen, R. Koole, J.W.J. de Folter, B.H. Erne, E. van Faassen and D. Vanmaekelbergh, *Dipolar Structures in Colloidal Dispersions of PbSe and CdSe Quantum Dots.* Nano Lett. **2007**. *7* (9): p. 2931-2936.

Chapter 3:

- R. Koole, G. Allan, C. Delerue, A. Meijerink, D. Vanmaekelbergh and A.J. Houtepen, *Optical Investigation of Quantum Confinement in PbSe Nanocrystals at Different Points in the Brillouin Zone.* Small **2008**. *4* (1): p. 127-133.

Chapter 4:

- R. Koole, P. Liljeroth, C. de Mello Donega, D. Vanmaekelbergh and A. Meijerink, *Electronic Coupling and Exciton Energy Transfer in CdTe Quantum-Dot Molecules.* J. Am. Chem. Soc. **2006**. *128* (32): p. 10436-10441.

Chapter 5:

- R. Koole, B. Luigjes, M. Tachiya, R. Pool, T.J.H. Vlugt, C. de Mello Donegá, A. Meijerink and D. Vanmaekelbergh, *Differences in Cross-Link Chemistry between Rigid and Flexible Dithiol Molecules Revealed by Optical Studies of CdTe Quantum Dots.* J. Phys. Chem. C **2007**. *111* (30): p. 11208-11215.

Chapter 6:

- R. Koole, P. Schapotschnikow, C. de Mello Donegá, T.J.H. Vlugt and A. Meijerink, *Time-Dependent Photoluminescence Spectroscopy as a Tool to Measure the Ligand Exchange Kinetics on a Quantum Dot Surface.* ACS Nano **2008**. *2* (8): p. 1703-1714.

Chapter 7:

- W.J.M. Mulder, R. Koole, R.J. Brandwijk, G. Storm, P.T.K. Chin, G.J. Strijkers, C. de Mello Donega, K. Nicolay and A.W. Griffioen, *Quantum Dots with a Paramagnetic Coating as a Bimodal Molecular Imaging Probe.* Nano Lett. **2006**. *6* (1): p. 1-6.

Chapter 8:

- R. Koole, M.M. van Schooneveld, J. Hilhorst, C. de Mello Donega, D.C.t. Hart, A. van Blaaderen, D. Vanmaekelbergh and A. Meijerink, *On the Incorporation Mechanism of Hydrophobic Quantum Dots in Silica Spheres by a Reverse Microemulsion Method.* Chem. Mater. **2008**. *20* (7): p. 2503-2512.

Chapter 9:

- R. Koole, M.M. van Schooneveld, J. Hilhorst, K. Castermans, D.P. Cormode, G.J. Strijkers, C. de Mello Donega, D. Vanmaekelberg, A.W. Griffioen, K. Nicolay, Z.A. Fayad, A. Meijerink and W.J.M. Mulder, *Lipid Coated Silica; a Nanoparticle Platform for Target-Specific Multimodality Imaging.* submitted **2008**.
- M.M. van Schooneveld, E. Vucic, R. Koole, Y. Zhou, J. Stocks, D.P. Cormode, C.Y. Tang, R.E. Gordon, K. Nicolay, A. Meijerink, Z.A. Fayad and W.J.M. Mulder, *Improved Biocompatibility and Pharmacokinetics of Silica Nanoparticles by Means of a Lipid Coating: A Multimodality Investigation.* Nano Lett. **2008**. *8* (8): p. 2517-2525.
- M.M. van Schooneveld, R. Koole, D.P. Cormode, C. Calgano, T. Skajaa, J. Hilhorst, D. 't Hart, Z.A. Fayad, W.J.M. Mulder and A. Meijerink, *Gold/Silica Nanoparticles Coated with Paramagnetic, Fluorescent and PEGylated Lipids: a Trimodal Contrast Agent.* submitted **2008**.

Other Publications:

- R. Koole, P. Liljeroth, S. Oosterhout and D. Vanmaekelbergh, *Chemisorption Determines the Photovoltage of a Ti/TiO2/Au/Dye Internal Electron Emission Photovoltaic Cell.* J. Phys. Chem. B **2005**. *109* (19): p. 9205-9208.
- S.F. Wuister, R. Koole, C. de Mello Donegá and A. Meijerink, *Temperature-Dependent Energy Transfer in Cadmium Telluride Quantum Dot Solids.* J. Phys. Chem. B **2005**. *109* (12): p. 5504-5508.
- K. Overgaag, W. Evers, B. de Nijs, R. Koole, J. Meeldijk and D. Vanmaekelbergh, *Binary Superlattices of PbSe and CdSe Nanocrystals.* J. Am. Chem. Soc. **2008**. *130* (25): p. 7833-7835.
- D.P. Cormode, T. Skajaa, M.M. van Schooneveld, R. Koole, P. Jarzyna, M.E. Lobatto, C. Calcagno, A. Barazza, R.E. Gordon, P. Zanzonico, E.A. Fisher, Z.A. Fayad and W.J.M. Mulder, *Nanocrystal Core High-Density Lipoproteins: A Multimodal Molecular Imaging Contrast Agent Platform.* submitted **2008**.

- W.G.J.H.M. van Sark, K.W.J. Barnham, L.H. Slooff, A.J. Chatten, A. Büchtemann, A. Meyer, S.J. McCormack, R. Koole, D.J. Farrell, R. Bose, E.E. Bende, A.R. Burgers, T. Budel, J. Quilitz, M. Kennedy, T. Meyer, S.H. Wadman, G.P.M. van Klink, G. van Koten, A. Meijerink and D. Vanmaekelbergh, *Luminescent Solar Concentrators – A review of recent results.* Submitted **2008**.

Book Chapter:

- W.J.M. Mulder, G.J. Strijkers, R. Koole, C. de Mello Donegá, G. Storm, A.W. Griffioen and K. Nicolay, *Bimodal Liposomes and Paramagnetic QD-Micelles for Multimodality Molecular Imaging of Tumor Angiogenesis.* **Nanoparticles in Biomedical Imaging:** Emerging Technologies and Applications, Eds.: Jeff W.M. Bulte & Michael M.J. Modo. Springer (2007).

Patent (pending):

- *"A Carrier Particle For Use In Bio-Applications":* R. Koole, W.J.M. Mulder, M.M. van Schooneveld, A. Meijerink, Z.A. Fayad, J. Hilhorst. (filed September 2007)

Curriculum Vitae

Rolf Koole was born on June 18th 1980 in Lomm, the Netherlands. In 1997 he obtained his high school degree ("*Gymnasium*") at the St. Thomascollege in Venlo. After high school, he spent one year at the College of the Siskiyous in California (US), where he predominantly concentrated on music, sports, and social activities. He subsequently started his study Chemistry at Utrecht University in the Netherlands in 1998, and obtained his propaedeutic diploma in 1999. In the academic year 2001-2002 he was a member of the board of the fraternity "Unitas S.R." and responsible for all finances. This was a full-time activity for which a one-year grant from the Utrecht University was received. After this he continued his study in chemistry and obtained his Master of Science degree in 2004 (*cum laude)*. His Master research was performed in the group of Condensed Matter and Interfaces (CMI) at the Utrecht University under supervision of Daniel Vanmaekelbergh, where he investigated a novel type of solid state solar cell.

After obtaining his Master Degree he joined the CMI group as a PhD student under supervision of Andries Meijerink and Daniel Vanmaekelbergh. The project was funded by the European Union ("Fullspectrum") and had the aim to search for photon-up converting materials based on semiconductor nanocrystals (quantum dots). Besides these fundamental investigations, an extended collaboration with Dr. W. Mulder from the Mt. Sinai Medical School of Medicine (New York) was established during his PhD, in which a biomedical application of quantum dots was explored. Most of the results of his PhD project are described in this thesis and published in scientific journals. Part of this work has resulted in a patent application. Oral presentations were given at several international and national conferences and meetings, and he was awarded a prize for the best oral presentation at the NanaX 3 conference in 2008 (Lecce, Italy). He received the second prize of the "DSM Science & Technology Awards 2008" for the collected work he performed during his PhD project.

During his PhD, he supervised four Master students and one Bachelor student, the analytical course of first year students, and a solar cell project for second year students.

From November 2008 he will work as a Research Scientist at Philips.